



TECHNISCHE  
UNIVERSITÄT  
WIEN

DISSERTATION

Defect chemistry in semiconductor-based  
amperometric electro- and  
photoelectrochemical devices

Ausgeführt zum Zwecke der Erlangung des akademischen Grades eines Doktors der  
Naturwissenschaften unter der Leitung von

**Prof. Dr. Dominik Eder**

E165

Institut für Materialchemie

Eingerichtet an der Technischen Universität Wien

Fakultät für Technische Chemie

von

**Paolo Rudatis**

01647959

Getreidemarkt 09/BC02 A20, 1060 Wien

Wien, am:

---

Unterschrift



*Dedicated to*

*my family, my friends, and various mentors  
met in my life journey.*

*For the shared love and inspiration.*



## Abstract

Surface and small bulk modifications of thin layers greatly affect their properties, e.g., the translation of voltage input to current output. The current intensity is a simple and processable signal, which is exploited by several devices. Some like field-effect transistors have the potential to imitate the human olfactory system; however, more generalised, to give rise to selective and sensitive detection devices for biomolecules. Nevertheless, some other devices like photoelectrochemical cells have the potential to render energy production sustainable.

On the one hand, this work focusses on simple sensing such as live pH detection with a LGFET and aims at controlling the functionalisation of GO used as channel for enhanced device sensitivities. On the other hand, the work also concentrates on the co-doping as valid synergistic approach for the performance improvement of hematite as PEC photoanodic template material.

Thermal treatments in different atmospheres lead to a less current-resistant GO which is referred to as rGO. According to the atmosphere, GO can deliver higher sensitivities to pH variations. Upon heating in protected atmosphere by means of a custom-made setup, the current intensity flowing through GO is monitored, and the arising current transients can be followed live. First, it is important that the heat is well conducted from the gas in the setup chamber, hence we see highest resistance and lowest performance upon usage of vacuum atmosphere. Upon comparison of Ar and 2.6% H<sub>2</sub>/Ar mixture, we see that H<sub>2</sub> does not affect chemically GO, though the slightly different behaviour is assigned to a much higher thermal conductivity than Ar only. By contrast, NH<sub>3</sub> affects chemically GO towards the lowest resistance and achieving remarkable pH sensitivities. These are comparable with reported rGO pH sensors, where the reducing agent was the reliable hydrazine hydrate.

The temperature ramp turns out crucial for effective defunctionalisation of GO and proper functionalisation of rGO. In fact, by applying a different synthesis method with higher ramp, NH<sub>3</sub> leads to a record pH sensitivity hovering around 60 mA pH<sup>-1</sup>. NH<sub>3</sub> might exploit its nucleophilic properties to enter the surface and the C-network of GO; while, contemporaneously, it might also exploit its great solubility and dissolve in the intercalated water that GO carries.

As earlier cited, the second main topic treats co-doping, and this is accomplished in an easy-synthesised photoanode template, *i.e.*, a hematite spin-coated thin film. It is the first time that Sb, Li co-doping is realised, and it is also the first time that direct Sb<sup>5+</sup>-doping is reported. The addition of the dopants is modest as high as a nominal at. 1%. The Sb<sup>5+</sup> oxidation state maintains in the mono- and co-doped samples and addition of Li<sup>+</sup> exhibits a

synergistic effect on the performance, which is already greatly expanded by  $\text{Sb}^{5+}$ . At 1.4 V vs RHE, the current increase is 67-fold compared to standard hematite thin film. The benefits might lie predominantly in the higher carrier concentration and a lower surface resistance. The  $J$ - $V$  curves do not suggest catalysed surface reaction. Of interest would be the application of the Fe(III)-OEC and reaction with hydrogen peroxide in the electrolyte.

Furthermore, the presence and management of  $V_0$  in  $\text{Li}^+$ -doped hematite shows curious first results, as if there would be a competition of the two species, in terms of space or photoelectrochemical contribute.

For both projects,  $I$ - $V$  or  $J$ - $V$  curve characterisation is performed on samples where single variables are sequentially altered. In the rGO FET project, GO current increase is live-monitored,  $I_{ds}V_g$  measurements are completing the final pH sensing results ( $I_{dst}$ ). In the co-doping project,  $J$ - $V$  curves are recorded without illumination, and additionally by chopping the illumination to extract more information. Results are also backed by comprehensive XPS, XRD, Raman characterisation, and moreover, by supplementary SEM and UV-Vis analysis. More characterisation and few extra sample batches are anyway needed to further strengthen what are still hypotheses.

## Zusammenfassung

Oberflächliche und kleine Bulkmodifikationen dünner Schichten beeinflussen ihre Eigenschaften stark, z. B. die Übertragung von Spannungseingang zu Stromausgang. Die Stromstärke ist ein einfaches und verarbeitbares Signal, das von mehreren Geräten verwertet wird. Einige wie Feldeffekttransistoren haben das Potenzial, das menschliche Geruchssystem zu imitieren; jedoch, allgemeiner, um zu selektiven und empfindlichen Nachweisvorrichtungen für Biomoleküle zu führen. Dennoch haben einige andere Geräte wie photoelektrochemische Zellen das Potenzial, die Energieerzeugung nachhaltig zu gestalten.

Einerseits konzentriert sich diese Arbeit auf einfache Sensorik wie die Live-pH-Detektion mit einem LGFET und zielt darauf ab, die Funktionalisierung von GO zu steuern, das als Kanal für verbesserte Geräteempfindlichkeiten verwendet wird. Andererseits konzentriert sich die Arbeit auch auf die Co-Dotierung als validen synergistischen Ansatz zur Leistungssteigerung von Hämatit als photoanodisches PEC-Templatmaterial.

Thermische Behandlungen in unterschiedlichen Atmosphären führen zu einem weniger stromfesten GO, das als rGO bezeichnet wird. Je nach Atmosphäre kann GO eine höhere Empfindlichkeit gegenüber pH-Schwankungen liefern. Beim Erhitzen in geschützter Atmosphäre mittels eines maßgeschneiderten Aufbaus wird die Stromstärke, die durch GO fließt, überwacht und die auftretenden Stromtransienten können live verfolgt werden. Erstens ist es wichtig, dass die Wärme vom Gas in der Setup-Kammer gut abgeleitet wird, daher sehen wir den höchsten Widerstand und die niedrigste Leistung bei Verwendung von Vakuumatmosphäre. Beim Vergleich von Ar und 2,6 % H<sub>2</sub>/Ar-Mischung sehen wir, dass H<sub>2</sub> GO chemisch nicht beeinflusst, obwohl das etwas andere Verhalten einer viel höheren Wärmeleitfähigkeit als nur Ar zugeschrieben wird. Im Gegensatz dazu beeinflusst NH<sub>3</sub> chemisch GO in Richtung des niedrigsten Widerstands und erreicht bemerkenswerte pH-Empfindlichkeiten. Diese sind mit berichteten rGO-pH-Sensoren vergleichbar, bei denen das Reduktionsmittel das zuverlässige Hydrazinhydrat war.

Die Temperaturrampe erweist sich als entscheidend für die effektive Defunktionalisierung von GO und die richtige Funktionalisierung von rGO. Tatsächlich führt NH<sub>3</sub> durch die Anwendung einer anderen Synthesemethode mit höherer Rampe zu einer Rekord-pH-Empfindlichkeit, die um 60 mA pH<sup>-1</sup> schwebt. NH<sub>3</sub> könnte seine nukleophilen Eigenschaften nutzen, um in die Oberfläche und das C-Netzwerk von GO einzudringen; während es gleichzeitig seine große Löslichkeit ausnutzen und sich in dem interkalierten Wasser auflösen könnte, das GO trägt.

Wie bereits erwähnt, behandelt das zweite Hauptthema Co-Dotierung, und dies wird in einer einfach synthetisierten Photoanodenschablone erreicht, d. h. einem mit Hämatit aufgeschleuderten dünnen Film. Es ist das erste Mal, dass Sb, Li-Co-Dotierung realisiert wird, und es ist auch das erste Mal, dass über direktes  $\text{Sb}^{5+}$ -Dotierung berichtet wird. Die Zugabe der Dotierstoffe ist bescheiden so hoch wie ein Nennwert 1%. Der Oxidationszustand von  $\text{Sb}^{5+}$  bleibt in den mono- und co-dotierten Proben erhalten und die Zugabe von  $\text{Li}^+$  zeigt einen synergistischen Effekt auf die Leistung, die durch  $\text{Sb}^{5+}$  bereits stark erweitert wird. Bei 1,4 V gegenüber RHE beträgt die Stromerhöhung das 67-fache im Vergleich zu Standard-Hämatit-Dünnschichten. Die Vorteile dürften vor allem in der höheren Ladungsträgerkonzentration und einem geringeren Oberflächenwiderstand liegen. Die  $J$ - $V$ -Kurven deuten nicht auf eine katalysierte Oberflächenreaktion hin. Interessant wäre die Anwendung des Fe(III)-OEC und die Umsetzung mit Wasserstoffperoxid im Elektrolyten. Darüber hinaus zeigen das Vorhandensein und die Handhabung von  $V_0$  in  $\text{Li}^+$ -dotiertem Hämatit merkwürdige erste Ergebnisse, als ob es eine Konkurrenz der beiden Spezies in Bezug auf den Platz oder den photoelektrochemischen Beitrag geben würde.

Für beide Projekte wird eine  $I$ - $V$ - oder  $J$ - $V$ -Kurvencharakterisierung an Proben durchgeführt, bei denen einzelne Variablen nacheinander geändert werden. Im rGO-FET-Projekt wird der Anstieg des GO-Stroms live überwacht,  $I_{\text{ds}}V_{\text{g}}$ -Messungen vervollständigen die endgültigen Ergebnisse der pH-Messung ( $I_{\text{ds,t}}$ ). Im Co-Dotierung-Projekt werden  $J$ - $V$ -Kurven ohne Beleuchtung aufgezeichnet und zusätzlich durch Zerhacken der Beleuchtung, um mehr Informationen zu extrahieren. Die Ergebnisse werden auch durch umfassende XPS-, XRD-, Raman-Charakterisierung und darüber hinaus durch ergänzende SEM- und UV-Vis-Analyse gestützt. Weitere Charakterisierung und einige zusätzliche Probenchargen sind ohnehin erforderlich, um die noch bestehenden Hypothesen weiter zu stärken.





# Table of contents

Abstract.....	I
Zusammenfassung.....	III
Table of contents.....	VI
List of abbreviations.....	IX
List of figures.....	XI
List of tables.....	XVI
<b>1 Introduction.....</b>	<b>3</b>
1.1 Current world challenges.....	3
1.1.1 Energy for development.....	3
1.1.2 Air pollution.....	3
1.1.3 Bioelectronic nose.....	4
1.2 Graphene oxide reduction.....	6
1.2.1 Dusted-off graphite oxide.....	6
1.2.2 Towards 2D.....	7
1.2.3 GO synthesis and structure.....	10
1.2.4 Approaches to GO reduction.....	14
1.2.5 Applications: towards sensing in liquid.....	15
1.3 Graphene-based LGFETs and pH sensing.....	16
1.3.1 Principles of FETs and LGFETs.....	17
1.3.2 Graphene-based LGFETs.....	18
1.3.3 pH sensing with FET.....	19
1.3.4 pH sensing with graphene-based LGFETs.....	20
1.4 Sb, Li co-doping in hematite-based photoanodes.....	22
1.4.1 Sunlight.....	22
1.4.2 Solar water splitting.....	24
1.4.3 Water oxidation with SC-liquid junctions.....	27
1.4.4 Material requirements.....	33
1.4.5 Hematite and co-doping.....	35
1.5 Motivation.....	37
<b>2 Materials and procedures.....</b>	<b>42</b>

2.1	Graphene oxide colloidal solution .....	43
2.2	Production of a graphene-based LGFET .....	44
2.2.1	GO deposition and anchoring.....	44
2.2.2	Graphene oxide reduction approaches .....	45
2.3	Production of hematite photoanodes.....	47
2.3.1	Synthesis of hematite thin film.....	47
2.3.2	Co-doping.....	48
3	Characterisation .....	50
3.1	Current-Voltage Characteristics .....	50
3.1.1	Principle .....	50
3.1.2	Applied in LGFET – Flow cell.....	51
3.1.3	Photocurrent-Voltage Characteristics .....	52
3.1.4	<i>In-situ</i> current monitoring.....	53
3.2	Spectroscopy .....	55
3.2.1	Fourier- transformed infrared spectroscopy (FTIR).....	55
3.2.2	Raman spectroscopy .....	56
3.2.3	UV-visible spectroscopy (UV-Vis).....	56
3.2.4	X-ray photoelectron spectroscopy (XPS) .....	57
3.3	X-ray diffraction (XRD) .....	59
3.4	Scanning electron microscopy (SEM) .....	61
3.5	Optical microscope.....	64
3.6	Profilometry .....	64
4	rGO as pH sensor in LGFETs .....	68
4.1	Introduction.....	68
4.2	Preliminary results.....	69
4.2.1	Optimisation and reproducibility <i>in-situ</i> current monitoring.....	69
4.2.2	SEM images after thermal treatment .....	71
4.2.3	For a more reliable XPS analysis .....	71
4.2.4	Raman on thermal treated GO .....	73
4.3	Effect of atmosphere in GO thermal reduction .....	74
4.3.1	Results and discussion .....	75
4.3.2	Conclusion and outlook.....	87

4.4	Linking functional groups and pH sensitivity .....	88
4.4.1	Results and discussion.....	88
4.4.2	Conclusion and outlook.....	95
4.5	Effect of heating ramp.....	97
5	Li, Sb co-doping to enhance OER in hematite photoanodes .....	102
5.1	Introduction.....	102
5.2	Results and discussion.....	104
5.2.1	UV-Vis .....	104
5.2.2	Raman spectroscopy .....	105
5.2.3	XPS analysis .....	106
5.2.4	XRD analysis .....	108
5.2.5	Photoelectrochemical performance.....	109
5.2.6	SEM analysis.....	112
5.3	Conclusion and outlook.....	112
5.4	Additional investigations .....	114
5.4.1	Effect of oxygen vacancies .....	114
5.4.2	Sb <sup>3+</sup> precursor and V <sub>o</sub> .....	118
5.4.3	Li <sup>+</sup> leaching experiments .....	121
	Bibliography .....	123
	Curriculum Vitae .....	150
	List of publications .....	151
	List of conferences.....	151
	Acknowledgements.....	153

## List of abbreviations

Abbreviation	Meaning
APTES/APTS	Aminopropyltetraethoxysilane
BE	Binding energy
CB	Conduction band
CCG/CMG	Chemically converted/modified graphene
CE	Counter electrode
CPS	Counts per second
CV	Cyclic voltammetry
CVD	Chemical vapour deposition
DI	Deionised
$E_F$	Fermi level energy
FET	Field-effect transistor
FT-IR	Fourier-transformed IR
FTO	Fluorine-doped tin oxide
GO	Graphene oxide
GO-IDE	GO anchored with APTES on IDE glass
HGO	Hummers and Offeman's graphene oxide
IDE	InterDigitated electrode
$I-V$	Current intensity-voltage characteristics
$I_{ds}/I_D$	Drain-source current
KE	Kinetic energy
$J-V$	Current density-voltage characteristics
LGFET	Liquid-gated field-effect transistor
LSV	Linear sweep voltammetry
OD	Oxidised debris
OEC	Oxygen evolution catalyst
OER	Oxygen evolution reaction
PBS	Phosphate buffer saline
PEC	Photoelectrochemical cell
PLD	Pulsed laser deposition
RE	Reference electrode
rGO/RGO	Reduced graphene oxide/cleaned from OD
RHE	Reversible hydrogen electrode
SCE	Standard calomel electrode
SAM	Self-assembled monolayer

SC	Semiconductor
SEM	Scanning electron microscopy
UV-Vis	Ultraviolet-visible light
VB	Valence band
$V_g/V_{GS}$	Gate-source applied potential
$V_0$	Oxygen vacancies
WE	Working electrode
XPS	X-ray photoelectron spectroscopy
XRD	X-ray diffraction

## List of figures

<b>Figure 1-1.</b> Current possible applications for systems based on reduced graphene oxide (here RGO). Adapted from <sup>41</sup> .....	6
<b>Figure 1-2.</b> A scheme of the three typical synthetic steps from raw material, graphite, to final product, reduced graphene oxide (or here CCG). Graphite is oxidised to graphite oxide and 3D structure is maintained. The exfoliation stage allows the separation of monoatomic layers, accessing the world of 2D and graphenic material. Graphene oxide can be stored in stable water colloidal suspensions and be reduced before usage or once deposited on surfaces. Adapted from <sup>38</sup> .....	8
<b>Figure 1-3.</b> Graphite oxide crystals separation, during “swelling” after mixing with diluted NaOH solution Adapted from <sup>76</sup> .....	10
<b>Figure 1-4.</b> The GO structures that have been proposed over the years. From <sup>83</sup> .....	13
<b>Figure 1-5.</b> a) Schematic of a typical transistor. b) <i>I-V</i> characteristics of the typical transistor to the left. On the two y-axes the drain current in log ( $\log I_D$ ) and in linear scale ( $I_D$ ), and on the x-axis the applied gate-source voltage ( $V_{GS}$ ). Adapted from <sup>170</sup> .....	18
<b>Figure 1-6.</b> a) Proposed reaction mechanism of APTS/APTES with GO. From <sup>36</sup> b) Single unit of APTES once the bonds with the transistor glass are formed. ....	21
<b>Figure 1-7.</b> a) World map of the specific photovoltaic power output. Adapted from <sup>194</sup> . b) Irradiance and spectrum of the solar radiation reaching the earth crust. Adapted from <sup>195</sup> ..	23
<b>Figure 1-8.</b> a) Typical semiconductors and their band gaps in respect to the water reduction and oxidation thermodynamic potentials. b) Representation of light absorption by a semiconductor towards overall water splitting. c) Schematic of the water splitting kinetics of a nanoparticle attempting overall water splitting. All adapted from <sup>196</sup> .....	25
<b>Figure 1-9.</b> a) Schematic of the depletion layer formation in junction SC/electrolyte A. SC has a Fermi level energy $E_F$ , while the electrolyte has an electrochemical potential $E(A/A^-)$ . b) Schematic of depletion layer formation in the same SC in junction with a different electrolyte B having electrochemical potential $E(B/B^-)$ . c) Representation of the SC band bending with the respective energy quantities. The created depletion layer is expressed by the depletion width, $W$ . Modified from <sup>201</sup> .....	28
<b>Figure 1-10.</b> Schematic of the two conditions of a photoanode. a) When a positive voltage is applied ( $V>0$ ) b) When a negative voltage is applied ( $V<0$ ). The applied voltage can only affect the A transfer, while $A^-$ is constant. Adapted from <sup>201</sup> .....	29
<b>Figure 1-11.</b> Theoretical maximum photocurrent ( $J_{max}$ ) as a function of the band-gap. ....	34
<b>Figure 2-1.</b> a) Representation of the purchased IDEs and zoom-in of the electrochemical cell. Modified from products brochure <sup>256</sup> . b) Production steps from empty IDE to rGO-IDE. ....	44

**Figure 2-2.** Picture of the two spin-coating solutions. On the left the standard one, whereas on the right the same solution with 100  $\mu\text{L}$  HCl addition.....48

**Figure 3-1.** a) Representation of the functioning LGFET during pH sensing operations. b) Picture of the real LGFET from outside. The inlet and outlet tubing for the 0.1x PBS electrolyte is visible, as well as, the gate rod, sealed and pointing down to where the IDE electrochemical cell will be placed. ....51

**Figure 3-2.** a) Current-voltage curves with photoanodes, light on (curve 1) and light off (curve 2). From <sup>197</sup>. b) Schematic of the photoelectrochemical cell with anode, photoanode, and the thermodynamics of the half reactions to enable water splitting. c) The three electrodes for photoelectrochemical characterisation and beaker with the 0.1M NaOH electrolyte.....52

**Figure 3-3.** a) Representation of the effect of an X-ray photon on an atom. b) A simplified scheme of an XPS apparatus and its main components. ....58

**Figure 3-4.** Schematic of the XRD working principle. ....61

**Figure 3-5.** a) Shining a sample with an electron beam provokes various phenomena. Three of them are exploited by TEM and the rest by SEM. b) The different emissions (electrons or X-rays) are originated at different sample depths and the sections have different sizes (bulb shape). ....62

**Figure 4-1.** a) One of the first samples to be live monitored during the thermal treatment. On y-axes current and temperature, on x-axis the time in minute. b) To check the reproducibility of the process several samples were treated in  $\text{H}_2/\text{Ar}$  atmosphere using a temperature ramp selected by means of the first experiments. c) By plotting the logarithm base 10 of the current, the starting current is visible. Contacting issues may cause signal instability. ....69

**Figure 4-2.** SEM micrographs of GO on IDE after the typical thermal treatment with  $\text{H}_2/\text{Ar}$  atmosphere ( $10^\circ\text{C min}^{-1}$  cooling/heating and max T 310 for 40 min). a) Micrograph at 500x magnification. b) Micrograph at 10'000x magnification.....71

**Figure 4-3.** Raman spectra of GO and rGOs. The measurements were carried out directly on the GO-IDE, which is noticeable by the upper tight image in every plot. To increase the reproducibility two spots of the samples were measured.....73

**Figure 4-4.** a) Current monitoring of thermal treatment conducted in presence of 4 atmospheres, such as vacuum (dark yellow), Ar (red),  $\text{H}_2/\text{Ar}$  (green), and  $\text{NH}_3$  (blue). In addition, the plot has been split in 4 chronological phases of different colours according to the temperature ramp changing points, namely, heating is the I phase (violet), holding the II phase (orange), cool-controlled the III phase (green), and cooling-uncontrolled as too slow the IV phase (red). b) Resistance and standard deviation of rGOs after the respective



thermal treatment in the 4 atmospheres. The colours are identical, *i.e.*, vacuum (dark yellow), Ar (red), H<sub>2</sub>/Ar (green), and NH<sub>3</sub> (blue).....75

**Figure 4-5.** a) *I-V* characteristics of LGFETs through rGOs after the respective GO thermal treatment in the 4 atmospheres. The gate voltage is swept between -0.8 and 0.8 V, whereas 0.1 V are applied between source and drain. Colours show continuity, specifically, vacuum (dark yellow), Ar (red), H<sub>2</sub>/Ar (green), and NH<sub>3</sub> (blue). b) Baseline control of LGFETs by applying a constant gate voltage -0.4 V and usual 0.1 V between source and drain.....77

**Figure 4-6.** a) XPS survey spectra of GO and rGO treated thermally in different atmospheres. b)c)d)e)f) C1s region detail spectra of GO and rGOs. g) N1s region detail spectra of NH<sub>3</sub>-rGO. ....80

**Figure 4-7.** In-situ XRD patterns of GO under thermal treatment in 4 atmospheres. To better explain what I peak and II peak are, a and b figures are added. a) XRD pattern of GO treated in vacuum atmosphere at 200°C temperature stage. b) XRD pattern of GO treated in vacuum atmosphere at temperature 250°C stage. c) XRD patterns at increasing temperatures in vacuum 3\*10<sup>-3</sup> mbar atmosphere. d) XRD patterns at increasing temperatures in 100% Ar atmosphere. e) XRD patterns at increasing temperatures in 100% H<sub>2</sub> atmosphere. f) XRD patterns at increasing temperatures in 100% NH<sub>3</sub> atmosphere. g) Trend of the observed peaks in XRD patterns in function of the temperature.....82

**Figure 4-8.** a) pH sensing response expressed in  $\Delta I_{ds} \mu A^{-1}$  vs time and obtained with a LGFET by applying a gate voltage -0.4 V and a source-drain voltage of 0.1 V. Different rGOs are employed in LGFET and come from different atmospheres, that is, vacuum (dark yellow), Ar (red), and NH<sub>3</sub> (blue). H<sub>2</sub>/Ar (green) is excluded due to high similarity with Ar. b) pH sensing response expressed in  $\Delta I_{ds} \mu A^{-1}$  vs pH value to underline the pH sensitivity of the diverse LGFETs. ....85

**Figure 4-9.** a) *I-V* characteristics of LGFETs through rGOs obtained with NH<sub>3</sub> atmosphere and two diverse thermal treatments, *i.e.*, in blue NH<sub>3</sub>, in purple NH<sub>3</sub> Schlenk. The gate voltage is swept between -0.8 and 0.8 V, whereas 0.1 V is applied between source and drain. b) pH sensing response expressed in  $\Delta I_{ds} \mu A^{-1}$  vs time. It is obtained with a constant applied gate voltage -0.4 V and an applied source-drain voltage of 0.1 V. The blue line represents NH<sub>3</sub> rGO, while the purple line denotes the NH<sub>3</sub> Schlenk rGO. c) pH sensing response expressed in  $\Delta I_{ds} \mu A^{-1}$  vs pH value to underline the pH sensitivity of the diverse LGFETs. ....89

**Figure 4-10.** a) XPS survey spectra of NH<sub>3</sub>-rGOs treated in setup and in Schlenk tube. b)c)d) C1s region detail spectra of NH<sub>3</sub>-rGOs.....91

**Figure 4-11.** O1s detail spectra of a)GO, b)NH<sub>3</sub>, and c)NH<sub>3</sub> Schlenk.....92

**Figure 4-12.** N1s detail spectra of a)NH<sub>3</sub> and b)NH<sub>3</sub> Schlenk with the respective components percentages in c) and d). ....93

**Figure 4-13.** a) Current monitoring measurement in presence of H<sub>2</sub>/Ar with extremely low heating /cooling rate 0.5°C min<sup>-1</sup> and holding T at 310°C for 40 min. Current monitoring measurements with additional step b) at 150°C with heating/cooling 10°C min<sup>-1</sup>, c) at 180°C with heating/cooling 10°C min<sup>-1</sup>, and d) at 180°C with heating at 50°C min<sup>-1</sup>. .....97

**Figure 5-1.** UV-Vis light absorption spectra of the hematite photoanodes vs clean FTO glass slide..... 104

Figure 5-2. a) Micro-Raman spectra of standard, Sb mono-doped, Li mono-doped, and Sb, Li co-doped samples. .... 105

**Figure 5-3.** a) XPS survey spectrum of the standard hematite sample. b) Fe element XPS detail spectrum of the standard sample. c) O, Sb elements XPS detail spectrum of the standard sample. d) O, Sb elements XPS detail spectrum of the Li mono-doped sample. e) O, Sb elements XPS detail spectrum of the Sb mono-doped sample f) O, Sb elements XPS detail spectrum of the Sb, Li co-doped sample. .... 107

**Figure 5-4.** a) XRD patterns of standard sample, Sb and Li mono-doped samples, and Sb, Li co-doped sample. b) Zoom-in on the (110) diffraction peak of plot figure 4a, range 2θ 37.0-39.0°..... 108

**Figure 5-5.** a) J-V curves light and dark recorded in 0.1 M NaOH with calomel electrode and Pt cathode. Light curves were carried out under a simulated solar light illumination of 100 mW cm<sup>-2</sup>. b) Details of current densities at high applied voltages (Faradaic regime). c) Light J-V curves recorded by chopping the light illumination. .... 109

**Figure 5-6.** SEM micrographs side view of broken photoanodes for thickness confirmation. .... 112

**Figure 5-7.** a) Detail of small oven fracture and glowing at extremely high T. b) Reported real temperature in the stove at a given set temperature. c) UV-Vis light absorption spectra of the hematite photoanodes standard sample, Std (solid line), and standard sample with higher amount of oxygen vacancies, Std (V<sub>0</sub>) (dotted line). d) Raman spectra of Std (violet) and Std (V<sub>0</sub>) (dark cyan) samples. e) XPS detail envelope spectra of O1s signal of Std and Std (V<sub>0</sub>). f) XRD patterns with focus on (110) peak of Std and Std (V<sub>0</sub>). g) J-V curves of Std and Std (V<sub>0</sub>) light and dark recorded in 0.1 M NaOH with calomel electrode and Pt cathode. Light curves were carried out under a simulated solar light illumination of 100 mW cm<sup>-2</sup>. h) Details of Std and Std (V<sub>0</sub>) light and dark current densities at high applied voltages (Faradaic regime). i) Light J-V curve of Std sample recorded by chopping the light illumination. j) Light J-V curve of Std (V<sub>0</sub>) sample recorded by chopping the light illumination..... 115

**Figure 5-8.** a) UV-Vis light absorption spectra of the hematite photoanodes, that is, Std (red solid line), Sb<sup>3+</sup> (blue dash dot), Li<sup>+</sup> (violet short dash), and Sb, Li (orange short dot). and standard sample with higher amount of oxygen vacancies, Std (V<sub>0</sub>) (dotted line). b) Micro-

Raman spectra of compared photoanodes, Std (red),  $\text{Sb}^{3+}$  (blue),  $\text{Li}^+$  (violet), and Sb, Li (orange). c)  $J$ - $V$  curves light and dark recorded in 0.1 M NaOH with calomel electrode and Pt cathode. Light curves were carried out under a simulated solar light illumination of  $100 \text{ mW cm}^{-2}$ . The sample performance under illumination are coloured, *i.e.*, Std (red),  $\text{Sb}^{3+}$  (blue),  $\text{Li}^+$  (violet), and Sb, Li (orange), while in the dark samples have thin black lines. d) Details of current densities at high applied voltages (Faradaic regime) in light and dark. e) Details of dark current densities of Std and  $\text{Li}^+$  samples at high applied voltages (Faradaic regime) with and without  $V_0$ ..... 119

**Figure 5-9.** a)  $J$ - $V$  curves light and dark recorded in 0.1 M NaOH and 0.01 M LiCl with calomel electrode and Pt cathode. Light curves were carried out under a simulated solar light illumination of  $100 \text{ mW cm}^{-2}$ . The sample performance under illumination and Li-buffered are coloured, *i.e.*, Std (red),  $\text{Sb}^{3+}$  (blue),  $\text{Li}^+$  (violet), and Sb, Li (orange), while in the dark samples have thin black lines. Sb, Li sample measured in electrolyte 0.1 M NaOH for comparison has dark green line. b) Details of current densities at high applied voltages (Faradaic regime) in light and dark in Li-buffered electrolyte and non-buffered. c) Light  $J$ - $V$  curve of Sb, Li sample in Li-buffered electrolyte recorded by chopping the light illumination. d) Light  $J$ - $V$  curve of Sb, Li sample in non-buffered electrolyte recorded by chopping the light illumination..... 121

After adding LiCl to a final 0.01 M concentration into the usual NaOH 0.1 M electrolyte, it is measured one more time the samples of Chapter 5. As a result, the trend is maintained while the photoactivity is generally lower (**figure 5-9a**). The gauged photocurrent at 1.4 V vs RHE goes from  $0.11$  to  $0.07 \text{ mA cm}^{-2}$ , which translates into a 1.6-fold or a 36% relative reduction. In Faradaic regime, it is still noticeable a general decrease, which is represented by the gap amongst stars and tilted squares (**figure 5-9a**). Also, the gap between  $\text{Li}^+$  mono-doped and Std decreases, not reaching anymore  $\sim 1.5 \text{ mA cm}^{-2}$ , but stopping at  $\sim 1.0 \text{ mA cm}^{-2}$ . By comparing the chopped  $J$ - $V$  light curves in **Figure 5-9c** and d,  $s/c$  and  $f/c$  ratios both augment with  $\text{Li}^+$  buffering. The most prominent growth is the  $s/c$  ratio 1.10 to 1.81, whereas the  $f/c$  ratio raises 2.00 to 2.21. The former one indicates a clear increase in recombination between CB electrons with surface holes (trapped or in form of oxidised species). The latter one suggests a moderately lower charge transfer efficiency at the interface. Furthermore, it must be said that the photoanodes might experience an aging, which is up to now uncertain, as aging experiments are yet to be planned..... 121

## List of tables

<b>Table 2-1.</b> Commercial chemicals involved in the syntheses, substrates preparation, and analyses.....	42
<b>Table 3-1.</b> Coefficients to convert voltage into degree °C for a type S thermocouple by exploiting the equation t_90. Modified from <sup>263</sup> .....	54
<b>Table 4-1.</b> Atomic concentration percentages of relevant elements from XPS surveys analysis conducted directly on the GO- and rGO-IDEs.....	71
<b>Table 4-2.</b> The current transients are ordered by splitting their behaviour in a determined phase. The current on-set and maximum are also highlighted as critical parameters. ....	75
<b>Table 4-3.</b> Atomic concentration percentages of relevant elements in NH <sub>3</sub> -rGO surveys. ....	91

# Chapter One

## Introduction

Die Absicht, dass der Mensch glücklich sei, ist im Plan der Schöpfung nicht enthalten.

The intention that humans should be happy is not included in the plan of creation.

---

Sigismund Schlomo Freud

Nel mezzo del cammin di nostra vita  
mi ritrovai per una selva oscura,  
ché la diritta via era smarrita. (...)  
Io non so ben ridir com' i' v'intrai,  
tant' era pien di sonno a quel punto  
che la verace via abbandonai.

Midway upon the journey of our life  
I found myself within a forest dark,  
for the straightforward pathway had been lost.  
I cannot well repeat how there I entered,  
so full was I of slumber at the moment  
in which I had abandoned the true way.

---

Dante Alighieri



# 1 Introduction

Chapter number one contextualises this PhD work in the historical development and state-of-the-art of the involved research topics. Moreover, it includes important scientific background tools.

## 1.1 Current world challenges

Humanity has never lived such a widespread prosperity. It is noticeable by looking at parameters, *i.e.*, schooling, life expectancy, and child and infant mortality.<sup>1-3</sup> However, further development of the society highly depends on two crucial factors energy and health. In order to understand how to scientifically approach those two worlds, it is important to look back into the history, and critically analyse the present for forward-looking plans.

### 1.1.1 Energy for development

The world population requires yearly an immense amount of energy to maintain wealth standards and to keep developing – about 170'000 TWh in 2019 mainly from fossil fuels.<sup>4</sup>

Yet, there is still a 13% of people in the world living without an electricity socket.<sup>5</sup> Furthermore, the global population is projected to grow up to 10.9 billion by 2100. Even considering the lowest growth rate, Earth must host 1.5 billion people more.<sup>6</sup>

In many world areas, energy means drinking water, better hygienic practices, access to education, relief from arduous work. Therefore, the energy issue represents a crucial challenge of our days and deserves particular attention and planning. There is no other way to offer to each human being a dignified life.<sup>7</sup>

### 1.1.2 Air pollution

Over last decade, much has been done in Europe to tackle what it is referred as air pollution.<sup>8</sup> Nonetheless, the concentrations of air pollutants in the Old Continent still exceed European Union and World Health Organisation limits.<sup>9-11</sup>

Air pollution is divided in ambient (outdoor) and household one. The typical substances that are harming human health or environment are numerous, *e.g.*, ground-level ozone, PM, VOCs, carbon monoxide, carbon dioxide, nitrogen dioxide, sulphur dioxide, methane, and ammonia. It is reported that 40% of nitrogen oxides and 40% of primary PM<sub>2.5</sub> originates from transport, whereas 60% of sulphur oxides result from energy production and distribution.<sup>12,13</sup>

Additionally, households remarkably contribute, not only for the inner household, but also for the outdoor. Hence, anthropogenic fuel combustion stands out as main responsible for air pollution. We differentiate the anthropogenic causes from the natural phenomena such as volcanic eruptions, sandstorms, burning forests, which also release significant quantities of pollutants into the air.<sup>9,14</sup>

According to the WHO statistics, 9 people out 10 breathe air that exceed air quality limits. Consequently, air pollution kills every year 8 million people, 4.2 million because of outdoor air pollution and 3.8 due to indoor one.<sup>14</sup> Air pollution affects human health in various manners – heart and pulmonary diseases, obstruction of respiratory system to infections and lung cancer.<sup>15,16</sup>

In 2015, 196 representatives agree with the Paris agreement to aim at confining global warming within 2 degrees Celsius, compared to pre-industrial values. Concretely, the countries committed themselves to peak the global greenhouse gas emissions as soon as possible, in order to arrive by 2050 at climate neutrality.<sup>17</sup>

The exploitation of clean energy sources offers an enormous chance of a sustainable development. In remote areas, low developed and off-grid, renewable sources can be used with small stand-alone plants preventing polluted households. In highly populated areas, the employment of clean fuels would enhance the air quality minimising the direct emission of PM and oxides.

Especially now that the COVID-19 crisis weighs heavily on the economies of all countries, the European Union believes in the renewable energy sources as base for a sustainable recovery.<sup>18</sup>

### **1.1.3 Bioelectronic nose**

The COVID-19 pandemic makes us remember how crucial a fast detection is, *e.g.*, in order to quickly act and isolate infection clusters. Additionally, it is essential that the device, which carries out the test, is small and mobile.<sup>19,20</sup>

To date, the recognition of biomolecules remains the unsolved challenge in an omnipresent device, such as our smartphone. With this only object, the senses, such as audition, tactile stimulation, and vision are commercialised. Nevertheless, olfaction and gustation account for a huge obstacle that researchers must still overcome. In this circumstance, the complication comes from the fact that olfaction and gustation are so-called chemical senses.<sup>21</sup> In smelling, for example, specific interactions between odorant and receptors occur that are later greatly amplified and expressed as an electrostatic signal.<sup>22-26</sup>



Particularly, the world of analysis would completely change with the discovery of a user-friendly detector like an “artificial nose” or “bioelectronic nose”.<sup>23,27-32</sup> Applications can be found everywhere in daily life, e.g., food and beverages quality control, environmental monitoring, disease diagnostics, security point. Concretely, from a smart fridge that tells to eat stored food before getting spoiled, to a smartphone transforming itself into a general practitioner giving a quick and reliable medical outcome plus prescription. And again, from targeted use of pesticides in extensive cultivations, to higher security at check points of airports, train stations, stadiums, and other hangouts.<sup>33-35</sup>

Therefore, mimicking a human nose represents a clear and delineated scientific goal. For that, keeping investigating on signal amplification, selectivity, versatility, robustness, portability of current devices is required.

## 1.2 Graphene oxide reduction

Recently, the reduction of GO accounts for one of the most exploited reactions, owing to the many research areas making use of bulk quantity of what is called rGO (also found as CMG or CCG); *e.g.*, chemistry, biochemistry, materials science, engineering, and physics (Figure 1-1).<sup>26,35-40</sup> The reaction can be conducted with different approaches, according to how reduced and how environmentally friendly we want the process to be, on top of specific intended applications.

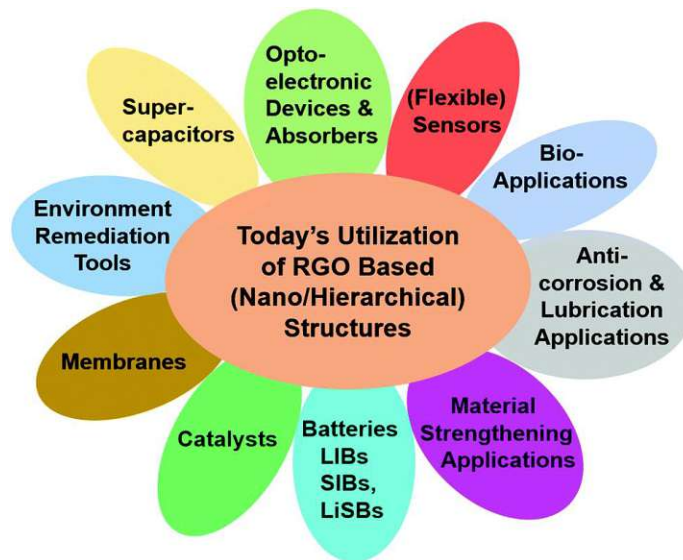


**Figure 1-1.** Current possible applications for systems based on reduced graphene oxide (here RGO). Adapted from <sup>41</sup>.

### 1.2.1 Dusted-off graphite oxide

Graphite oxide is everything but novel. However, the perspective, from which we look at it, has drastically changed in the last decade. In 1859, Brodie conducts extensive studies on the reactivity of graphite because of interesting results particularly upon its oxidation.<sup>42</sup>

With the following bullet list, I summarise some of Brodie's key findings:

- i. By mixing Ceylon's graphite with nitric acid and potassium chlorate, a peculiar compound of carbon in the form of graphite forms.
- ii. Crystals of this compound were "unfortunately too thin and too imperfect to allow a reflective goniometer measurement".
- iii. The "constitution" of the compound, namely the stoichiometry C:H:O, lies constant from the fourth oxidating treatment on.
- iv. According to the investigations, the oxidised graphite belongs to the class of acids, but it turns out "bibasic" by reacting with barium hydroxide (baryta water).

With that, Brodie provides fundamental concepts to the whole graphite community, i.e., the oxidation of graphite leads to another stable material, the produced compound is “thin” and highly defective, and it carries functional groups, which makes it acid and with basic properties too.

Staudenmaier modifies the oxidation of Ceylon’s graphite by adding sulfuric acid to Brodie’s mixture, namely, nitric acid and potassium chlorate.<sup>43</sup> By doing so, no warm-up of the chlorate takes place and thus it is safe to handle even greater quantities of graphite. Interestingly, Staudenmaier refers to graphite oxide as “graphitic acid” or “acid of graphite”, accepting the mainly acidic behaviour seen forty years earlier by Brodie.

To find the last crucial step for the synthesis of graphite oxide, we must wait precisely 60 more years. In 1958, Hummers and Offeman publish their synthesis and they finally name the material graphite oxide.<sup>44</sup> In their approach, they minimise even further the explosion danger and time consumption, because potassium permanganate substitutes the huge amount of potassium chlorate used by Staudenmaier. Next, Hummers and Offeman employ water peroxide to bring manganese into solution as sulphate, hence the suspension turns bright yellow.

Until few decades ago, graphite oxide was only considered as a mere chemical compound as many others. The turning point is represented by the advent of graphene – the revolutionary 2D carbon allotrope.<sup>45–47</sup>

### 1.2.2 Towards 2D

Graphene is called the wonder material because of its outstanding properties – electric and thermal conductivity, mechanical strength, surface area, light weight. It is the 2D material that Wallace had been calculating about, nonetheless nobody saw concretely until 2004.<sup>45</sup> It was synthesised for the first time by Geim and Novoselov. The made step was significant since authors claimed years before 2D materials would not be thermodynamically stable. Theoretical calculations and experiments were supporting each other. On the one hand, 2D materials would have suffered too much from thermal fluctuations thus leading to displacement of atoms.<sup>48</sup> On the other hand, it was observed a drop of melting points at thinner films and the segregation into islands or decomposition of structures with fewer than a dozen layers.<sup>49</sup> Therefore, Geim and Novoselov, who could demonstrate the opposite, were awarded in 2010 with the Nobel Prize in physics.

The exfoliation of graphene let the era of two-dimensional materials start. Along with the new 2D carbon allotrope, many other 2D materials began to find their way in materials sciences and respective applications, *e.g.*, molybdenum sulphide, tungsten selenide,

phosphorene, *etc.*<sup>50-53</sup> Subsequently, the first major challenge to solve was allowing production of quality 2D-materials in bulk quantities at reasonable price. Still today, albeit the mechanical exfoliation or “scotch-tape method” delivers qualitatively the best graphene, it is not suitable for mass production and it also offers small areas.<sup>54</sup> Instead, CVD overcomes the area limitation, though graphene is not monocrystalline, and with the transfer step contaminations are added to the graphene sheet.<sup>55,56</sup> Furthermore, an additional synthetic route is the exfoliation in liquid phase; however, the final suspension contains only up to a 20% of monolayered flakes.<sup>57</sup>

One way to address those issues, it is using GO as precursor of graphene or, better said, of a graphene-like compound (that is why also found as CCG, CMG – chemically converted, modified graphene).<sup>58</sup> Thus, the focus completely shifts to GO, another material belonging to the 2D family, its synthesis, *i.e.*, oxidation and exfoliation, and then reduction (Figure 1-2). GO can be produced in bulk quantities in water; hence its synthesis is cheap and uncomplicated.

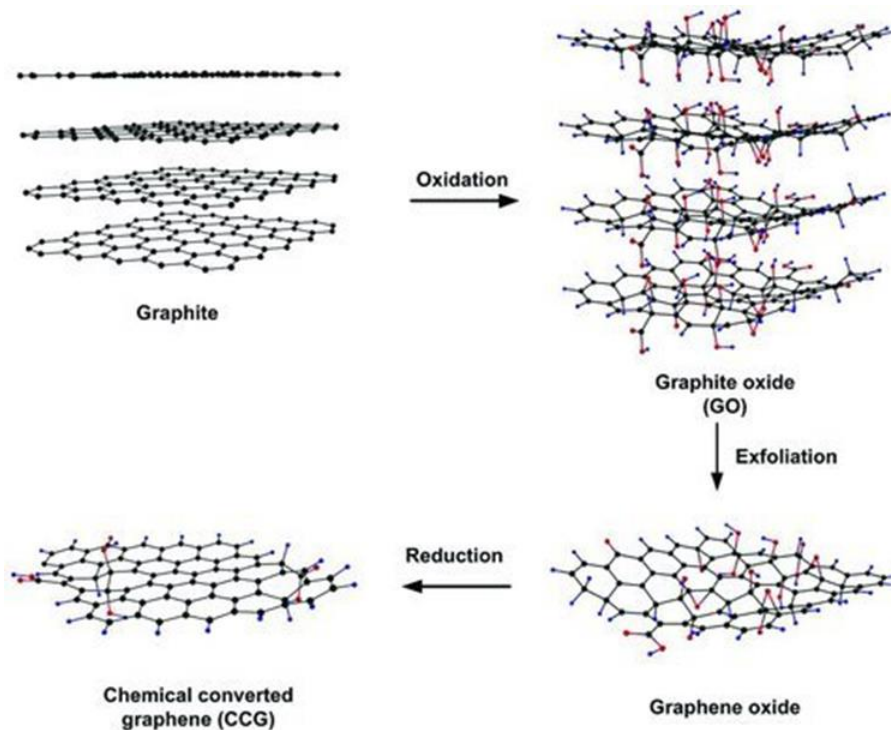


**Figure 1-2.** A scheme of the three typical synthetic steps from raw material, graphite, to final product, reduced graphene oxide (or here CCG). Graphite is oxidised to graphite oxide and 3D structure is maintained. The exfoliation stage allows the separation of monoatomic layers, accessing the world of 2D and graphenic material. Graphene oxide can be stored in stable water colloidal suspensions and be reduced before usage or once deposited on surfaces. Adapted from <sup>38</sup>.

By using GO, we can pick up other two positive aspects – storability and uncomplicated deposition.<sup>36,59,60</sup> In fact, GO is said as water-dispersible, it can be stored for months in quite concentrated water colloidal solutions without observing any aging or agglomeration issues. Moreover, GO nanosheets or nanoflakes can be deposited directly from water suspensions onto surfaces with remarkably high and atomic-thin coverages, if needed with the help of appropriate linkers too.<sup>61–63</sup>

Like graphene, GO displays a honeycomb structure, where C atoms  $sp^2$ -hybridised constitute the smallest and hexagonal unit cell. However, GO often carries with it many defects, which commonly occur as oxygen-containing functional groups, as the name of the compound suggests. Moreover, generous amounts of vacancies, edges and wrinkles can be found.<sup>64–66</sup>

In the opinion of various authors, GO accounts for the cheapest and most practical source of graphenic material.<sup>59,67,68</sup> Nevertheless, a fast and uncomplicated full GO reduction to graphene is hardly feasible in normal conditions.<sup>69</sup> Particularly, in the field of devices, the reduction of GO must occur once the GO colloidal solution is already safely deposited on the substrate of destination. Therefore, extremely elevated temperature treatments and aggressive chemicals should be avoided. Thus, the substantial differences between a well-reduced rGO and Gr lie on:

- i. Left oxygen-containing functional groups
- ii. Carbon atom vacancies
- iii. Edges
- iv. Size of the crystals

Yet, those points of difference do not make GO less appealing. On the contrary, recent works are using pristine for selective introduction of defects.<sup>70–72</sup> Hence, being able to control something, which in first approximation are reactive sites, can turn GO into a flexible and versatile chemical tool.<sup>72–74</sup> In other words, reaching such fine-tuning opens the doors to much more chemistry compared to pristine graphene.<sup>36,75</sup>(see [section 1.2.5](#)).

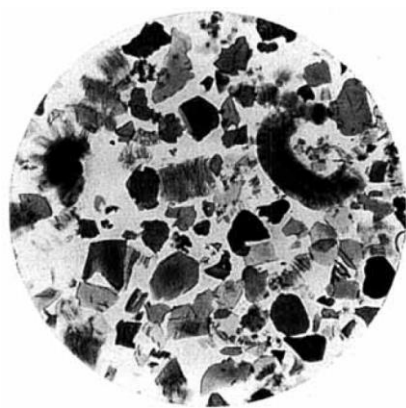


**Figure 1-3.** Graphite oxide crystals separation, during “swelling” after mixing with diluted NaOH solution Adapted from <sup>76</sup>.

In contrast with graphene, GO does not seem to have a clear 2D story. In 1937, there was a turning point with Hofmann and Koenig’s study.<sup>76</sup> After mixing graphite oxide with water and especially with alkali solutions, Hofmann and Koenig confirm the weakness of graphite oxide intramolecular forces (Staudenmaier’s synthesis – potassium chlorate, sulphuric, and nitric acid). With water already, graphite oxide lamella disperse single crystals can be separated into an accordion-like layer of sheds. In Figure 1-3, Hofmann and Koenig offer a microscope image of the mixture with sodium hydroxide in the first phases and predict, upon gentle shaking, the possibility to obtain an eucolloidal solution only made of single layer planes. In this study, a significant amount of information arises from the employment of X-ray diffraction analysis, because it correlates with the graphite oxide interlayer distance. Therefore, intriguing outcomes regarding water as strongly adsorbed molecules in graphite oxide interlayers are showed. In 1962, Hofmann comes back with Boehm and co-authors to graphite oxide and its reduction with hydrazine hydrate.<sup>77</sup> In this investigation, through adsorption with methylene blue, electron microscopy and again XRD diffraction, the researchers state to have synthesised monoatomic layers of carbon. However, the term 2D was forged only after the exfoliation of graphene, as graphene properties drastically diverge from graphite ones.<sup>45</sup> Moreover, those characteristics could be theoretically calculated without too many obstacles, which are present when approaching defective materials as graphite oxide.

### 1.2.3 GO synthesis and structure

From the last two sections, it has manifestly appeared that history of graphene oxide and graphite oxide are strictly related. To date, the scientific community is also aware that the synthesis methods involving a graphite oxide-graphene oxide step are the only capable to provide bulk amount of graphene materials.<sup>78,79</sup> The essential difference between the two



oxides lies on the exfoliation or also called delamination process<sup>80</sup>, which, as highlighted before in [subsection 1.2.2](#), can already occur at the harsh conditions of graphite oxidation. State-of-the-art synthesis of GO still makes use of all the before cited routes to graphite oxide, of which especially Brodie's and Hummer's methods stand out ([see subsection 1.2.1](#)). On the one hand, Brodie's method offers rather pure GO, though enhanced explosion danger. On the other hand, Hummer's method is rather safe even with big amounts of reagents, but it leaves more contaminants, such as sulphur, manganese.<sup>81,82</sup>

Method	Oxidant	Reaction media	Carbon-to-oxygen ratio <sup>a</sup>	Raman spectral $I_D/I_G$ ratio <sup>a</sup>	Charge-transfer resistance ( $R_{CT}$ ) <sup>a</sup> (k $\Omega$ )
Staudenmaier <sup>9</sup>	KClO <sub>3</sub>	Fuming HNO <sub>3</sub>	1.17	0.89	1.74
Brodie <sup>10</sup>	KClO <sub>3</sub>	HNO <sub>3</sub> + H <sub>2</sub> SO <sub>4</sub>	—	—	—
Hofmann <sup>11</sup>	KClO <sub>3</sub>	Non-fuming HNO <sub>3</sub>	1.15	0.87	1.68
Hummers <sup>12</sup>	KMnO <sub>4</sub> + NaNO <sub>3</sub>	Conc. H <sub>2</sub> SO <sub>4</sub>	0.84	0.87	1.98
Tour <sup>13</sup>	KMnO <sub>4</sub>	H <sub>2</sub> SO <sub>4</sub> + H <sub>3</sub> PO <sub>4</sub>	0.74	0.85	2.15

**Table 1-1.** From earlier to novel GO synthesis methods accompanied by typical evaluation parameters. Modified from <sup>83</sup>.

The full graphite oxide exfoliation to graphene oxide comes surely down to the purity of the raw material and the oxidising agents. In fact, purification of hetero-atomic contamination from flake graphite, the most common source of graphite for chemical reactions, has become a common operation.<sup>84-86</sup> Well-oxidised GO, from natural graphite with high crystallinity, can be readily dispersed in water.<sup>59,81,87</sup> The isolation of single atomic layers is a final goal of graphene oxides stable suspensions, whether water-based or not.<sup>59,88</sup> Here again the complexity of the diversely synthesised oxides of graphite with, as well, the later modifications.<sup>89</sup> On one side, Brodie's method introduces more in-plane hydroxyl groups, which, in water, with small amount of NaOH can be deprotonated, leaving charged sheets and a greater electrostatic repulsion between the layers.<sup>76,81</sup> On the other side, Hummer's method, not only preferentially modifies the sheets with carbonyl groups (debatable if only in-plane C=O), but also, it lets the single layers be well functionalised from both sides.<sup>81,90,91</sup> In Hummer's, a crucial reaction is the hydrolysis, which open the doors to many O-containing functional groups and expand what has become a charged atomic layer. Thus, it allows the repulsion and dispersion of single sheets in water solution. In this process, smaller and thinner starting graphite flakes along with high crystallinity prolongate the oxidation process leading to better exfoliation.

In other 2D materials, the exfoliation typical method such as sonication, brings to single layers of the initial stacked material.<sup>92,92-94</sup> Ultrasound has some serious consequences on GO sheets, namely fragmentation, particularly the larger sheets.<sup>95,96</sup> Hence, it is typically not

beneficial for many purposes or employed with mild conditions. By contrast, perfected purification practices of the product are a fundamental part of the synthetic procedure, to reach high level of contaminants removal. Previously, sulphur and manganese were mentioned for Hummer's method, though in Brodie's GO there is chlorine, which also has a good affinity with atomic carbon.<sup>89,97</sup>



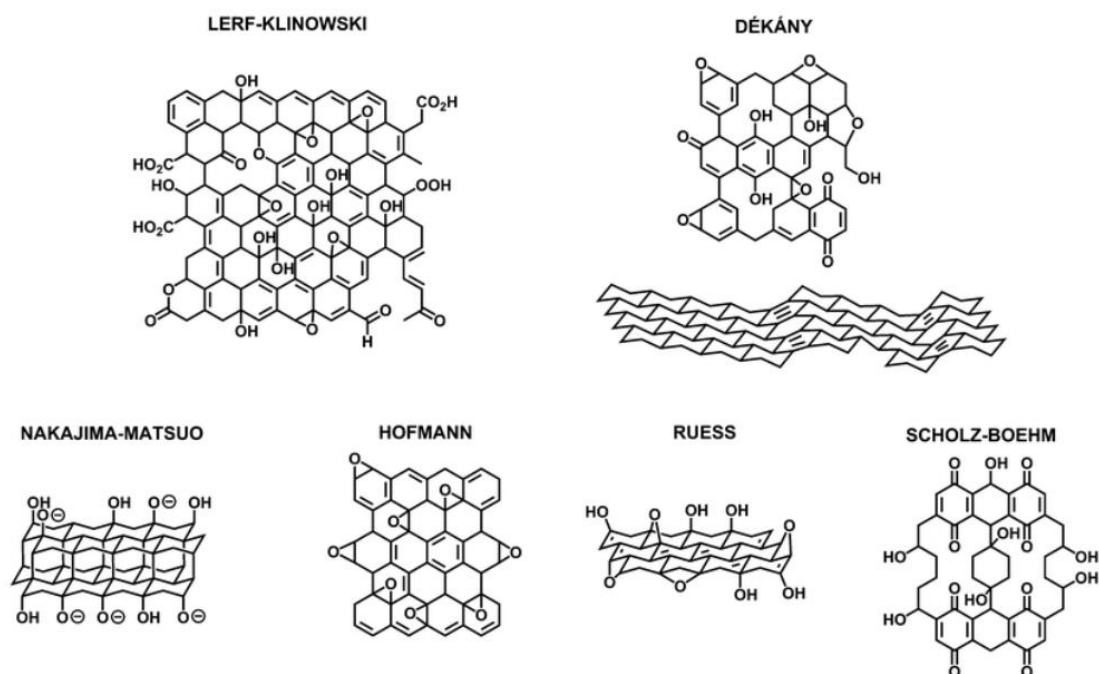


**Figure 1-4.** The GO structures that have been proposed over the years. From <sup>83</sup>.

As previously discussed, the structure of GO differs significantly according to the utilised method. Thus, we can define graphene oxide as a class of materials, rather than a single composition. As a result, it would be auspicious to define GO with reliable parameters and characterisation, to limit batch-to-batch variations and so reproducibility issues.

Hofmann's and Tour's complete the spectrum of the most relevant methods for the water-based synthesis of graphene oxide.<sup>76,98</sup> Amongst them, Tour's route represents the very last evolution of Hummer's method, and it carries the lowest carbon-to-oxygen ratio. Certainly, the presence of, at least, five synthetic approaches do not simplify the agreement on a structural model. Nonetheless, Lerf-Klinowski's hypothesis is the most widely accepted for a generic description of GO and, in fact, the most inclusive in terms of functionalities (see **Figure 1-4**). It envisages edge and in-plane hydroxy and epoxy groups. By contrast, carbonyl, carboxyl groups occur less frequently and principally at edges. Furthermore, not excluded, yet in small amount at those edges, hydroperoxides and aldehydes can be found. Often, carbonyl and aldehydes are formed stabilised due to  $\alpha$ - $\beta$  unsaturations. Notably, a fundamental change in the evolution of the models was determined by the confirmation of carbon atom vacancies, first proposed by Scholz and Boehm. Those holes interrupt the C backbone and chemically behave like edges. Therefore, the more disrupted and the smaller the GO sheets, the higher the proportion of edge-preferential functional groups, over the total. Dissimilar from other models in Lerf-Klinowski's one, there are significant conductive portions in the GO layer made of C-C  $sp^2$ .

## 1.2.4 Approaches to GO reduction

Owing to the potential of the graphite oxide-GO step towards graphene-like materials, GO reduction has gained a huge amount of interest, representing one of the most researched reactions of the last two decades. Researchers have exploited a plethora of approaches endeavouring to suit the final application of rGO and the support on which GO was deposited.<sup>36,59,99-107</sup>

In this sense, there is a first needed distinction between the evolving fields. Namely, there is a scientific community focusing principally on the GO reduction itself, trying to restore graphene outstanding properties.<sup>69,108-110</sup> Whereas there is another scientific community, which runs for application-targeted GO reduction, and hence devices.<sup>111-113</sup> Furthermore, there is a third party that goes the other way around, by generating defects into the most pristine graphene, *e.g.*, doping and carbon vacancies.<sup>70,114-116</sup>

Therefore, a brief overview is given of most representative studies, although the focus remains on the final application of this thesis, *i.e.*, the after-deposition GO reductions. In the first examples, the comparison amongst the results of the reductions is based on the degree of reduction (C:O ratio, conductivity), while it heads always deeper into the aimed applications and practicality of the chemical.

In colloidal dispersions, the only way goes through chemical or electrochemical approaches. The successful chemical methods, we find hydrazine monohydrate, ascorbic acid, sodium borohydride, and hydroiodic acid. In general, metal hydrides are too reactive to work in water-based solutions.

Indeed, that is the great advantage of the oldest and effective hydrazine monohydrate, which also displays undeniable weaknesses, namely, its carcinogenicity and leading to rGO agglomerates.<sup>117,118</sup> However, sodium borohydride could demonstrate its efficacy in reducing GO, owing to a kinetically slow hydrolysis of a freshly-prepared solution, though alcohol impurities must be expected.<sup>106,119</sup> By contrast, ascorbic acid is extremely stable in water and non-toxic with hydrazine-like performances, C:O ratio of 12.5 and conductivity of 77 S/cm.<sup>120</sup> Moreover, ascorbic acid does not allow rGO agglomeration. In terms of degree of reduction, hydroiodic acid overtakes all the previously mentioned compounds, taking GO to a rGO with 15 C:O ratio and conductivity of about 300 S/cm. Here, the tensile strength comes to support HI reduction, in case the formation of a flexible film is desirable.<sup>121,122</sup>

Furthermore, in solution GO can be reduced by CV. Only one scan is enough to irreversibly reduce GO. Interestingly, the best work highlighted the role of the hydroxonium cation, *i.e.*, low pH, better reduction, which resulted in a 23.9 C:O ratio and 85 S/cm conductivity. Wet-

reductions of GO were also carried out coupled with semiconductors photocatalytically, and by means of supercritical water solvothermally.<sup>123-125</sup>

Because of what was stated in this and previous sections, that is, aim of thesis and urge for GO after-deposition reduction, let us now shine some light onto the more suitable reduction approaches to solid-state GO.

In this circumstance, the most common reduction is the thermal-mediated approach. It is practical, fast, effective (bulk conductivities 10-23 S/cm) and, to a certain extent, cheap. The inexpensiveness factor comes mainly from the chance to reduce GO with thermal mediation at low temperatures, as industrial process heating operations usually are extremely demanding.<sup>126</sup> There is a fair agreement on the fact that O-containing functionalities can be stripped from GO sheets according to applied temperatures.<sup>99,127-129</sup> In other words, it appears that there is a sequence of temperatures allowing selected removal of O-containing functional groups from solid-state GO. However, at extremely high heat exposures in air, 800-1000°C the C-C bonds crack, and topological defects as well as vacancies form. Furthermore, although treatments can remove a big portion of the main O-containing functionalities, losses of material up to 30% are expected, due to the release of carbon dioxide. Not only thermal-mediated approaches reduce GO, but they can also realise proper exfoliation to 80% of single sheets.

There are other ways to give thermal energy to solid-state GO, such as, through microwaves and photons. Here, the profit, in terms of saved amount of time, is remarkable. Microwaves enable a 1-minute reaction to rGO<sup>104</sup>, while not much more is taken for a flash reduction with a strong xenon lamp or a femtosecond laser beam.<sup>130,131</sup>

Furthermore, there is the option of multi-step GO reduction approaches, by paying attention to single treatment effects.<sup>26,129,132,133</sup> However, to avoid unpleasant misunderstandings, the parameters, through which the GO reduction is evaluated, must be carefully considered. The graphene semi-metallic behaviour does not appeal photo-electronic devices and transistors researchers unless functionalised, C-vacant, or edge-controlled. Nanoscaling, selectivity, and LODs highly depend on these characteristics.

### 1.2.5 Applications: towards sensing in liquid

Graphene is the *wonder* material, but it is not the material for each application, hence carefulness is necessary when speaking of striving for complete reduction of GO. Defects often make graphene, and so partially-reduced GO, active for a defined task or even better performing. This sums up to the graphene issue for device-oriented mass production, which remains, to date, unsolved. Diversely, a full restoration of C-C sp<sup>2</sup> bonding, healing of C-

vacancies, and edges of GO would make it like pristine graphene and shrink the band-gap.<sup>134-136</sup> In this regard, photoluminescence investigations showed semiconductor characteristics in proper functionalised graphene.<sup>137,138</sup>

In fact, energy-related materials<sup>123,139-141</sup>, field-effect transistors (FET)<sup>25,37,142,143</sup>, sensors<sup>112,113,132</sup>, and biomedical applications exploit mainly the rGO semiconducting behaviour. Nevertheless, rGO also finds, thanks to the mass production, broader utilisation in material sciences, *i.e.*, polymer composites<sup>144,145</sup>, conductive coatings<sup>146,147</sup>, and “paper-like” materials<sup>148-150</sup>.

In this thesis work, the focus of the first project (see [Chapter 4](#)), will be on pH sensing with rGO-based LGFETs, while the initial aim was to go further using rGO-LGFET as platform for biosensing, and specifically, a bioelectronic nose. With such devices, the major goal typically lies in the detection of biomolecules from electrolytes, and that is, where those usually are, or will end up for the sensing operation. Here, the neat separation between graphene and rGO, when both are micro-sized and functionalised (with biomarkers) sheets, gets increasingly blurred. Thus, I find it logical to mention the achievements not only in LGFETs, but also in “in-liquid” graphene-based biosensors together. These allowed manifold and noteworthy detections of biomolecules, *i.e.*, oligonucleotides<sup>151</sup>, ssDNA<sup>152</sup>, DNA polymorphism<sup>153</sup>, hormones<sup>154</sup>, immunoglobulins<sup>155</sup>, enzymes<sup>156</sup>, proteins<sup>157</sup>, plus chemical weapons<sup>158</sup>, pesticides<sup>159</sup>, odorants<sup>160</sup>. A huge breakthrough is displayed by a rGO-based LGFET with the discernment of two odorant molecules by means of a single-carbon-atom resolution.<sup>161</sup>

Furthermore, it is important to underline that in “in-liquid” graphene-based biosensors diverse physical and chemical principles are required for the read-out of interacting analytes. Precisely, I have already mentioned transistor (see following section for details), though there are many more, namely, impedance<sup>162</sup>, fluorescence<sup>163</sup>, electrochemistry<sup>164</sup>, luminescence<sup>165</sup>, SPR<sup>166</sup>, Raman<sup>167</sup>.

### 1.3 Graphene-based LGFETs and pH sensing

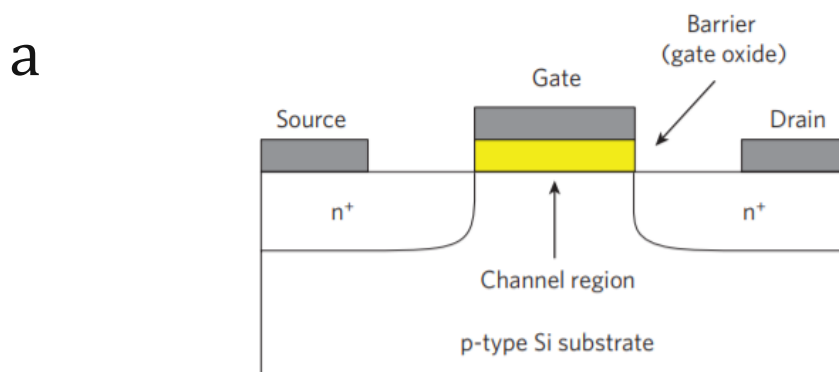
In this section, I will focus on describing the working principles, through which an FET and hence a LGFET can give a readable output. I will briefly go through the evolution of pH detection highlighting the stages that led to graphene-based FETs for the assessment of this fundamental water solutions property. Subsequently, I will move to the attempts with graphene-based devices, graphene and rGO channeled FET to sense pH changes in water-based electrolytes, commonly buffers.

### 1.3.1 Principles of FETs and LGFETs

FETs are devices based on four essential parts. Three of them are contacts, that is, source, drain, and gate. The remaining one is the channel; thanks to whose conductance modulation the three contacts can communicate. The gate is in physical contact with the channel region, while source and drain are not (**Figure 1-5a**). Typically, a voltage is applied between gate and source and through the channel region charge carriers may travel. Whether that happens or not, it comes down to the applied voltage. At too low voltages, there is no electric current flowing via the channel region ( $V_{GS} = 0$ ) (**Figure 1-5b**).

The transistor can be deemed “switched on” when  $V_{GS}$  is equal to  $V_{DD}$ , the maximum voltage given to the system. However, the crucial region is the voltage before the threshold ( $V_{Th}$ ), the steeper the slope in the subthreshold region, the better for the switch-on features.

Still today, FET industry lies on a single type of device, *i.e.*, silicon metal-oxide semiconductor FET, MOSFET (turned to CMOS), and the performance increase upon making it the smallest.<sup>168</sup> Current mass-produced processors count two billion MOSFETs, principally with gate lengths of about 30 nm. However, it seems the sector has reached a stasis. With the downscaling, few intrinsic limitations have come up, such as threshold-voltage roll-off, drain-induced barrier lowering, and impaired drain-current saturation. Therefore, graphene as 2D and wonder material holds the promises to overcome them. To date, its achievements are coming sooner than CNTs ones.<sup>169</sup>



b

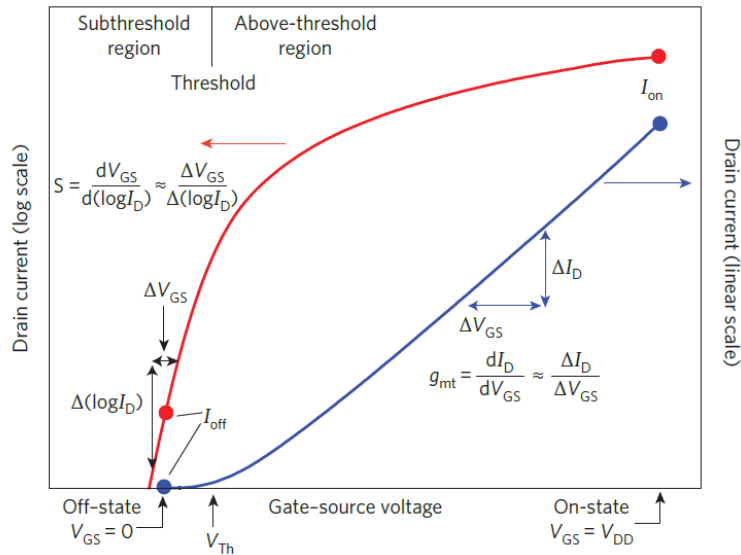


**Figure 1-5.** a) Schematic of a typical transistor. b)  $I$ - $V$  characteristics of the typical transistor to the left. On the two y-axes the drain current in log ( $\log I_D$ ) and in linear scale ( $I_D$ ), and on the x-axis the applied gate-source voltage ( $V_{GS}$ ). Adapted from <sup>170</sup>

By contrast, in LGFETs or SGFETs, the gate is immersed into a solution, which functions as a dielectric and enables the communication with the other two contacts, source and drain. When a potential is applied between gate and source (in the field often named  $V_g$ ), the anions and cations arrange in the liquid electrostatically according to a Debye's sphere concept. In 1972, Bergveld published his seminal work employing a FET in liquid environment to sense  $\text{Na}^+$  cations, hence called ISFET.<sup>171</sup> A breakthrough that did not gain much interest until carbon materials begun their era, *i.e.*, first in LGFET with a diamond demonstration<sup>172</sup>, then CNT and shortly later with graphenes. However, already with the initial application it was noticed that those materials could be biocompatible, which is a crucial property for biosensing goals.

### 1.3.2 Graphene-based LGFETs

The limitations that were impeding the nanoscaling of FETs transforming the nano-channeled MOSFETs in a challenge to be paid at the devices purchase, have therefore widened the gap between research and market. Moreover, it has enhanced the rush for novel material, which peaked with the advent of CNTs, and especially of graphene. As in FETs that then become GFET, graphenic materials has rapidly found application in LGFETs. And these become graphene-based or graphene-channeled devices.

Amongst the many reported properties, graphene presents biocompatibility<sup>173</sup>, nanoscaling and stretchability<sup>174</sup>, and also functionalisability<sup>71,175,176</sup>. These are extremely appealing for novel LGFETs. For example, nanoscaling not only offers the pros already in mentioned in

[section 1.3.1](#), but it also minimises the amount of material for each transistor. Here, bulk quantity of years-lasting mother solutions is in the tenths of millilitres order of magnitude.<sup>26,177</sup> Whereas, biocompatibility is extremely necessary to maintain the mild conditions for biomolecules to function in all their specificity and selectivity. Functionalisation is essential to tune or attach at/on the channel the appropriate interacting species.

As a result of published studies on CNTs, the hardest part of the swapping with graphene has come only from the material synthesis, because the systems and supports are almost identical.<sup>178</sup> Like CNTs, graphene and rGO have also enabled sensing of biomolecules and went beyond it. However, the typical application that is firstly explored is always about, to a certain extent, simple electrostatic-driven sensing. In addition to many cations or anions, sensing of pH values keeps holding great attention, since mechanistically unclear and to win the big power consumption of pH-sensitive glass electrodes.

### 1.3.3 pH sensing with FET

Based on the theory of SFET<sup>179</sup>, the sensing of ions in solution by means of transistors dates to 1970 with Bergveld's investigation<sup>180</sup>. The employment of a transistor as a chemical sensor could reduce cost and size, and allow high input and low output impedance measurements, that is, obstacles in common glass electrodes for pH detection. In Bergveld's ISFET, a conducting channel is not obtained only via a metal gate with an applied potential, but also from oxide charge. Such charge is controllable even when the transistor is immersed in a water solution, without gate. Having silicon oxide, the ability of glass to hydrate, a double layer at the solution-oxide arises. Though, there is another double layer formed by a second interface, *i.e.*, the oxide-silicon one. Hence, in the circumstance the oxide thickness is little enough, the interaction between the two double layers is allowed, showing then a dependency from the ion activity of the solution. Therefore, a variation in ion activity can be detected as a variation of channel conductance.

Other inorganic semiconductors, oxides and not, were investigated as promising pH-sensitive channels.<sup>181</sup> Considering all the studied materials, Ta<sub>2</sub>O<sub>5</sub> has appeared to be the best performing.<sup>182</sup> Furthermore, not only layers or films have played a role in the art of pH sensing, but also their morphology. The modification of morphology brings along two major contributes, namely, the alteration of electronic properties and diminution-enhancement of surface area. In this sense, 1D-materials, thus subjected to important morphological control, such as wires or tubes, have also demonstrated to be highly-sensitive to pH changes.<sup>183-185</sup>



However, albeit the detection of hydroxonium cations,  $\text{H}_3\text{O}^+$ , or also simplified  $\text{H}^+$ , is one the most studied detections of all owing to its relevance<sup>186</sup>, it still displays discrepancies in the clear identification of the sensing driving force. Supra-Nernstian performances were observed and motivated with adsorption of  $\text{OH}^-$  anions in GFETs. However,  $\text{H}_3\text{O}^+$  sensing capability is, in the bioelectronics community, traditionally seen as the electrostatic interaction or repulsion charged species. This considered, in biological electrolytes exists a microcosmos of moving analytes, fixed recognition units, competition, and signal transduction. Let us then look a bit more into detail of this device with the coming specific subsection.

### 1.3.4 pH sensing with graphene-based LGFETs

Graphene was the first 2D material to be utilised in channelling a LGFET. In 2008, Ang and co-workers reported that graphene can work contemporarily as transducer and pH-sensitive layer.<sup>187</sup> By applying negative gate voltages, they observe supra-Nernstian pH sensitivities up to 99 mV/pH. Nevertheless, few years later, graphene was also reported to be a poor pH-sensitive channel.<sup>188</sup> Therefore, there are differing opinions regarding the fine mechanism of the pH detection, *i.e.*, the triggering events of the electric field modification.

By contrast, there is more consensus about the rGO-based LGFET pH sensing driving force. Let alone the size of the crystals – which is slightly less relevant for the reasons of [section 1.2.2](#) – the rGO sheets are seen as alternating mixture of graphene and graphene oxide areas. Thus, there are areas that can likely better allow the transport of charge carriers, while the are others with an abundant presence of O-containing functionalities that can likely better interact with  $\text{H}^+$ . Sohn and collaborators particularly highlight that the capability of rGO to recognise pH changes lies in the presence of -OH and -COOH groups.<sup>37</sup> As already mentioned in [section 1.2.4](#), a partial reduction of GO is in fact more auspicial, hence offering a certain degree of conductivity, but also preserving an important amount of crucial sensing units.

However, we have seen in the hexagonal C structure of CNTs the possibility to host  $\text{HO}^-$  anions for a successful pH detection, those groups are additional sensing units., as well claimed by Ang and co-authors.<sup>189,190</sup> Note that it could not be excluded a combined effect, so far.



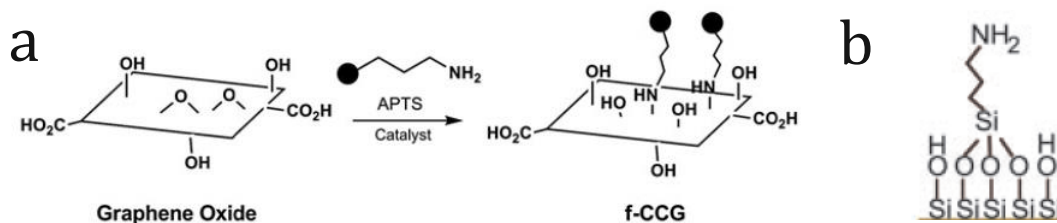


**Figure 1-6.** a) Proposed reaction mechanism of APTS/APTES with GO. From <sup>36</sup> b) Single unit of APTES once the bonds with the transistor glass are formed.

Again, from a synthetic point of view, the benefit of channeling LGFET with rGO instead of graphene is addressed (see [1.2.3](#) and [1.2.4](#)). In fact, for this specific application the explained concepts are valid, *e.g.*, GO storage and deposition, inexpensiveness of GO synthesis and method.

More than in the previous section, the topic of the anchoring becomes significant due to the assembly of the device. Here, there are usually two ways to go, according to the channel material. In case of graphene, the anchoring is not necessary, as the gold contacts are typically deposited in a second step on the already transferred or epitaxially grown layer.

However, with GO, the deposition is frequently and willingly carried out via drop casting onto the support. By doing so, the GO sheets have more chance to arrange on their own, agglomerating in islands (I remind of [subsection 1.2.3](#)), while air-drying on the sensing area. Hence, the role of the anchoring is both, to enable stable binding between flakes and support (often SiO<sub>2</sub>, or glass-like material as in this thesis), and to deliver the best coverage of the selected area. Lately, the presence of APTES as SAM on the sensing area is indispensable; and therefore, widely employed and studied (proposed mechanism of APTES-GO bonding, **Figure 1-6**).<sup>25,26,36,37</sup>

In this work, I make use of APTES as optimal linker between support SiOH groups and GO epoxy groups, and additionally, of a common GO reduction procedure (see [section 1.2.4](#)) with hydrazine hydrate (gaseous) to study its pH sensitivity in LGFET. Next, I base my investigation on developing and comparing new reduction approaches on GO, so that hydrazine hydrate may be substituted successfully in the near future. The final comparison will be based on the application, *i.e.*, rGO as LGFET channel and pH sensor.

## 1.4 Sb, Li co-doping in hematite-based photoanodes

Herein, I will mention the relevant theory behind the photoelectrocatalytic water oxidation, or sometimes abbreviated and generalised as solar water oxidation. Specifically, I will underline the type of light the sun offers, how to harness it best, and ultimately, the interfacial phenomena at the SC-liquid junction. I will explain the choice of hematite as template material for the co-doping investigation, and moreover, provide a short summary of the morphological and catalytic evolution of the hematite as photoactive compound, reaching its doping and state-of-the-art.

### 1.4.1 Sunlight

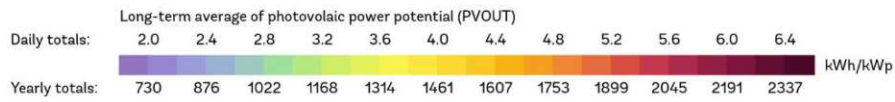
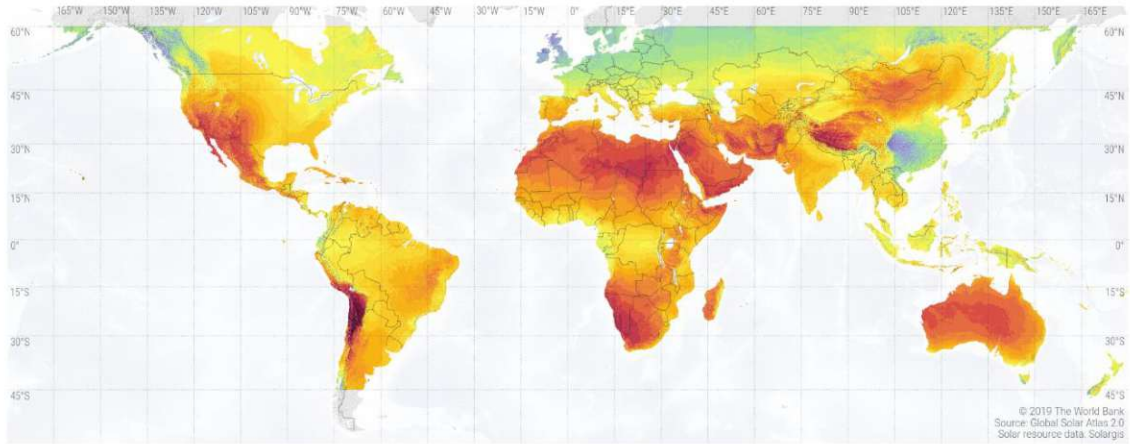
The Sun is the star, which allows life and allowed life to start. Through marine photosynthesis oxygen was released into the atmosphere progressively up to about 21% of the current atmospheric concentration.<sup>191</sup> In fact, the Sun accounts as one the largest sources of renewable energy on Earth. Sunrays form by sequences of nuclear reactions converting hydrogen into helium, therefore extremely dangerous. Fortunately, those are partially shielded, *i.e.*, reflected, and adsorbed, through terrestrial magnetic field and atmosphere. Nonetheless, considering the losses, the location, and diurnal, seasonal, annual oscillations, Earth's crust receives every second around  $240 \text{ W m}^{-2}$ . Which is 122.4 TW per second, if multiplied by  $5.1 \times 10^{12} \text{ m}^2$  of Earth surface.<sup>192</sup> For a clearer picture of what this information means, in **Figure 1-7a** is reported the solar-to-power conversion potential of photovoltaics, resulting from a rigorous calculation model.<sup>193</sup> Not to be forgotten, the sea surface is not considered in the picture

Of this huge and almost never-ending energy supply, we can photochemically use only a portion; namely, simply expressed, the one allowing electronic promotion to conduction band or to excited state of, respectively, materials or molecules. For example, plants exploit the same phenomenon. Moreover, the irradiance of the sunlight spectrum reaching the crust is made of about 10% UV, approximately 40% visible, and around 50% IR light (**Figure 1-7b**).

Thus, in the search for photoactive compounds, the two highlighted requirements are already reducing the number of suitable candidates, which to be successful should preferably absorb the visible light spectrum.

**SOLAR RESOURCE MAP**  
**PHOTOVOLTAIC POWER POTENTIAL**

a



**Spectrum of Solar Radiation (Earth)**

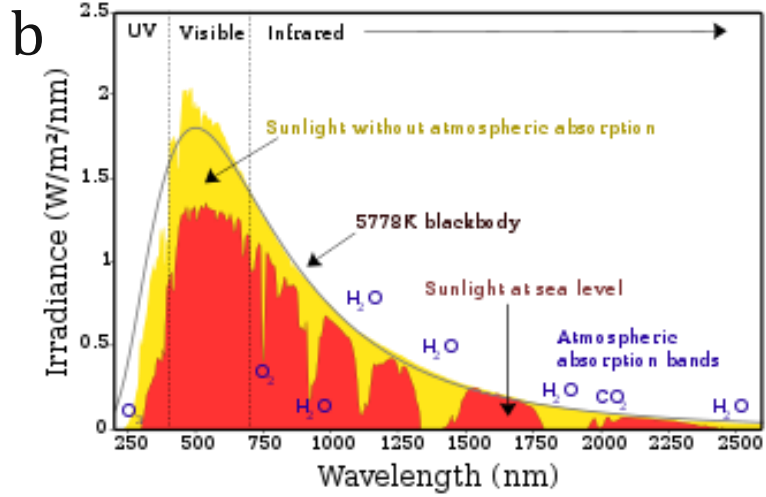


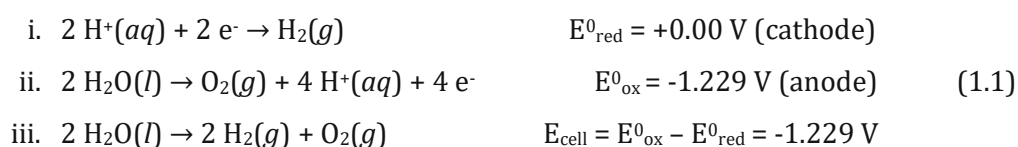
**Figure 1-7.** a) World map of the specific photovoltaic power output. Adapted from <sup>194</sup>. b) Irradiance and spectrum of the solar radiation reaching the earth crust. Adapted from <sup>195</sup>.

## 1.4.2 Solar water splitting

The splitting of water mediated by solar light is one of the numerous reactions that tries to exploit the free, abundant, and renewable energy source, that is the Sun. Undoubtedly, solar water splitting lies at the top of the most interesting topics in science, due to the relevance of the climate and energetic issues (see [section 1.1](#)), but also because water is away from deserts or drought-exposed environments, a basic and affordable compound in daily life. Eventually, sea water can also be utilised as water-based electrolyte for water splitting with lower efficiencies.

However, sunlight is an intermittent source of energy, as it has come out from the previous section. Hence, storage of sunlight in the form of chemical bonds is ideal, particularly, if the products of this “solar synthesis” are easily storable and recombining. The idea reminds of what plants have been doing ever since.

The reaction of solar water splitting can be approached from a thermodynamic point of view, which defines the theoretical electrode potentials needed to realise the step from reagent  $\text{H}_2\text{O}$  to products  $\text{O}_2$  and  $\text{H}_2$ , so the respective gas evolutions. The overall water splitting can be seen as the occurrence of two electrochemical half-reactions, which can later be coupled into one cell:



As the standard hydrogen electrode is the reference in the table of reduction potentials, it possesses a reduction potential of 0.00 V (pH 0, at 298.15 K and 101.325 kPa). Instead, the oxidation of oxygen to water is a non-spontaneous process with an oxidation electrode potential of -1.229 V. Therefore, if coupling the two reactions, the cell potential results into a negative thermodynamic value, which is the minimum threshold we must provide to let the reaction run. However, in a real electrochemical process the theoretical cell potential value is not enough to let the reaction begin and thus, what must be provided to the water splitting system is an overpotential.

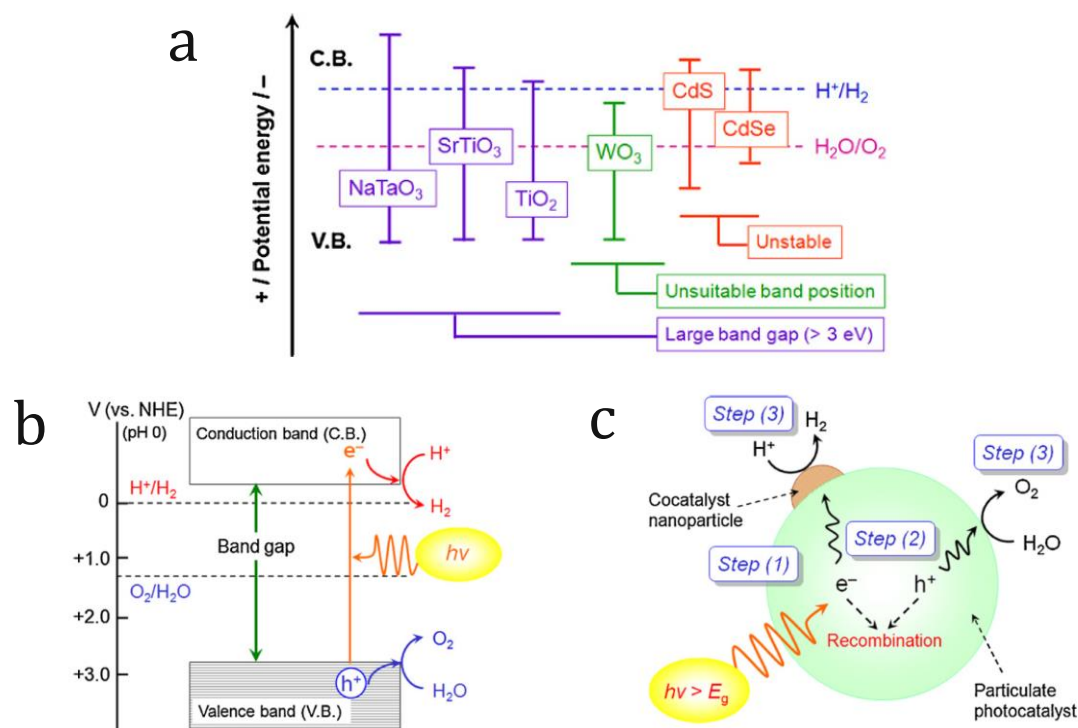


**Figure 1-8.** a) Typical semiconductors and their band gaps in respect to the water reduction and oxidation thermodynamic potentials. b) Representation of light absorption by a semiconductor towards overall water splitting. c) Schematic of the water splitting kinetics of a nanoparticle attempting overall water splitting. All adapted from <sup>196</sup>

Nonetheless, the value 1.229 V is a fundamental starting point to find matching materials, that could lead to an overall water splitting or to partially catalysed reduction or oxidation of water (**Figure 1-8a**). Particularly, in semiconductors what should match are the positions of CB and VB. On the one hand, CB, a combination of empty d orbital of a transition metal or s, p orbitals of a metal, should lie above the H<sup>+</sup>/H<sub>2</sub> potential energy. On the other hand, VB, in a traditional metal oxide SC, a combination of O2p orbitals, is more positive than the water oxidation potential (3 V vs 1.23 V). The artificial measurement unit, electronvolt, eV, sets a crucial bridge between electrodynamics and band gap understanding, in other words, the needed theoretical potential for water electrolysis and the needed photon energy for the electron jump of a candidate SC. Therefore, 1.23 V is comparable to 1.23 eV and, in fact, the theoretical photon energy to be absorbed by a SC to carry out the overall water splitting is about 1000 nm. Nonetheless, due to inherent energy losses in the migration of charge carriers on top of the overpotentials for the gases evolution at the electrode, the minimum required band gap hovers around 2 eV (**Figure 1-8b**).

The reaction of solar water splitting can also be understood under the magnifier lens of kinetics. The 1.23 V, plus overpotential, tells us the driving force we need to give to the

system, yet we do not know how long this reaction is going to take once the required potential is at disposal. Hence, the kinetics and the variable time are also crucial in the holistic approach for a successful water splitting. As represented in **Figure 1-8c**, albeit the thermodynamic requirements are fulfilled and the driving force is sufficient to allow the reaction to happen, there are three kinetic steps, which can significantly lower charge carrier collection, and their exploitation to H<sub>2</sub> and O<sub>2</sub> evolution. The first step consists of a very frequent cause for poor photon-to-hydrogen conversion, *i.e.*, recombination of photo-generated charge carriers. The exciton forms and the photo-generated holes and electrons spatially split, but they cannot do it enough to escape the return attraction force and annihilate each other, releasing the absorbed energy. Second, there is the migration of the charge carriers, which could survive the annihilation. Not only the migration considers the path through the SC bulk, but also the access to the surface, catalyst is involved. Third, once that the photo-generated charges are sitting at the interface they are asked to enable the evolution of O<sub>2</sub> and H<sub>2</sub>, *e.g.*, trap states could impede it.

Of the two reactions that the photo-generated charge carriers should give rise to, the water oxidation is the most complicated. Thermodynamically, we see it because water oxidation needs a stronger potential, so creating very harsh conditions, which is also demonstrated by corrosion of SCs, such as CdS and CdSe. Kinetically, we know that multielectron charge transfer processes are intrinsically slow, due to the low probability of finding many electrons close to each other at the same time. And in the water oxidation circumstance, the OER needs 4 electrons to sit somewhere near for a single event.



### 1.4.3 Water oxidation with SC-liquid junctions

The water splitting bottleneck is the evolution of oxygen at the anode, hence the greater effort of the scientific community has been put into its catalysis and improvement. In the context of water splitting, the term photoelectrochemistry means the manner to approach the water separation by physically isolating the two gas evolutions, O<sub>2</sub> and H<sub>2</sub>. And this is done by means of two different electrodes. The work of Fujishima and Honda is accepted by all researchers as the first SC solar water splitting demonstration.<sup>197</sup> Still, Gerischer has also concretely contributed to the cause.<sup>198</sup> However, Fujishima and Honda's report accounts not only for being the milestone of photoelectrochemical water splitting<sup>199</sup>, but also for being the milestone of photocatalytic water splitting.<sup>200</sup> – two branches of the same discovery.

To keep focusing on this PhD work, I will only explain one of the possible PECs, namely the n-type photoanode. It must be said that the utilisation of the common photoanodic n-type semiconductor as WE, and platinum wire/electrode as CE, showed two advantages. On one side, it allows a much broader and fruitful comparison within different research laboratories; and on the other side, it enables the practical application of many materials, which are not thermodynamically suitable for the overall water splitting.

In the n-type photoanode PEC, the presence of a n-type SC-liquid junction (also known as n-type SC-electrolyte junction) determines a depletion layer in the SC in proximity to the junction, and thus a band bending. The degree of the band bending comes down to the number of depleted charges, and it takes place every time there is a junction with a SC and a medium, which can accept more or less charge carriers (**Figure 1-9a-b**).

As already partially explained, the band bending arises from inherent characteristics of the joint compounds. Therefore, we have on the one hand, the energy of the SC Fermi level ( $E_F$ ), while, on the other hand, there is the energy of the electrolyte electrochemical potential ( $-qE^\circ$ ). In presence of a typical n-type SC and electrolyte (A/A<sup>-</sup>) junction, electrons flow from SC to the electrolyte and it is the Fermi level of the SC that shifts down to the energy of the electrolyte electrochemical potential ( $-qE^\circ(A/A^-)$ ). This is also due to the numeric gap in charges between SC and electrolyte, the electrolyte in comparison to SC has almost an infinite amount of charge for compensation. Once that the equilibrium is reached, the depletion layer is created, and the bigger the energy gap between  $E_F$  and  $-qE^\circ(A/A^-)$ , the physically wider the depletion layer will be (**Figure 1-9c**). A “thick” depletion layer is a crucial aspect to increase the driving force of the water splitting and prevent recombination, because it promotes the spatial separation of the photo-generated exciton, *i.e.*, it drives and keeps hole and electron apart.

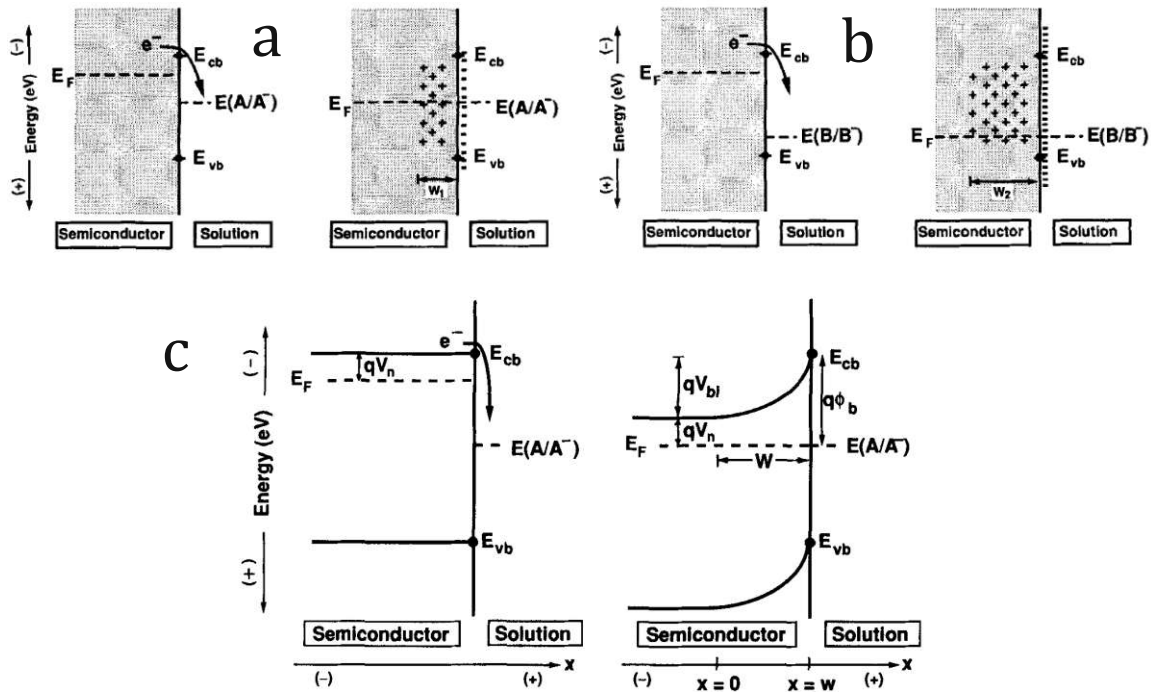


**Figure 1-9.** a) Schematic of the depletion layer formation in junction SC/electrolyte A. SC has a Fermi level energy  $E_F$ , while the electrolyte has an electrochemical potential  $E(A/A^-)$ . b) Schematic of depletion layer formation in the same SC in junction with a different electrolyte B having electrochemical potential  $E(B/B^-)$ . c) Representation of the SC band bending with the respective energy quantities. The created depletion layer is expressed by the depletion width,  $W$ . Modified from 201

Deriving from the kinetic equations of electron charge transfer between SC and electrolyte, and the opposite transfer, the photoanode current in the dark with an applied bias voltage ( $V$ ) obeys the diode equation:

$$I = -I_0 \left[ \exp\left(-\frac{qV}{kT}\right) - 1 \right] \quad (1.2)$$

where  $I$  is the current intensity at the interface.  $I_0$  is the exchange current, which includes parameters like the rate constant of the electron-transfer into the electrolyte, the electron concentration at equilibrium at the SC surface, electrode area, electric charge, and the concentration of acceptor species at the electrode surface.



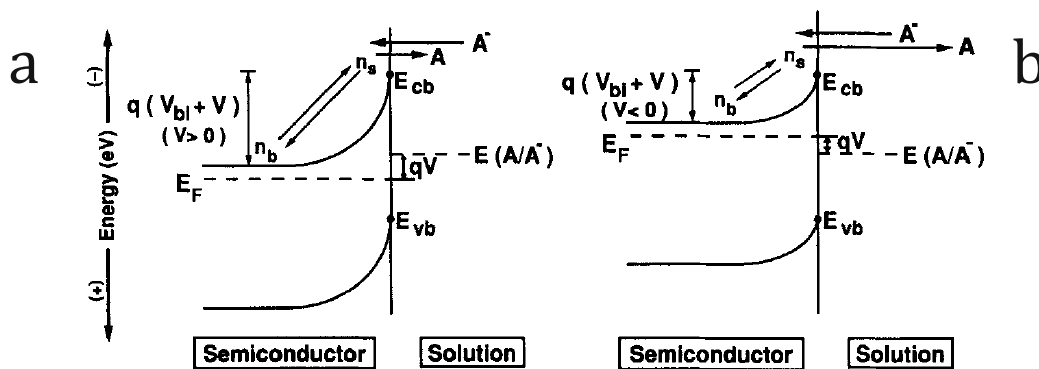
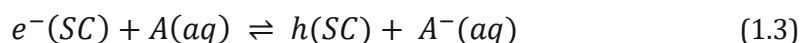


**Figure 1-10.** Schematic of the two conditions of a photoanode. a) When a positive voltage is applied ( $V > 0$ ) b) When a negative voltage is applied ( $V < 0$ ). The applied voltage can only affect the  $A$  transfer, while  $A^-$  is constant. Adapted from <sup>201</sup>

Necessarily, there are two conditions to the equation:  $V > 0$  and  $V < 0$  (**Figure 1-10**). The former is called the reverse bias because it leads to reagents, the latter to products in the equation, which describes the interfacial electron-transfer and follows:



where products and reagents are obtained if, respectively, a reduction or an oxidation occur.

The conditions of reverse bias and forward bias, and our influence on them, are much clearer if in the equation (nX) we distribute the term  $-I_0$ . Consequently, it will appear the following equation:

$$I = -I_0 \exp\left(-\frac{qV}{kT}\right) + I_0 \quad (1.4)$$

where we notice two distinct parts of opposite sign, hence we can visualise it, as if there are two current contributes of opposite direction. The first contribute is dependent on the bias voltage ( $V$ ) and goes from electrolyte to SC, whereas the second contribute is independent on the bias voltage and heads from SC to electrolyte, vice versa, the injection of electrons. Thus, by modifying the applied bias voltage,  $V > 0$  e  $V < 0$ , we decrease or increase the Fermi energy, nonetheless this is only affecting the current flowing from electrolyte to SC, *i.e.*, the injection of electrons into the liquid phase. While the injected electrons into the SC remain constant. Simply, the measurable net output current is the result of the difference of the two currents, though there is only one current, with which we can play.

Under illumination, the situation does not vary substantially. We must consider the two types of charge carriers that can be generated, namely, majority and minority charge carriers. The current arising from the majority charge carriers obeys the diode equation, yet it is so small compared to the thermal ionisation of dopant ions that can be neglected. By contrast, the current arising from the minority charge carriers is connected to the absorbed light intensity. Upon a sensible approximation that considers all the photogenerated charge carriers separated and collected thanks to a strong built-in voltage, the originated photocurrent is equal to the photon flux received by the SC, which is multiplied the elementary charge  $q$ . We can then write the equation for the overall current intensity of the junction:

$$I = I_{\text{ph}} - I_0 \left[ \exp\left(-\frac{qV}{kT}\right) - 1 \right] \quad (1.5)$$

where the only different term from Eq(nX) is the current formed by the photogenerated minority charge carriers ( $I_{\text{ph}}$ ). Note that the photocurrent is positive, hence it is an oxidative current, exactly like the constant current independent from the formed by the n-type SC-electrolyte junction.

In such an illuminated n-type SC-electrolyte junction, an important parameter is the voltage at open circuit ( $V_{\text{OC}}$ ), which is a strong indication of the driving force of the junction (immersed electrode). The  $V_{\text{OC}}$  is the voltage at  $I=0$ , namely, when no current flows through the system. We set this condition, plus consider  $I_{\text{ph}} > I_0$ , which is often the case, and we arrive at a relatively simple equation for  $V_{\text{OC}}$ :

$$I_{\text{ph}} = I_0 \left[ \exp\left(-\frac{qV}{kT}\right) - 1 \right] \quad (1.6)$$

$$V_{\text{OC}} = \frac{kT}{q} \ln\left(\frac{I_{\text{ph}}}{I_0}\right) \quad (1.7)$$

where the open-circuit voltage depends logarithmically on the photocurrent. As a result, the  $V_{\text{OC}}$  depends logarithmically on the light intensity, since photocurrent and adsorbed photon flux are linearly proportional, and we have accepted the “photon-to-carrier 100% collection” assumption. On the contrary, the  $V_{\text{OC}}$  decreases logarithmically with increasing the oxidation current  $I_0$ , which represent the tendency to repriminate charge-transfer

equilibrium. Thus, the lower the current, the slower the interfacial equilibration, the easier is to have high photovoltages.

Furthermore, another significant parameter in the field of energy conversion is the short-circuit current density ( $J_{SC}$ ), which gauges the collection efficiency of the photogenerated charge carriers. From Eq with the condition of  $V=0$ , it results that the overall current is given by the photocurrent  $I_{ph}$ .  $J_{SC}$  is calculated by only dividing photocurrent by the illuminated junction area  $A$ ,  $J_{SC} = I_{ph}/A$ .

So far, all the previous parameters describe thermodynamic physical quantities, but kinetics is extremely relevant for the surface catalysis, and thus for the final performance. For example, in materials such as hematite, an efficient surface catalyst can almost double the output photocurrent.<sup>202</sup> Additionally, not all the electron-hole pairs generated by the SC light adsorption can be separated and measured as photocurrent, but the following equation defines the PEC photocurrent in real systems:

$$J_{PEC} = J_{abs} * \eta_{sep} * \eta_{ox} \quad (1.8)$$

where the two efficiencies,  $\eta_{sep}$  and  $\eta_{ox}$ , turn an ideal system into a real one. The bulk separation efficiency,  $\eta_{sep}$ , is the percentage of holes that can be separated and reach the surface. While the charge injection efficiency,  $\eta_{ox}$ , is the percentage of holes that can be injected into the solution, *e.g.*, if an easy-oxidisable species is on purpose added to the electrolyte, the charge injection efficiency equals 1 and leaves the product unchanged.

However, albeit the 1.7 equation is elegant, it only provides an indicative result of the driving force of a given photoanode. Routine experiments depend much more on practical current output, and therefore, on equation 1.8. Then, if the photocurrent is  $J_{PEC}$  and it measured with  $JV$  measurements, gauging  $\eta_{sep}$  and  $\eta_{ox}$  is not straightforward.

In this thesis work, I make a large use of the photocurrent measurements, because great and fast is the information output for a photoanode. Unfortunately, explaining the why the recombination of photo-generated charge carriers lessens or strengthens needs a greater amount of time and efforts. Thus, it is not done for explorative purposes.

Eventually, to finally compare different PEC cells even with dissimilar working principles, an essential parameter is the solar-to-hydrogen efficiency,  $\eta_{STH}$ . Such efficiency is used for highly performing devices, and it can be calculated by dividing the total output energy by the total input energy:

$$\eta_{\text{STH}} = \frac{\text{total output energy}}{\text{total input energy}} = \frac{\Delta G * r_{\text{H}_2}}{P_{\text{in}} * A} \quad (1.9)$$

where  $\Delta G$  is the Gibbs free energy ( $237 \text{ KJ mol}^{-1}$ ),  $r_{\text{H}_2}$  is the hydrogen production rate in  $\text{mol s}^{-1}$ ,  $P_{\text{in}}$  is the incident photon flux ( $100 \text{ mW cm}^{-2}$ ) and  $A$  is the area of the photoanode under illumination ( $\text{cm}^2$ ). In the measurement of the area, there is a debate amongst different solar water splitting branches. Should it be used the geometrical or the effective area in the equation? But then how to exact determine the surface area? In the field solar water splitting with inorganic SC thin films, it is common to use the geometrical one. While with organic compounds at work, it is typical to calculate the effective one, which is also needed for the Randles-Sevcik's equation and the TOF calculation, whether possible.<sup>203</sup>

#### 1.4.4 Material requirements

The target of efficiency for a feasible industrial upscale of PECs is given by 10% STH conversion.<sup>204</sup> To date, no n-type inorganic SC with under- and overlayer (*i.e.*, OEC) can offer such a performance on a 1 cm<sup>2</sup> scale, let alone upscaling the PEC area. In the last 30 years, the enhancement rate for n-type SC PECs has not given big signs of acceleration.<sup>205</sup> Though much has been done towards the fundamental understanding of water oxidation mechanisms and charge carriers dynamics in the SC bulk (efficiency terms in equation 1.8).<sup>206-211</sup> As the thesis work is not focused on performance but on fundamental research, the interest for the efficiency slightly fades. Herein, the n-type inorganic SC is solely taken as a reliable template. Nevertheless, to find a matching candidate for the role of photoanodic material, there are several requirements, which need to be fulfilled or at least considered:

1. Appropriate band gap, around 2.1 eV
2. Matching bands position
3. Fast charge transfer
4. Stable at operating conditions
5. Earth abundant
6. Inexpensive
7. Non-toxic

The band gap energy is the first one written because the most important parameter of all. From the band gap energy along with an assumed 100% IPCE, it is easy to calculate the maximum light current density that can be extracted by a given material (**Figure 1-11**). Due to the needed overpotentials (see [subsection 1.4.2](#)), much smaller semiconductors band gaps than 2 eV would not be able to lead to photoanodic oxidation of water, although it would give an advantage according to the maximum theoretical current, as shown in **Figure 1-11**.

Moreover, the bands position plays a significant role for two reasons. On the one hand, due to the charge injection, finding a compromise between fast charge transfer and slow back reaction. On the other hand, owing to the thermodynamical charge separation abilities of the SC, *i.e.*, the broader the depletion layer, the more pronounced the band bending, the greater the driving force to charge separation (**Figure 1-9**).

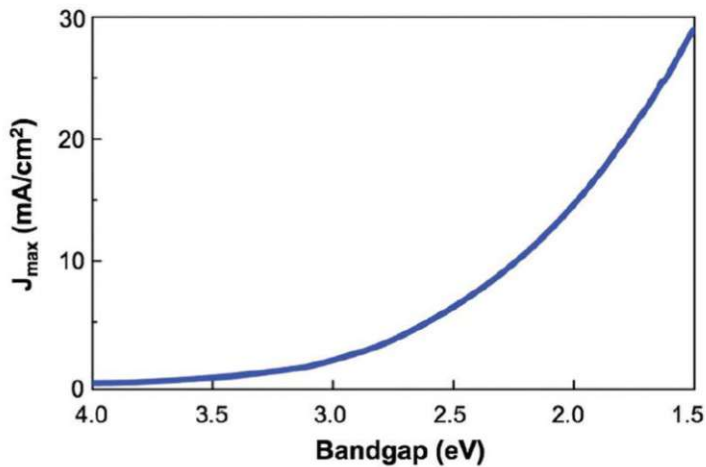


**Figure 1-11.** Theoretical maximum photocurrent ( $J_{\max}$ ) as a function of the band-gap.

The fast charge transfer is to be intended both in the bulk and at the interface. Typically, the toughest obstacle of the water oxidation itself lies at the interface and, if not, doping approaches can greatly boost poor bulk conductivities and solve the problem.<sup>202</sup> Then, the difficult part shifts to the interface where novel and more efficient catalysts are needed.<sup>212</sup>

To the facts, many SCs that have the most attractive optical properties have major stability limitations. In [section 1.4.2](#), those were briefly mentioned. Anions such as  $S^{2-}$  and  $Se^-$  get promptly oxidised by the photogenerated holes, hence the conditions at which they should work are too demanding.<sup>213,214</sup>

Cost, abundance, and non-toxicity can be included in a single keyword – sustainability. A concept that applies in the market and environmentally.

### 1.4.5 Hematite and co-doping

Iron oxide is one of the most abundant compounds on Earth, hence extremely stable. Additionally, elementary iron appears in many minerals, and it is the fourth element in weight to take part in the Earth's crust with approximate 5%. Therefore, the existence of an n-type SC made of iron and oxygen is already fulfilling three requirements from [section 1.4.4](#), and particularly those related to sustainability. Moreover, the  $\alpha$ -geometry of iron oxide is not only an n-type SC, but it is also an extremely good light absorber, with a band gap of 2.1 eV. Additionally, hematite is stable in water from medium to high pH values and to even high applied bias voltages.

By contrast, hematite faces great challenges to accomplish the potential 15.5% STH conversion efficiency.<sup>215</sup> After 20 years of deep research on hematite gone through constant improvements in nanostructuring and surface catalysis, only one third of the theoretical photocurrent has been obtained, 4.32 of 12.8 mA cm<sup>-2</sup> calculated.<sup>202</sup> Even, the record has arrived with a deluxe version of a photoanode, namely, Pt-doping, Sn-doping-diffusion, and Co-Pi as OEC.

By taking a closer look at the limitations of hematite itself, charge transfers in the bulk and at the surface are poor and the water oxidation is slow.<sup>216,217</sup> The first one relates to an inherent hematite problem, namely the scarce electron mobility<sup>218</sup>, and a too short hole diffusion length.<sup>219,220</sup> The second one, it is the consequence of surface trap states and a far-from-optimal catalytic sites.<sup>221-223</sup> Therefore, doping has been widely employed in hematite with solar water oxidation application. For example, the indispensable high activation temperature principally applied on hematite films deposited on FTO enables the conditions for Sn diffusion, and hence Sn-doping.<sup>224</sup> Hematite photoanodes have been extrinsically doped with many metals Sn, Ti, Zr, Si, Nb, Pt, Mn, Ge, Sb as electron donors, and with Cu, Mg, as electron acceptors.<sup>202,225-234</sup> Non-metal dopant such as F and P have also displayed advantages in the extrinsic doping of hematite<sup>216,218</sup>, while the introduction of oxygen vacancies, being O<sup>2-</sup> the counterion in the oxide, can function as intrinsic dopant.<sup>208,211,217,235,236</sup>

As already reported in few cited articles, the doping can often help in one or some aspects of the electrode photoactivity. Nevertheless, the effect of the doping is confined. To allow a further boost of the performance, there are other left-out aspects that can be modified. And occasionally, this is doable through a parallel doping, *i.e.*, a co-doping.

In solar water splitting, the synergetic effect of co-dopants dates back to 2004, when Luo et al co-doped titania photocatalyst with Cl<sup>-</sup> and Br<sup>-</sup>.<sup>237</sup> By introducing the two dopants they

could narrow the band-gap and increase the photocatalytic activity. Previously no photocatalysis was involved, co-dopings were realised and authors could just observe the consequences, whether the dopants once in the material interact with each other, or whether the electrochemical capacity and cathodic properties can be improved.<sup>238,239</sup>

By contrast, co-doping in photoelectrodes based on metal oxides is a recent trend, that has only lately appeared.<sup>240-242</sup> Due to its particularly sluggish charge carriers mobility, hematite has already been used more than other semiconductors for co-doping, and it was one of the first reported.<sup>243,244</sup> As doping does, co-doping of hematite typically extra enhances electrical conductivity and charge carrier density. <sup>245,246</sup> Nonetheless, it can also mild the concentration of defects, hence promoting the charge separation yield in the space charge layer.<sup>247</sup>

In [Chapter 5](#), I consider these concepts in order to explore co-doping on hematite template thin films in the shape of photoanodes for solar water oxidation. The study includes two species  $\text{Li}^+$  and  $\text{Sb}^{5+}$  added to a water-based spin-coating solution. At these conditions, the Sb addition is challenging, because it is carried out with a very hydrolysable precursor, namely  $\text{SbCl}_5$ .



## 1.5 Motivation

The graphene-based LGFET is a highly complicated system, owing to the numerous graphene materials syntheses and their modifications. Thus, I endeavoured to mention in the previous sections, [1.2](#) and [1.3](#), the origin, structure, and properties of the material classes firstly. Moreover, by using sheets or flakes, a reliable anchoring becomes essential, and this is often the case for GOs. As aforementioned, also the reduction approaches offer several possibilities.

In fact, there are conflicting explanations found in the published literature, which however leave some free space for other attempts to further rationalize the pH sensing of graphene-based LGFETs.<sup>37,187,188,248</sup> In this complexity, the reactivity of graphene materials is certainly another variable to be controlled. Incorporation of N-atoms as dopants (substitutional) or as functional groups (with in-plane, both sides, or edge chemical reactions) can occur.<sup>36,242,243</sup>

As GO possesses undeniable benefits, it is necessary to speak of its deposition. Typically, the anchoring of graphene sheets/flakes often includes APTES (see [subsection 1.3.4](#)). Then, the reduction is carried out afterwards with the risk of accidental doping of rGO, or even direct APTES-H<sup>+</sup> interaction detected as electric field variation. Furthermore, although almost 90 years old, hydrazine hydrate, or multi-step including hydrazine hydrate, remains a top reduction medium for GO.<sup>76,101</sup> Hydrazine hydrate is not only efficiently reducing, but also provides GO with N-introduction, which may be crucial for GO properties and the overall device performance.<sup>101,117</sup> This can happen either in liquid or in gas phase.

A similar help should arise from NH<sub>3</sub> reduction, which leads to a simultaneous reduction and N-incorporation, with the advantage of being clearly less toxic than hydrazine.<sup>102,249</sup> Again, the reduction time could further support an ideal GO modification.<sup>250-252</sup> A comparison of different reduction atmospheres and approaches, along with a careful investigation may bring to new insights into pH sensing mechanisms, and the chemistry of graphene derivatives. To which extent should GO be reduced to be best at LGFET pH detection? Which dopants and functional groups can alter the detection? At the same time, the pH detection becomes itself an analytical method in a symbiotic correlation, rather than a final application only.

By following [section 1.4](#), the intent of the second project is to explore a novel co-doping with the combination of Sb with oxidation state 5+ and Li<sup>+</sup>. The way, how I envision it, is an approach, which is based on simplicity and reproducibility.

On the one hand, the relevance of subsections [1.1.1](#) and [1.1.2](#) calls for a method which is straightforward and sustainable. Thus, I choose to work with water solutions and hematite.

On the other hand, the uncomplicated process should also enable reproducibility. Hence, by using compact thin films and spin-coating deposition, I assume to minimise the number of involved variables. Furthermore, for the fundamental purpose of this study, I intentionally spare the activation annealing, so that no Sn diffusion takes place.<sup>253</sup> This renders the study unique, as the common operation involves the 800°C activation, especially for solution-based methods.

In literature, the doping of hematite with  $\text{Sb}^{5+}$  shows a remarkable increment from the undoped samples<sup>232</sup>, while  $\text{Li}^+$  doping shows clear pluses only in  $\text{BiVO}_4$  photoanodes<sup>254</sup>. The advantage of using  $\text{Sb}^{5+}$  has not encountered a co-doping trial with an additional cation yet, in particular with a cation with a lower oxidation state than iron in hematite. A hint this pathway is accessible and worth to be taken arises from Ru doping of hematite, where Ru shows different oxidation states.<sup>247</sup> Since in hematite is observed that the photo-generated holes and electrons are likely to recombine in short time scales<sup>225</sup>, an effort in the direction of enlarging the charge separation yield is needed. Therefore, the co-doping approach attempts at generating through co-doping double-donor-acceptor centres.

Moreover, a further novelty contribute is given by the verification of the feasibility of the *in-situ* doping of hematite with  $\text{Sb}^{5+}$  cation. To the best of my knowledge, using a highly hydrolysable  $\text{Sb(V)}$  precursor in water-based deposition solutions accounts for a challenge that have not been solved yet, as well as the simultaneous doping with  $\text{Sb}^{5+}$  and  $\text{Li}^+$ .



# Chapter Two

## Materials and procedures

La mafia non è affatto invincibile, è un fatto umano e come tutti i fatti umani ha un inizio e avrà anche una fine.

The Mafia is not at all invincible, it is a human fact, and like all human facts, has a beginning and will also have an end.

---

Giovanni Falcone

Lerne von der Geschwindigkeit der Natur: Ihr Geheimnis ist Geduld.

Learn from the speed of Nature: its secret is patience.

---

Anonymous – Bergsteiger



# 2 Materials and procedures

Chapter number two puts together all the experimental work, starting from the compounds (Table 2-1) and arriving at the methods for materials synthesis and preparation.

**Table 2-1.** Commercial chemicals involved in the syntheses, substrates preparation, and analyses.

Compound	Composition	CAS	Supplier	Purity
<b>(3-Aminopropyl)triethoxy-silane (APTES/APTS)</b>	C <sub>9</sub> H <sub>23</sub> NO <sub>3</sub> Si	919-30-2	Sigma Aldrich	99%
<b>Acetone</b>	C <sub>3</sub> H <sub>6</sub> O	67-64-1	-	Techn.
<b>Ammonia (gas)</b>	NH <sub>3</sub>	7664-41-7	Messer	-
<b>Antimony(III) chloride</b>	SbCl <sub>3</sub>	10025-91-9	Fluka	≥99.0%
<b>Antimony(V) chloride</b>	SbCl <sub>5</sub>	7647-18-9	Sigma Aldrich	99%
<b>Ethanol</b>	C <sub>2</sub> H <sub>6</sub> O	64-17-5	-	Techn.
<b>Ferric chloride hexahydrate</b>	FeCl <sub>3</sub> ·6H <sub>2</sub> O	10025-77-1	Merck	For analysis (≥99.0%)
<b>Hydrochloric acid</b>	HCl	7647-01-0	-	Techn. (35-37%)
<b>Hydrogen peroxide</b>	H <sub>2</sub> O <sub>2</sub>	7722-84-1	-	30%
<b>Lithium chloride</b>	LiCl	7447-41-8	Sigma Aldrich	≥99%
<b>Polyethylenglycol bisphenol A epichlorhydrin copolymer</b>	[C <sub>15</sub> H <sub>16</sub> O <sub>2</sub> ·C <sub>3</sub> H <sub>5</sub> ClO·(C <sub>2</sub> H <sub>4</sub> O) <sub>n</sub> ·H <sub>2</sub> O] <sub>x</sub>	42617-82-3	Sigma Aldrich	-
<b>Potassium hydroxide</b>	KOH	1310-58-3	Merck	-
<b>Sodium hydroxide</b>	NaOH	1310-73-2	Riedel de Haen	For analysis (≥98.0%)
<b>Sulphuric acid</b>	H <sub>2</sub> SO <sub>4</sub>	7664-93-9	-	Techn. (98%)

## 2.1 Graphene oxide colloidal solution

The synthesis of GO was carried out at the University of Bayreuth, and the pH measurements were done in collaboration with AIT (Austrian Institute of Technology), the GO was received and employed for the first project ([Chapter 4](#)).

Albeit various GOs were synthesised and tested at the University of Bayreuth, in this thesis only the Hummers GO (HGO) was used.<sup>255</sup> Briefly, the synthesis method, which was followed to produce the concentrated GO solution ( $4.28 \text{ mg mL}^{-1}$ ) is reported hereafter.

Natural flake graphite (1 g, 125-250  $\mu\text{m}$ , *Reinstflocke* RFL 99.5, Kropfmühl AG) and  $\text{NaNO}_3$  (1-2 g, Sigma) were mixed with conc.  $\text{H}_2\text{SO}_4$  (40 mL, 98%, Sigma) until flakes turn blue (microscope confirmation necessary). In absence of it, a greater amount of  $\text{NaNO}_3$  must be added, and the mixture must be stirred further. Next,  $\text{KMnO}_4$  (4 g, Sigma) was added over 3 h to get to a dark-green and highly viscous suspension. This was then overnight mixed in an overhead shaker – a soft sound should be heard by opening the bottle. The resulting highly viscous brown slurry was later poured into ice-cooled DI water (30 mL).  $\text{H}_2\text{O}_2$  (about 2 mL, 30% Sigma) was added to dissolve the formed  $\text{MnO}_2$ , and it was poured until the solution turned golden and no more bubbling was observable. Purification of GO was conducted by repeated washing/centrifuging (3 times, 10 min, 5000-10000 rpm) and subsequent dialysis to reach 2-10  $\mu\text{S cm}^{-1}$  ionic conductivity.

## 2.2 Production of a graphene-based LGFET

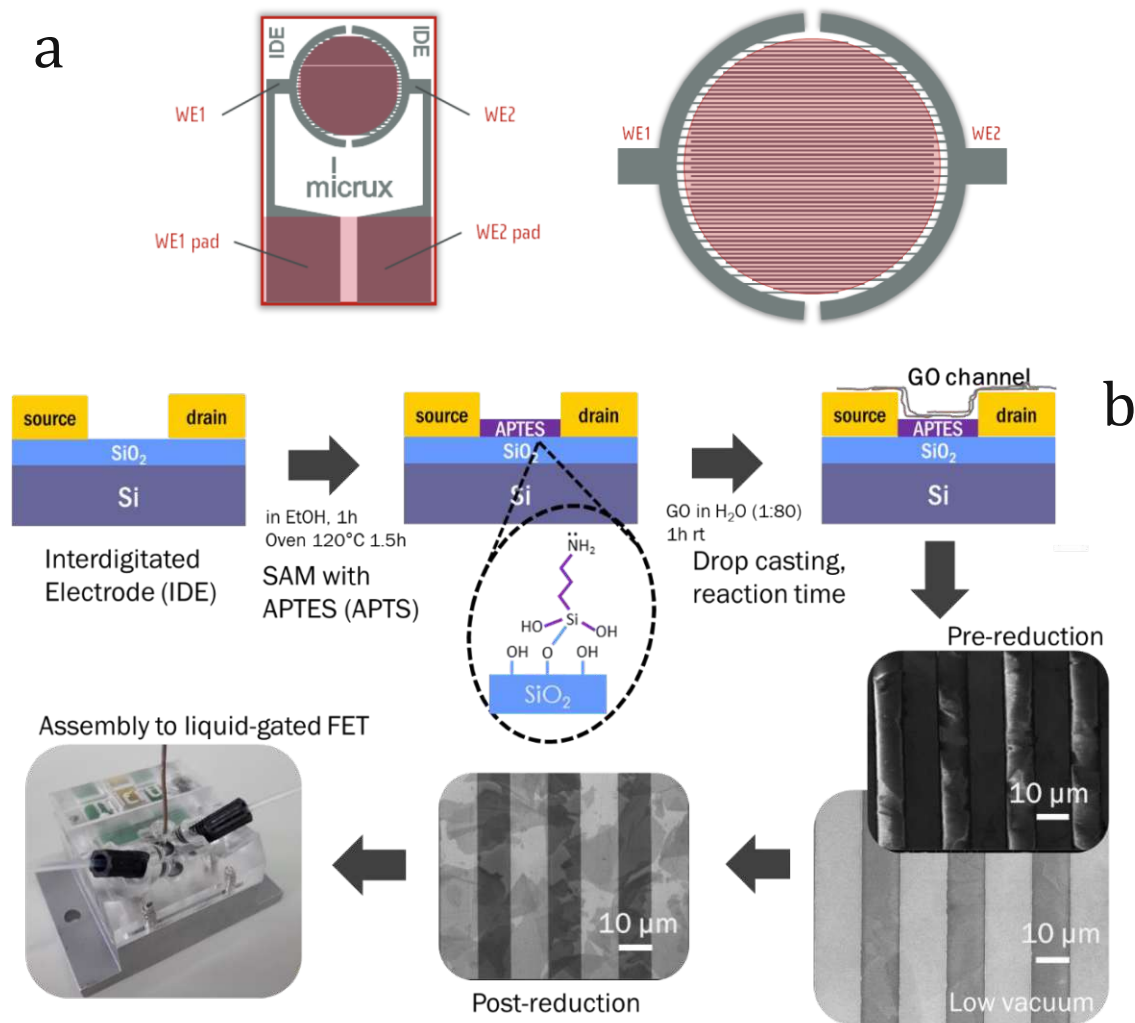


**Figure 2-1.** a) Representation of the purchased IDEs and zoom-in of the electrochemical cell. Modified from products brochure<sup>256</sup>. b) Production steps from empty IDE to rGO-IDE.

### 2.2.1 GO deposition and anchoring

As electrodes for the FETs, Micrux® commercial InterDigitated Electrodes (IDE) were used (Figure 2-1a). One electrode consists of two rectangular gold pads, called WE1 and WE2 pads, the typical source and drain, which were used for the device contacting. The contacts are then reaching a circular patterned area, named electrochemical cell (3.5 mm  $\varnothing$ ). The gold contacts in the electrochemical cell are 10  $\mu\text{m}$  broad, 10  $\mu\text{m}$  thick, and also spaced 10  $\mu\text{m}$ . The aim is to maximise the function of the channel material.

The IDEs were first thoroughly cleaned with acidic piranha solution (a 3:1 mixture sulfuric acid and hydrogen peroxide), generously rinsed with DI water, and dried with compressed air (first phase of Figure 2-1b).



A SAM was generated by immersing the IDEs for 1 hour in an ethanol solution 0.1M APTES (3-aminopropyltriethoxysilane or also called APTS). Next, the IDEs were rinsed with ethanol to wash off the too loosely bounded APTES units. Moreover, to conclude the condensation reaction were annealed in oven at 120°C for 1.5 hours. As a result, strong Si-O bonds should arise. Successively, 15  $\mu\text{l}$  of 1:80 diluted GO solution were dropcasted onto the electrochemical cell by means of a  $\mu$ -pipette. The nanoflakes droplets were left reacting with APTES for 1 hour at ambient conditions in order to be electrostatically anchored. APTES amino groups are positively charged, and hence attract GO negatively charged flakes.<sup>142,257</sup> After the waiting time, the IDEs were rinsed with abundant DI water to remove the GO excess and an atomically-thin graphene-like layer was left behind. And again, the GO-IDEs were dried with compressed air.

## 2.2.2 Graphene oxide reduction approaches

Various reduction atmospheres and approaches were employed in this work. All the different methods are listed with a short title for simplifying the information search. Conditions of reduction for *in-situ* XRD, as relevant data for Chapter 4, are also listed.

### *Reduction and in-situ current monitoring in custom-made set-up*

The reduction set-up was a custom-made system made of a stainless-steel chamber, an alumina heating plate furnished with a thermocouple type S, contacting arms with clamps for metal or alloy needles, an amperemeter, a heating system, valve with possibility of connection for several gases, a vacuum pump, and the respective read-out electronics. The chamber could be hermetically sealed, to avoid any leak of harmful gases in case of overpressure.

The samples were introduced one by one for reduction/measurement, each time carefully contacted with the stiff Pt/Ti needles, and the help of a microscope. The constant contacting turned out to be a major problem with the changing temperature, as without contact the measured current was null. Only then, the chamber lid could be placed on top of the cylinder and manually sealed. The chamber was cycled 2 times with corresponding gas and vacuum, except when only vacuum was applied. In that circumstance, the pump stayed connected until the pressure remained unchanged for 30 s. In presence of gas, with the final gas loading, a slight overpressure was set to exclude any potential leaks.

With the reduction set-up, 4 atmospheres were investigated, namely, vacuum, Ar, 2.4% H<sub>2</sub>/Ar mixture, and NH<sub>3</sub>. Additionally, static and flow gas modes were explored to exclude variations (no difference observed). While measuring the current, which was initially forced

through the channeling GO, the heating system enabled temperature ramps. An optimisation of the heating ramp in light of reproducibility, time-consumption, and GO current increase, delivered a ramp of  $10^{\circ}\text{C min}^{-1}$  (see preliminary results at section 4.2). The ramp would take the temperature from room to  $310^{\circ}\text{C}$ , held it 40 min, and then controlled cool at  $10^{\circ}\text{C min}^{-1}$ .

#### *Schlenk tube $\text{NH}_3$ reduction*

The size of the Schlenk was selected large enough to accommodate two samples. The samples were gently let slide to the bottom of the Schlenk always facing up. Usually, the two sits in contact with their side and only slightly tilted. A heat gun with its heating aperture was placed exactly below the Schlenk tube bottom at 2 cm distance and the Schlenk was securely clamped at the fume hood frame. The temperature of the heat gun was set at  $310^{\circ}\text{C}$ . However, the temperature felt by the inner Schlenk tube bottom was  $220^{\circ}\text{C}$ , which could drop up to  $10^{\circ}\text{C}$  moving to the tube side. The temperature was assessed with a wire temperature sensor, touching the bottom of the tube. The target temperature was at least  $200^{\circ}\text{C}$  according to the reported GO literature. The sensor also provided information on the ramp too, *i.e.*, the inner tube bottom heated up at about  $50^{\circ}\text{C min}^{-1}$ . That means that maximum temperature was reached within 5 minutes. Once that the heat gun was turned on and correctly placed, the heating would last 1 h. Next, the heat gun was turn off, and as soon as the samples would cool down at room temperature, they were ready to be measured.

The alternative method was developed in light of some safety concerns for  $\text{NH}_3$  handling in the reduction set-up, and also the needed amount of time for a single sample reduction. The heating system could have eventually permitted higher heating ramps, but surely it would have come near the machine limit.

#### *Hydrazine hydrate reduction*

As reported elsewhere<sup>25,26,37,142</sup>, 1 ml of hydrazine hydrate was dropped at the inner rim of a glass petri dish, while the GO-IDEs were laid in the middle, avoiding direct contact. The glass lid was sealed with Kapton® scotch-tape, and the closed petri was given into an oven located in a fume hood. The reaction was run overnight at  $80^{\circ}\text{C}$  for 8 h. The so-prepared rGO-IDEs were then ready for further analyses or pH detection.

## 2.3 Production of hematite photoanodes

FTO is initially cut into 2x4 cm slides. Only later, the slides are cut into 2x1 cm photoanodes ready for testing. The 2x4 FTO slides are carefully cleaned by taking hint from a systematic cleaning procedure.<sup>258</sup> With all the following cleaning media, the FTO slides are sonicated for 15 mins in a beaker, namely, washing soap-water mixture, acetone, and ethanol. The slides must be well covered in the beaker with the respective solution. Few recommendations after the soap-water sonication – the slides are rinsed and singularly blow-dried with compressed air and the beaker rinsed from soap rests. The cycle with the cleaning media is to be repeated. Only after a second cycle, the slides are sonicated for 20 mins in a 0.1 M KOH solution. To remove rests of KOH, the FTO slides are sonicated for 20 mins and generously rinsed with DI water. In case some slides are immediately needed, the slides must be also blow-dried, otherwise they can be stored in DI water in a capped beaker until needed.

### 2.3.1 Synthesis of hematite thin film

In a typical solution,  $\text{FeCl}_3 \cdot 6\text{H}_2\text{O}$  (0.54 g) was dissolved in 20 mL DI water. Under gentle stirring, polyethylenglycol bisphenol A epichlorhydrin (0.54 g) was also added and dissolved. Then, the solution was ready to be spin-coated, and this was accomplished by means of a Pasteur pipette. To make a first layer, around 2 mL of the solution was necessary to entirely cover the FTO area due to the bad wetting. Meanwhile, the FTO slide was properly masked with scotch tape and just the deposition area was free. It must be said that of 2 mL the majority was wasted in the first spin-coating step. To achieve a sufficient light absorption, 4 layers were deposited, each layer was deposited at 1000 rpm for 9 s and 2000 for 30 s. After each deposition, the scotch tape was removed, and the electrode was annealed at 550°C to form hematite. The required amount of solution was later greatly reduced to ~500  $\mu\text{L}$  thanks to the better affinity with hematite. The electrode was then cut into photoanodes with photoactive area of 1x1 cm.

### 2.3.2 Co-doping

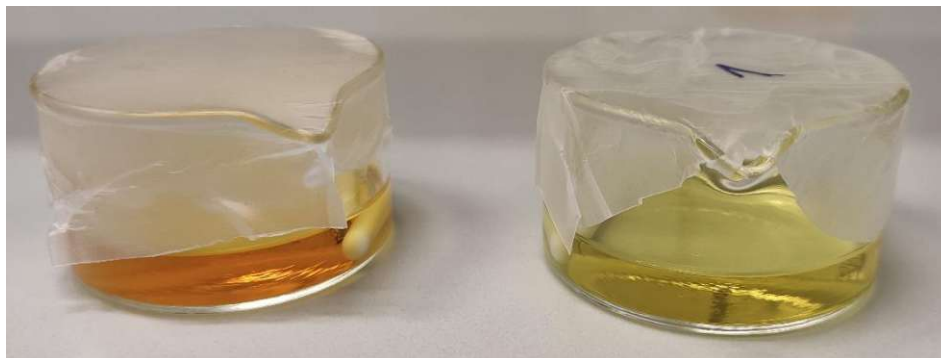


**Figure 2-2.** Picture of the two spin-coating solutions. On the left the standard one, whereas on the right the same solution with 100  $\mu\text{L}$  HCl addition.

In order to dope hematite *in-situ*, the precursors for co-doping were added directly to the spin-coating solutions. However, to enhance the reproducibility and minimise errors, the amount of precursors are taken from mother solutions. LiCl (0.0424 g, 0.001 mol) was dissolved in 10 mL DI water, to obtain a 0.1 M solution. To get the same solution concentration,  $\text{SbCl}_5$  (0.299 g, 0.001 mol) was dissolved in 10 mL of concentrated HCl (36%). Therefore, to add a nominal 1 at% of dopants over mol of formed  $\text{Fe}_2\text{O}_3$ , 100  $\mu\text{L}$  needed to be transferred to the respective spin-coating solution. 4 solutions were prepared including standard samples, two mono-doped samples ( $\text{Sb}^{5+}$  and  $\text{Li}^+$ ) and the co-doped sample. The HCl greatly inhibits the hydrolysis and stabilises the solution. No signs of hydrolysis were observed after about 2 years. As water and concentrated HCl were added to dope the spin-coating solutions, all the solutions were compensated with the missing solvents. Nevertheless, HCl addition slightly changes the solution viscosity and colour (see **Figure 2-2**). In particular, the viscosity factor could turn out in thinner deposited layers, which are not easily recognisable.

Moreover,  $\text{Sb}^{3+}$  was explored by following the same procedure. Also there, concentrated HCl was employed to exclude any risks of hydrolysis. To prepare the mother solution,  $\text{SbCl}_3$  (0.228 g, 0.001 mol) was dissolved in 10 mL conc HCl (36%).

Note, all spin-coating solutions are usually fresh-prepared, especially the ones containing  $\text{SbCl}_5$ , which hydrolyses within 36-48 h at those conditions (figure ).

# Chapter Three

## Characterisation

I think I could stand anything, any suffering, only to be able to say and to repeat to myself every moment, 'I exist.' In thousands of agonies – I exist. I'm tormented on the rack – but I exist! Though I sit alone in a pillar – I exist! I see the sun, and if I don't see the sun, I know it's there. And there's a whole life in that, in knowing that the sun is there.

---

Fyodor Dostoyevsky

Don't give yourselves to these unnatural men – machine men with machine minds and machine hearts!

You are not machines!

You are not cattle!

You are men!

---

Charlie Chaplin

# 3 Characterisation

Chapter number three lists the characterisation methods used for this thesis and highlights their theoretical working principles. Furthermore, it also describes the methods from a practical point of view, always minding how the data were collected.

## 3.1 Current-Voltage Characteristics

With  $I$ - $V$  characteristics, or  $I$ - $V$  curve, it is possible to measure the electrical properties of a given material, device, circuit. A voltage is applied, and a charge motion is induced according to the nature of the sample.

### 3.1.1 Principle

Current-voltage characteristics means to apply a varying potential in the time and to measure a resulting current. That translates into three important facts, *i.e.*, there is an applied potential bias, its scan rate, and an amperemeter. The outcome of current-voltage characteristics relates the recorded current with the potential of the working electrode. Such is a 2D plot called  $I$ - $V$  curve, or  $J$ - $V$  curve, in case the analysed area corresponds to the unit.

Generalising, a great impact on this has been given first from the developments of voltammetry, which has old origins. Another significant breakthrough is represented by the first three electrodes potentiostat (Hickling 1942).<sup>259</sup> In his work in 1948, Randles highlights the importance of the “current-voltage curves” and comments on them. He uses a cathode ray oscillograph (rapid response is crucial), a micro-electrode, and applies a rapid potential sweep, making the whole operation fast, and hence practical.<sup>260</sup>

In this thesis,  $I$ - $V$  characteristics has been widely utilised and thus they deserve particular attention. Both final applications of this thesis are based on an electrical measurement, either the pH sensing/transfer characteristics or the photoanodic water oxidation. Certainly, compared with the past, now the current-voltage measurements are fast and quite reliable, if few variables are considered or better when constant. This section is especially written for understanding and contextualising the coming data.

### 3.1.2 Applied in LGFET - Flow cell

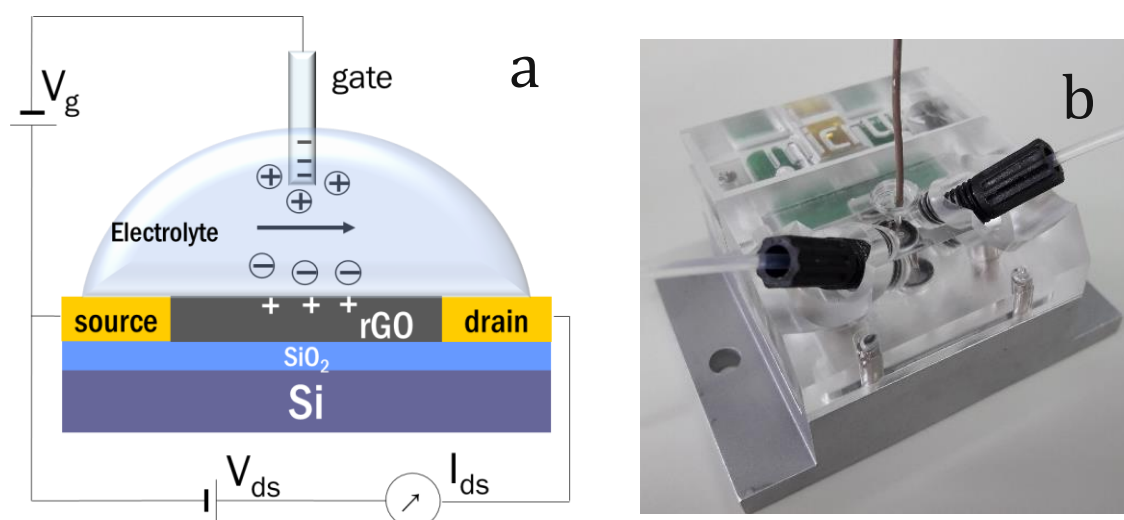


**Figure 3-1.** a) Representation of the functioning LGFET during pH sensing operations. b) Picture of the real LGFET from outside. The inlet and outlet tubing for the 0.1x PBS electrolyte is visible, as well as, the gate rod, sealed and pointing down to where the IDE electrochemical cell will be placed.

A custom-made all-in-one flow compatible platform ordered from MicruX Technologies was utilised to measure both pH sensing and the channel transfer characteristics (practically  $I$ - $V$  characteristics). To move the liquid flow of 0.1x PBS solvent in and out a peristaltic pump with  $400 \mu\text{l min}^{-1}$  was employed. The probe station was a Keithley 4200. A 0.1 V source-drain bias was constantly applied, while the gate voltage was set at -0.4 V, unless stated otherwise. Typically, for the pH sensing measurements of this work, a constant gate voltage was employed, and for the transfer characteristics, a -0.8-0.8 V sweeping gate voltage was used ( $I_{ds}V_g$  or  $I_dV_g$ ). Though, there is an additional measurement to verify the current and its drift ( $I_{ds,t}$  or  $I_{d,t}$ ), and in contrast with the  $I_{ds}V_g$  and pH sensing, keeps both gate voltage as well as the PBS pH constant.

### 3.1.3 Photocurrent-Voltage Characteristics

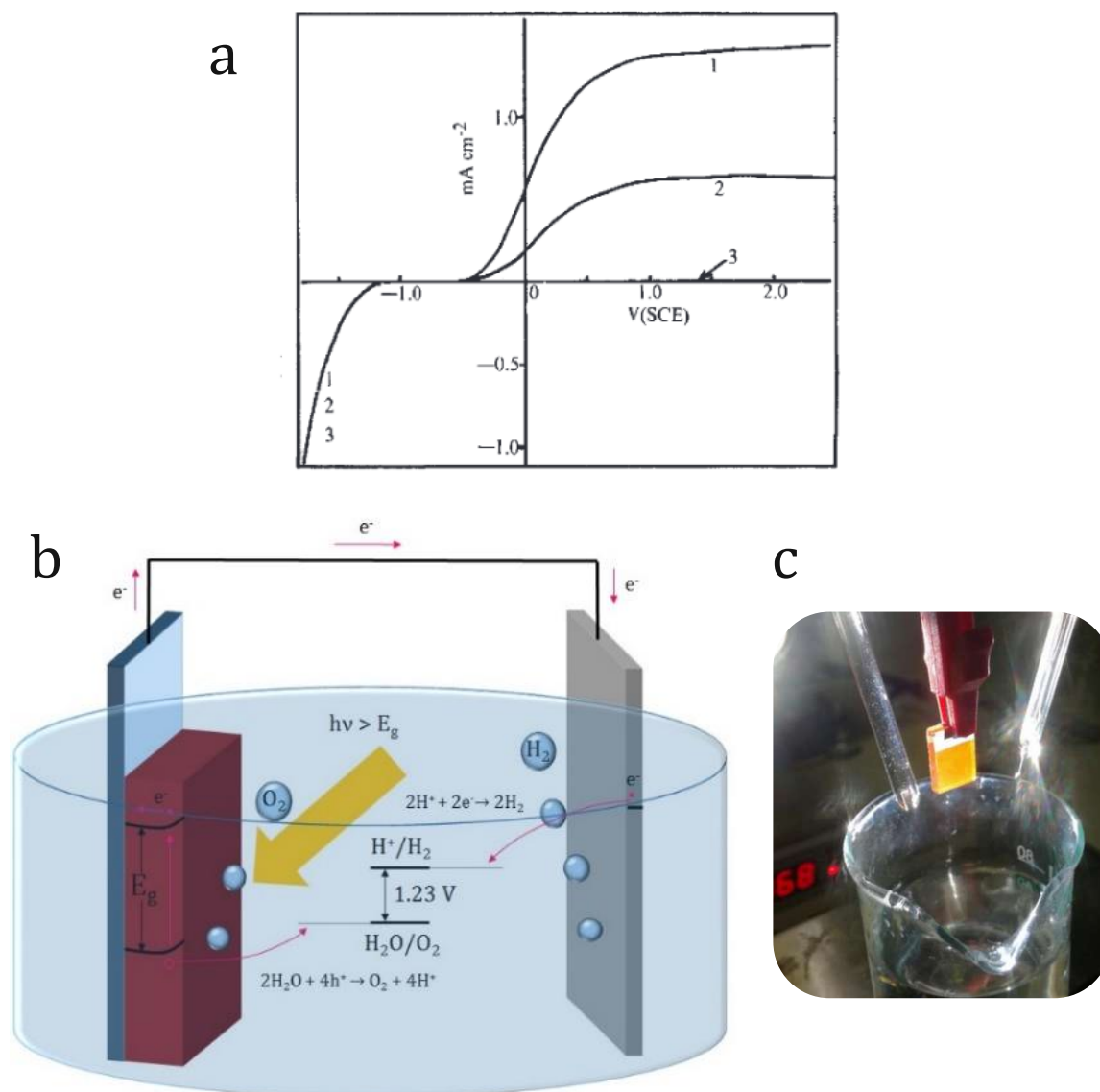


Figure 3-2. a) Current-voltage curves with photoanodes, light on (curve 1) and light off (curve 2). From <sup>197</sup>. b) Schematic of the photoelectrochemical cell with anode, photoanode, and the thermodynamics of the half reactions to enable water splitting. c) The three electrodes for photoelectrochemical characterisation and beaker with the 0.1M NaOH electrolyte.

In the field of photoelectrochemistry, in 1972 Fujishima and Honda characterise with a potentiostat and a SCE the early TiO<sub>2</sub> thin-film electrodes.<sup>197</sup> Since then, not much has changed in the  $I$ - $V$  characterisation of thin-film photoanodes. They recorded two currents, one while under illumination, and another one without illumination. The difference between these two currents is intended as the photoactivity. The current generated under illumination is typically referred to as the photocurrent, which can be sometimes misleading. A regular alternation of light and dark phases has been called chopped illumination and gives rise to current transients. Only in a second moment, current



transients have been considered as additional relevant information in the overall photoelectrochemical characterisation.<sup>261,262</sup> More details about data interpretation follows in [subsection 5.3.5](#).

In this work, the  $J$ - $V$  curves were recorded at 25°C with a 0.1 M NaOH electrolyte (pH 13.1), thus, the RHE potential was calculated accordingly. The three electrodes were immersed all together in the same beaker with ~50 mL electrolyte. As counter, working, and reference electrode, respectively, a photoanode under testing, a platinum electrode, and a standard calomel electrode were used. The potentiostat allowing the  $J$ - $V$  curves was a PGSTAT302N by Metrohm, while a Xe lamp with a Newport 1.5 AM G filter was employed for illumination. The distance, at which the testing photoanode was fixated in order to attain 1 Sun, was adjusted using a Thorlabs power energy meter provided with a photodiode power sensor. Dark and chopped measurements were manually realised. After each measurement involving electrolyte dipping, the photoanodes were generously rinsed with DI water and blow-dried.

### 3.1.4 *In-situ* current monitoring

The system, which permitted the current monitoring of the GO channel while reducing, has been almost entirely described in [section 2.2.2](#), because of convenience. The used thermocouple was a type S, hence the conversion of voltage to temperature was enabled by applying the expansion equation and the coefficients given by literature (**Table 3-1**).<sup>263</sup> The equation is of the form:

$$t_{90} = d_0 + d_1 * E + d_2 * E^2 + \dots$$

while the inverse coefficients and the errors according to each temperature and voltage subrange are tabled as follows

	Inverse coefficients for type S			
<b>Temperature range</b>	-50	250	1064	1664.5
	250	1200	1664.5	1768.1
<b>Voltage range</b>	-0.235	1.874	10.332	17.536
	1.874	11.950	17.536	18.693
<b>d<sub>0</sub></b>	0.000E+00	1.292E+01	-8.088E+01	5.334E+04
<b>d<sub>1</sub></b>	1.849E+02	1.466E+02	1.622E+02	-1.236E+04
<b>d<sub>2</sub></b>	-8.005E+01	-1.535E+01	-8.537E+00	1.093E+03
<b>d<sub>3</sub></b>	1.022E+02	3.146E+00	4.720E-01	-4.266E+01
<b>d<sub>4</sub></b>	-1.522E+02	-4.163E-01	-1.442E-02	6.247E-01
<b>d<sub>5</sub></b>	1.888E+02	3.188E-02	2.082E-04	0.000E+00
<b>d<sub>6</sub></b>	-1.591E+02	-1.292E-03	0.000E+00	0.000E+00
<b>d<sub>7</sub></b>	8.230E+01	2.183E-05	0.000E+00	0.000E+00
<b>d<sub>8</sub></b>	-2.342E+01	-1.447E-07	0.000E+00	0.000E+00
<b>d<sub>9</sub></b>	2.798E+00	8.211E-09	0.000E+00	0.000E+00
<b>Error range</b>	-0.02	-0.01	-0.0002	-0.002
	0.02	0.01	0.0002	0.002

**Table 3-1.** Coefficients to convert voltage into degree °C for a type S thermocouple by exploiting the equation  $t_{90}$ . Modified from <sup>263</sup>.

A missing detail is the applied voltage to induce a current between source and drain through the thin GO layer, which was as high as 0.1 V. Again, the voltage was applied via the two Pt/Ti needles, which showed some contractions and expansions during the thermal treatment causing the operator to spend much time to check and adjust any possible needle detachment on site. As a result, the system was extremely interesting from the GO characterisation point of view, however, it was slightly less from the efficiency perspective of the GO reduction.

## 3.2 Spectroscopy

Spectroscopy defines a branch of scientific analysis methods that involve the interaction of electromagnetic radiation with the specimen. Typically, the result of the interaction is characteristic of the analysed substance. According to the type of interaction and exciting source, the several spectroscopies are defined.

### 3.2.1 Fourier- transformed infrared spectroscopy (FTIR)

Using infrared electromagnetic radiation,  $200\text{-}4000\text{ cm}^{-1}$ , it is possible to excite vibrational levels. Namely, a given molecule has vibrational modes depending on its symmetry that the absorption of IR wavelengths can activate. The rule of the degrees of freedom says that the vibrational modes are  $3N-5$  for linear, and  $3N-6$  for non-linear molecules. This is simply calculated considering the 3 cartesian coordinates for each atoms of the molecule and subtracting translational and rotational modes – linear molecules have only 2 rotational degrees of freedom. In the case of diatomic molecules, they can be treated as springs and the harmonic oscillator applies. For triatomic molecules or more complicated molecules, symmetry and point groups can clearly identify the IR active modes. Selection rules for IR spectroscopy necessitate a dipole moment variation throughout the corresponding vibration. By knowing that the water molecule belongs to a  $C_{2v}$  symmetry group, it turns out that water has a reduced representation ( $\Gamma_{\text{red}}$ ) equal to  $2 A_1$  symmetry modes and  $1 B_2$ , and those are exactly the IR active modes.

In organic chemistry, IR spectroscopy is traditionally different due to the complexity of the molecules structure. Thus, the identification of the modes goes through functional groups, reliable standards were tabled. Functional groups of an analysed compound can be found by means of comparison, namely depending on peak shape, intensity, and frequency range.

The convenience of the Fourier-transformed IR comes down to the measurement time. The Michelson interferometer sends all frequencies and the interferogram is later frequency-resolved to usual spectrum via the Fourier transformation.

In this work, a Perkin Elmer Fourier Transform infrared spectrometer (FT-IR) Spectral UATR-TWO with a spectrum Two Universal ATR (Single Reflection Diamond) accessory was exploited to attempt the characterisation of GO and rGO samples in the form of films and of powder.

### 3.2.2 Raman spectroscopy

Raman spectroscopy is another vibrational spectroscopy, which however has diverse selection rules from IR spectroscopy. It involves radiation scattering and requires a polarisation change of the molecule while excited. Light can be scattered elastically (Rayleigh scattering), or it can experience red (Stokes) or blue shift (anti-Stokes scattering). The greatest part of it undergoes Rayleigh scattering, still anti-Stokes and Stokes scatterings provide information concerning rotational and vibrational transitions. In a molecule such as CO<sub>2</sub>, point group symmetry D<sub>2h</sub>, the power of Raman is concrete and complement IR; *e.g.*, symmetrical stretching of CO<sub>2</sub> is IR inactive, but Raman active, whereas the asymmetrical stretching displays the opposite behaviour.

Furthermore, Raman spectroscopy stands out as important tool for the characterisation of sp<sup>2</sup>-based carbon materials, such as graphite, graphene and CNTs. The typical evaluation considers D/G band ratio<sup>101,264–266</sup> However, GO or rGO are highly-defected because of the harsh conditions of synthesis route, and hence require novel fittings or more holistic views.<sup>267</sup>

In this thesis, Raman measurements were carried out with a LabRAM HR800 (HORIBA Co.Ltd.). The source was a laser Ne:YAG diode and the 520.8 cm<sup>-1</sup> Si Raman peak was used for calibration.

### 3.2.3 UV-visible spectroscopy (UV-Vis)

UV-Vis spectroscopy is a spectroscopic technique, in which the exploited electromagnetic radiation is ultraviolet and visible light (wavelength range 180-800 nm). The radiation induces electronic transitions in the analysed, atoms, molecules, or materials. The phenomena, to which the UV-Vis spectroscopy comes down are absorption and reflectance. In UV-Vis spectrophotometers, the wavelength is typically scanned from broader to narrower and the y-axis of a common plot shows the absorbance or the transmittance of the analyte. A fundamental milestone of UV-Vis spectroscopy involves solution samples (non-scattering samples), and it is the absorption Beer-Lambert law:

$$A = \log_{10} \left( \frac{I}{I_0} \right) = \epsilon l c \quad (3.1)$$

where the  $A$  is the absorbance, the  $I$  and  $I_0$  are the attenuated light intensity and the non-attenuated light intensity,  $\epsilon$  is the molar extinction (or attenuation) coefficient,  $l$  the optical path (in cm), and  $c$  the solution concentration. Therefore, with tabled molar extinction

coefficients or calibration curves, a measured absorbance can be transformed into the concentration of the desired analyte. The spectrophotometer normally measures the percentage transmittance ( $\%T = I/I_0 * 100\%$ ), which is then converted to absorbance ( $A = -\log(\%T/100\%)$ ).

The treatment of the electronic transitions for molecules follows the chemical description of HOMO-LUMO, based as MO theory. On the contrary, for solids the treatment follows a more physical description with VB-CB, based on the k-vector and thus the Bloch's theorem. However, both treatments work and lead to the definition of compounds, and their UV-Vis absorption bands.

A small parallelism of the Beer-Lambert law in solids is depicted by the absorbance of thin films ( $A = \alpha \times d$ ) and the light attenuation could be described by the optical absorption depth  $\alpha$  ( $\alpha^{-1}$  in nm).<sup>268,269</sup> The reciprocal value of  $\alpha$  is a characteristic distance of a material, by which the light drops its intensity of a factor  $1/e$  (~36%). However, an important parameter,  $x$ , the film thickness (nm) is given by SEM analysis (see [subsection 5.3.6](#)).

Without considering SEM, UV-Vis spectroscopy offers a hint about film thickness. Moreover, absorption intensity can also be related to defects such as oxygen vacancies, *e.g.*, this was observed in hematite thin films.<sup>236</sup>

Measurements were carried out with a Jasco V-670 UV Vis spectrophotometer. The FTO slides were typically glued at a handmade paper window, which enabled the hematite deposited area to be properly exposed to the source light and almost completely vertical. As blank, it was utilised a non-deposited cleaned FTO glass slide.

### 3.2.4 X-ray photoelectron spectroscopy (XPS)

XPS is a surface-sensitive technique that provides information about the surroundings and oxidation states of elements, along with quantitative chemical composition. XPS relies on the photoelectric effect, namely, the phenomenon that involves the interaction of X-ray photons with atoms that will consequently emit inner shell electrons as photoelectrons (see **Figure 3-3a**).

**Figure 3-3b** schematises the XPS instrumentation where the aforementioned phenomenon is exploited. Essential is the monochromatised X-ray source, for example Al- $K_{\alpha}$ , which is directed onto the selected sample spot. The emitted photoelectrons are then collected and concentrated through the electron lens to reach the hemispherical analyser. There, electromagnetic lenses separate the photoelectrons depending on the energy levels. At the end of their path, the separated photoelectrons reach the photodetector, where they are counted for a given kinetic energy (KE). By knowing the incident photons wavelength and

the work function of the spectrometer, the binding energy (BE) can be calculated. Contrary to KE, the BE of an electron is distinctive of the material and of the original atomic state. Energetically, it is crucial that spectrometer and sample are in conductive contact, as the Fermi levels must align. However, there is no alignment of the work functions too, *i.e.*, sample one,  $\Phi_{sample}$ , and spectrometer (detector) one,  $\Phi_{spec}$ . As a result, there is an additional gap that the energy of the incident photons should cover, the difference  $\Phi_{spec} - \Phi_{sample}$ . Therefore, the remaining energy is KE that is measured immediately at the arrival of the photoelectrons at the detector. All the information translated into equations:

$$KE = h\nu - BE - (\phi_{sample} + (\phi_{spec} - \phi_{sample})) \quad (3.2)$$

$$BE = h\nu - KE - \phi_{spec} \quad (3.3)$$

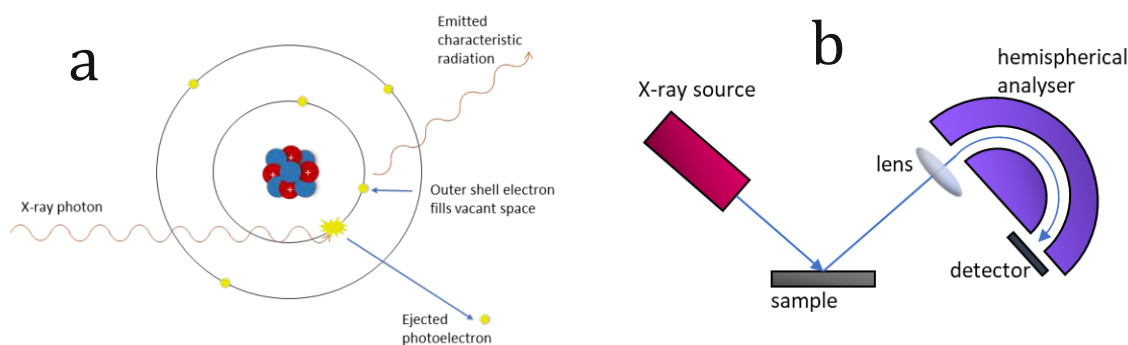


**Figure 3-3.** a) Representation of the effect of an X-ray photon on an atom. b) A simplified scheme of an XPS apparatus and its main components.

Owing to short mean free paths of electrons in solids, XPS is limited to surface analysis reaching depths in the order of 1-10 nm. On the contrary, detection limits can oscillate more according to the analysed substance, from 0.01 at.% to 3 at.%.<sup>270</sup> Completely excluded are instead H and He, which have too low photoelectron cross-sections. Furthermore, albeit the increasing chances to measure in ambient pressure, UHV is still a common and almost mandatory operational condition. Gas molecules can collide with the ejected photoelectrons altering the measurement. Also, as previously suggested, the sample conductivity is crucial for the alignment of the Fermi levels, but also to avoid charging effects.

In this thesis, the measurements were conducted with SPECS XPS spectrometer provided with a monochromatised Al-K $\alpha$  X-ray source ( $\mu$ Focus 350) and a hemispherical WAL-150 analyser (acceptance angle: 60°). Depending on the sample and its substrate, the measured samples were either fixated at the sample holder with small metal clamps or with carbon tape. Pass energies of 100 eV and 30 eV were used for survey and detail spectra, along with

1 eV and 100 meV energy resolutions, respectively (additional detail information: excitation energy: 1486.6 eV, beam energy and spot size: 70 W onto 400  $\mu\text{m}$ , angle:  $51^\circ$  to sample surface normal, base pressure:  $5 \cdot 10^{-10}$  mbar, pressure during measurements:  $2 \cdot 10^{-9}$  mbar).

CASA XPS software was employed for data treatment, with typical transmission corrections, *i.e.*, Shirley background and Scofield sensitivity factors. Unless differently stated, the charge correction based on the adventitious carbon (mixture of C-C  $\text{sp}^3$  and little  $\text{sp}^2$ ) was always utilised, so that its peak lies at BE 284.8 eV.<sup>271</sup>

Albeit a powerful technique, XPS could also lead to relevant mistakes. In the two main projects that will be presented, the XPS analysis was interpreted in the light of other results and ample corroborating literature. In the rGO project, particularly important were the atomic percentages (at.%) of the composition quantifications. Nevertheless, atomic thin layers and inhomogeneous films compromise the usual detection limit of about 0.1-1 at.%.

### 3.3 X-ray diffraction (XRD)

The X-ray diffraction is practically based on elastic scattering from the electron. A regular array of scattering points produces a regular array of spherical waves. These waves can interfere destructively and cancel one another. Nonetheless, they also interfere constructively as described by the fundamental Bragg's law:

$$n\lambda = 2d \sin\theta \quad (3.4)$$

where  $n$  is an integer,  $\lambda$  is the X-ray wavelength,  $d$  is the distance between the two scattering points, and  $\theta$  is the Bragg angle (see **Figure 3-4**). In case of a crystal,  $d$  is the lattice spacing. XRD is a great technique to characterise large crystals because they give out patterns with sharp peaks, whereas smaller crystals lead to broadening of the signals. Although broadening is a disadvantage, the observation could be used to corroborate the presence of defects. Furthermore, XRD according to the lattice geometry identifies material phases, its quantitative relevance and texture orientation. Nevertheless, to calculate the mean size of the crystal domain from the broadening, the Scherrer equation applies:

$$D = \frac{K\lambda}{\beta \cos\theta} \quad (3.5)$$

with  $D$  the mean size of the crystal domains,  $K$  the shape factor,  $\lambda$  the X-ray wavelength,  $\beta$  the FWHM, and again,  $\theta$  the Bragg angle. Note that the Scherrer equation offers only a lower

limit of the crystal size, as there might be signal broadening due to additional instrumental weaknesses.

XRD is a powerful technique to evaluate changes in the interlayer distance in graphene materials<sup>99</sup>, albeit it is still difficult to rely only on the diffraction patterns when materials are extremely defected, such as GO and rGO. Compared to XPS, XRD analysis offers more comprehensive information, which is especially important to understand inhomogeneity and phase segregation. On the one hand, XRD detected X-rays reach deeper layers of the investigated material, a clear example is given in [subsection 5.3.4](#). On the other hand, it analyses wider spot sizes, in the order of mm<sup>2</sup>-cm<sup>2</sup>. Furthermore, some *in-situ* studies were conducted on GO samples with temperature increase and exposure to different atmospheres (vacuum, air, NH<sub>3</sub>, H<sub>2</sub>).



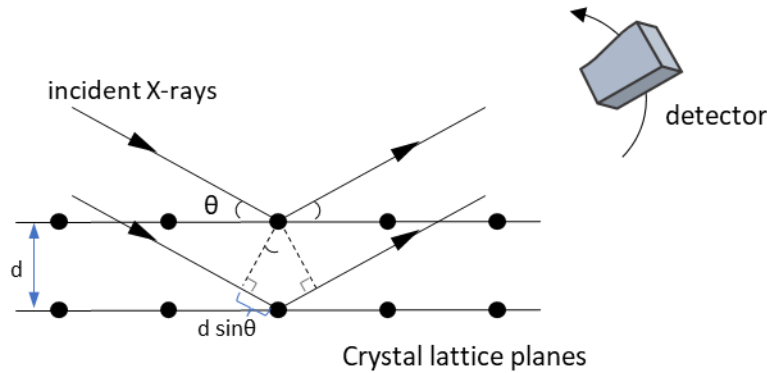


**Figure 3-4.** Schematic of the XRD working principle.

In this work, X-ray diffraction (XRD) was performed using an XPert III: PANalytical XPert Pro MPD ( $\theta$ - $\theta$  Diffractometer) for the *in-situ* experiments and an XPert II: PANalytical XPert Pro MPD ( $\theta$ - $\theta$  Diffractometer) for the *ex-situ* experiments. The sample was placed on a sample holder and irradiated with a Cu X-ray source (8.04 keV, 1.5406 Å). The signal was acquired with Bragg-Brentano  $\theta$ / $\theta$ -diffractometer geometry ranging from 20° to 80° degrees for hematite or from 5° to 30° for GO/rGO. The detector system was a semiconductor XCelerator (2.1°) detector. Mirrors were utilised to filter the rays replacing beta filters.

The *in-situ* experiments on GO were carried out under air, vacuum, pure H<sub>2</sub> and NH<sub>3</sub>, with flow and static. Additionally, temperatures were ranging from 25 °C to 700/800 °C without a controlled ramp. Nevertheless, the steps were short at lower temperatures, namely 50°C increase until 400°C, and up to higher temperatures the given step was 100°C.

### 3.4 Scanning electron microscopy (SEM)

SEM is an electron microscopy; thus, it uses an electron beam to send small wavelength of electrons to interact with matter. Abbe equation defines that the resolution, in an ideal optical system, strongly comes down to the wavelength of the irradiated particles:

$$d = \frac{0.61 \lambda}{n \sin \alpha} \quad (3.6)$$

where  $d$  is the resolution,  $\lambda$  is the wavelength of the incoming particle,  $n$  is the free space refractive index, and  $\alpha$  is the semi-angle in radians. If the resolution depends on the wavelength, it means that visible light photon will resolve an image to a maximum, which is about 0.2  $\mu\text{m}$ , considering small aberrations of optical lenses.

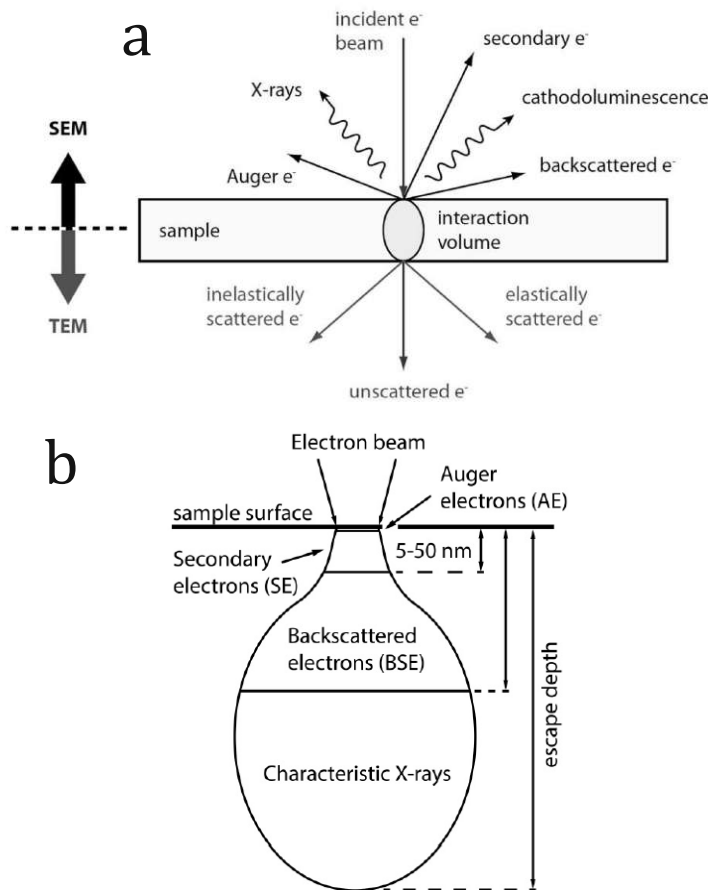


**Figure 3-5.** a) Shining a sample with an electron beam provokes various phenomena. Three of them are exploited by TEM and the rest by SEM. b) The different emissions (electrons or X-rays) are originated at different sample depths and the sections have different sizes (bulb shape). From 272

By contrast, the resolution in electron microscopes relates to the speed of electrons (*i.e.*, acceleration voltage,  $U$ ) and the extent of aberrations.

When a focused electron beam shines onto a sample, it scatters electrons in several ways, as depicted in **Figure 3-5a**. Amongst these, secondary and backscattered electrons for scanning electron microscopy (SEM) purposes, X-rays for energy-dispersive X-ray spectroscopy (EDX), scattered electrons for transmission electron microscopy (TEM). The great advantage is that scattering factor is unique for each material.

SEM electron beam focuses onto a small spot of the sample and the detector collects the secondary electrons along the sample. The conversion is such that the collected electrons from each spot according to their amount turn into to a corresponding pixel brightness. As observable by **Figure 3-5b**, the low SEM acceleration voltage (max. 40 kV) generates secondary electrons lower than 50 eV, with escape depths of 5-50 nm. On the contrary, secondary electrons that do not escape, though travel horizontally, cannot be identified prior to interaction with the sample. As a result, rough surfaces can increase the contrast

(surface charging effect), since they emit more electrons and look brighter. Furthermore, a raised scattering probability can also strengthen the contrast (“Z contrast”), and this comes from materials with superior electron density. Albeit the effect is not strong in SEM, with significant Z disparities it becomes noticeable.

This work used a FEGSEM Quanta 200 (USTEM, TUWien) by collecting secondary electron under high vacuum ( $10^{-6}$ ). Surface sputtering AuPd of few nm was attempted to reduce surface charging effect and enable better micrographs.

### 3.5 Optical microscope

As expressed before by the Abbe equation (eq. (3.6)), the resolution depends on the wavelength of the incoming entities. Therefore, in case the entities are light photons, as in optical microscope, the image resolution will reach a maximum of about 0.2  $\mu\text{m}$ , always considering the lenses aberrations.

In this thesis, a Zeiss Imager.M1m was used to determine the pattern in UV-photolithography treated samples, with a maximum zoom lens Zeiss 50x. A Zeiss 100x was available, however not necessary for the purpose.

### 3.6 Profilometry

With profilometry is meant an analytical technique, whose action is measuring a surface's profile, aiming at the quantification of its roughness. While the origin of the profilometry technology arises from a stylus with surface contact, several modern devices can measure the surface topography without it. On one side, the principle of a stylus-profilometer is the diamond stylus itself, whose height adjustments are converted into a digital signal and presented as an xy/xyz plot. The stylus radius oscillates from 20 to 50 nm, and its applied force hovers between 1 and 50 mg. On the other side, if the contact does not occur, the technique tendentially recalls other imaging analysis or sensing, *e.g.*, confocal microscopy, laser triangulation, etc.

The benefits of leaving untouched the sample is surely the absence of surface wear. Additionally, non-contact profilers show higher speed of analysis, as the scan rate is not dictated by the surface. By contrast, contact profilers can dig into surface contaminants and have a more realistic feel of the surface. Moreover, the stylus radius can go down to 20 nm, a step forward than the light optical profiling, and the vertical resolution is also remarkable falling to sub-nm.

In this work, a Dektak XT Bruker was used, with stylus tracking force 1 mg, stylus type radius 2.5  $\mu\text{m}$ , range 524  $\mu\text{m}$  and 65.5  $\mu\text{m}$ .

The profilometer could detect hematite-FTO steps of around 60-90 nm and with an adequate error. However, the characterisation of additional samples of the same nature did show significant complications, *e.g.*, drifting flat surfaces, exaggerated and swollen rims. This occurred without parameters alteration.



# Chapter Four

## rGO as pH sensor LGFET

Alcune persone ti mostreranno l'oscurità pesante della notte e gli alberi muoversi come figure terrificanti, altri invece ti faranno notare il fuoco acceso e poi, seguendo le faville, le stelle. Decidi, ogni volta, chi è il tua guida.

Some people will show you the heavy darkness of the night and the trees moving as terrifying figures, some others however will make you notice the burning fire and then, following the sparks, the stars. Choose, every time, who is your guide.

---

Myself

The only way to do great work is to love what you do. If you haven't found it yet, keep looking. Don't settle.

---

Steve Jobs



# 4 rGO as pH sensor in LGFETs

In Chapter Four, rGO is used in a FET live pH sensor. As earlier mentioned, such sensor can also be employed as analytical method to dig deeper into the GO degree of reduction and its functional groups. Detailed and systematic characterisation is a crucial part of the Chapter architecture.

## 4.1 Introduction

The pH sensing can be carried out in several ways as pointed out in [section 1.3](#). One of them is the FET, earlier launched as ISFET.<sup>181,273,274</sup> The advantage of a transistor as ion sensor would be the amplification and parallel energy saving, as a limiting factor in common pH meters is the high electric resistance from 50 to 500 M $\Omega$ .<sup>275</sup>

Graphene materials, namely graphene and reduced graphene oxide, have already displayed remarkable pH detection capabilities, by using only atom-thin layers in surprisingly small FETs.<sup>37,187,248</sup> Moreover, graphene oxide benefits of big scale production with modest costs.<sup>276,277</sup> Thus, the reduction of GO becomes extremely relevant, and precisely if that is a controlled reduction, which seems the only way to improve devices with specific application, *e.g.*, FETs.<sup>278</sup>

However, multiple explanations concerning the pH detection mechanism do not facilitate the duty.<sup>37,187,188,248,279</sup> Much understanding of single applications should be gained in order to target the partial reduction of GO. Furthermore, live monitoring of the reduction is a key feature to finally select the conditions and the method to realise an optimal controlled reduction.<sup>280</sup>

In this Chapter, *in-situ* techniques and profound XPS characterisation enable to draw sensible correlations between what is seen in the flow cell and actual defects in rGO.



## 4.2 Preliminary results

In the preliminary results, I include information and data, which were chronologically collected earlier, and thus were fundamental to optimise methods and hint wiser analysis approaches. In fact, it is intended as a bridge from Chapters 2 and 3 to the specific findings of Chapter 4 and later Chapter 5.

Due to the importance of the information towards a critical scientific method, particularly relevant are the initial data of *in-situ* current monitoring, XPS analysis, and Raman analysis.

### 4.2.1 Optimisation and reproducibility *in-situ* current monitoring

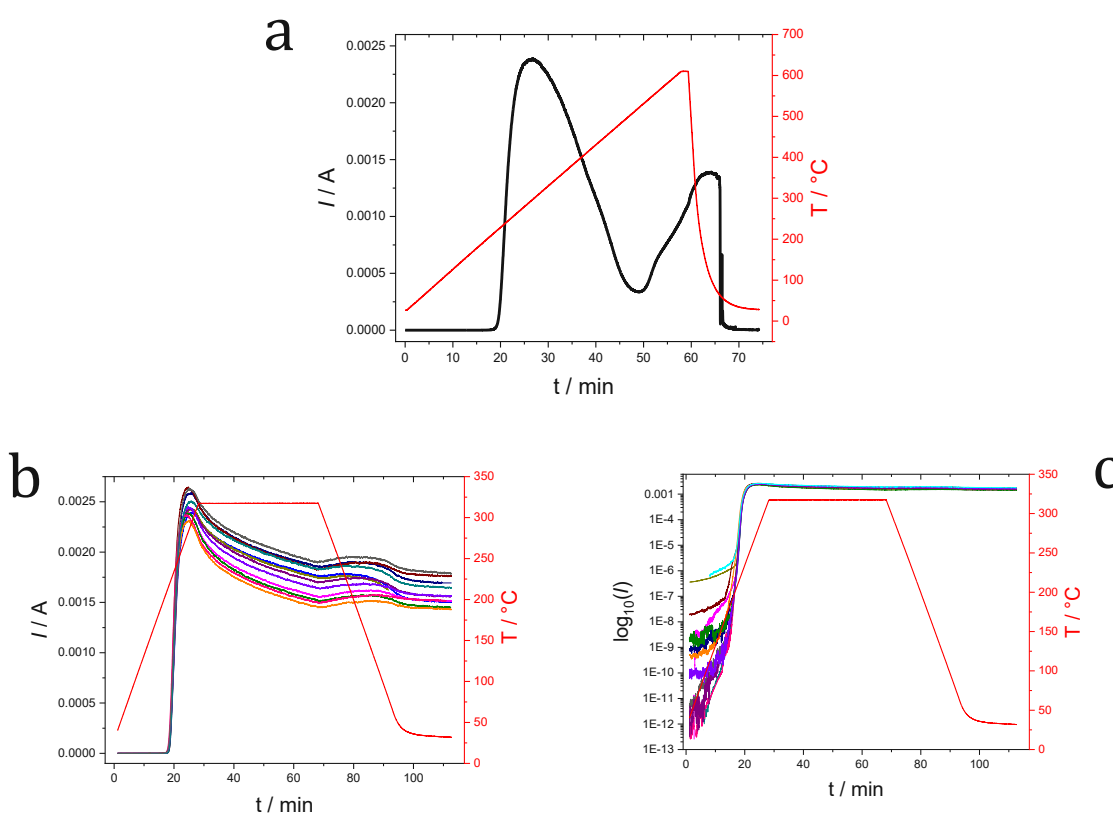


**Figure 4-1.** a) One of the first samples to be live monitored during the thermal treatment. On y-axes current and temperature, on x-axis the time in minute. b) To check the reproducibility of the process several samples were treated in H<sub>2</sub>/Ar atmosphere using a temperature ramp selected by means of the first experiments. c) By plotting the logarithm base 10 of the current, the starting current is visible. Contacting issues may cause signal instability.

In order to understand what is the maximum temperature at which treating the GO-IDEs, a sample was heated in H<sub>2</sub>/Ar atmosphere up to 600°C with 10°C min<sup>-1</sup>, while the cooling was not controlled (**Figure 4-1a**). At ~310°C, the sample shows only peak upon heating, and its highest current hovers around 0.024 A. By contrast, upon cooling, another peak is visible.

Likely, at already 500°C, an irreversible melting of the thin glass, of which is made the IDE, starts degrading. At the end of the process, the gold pads look green/blue – that is the colour of the gold facing the glass normally. A second confirming trial was performed to verify the observation and exclude mistakes. It must be said that in the cooling section at about 70°C, the current drops surprisingly fast and the final current and trend might be affected.

However, to avoid any sample damage and according to the current behaviour, I apply 310°C as maximum heating temperature and keep the ramp at 10°C min<sup>-1</sup>(see **Figure 4-1b-c**). Upon applying these conditions, the current maximum is achieved before the temperature tops. By holding the temperature at 310°C, the current falls exponentially until the cooling begins. The decrease can be estimated around 0.75 mA. Upon cooling, the current bounces up and down and finally stabilises at ~0.016 A. Furthermore, **Figure 4-1b** displays that the temperature onset is around 210°C and that, for each sample the noteworthy change in current occurs within 7 minutes. In addition, **Figure 4-1c** points out that the current starting points lie between 10<sup>-10</sup> and 10<sup>-6</sup> A, which is a rather significant gap. This can be a direct consequence of the presence of intercalated water and loose flakes. Though, high reproducibility is then shown when samples are heated.

## 4.2.2 SEM images after thermal treatment

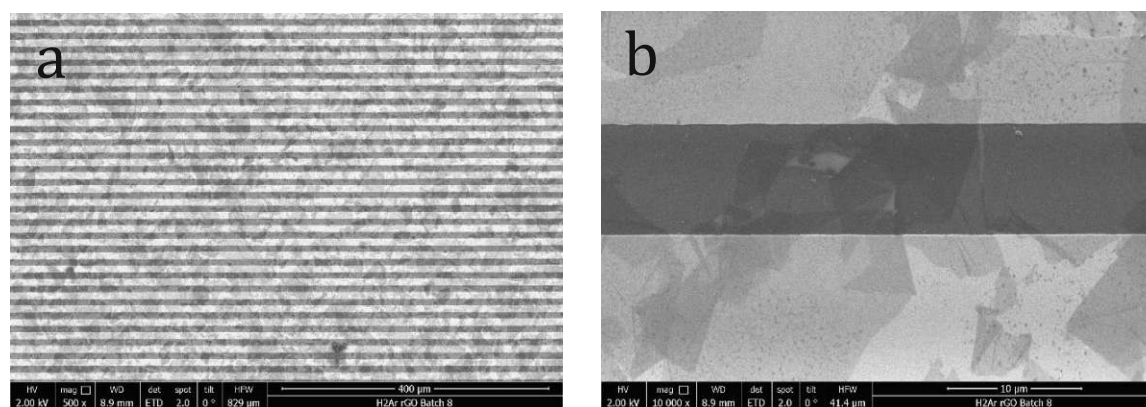


**Figure 4-2.** SEM micrographs of GO on IDE after the typical thermal treatment with H<sub>2</sub>/Ar atmosphere (10°C min<sup>-1</sup> cooling/heating and max T 310 for 40 min). a) Micrograph at 500x magnification. b) Micrograph at 10'000x magnification.

After the applied thermal treatment in presence of the H<sub>2</sub>/Ar atmosphere, clear typical images of rGO can be studied.<sup>26,142,257,281,282</sup> In **Figure 4-2a** and **Figure 4-2b**, we see two magnifications of SEM micrographs. From the lower magnification 500x micrograph, it can be noticed that the rGO flakes cover quite evenly the electrochemical cell, which is easily identified thanks to the interdigitated electrodes and SiO<sub>2</sub> array. The size of the deposited flakes goes from few μm to 100 μm in length or width. The layer looks mainly monoatomic with frequent overlapping to diatomic layer. The stacking gets to a maximum of three atomic layers in rather small areas. From the higher magnification 10000x micrograph, the flakes evidently exhibit the first visible defects, *i.e.*, wrinkles and darker spots.

## 4.2.3 For a more reliable XPS analysis

Sample	at. % from survey						
	C	O	N	Si	Au	O	N
GO 1	48.4	32.0	2.2	10.3	7.1	31.35	2.2
GO 2	46.3	30.7	2.2	12.0	8.9		
H <sub>2</sub> /Ar-rGO1	56.4	24.0	2.7	9.7	7.3	24.35	2.35
H <sub>2</sub> /Ar-rGO2	56.0	24.7	2.0	10.2	7.0		
NH <sub>3</sub> -rGO1	53.4	24.6	4.1	9.1	8.9	23.35	3.7
NH <sub>3</sub> -rGO2	55.0	23.1	3.3	10.1	8.5		

**Table 4-1.** Atomic concentration percentages of relevant elements from XPS surveys analysis conducted directly on the GO- and rGO-IDEs

GO and rGO were analysed by XPS directly on the support IDE. To reduce GO to rGO with the two gases, H<sub>2</sub>/Ar and NH<sub>3</sub>, the custom-made set-up was employed. **Table 4-1** reports the atomic percentages for 5 expected elements, C, O, N, Si, and Au. Remarkable or at least detectable amounts of the first three elements are expected in or at the GO/rGO layer. On the contrary, Si and Au are expected in the electrochemical cell of the IDE, owing to contacts and the supporting glass material. As the XPS spot size is 400 μm, two spots are selected to enable a more reliable sampling. Hence, crucial elements, namely O and N, are averaged. The O should suggest the degree of reduction, and N should occur in rGO as doping atoms or functional groups.

Upon comparison of the table numbers, we see values that are oddly oscillating, because in one spot there may be more GO/rGO than in the other one. However, the readable information here results in two points, *i.e.*, the deoxygenation and the N increase. On the one hand, the deoxygenation corroborates the GO partial reduction.<sup>283,284</sup> On the other hand, the growth of N at% is consistent with a N doping or functionalisation of GO.<sup>102,249,285</sup> Nevertheless, the actual conclusions are dissimilar. Namely, GO-IDE displays already significant N at%, hence N1s detailed analysis on GO anchored with APTES would presumably be an analysis with ambiguous results. Furthermore, if the N1s detail spectra is carried out on a 400 μm spot with 2-max 3 atomic layers, and in addition the at% is 3.7±0.4%, the signal will be too small to be fitted in its components.

#### 4.2.4 Raman on thermal treated GO

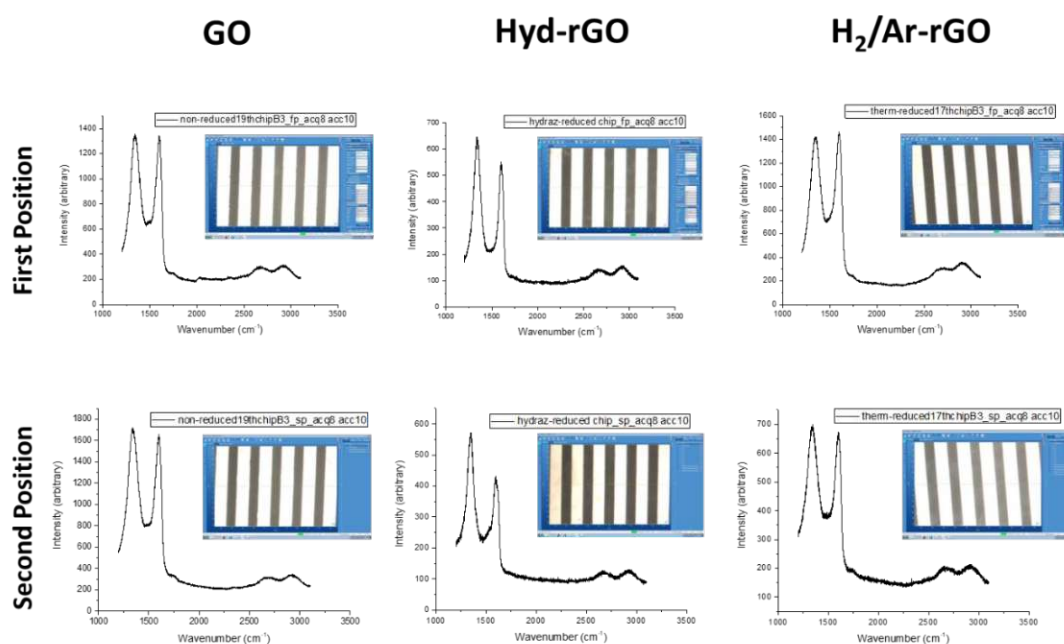


**Figure 4-3.** Raman spectra of GO and rGOs. The measurements were carried out directly on the GO-IDE, which is noticeable by the upper tight image in every plot. To increase the reproducibility two spots of the samples were measured.

Raman measurements of **Figure 4-3a-f** were conducted directly on the samples. GO and H<sub>2</sub>/Ar-rGO spectra do not show a clear D/G band ratio alteration, as it is manifest for the Hyd-rGO. This is already a valid reason to carefully characterise with Raman spectroscopy thermally treated GO, in these conditions. Nonetheless, we can draw some preliminary conclusions from these data.

However, first a preamble is needed by adding the above mentioned information concerning the *in-situ* current monitoring of the reduction, and the XPS characterisation. On one side, it is difficult to exclude that the thermal treatment of GO along with removing intercalated water, it also deoxygenates GO flakes upon removal of debris.<sup>286</sup> On the other, it is reported that the only a small enhancement in the content of deoxygenated carbon can cause a substantial expansion of the electrical conductivity.<sup>280,287</sup> Additionally, another matter is the highly defected GO lattice, which includes the size and edges of the flakes (sheets, ribbons, etc.).<sup>280,288</sup>

In light of the reported data, H<sub>2</sub>/Ar-treated rGO (**Figure 4-3a** and **c**) displays a 0.97 D/G band ratio compared to the 1.01 of the reference GO. A same effect of the thermal treatment is observable elsewhere<sup>283,289</sup>, and corroborates the hypothesis of a partial reduction. In fact, the reduction can easily be limited to small areas of the GO flakes layer, particularly carboxy

groups at edges.<sup>101,290,291</sup> Furthermore, the effect of intercalated water elimination on the removal of functional groups and on creation of C vacancies is still unknown.

### 4.3 Effect of atmosphere in GO thermal reduction

NH<sub>3</sub>, in liquid<sup>292,293</sup>, simple gas exposure<sup>102</sup>, or plasma exposure<sup>294,295</sup>, has already demonstrated to induce relevant and advantageous alterations of GO, i.e., from doping to functionalisation. H<sub>2</sub> plasma<sup>296</sup> or as H<sub>2</sub>/Ar mixture, with plasma<sup>297</sup> and without<sup>298</sup>, have also been employed. Vacuum has only been coupled with other techniques, either sequentially<sup>26</sup> or simultaneously<sup>299</sup>. More rarely, pure Ar has gained attention<sup>149,300</sup>, as likely N<sub>2</sub> is cheaper would lead to a similar rGO.

To control rGO channeling and pH sensing properties, I explore the effect on GO thermal-assisted reduction of 4 different atmosphere, namely, vacuum ( $1 \times 10^{-3}$  mbar), 2.4% H<sub>2</sub>/Ar, 100% Ar, and 100% NH<sub>3</sub>. To appreciate how the thermal treatment in these conditions affects the GO partial reduction, the current flowing through the GO/rGO channel was constantly recorded.

### 4.3.1 Results and discussion

#### 4.3.1.1 Current live monitoring to rGO-FETs

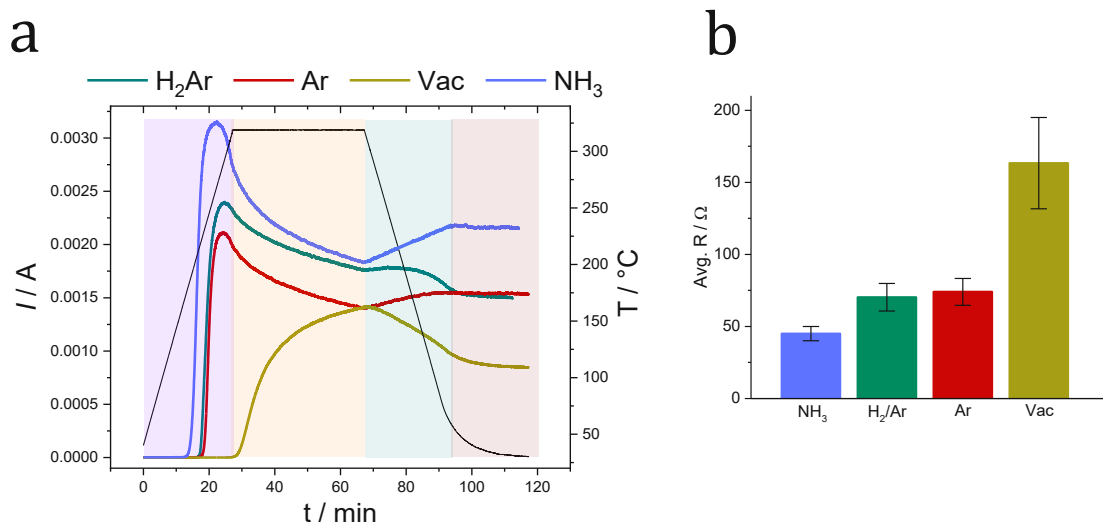


**Figure 4-4.** a) Current monitoring of thermal treatment conducted in presence of 4 atmospheres, such as vacuum (dark yellow), Ar (red), H<sub>2</sub>/Ar (green), and NH<sub>3</sub> (blue). In addition, the plot has been split in 4 chronological phases of different colours according to the temperature ramp changing points, namely, heating is the I phase (violet), holding the II phase (orange), cool-controlled the III phase (green), and cooling-uncontrolled as too slow the IV phase (red). b) Resistance and standard deviation of rGOs after the respective thermal treatment in the 4 atmospheres. The colours are identical, *i.e.*, vacuum (dark yellow), Ar (red), H<sub>2</sub>/Ar (green), and NH<sub>3</sub> (blue).

The result shows four curves, which are separated in four phases (**Figure 4-4a**). For convenience, the phases are almost identical to the temperature ramp, *i.e.*, heating, holding, cooling, adjustment to room temperature. In **Table 4-2**, I intend to simplify the read-out of **Figure 4-4**. There, the most relevant information is offered by the current trends themselves. The current values are indicative, as the taken samples are representatives of the batches. As a result of the **Table 4-2**, NH<sub>3</sub> and Ar display the exact same behaviour, but NH<sub>3</sub> has an earlier on-set and boost in current. Since Ar is a typical inert gas, NH<sub>3</sub> seems to react with GO while heating. Literature findings strongly agree on the possibility of simultaneous reduction and N-doping (see [section 1.2.4](#)).<sup>102,249,295</sup>

	I phase	II phase	III phase	IV phase
<b>Vacuum</b>	increase	increase (on-set)	Decrease (max)	steady
<b>Ar</b>	increase (on-set, max)	decrease	increase	steady
<b>H<sub>2</sub>/Ar</b>	increase (on-set, max)	decrease	bump	steady
<b>NH<sub>3</sub></b>	increase (on-set, max)	decrease	increase	steady

**Table 4-2.** The current transients are ordered by splitting their behaviour in a determined phase. The current on-set and maximum are also highlighted as critical parameters.

Another property, which surely plays a role is the thermal conductivity of the gases. The discrepancy between Ar and H<sub>2</sub>/Ar is only a 2.4% H<sub>2</sub>, which even in the purest case is not reported as reduction medium for GO, unless as plasma. Gas H<sub>2</sub> (P=0) owns a thermal conductivity of 186.6 mW m<sup>-1</sup> K<sup>-1</sup> at 300 K, while NH<sub>3</sub> and Ar (P=0) own a corresponding 25.1 and 17.7 mW m<sup>-1</sup> K<sup>-1</sup> at 300 K. This corroborates the fact that the thermal conductivity could affect the recorded current provoking the bump visible in the plot. For its part, vacuum is a terrible thermal conductor, whose conductivity approximates 0.001 mW m<sup>-1</sup> K<sup>-1</sup> at 300 K. The late on-set and current maximum are consistent with the low value.

To double check current recorded by the set-up for, the resistance of the channel was systematically measured with a multimeter after each reduction (see **Figure 4-4b**). The outcome agrees with the final steady current given by the custom-made set-up. NH<sub>3</sub> offers resistances around 45 Ω, H<sub>2</sub>/Ar and Ar of 70 and 74 Ω, and vacuum with a significant variance of ±31 Ω and touches an average of 163 Ω. The resistance before the thermal treatment was also measured resulting in resistance overloads or at least of about 10<sup>6</sup> Ω (remind of **Figure 4-1c**).

#### 4.3.1.2 rGO-FETs current-voltage characteristics

As described in [subsection 3.1.2](#), the rGO properties as a transistor channel are determined through the transfer characteristics measurements and the corresponding  $I_{ds}V_g$  plot. Upon sweeping of the applied gate voltage, the current ideal semiconductors follows a typical parabola shape. In  $I_{ds}V_g$  plots, a crucial data point is the Dirac point, the parabola minimum that defines the contribution of electron and hole carriers to the generated current. In this circumstance (**Figure 4-5a**), except for NH<sub>3</sub>- rGO Dirac point at -0.20 V, the remaining rGOs show positive Dirac point voltages. Vacuum treatment gives a Dirac point potential of 0.11 V, whereas both Ar and H<sub>2</sub>/Ar give it a 0.20 V. Furthermore, the Dirac point current is highest for NH<sub>3</sub> treatment, lower for H<sub>2</sub>Ar and Ar, and lowest for vacuum, respectively 1.10 , 0.30, 0.28, and 0.11 mA. Here, we can see the trends of Dirac point potential and current through two types of lenses, namely, the degree of reduction and chemical modifications (doping, functionalisation).

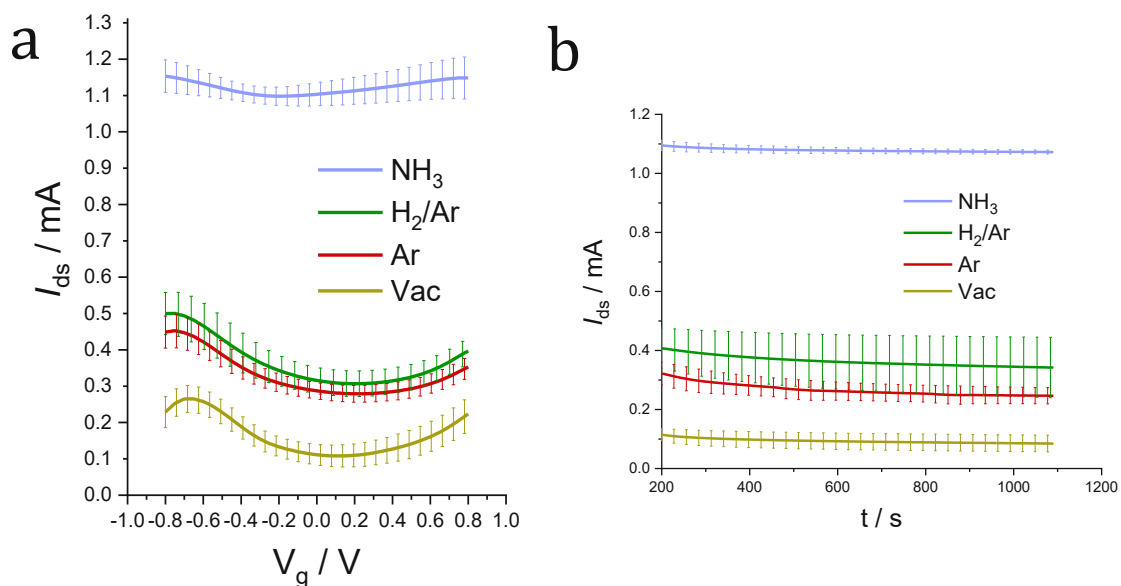
The Dirac point current, strictly connected with the current and resistance measured in the previous section, hints a ranking of reduction efficiency. In other words, the better GO reduces, the higher the Dirac point current. If the same concept applies to the Dirac point potential, we can say that the right shift of Ar and H<sub>2</sub>/Ar compared to vacuum, arises from a better reduction. However, the easiest removal of functional groups involves carboxyl



groups<sup>290,301</sup>, which should induce a Dirac point potential right shift<sup>302</sup>. On the contrary, we see here the theoretical “better reduced” GO has a more positive Dirac point potential.

Another uncommon feature is the maximum of vacuum rGO at about -0.7 V, which should suggest the presence of an oxidisable species at the GO surface. However, something that has been considered in the GO investigation of its thermal treatment is the presence of highly oxidised debris (OD).<sup>286,303</sup> That is consistent with the less positive Dirac point potential of vacuum rGO. In case, we can deem that the ODs are covered with O-containing functional groups, we can also hypothesise that these groups could slow down travelling holes. Thus, these holes will contribute less to the measured current.

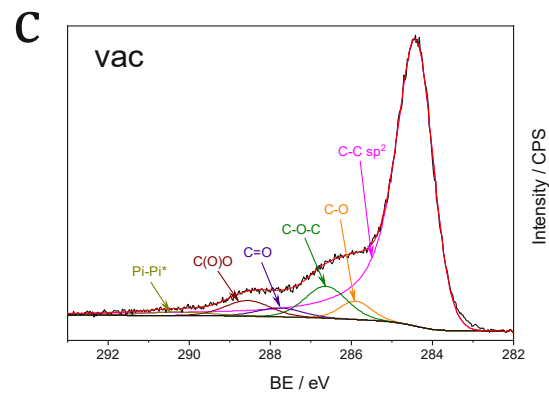
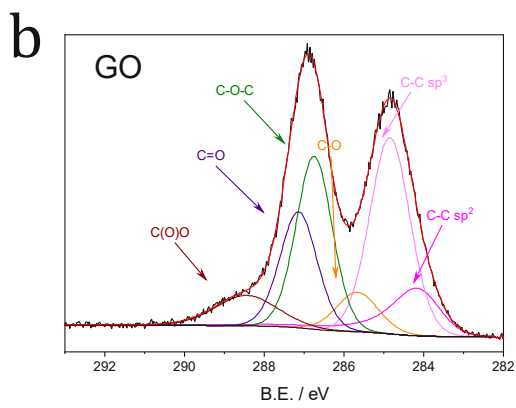
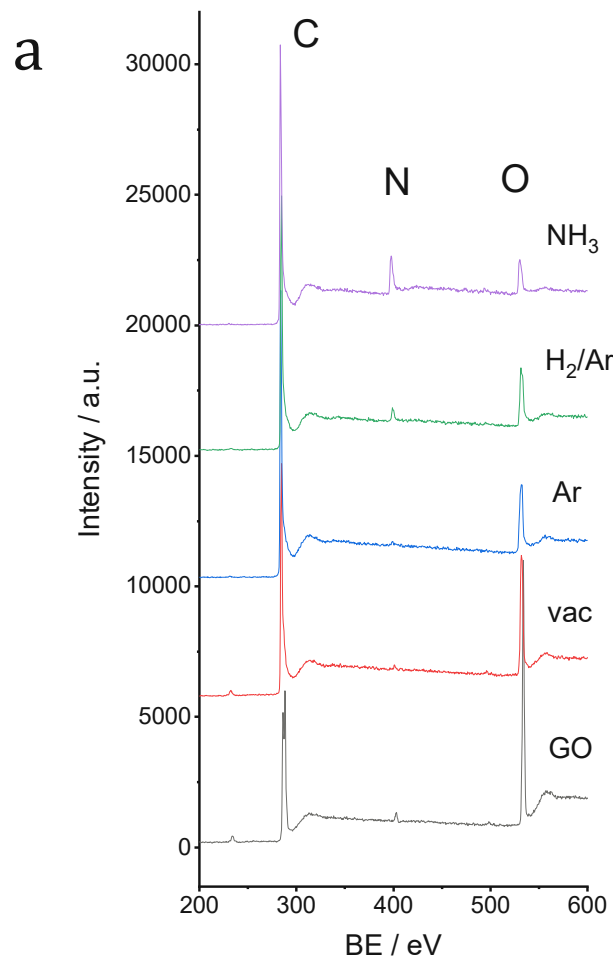
Furthermore, I cannot exclude that the ODs are also more like agglomerates that have a highly oxidised outer shell and a graphitic inner core. Hence, the agglomerates, that are not cleaned through thermal treatment, might be responsible for the vacuum-rGO -0.7 V maximum due to their oxidisable core. As a result of the now discussed data, the Dirac point potential and current alterations of NH<sub>3</sub>-GO could be originated from a better cleaning properties of NH<sub>3</sub> over the ODs. Nevertheless, GO was reported to be reduced and N-doped following a NH<sub>3</sub> thermal treatment.<sup>102,285</sup> It must be said, that the Dirac point potential shift and current enhancement are remarkable. Therefore, the only effect of NH<sub>3</sub> as cleaning medium can be sensibly excluded.



**Figure 4-5.** a)  $I$ - $V$  characteristics of LGFETs through rGOs after the respective GO thermal treatment in the 4 atmospheres. The gate voltage is swept between -0.8 and 0.8 V, whereas 0.1 V are applied between source and drain. Colours show continuity, specifically, vacuum (dark yellow), Ar (red), H<sub>2</sub>/Ar (green), and NH<sub>3</sub> (blue). b) Baseline control of LGFETs by applying a constant gate voltage -0.4 V and usual 0.1 V between source and drain.

By keeping the gate voltage constant, as in **Figure 4-5b**, we observe the current drift. The reproducibility and stability are important parameters for the FETs. On the one hand, the reproducibility can vary remarkably by comparing same treatments, but in different sample batches. This the example of H<sub>2</sub>/Ar, while NH<sub>3</sub> samples, although from the same batch and with highest current, offer the tiniest standard deviation. On the other hand, the current stability calculated with two values, *i.e.*, the “first drift” between 200 and 300 s and the “second drift” between 200 and 600 s. To consider the current intensity in the calculation, the two values were normalised for the measured current of the respective sample at 200 s. NH<sub>3</sub> treatment shows a maximum current drop 200-300 s within 1%, and a 200-600 s current drop within 2%. Ar and H<sub>2</sub>/Ar-treated GO exhibit less stability, in the best case, with a first drift of 6.8% and second drift of 14.8%. Interestingly, vacuum samples are more stable (in the best case 3.9 % and 9.3 %, for first and second drift) probably taking advantage from lower current at 200 s.

### 4.3.1.3 XPS analysis



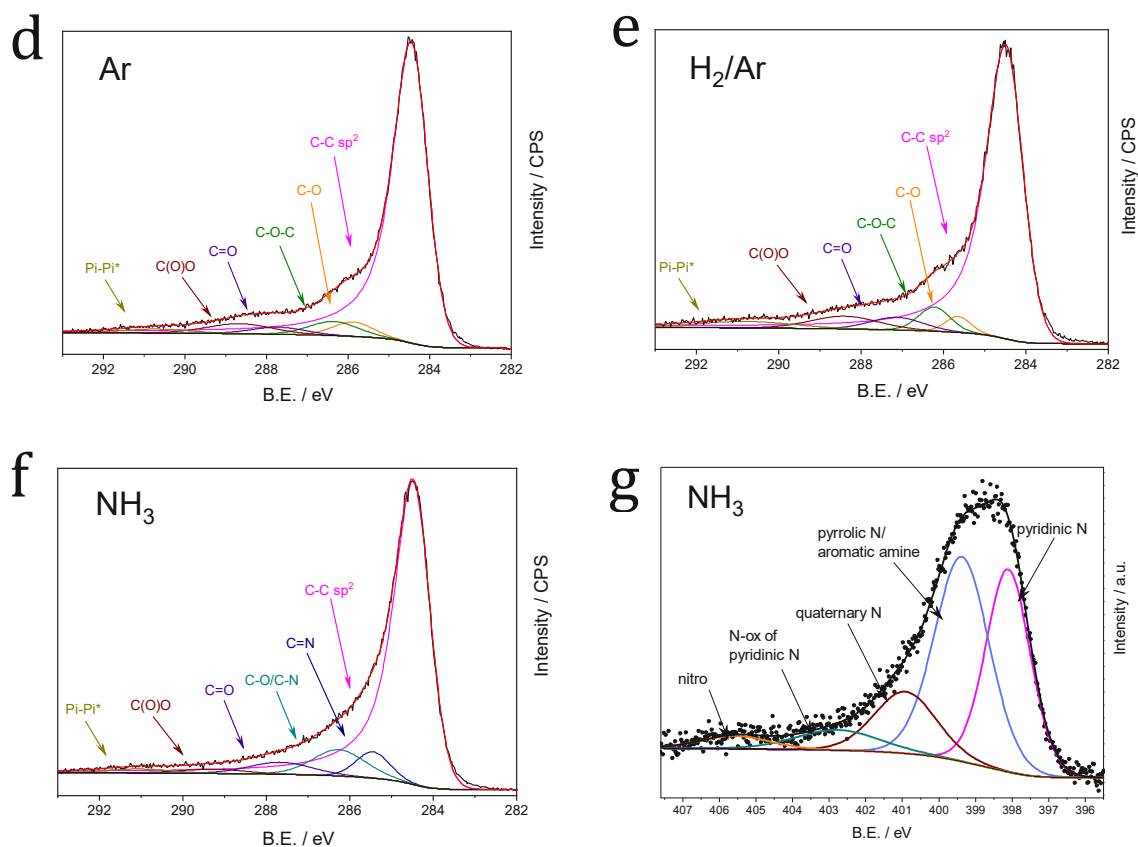


**Figure 4-6.** a) XPS survey spectra of GO and rGO treated thermally in different atmospheres. b)c)d)e)f) C1s region detail spectra of GO and rGOs. g) N1s region detail spectra of NH<sub>3</sub>-rGO.

XPS surveys highlight the atomic concentration percentage of the selected elements (**Figure 4-6a**). The surveys were carried out on GO deposited on common p-type Si wafers, which were treated with the same procedure as the samples. The typical C, N, and O peaks appear at BE of 285, 400, and 532 eV, respectively<sup>304–306</sup> Excluding NH<sub>3</sub>, the trend followed by C or O at% is to a certain extent inversely proportional, *i.e.*, the worst cleaned/reduced displays the greatest O at% and smallest C at%, while the best displays the opposite. Hence, GO reference has 68-69 C at% and 30-31 O at%, whereas Ar-H<sub>2</sub>/Ar have 84-85 C at% and 13-14 O at%. Albeit NH<sub>3</sub> has 6-7 O at%, C at% hovers around 83-84, because the presence of N is considerable up to 10-11 at%. Small N at% occurs in other samples too, usually below 1%, depending on the analysed spot. Nevertheless, higher amounts are detectable, likely due to impurities or difficult integration of modest signal.

In C1s detail spectra, **Figure 4-6b-f**, it was applied a calibration adjustment according to previous XPS studies. Namely, for GO the highest intensity was moved to BE 284.8 eV assuming a mixture of C-C sp<sup>3</sup> and sp<sup>2</sup> as in adventitious carbon.<sup>307,308</sup> By contrast, for rGO the highest intensity was shifted to BE 284.5 eV (for convenience lower resistive GO stays rGO).<sup>309,310</sup> Consequently, the fitted components are hydroxyl groups at BE 285.6 to 286.4

eV, epoxy at BE 286.1 to 286.8 eV, carbonyl at BE 287.0 to 287.7 eV, carboxyl at BE 288.3 to 289.3 eV, and the tail assigned to pi-pi\* stacking at BE 290.8 to 291.2 eV.<sup>284,306,311</sup> A certain degree of reduction/cleaning trend is intuitable by looking at the intensity of the components peaks. Thus, the detail spectra are consistent with the survey spectra and can qualitatively identify particularly the C-O functionalities.

Owing to its elemental abundance, N1s detail spectrum is presented for NH<sub>3</sub> treatment. We can observe four main peaks, which are related to N-containing functional groups in rGO. At lower BE, 398.4 to 398.6 eV, we label pyridinic N, BE 399.6 to 399.8 eV pyrrolic N, aromatic NH<sub>2</sub> and pyridone N, BE 401.0 to 401.1 quaternary N and at higher BE 405.7 to 405.9 eV N-oxides of pyridinic N<sup>305,306,312</sup>.

The XPS results corroborates the proposition that NH<sub>3</sub> chemically interact with GO. Moreover, the N1s detail spectrum confirms with the pyridinic presence that N is a dopant in the analysed rGO.<sup>312-314</sup> However, another group that enters the lattice is quaternary N, while the remaining components are practically surface ones belonging to GO functionalisation.

### 4.3.1.4 XRD analysis

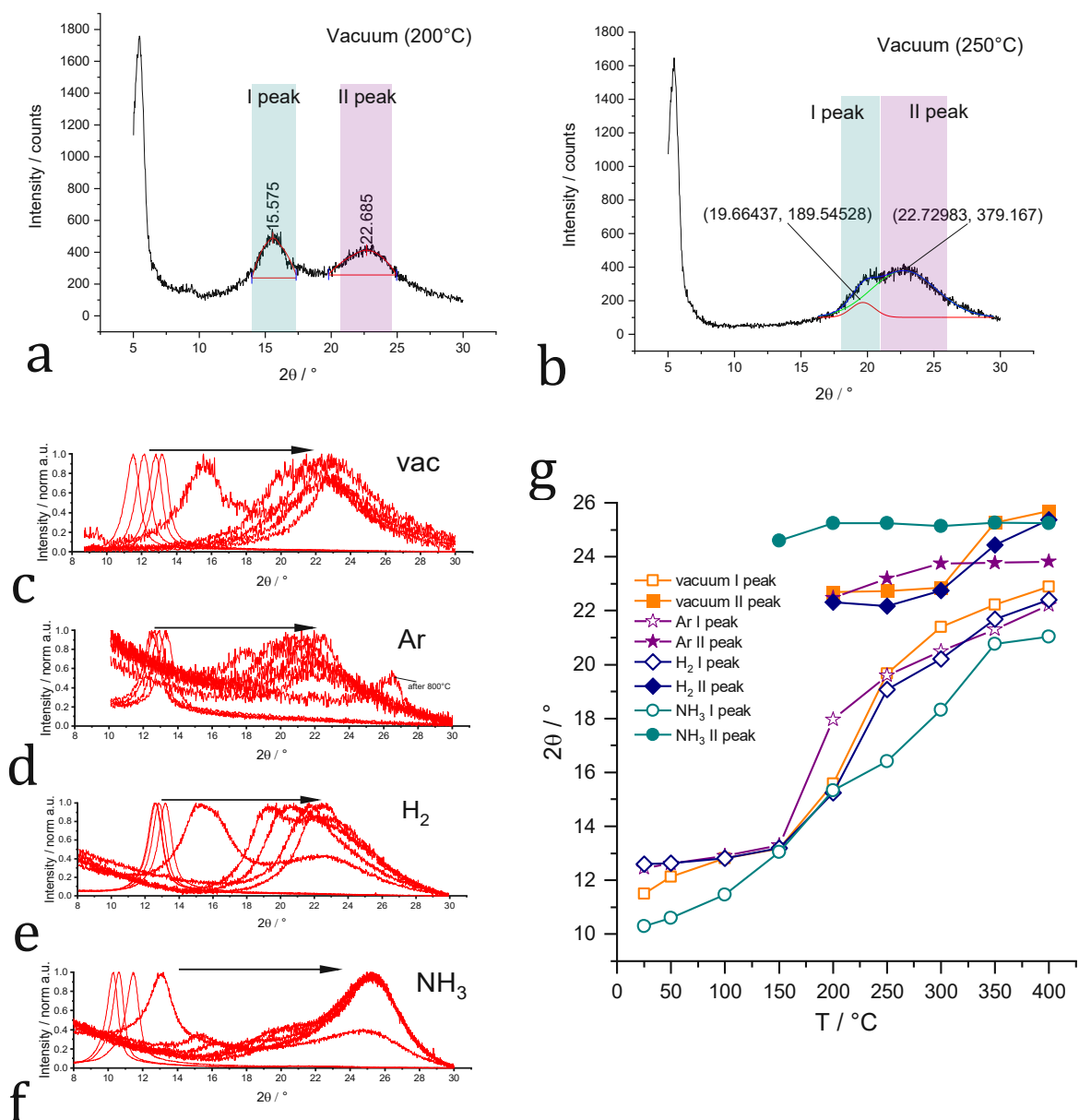


**Figure 4-7.** In-situ XRD patterns of GO under thermal treatment in 4 atmospheres. To better explain what I peak and II peak are, a and b figures are added. a) XRD pattern of GO treated in vacuum atmosphere at 200°C temperature stage. b) XRD pattern of GO treated in vacuum atmosphere at temperature 250°C stage. c) XRD patterns at increasing temperatures in vacuum  $3 \cdot 10^{-3}$  mbar atmosphere. d) XRD patterns at increasing temperatures in 100% Ar atmosphere. e) XRD patterns at increasing temperatures in 100% H<sub>2</sub> atmosphere. f) XRD patterns at increasing temperatures in 100% NH<sub>3</sub> atmosphere. g) Trend of the observed peaks in XRD patterns in function of the temperature.

The diffraction patterns measured *in-situ* under different atmospheres show a common trend, *i.e.*, a shift of the observed I and II peaks to higher  $2\theta$  values (**Figure 4-7c-g**). However, a faster shift is observed for the I peak, this is displayed by comparing vacuum heat treatment of GO at 200 and 250°C (**Figure 4-7a and b**). According to how little amount of GO is under heat treatment, the curves can develop more noise (vacuum and argon case, **Figure 4-7 c-d**), nevertheless raw data were preferred. In order to better grasp how the peaks maximum varies depending on the temperature, it was plotted the graph in **Figure 4-7g**. Before 150°C, the  $2\theta$  there are already relevant differences.  $\text{NH}_3$  treatment holds the lowest I peak  $2\theta$  values, while vacuum one the lower values until 100°C. Ar atmosphere displays some general uncommon features, both in the I peak and in the II peak. In fact, the sample was prepared after the analysis of  $\text{H}_2$  and  $\text{NH}_3$  and likely with lower amount. As a result, we see a bundling of  $2\theta$  values between 150 and 200°C, with the exclusion of Ar. Interestingly,  $\text{NH}_3$  II peak is the first appearing at 150°C, whereas the other atmospheric conditions do not show any maximum yet. The remaining atmospheres exhibit a II peak only from 200°C. At higher temperatures, if we can be said that  $\text{NH}_3$  I peak keeps owning the lower values, its II peak has the highest  $2\theta$  values until 350°C, when it crosses vacuum and  $\text{H}_2$  II peak. Amongst 300 and 350°C, there is a remarkable jump of the vacuum and  $\text{H}_2$  II peak from around 22.5° to 24.5°  $2\theta$  values.

If we allow via Sherrer equation to roughly link the peak maximum with the interlayer distance, it is possible to qualitatively conjecture how the interlayer distance modifies. Hence, with lower and higher  $2\theta$  values, respectively expansions and compressions<sup>.128,311,315,316</sup> For this purpose and in light of the analysis conditions, knowing with more detail the number of layers and the figures of the interlayer distances would not enable better conclusions.

Summing up, considering the issues of Ar sample, we can generally state that none of these atmospheres; that is, vacuum,  $\text{H}_2$ , and Ar chemically interact on GO, not even pure  $\text{H}_2$  at these conditions. Significantly,  $\text{NH}_3$  can generously expand the interlayer distance already at room temperature. This is likely to be an interaction with  $\text{NH}_3$  and GO or the ODs too. Furthermore, it must be underlined that  $\text{NH}_3$  also has a high solubility in water, 32 g per 100 mL at 25°C<sup>317</sup> (for comparison Ar 62 mg L<sup>-1</sup> at 20°C<sup>318</sup>). Additionally, in the way it is prepared, GO contains intercalated water profusely, which it may swell.<sup>319-321</sup> As graphite's only peak lies at 26.2°  $2\theta$ , the approaching of the II peak to that number should be a sign of graphitisation. In this regard,  $\text{NH}_3$  is the first displaying a II peak and it has the faster II peak shifting right. Therefore, we can conclude that  $\text{NH}_3$  is the atmosphere that better boost the graphitisation. Again, if this is the removal of debris, reduction, or a combination of the two

events, XRD cannot clearly identify it. Finally, I might ascribe the little vacuum expansion at low temperatures to the vapour formation of intercalated water or its slow removal.



#### 4.3.1.5 rGO-FETs pH sensing

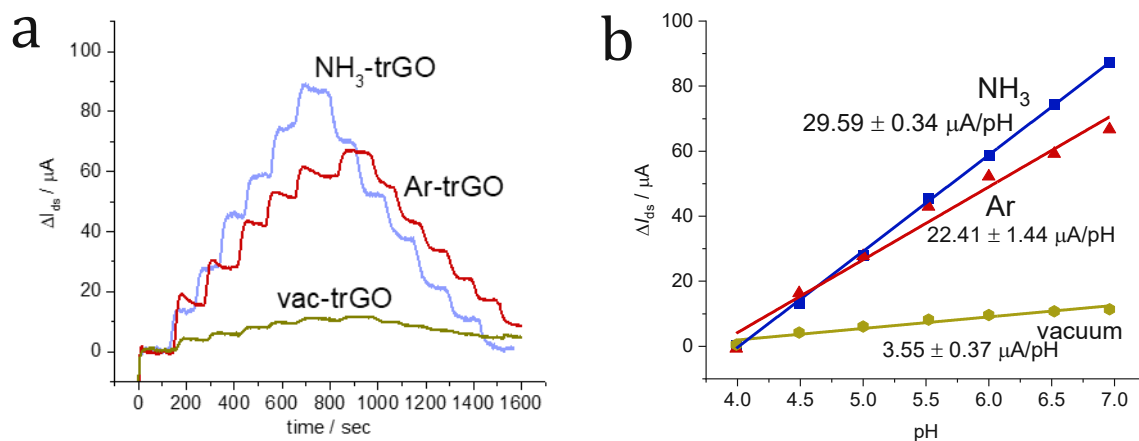


**Figure 4-8.** a) pH sensing response expressed in  $\Delta I_{ds} \mu A^{-1}$  vs time and obtained with a LGFET by applying a gate voltage  $-0.4$  V and a source-drain voltage of  $0.1$  V. Different rGOs are employed in LGFET and come from different atmospheres, that is, vacuum (dark yellow), Ar (red), and NH<sub>3</sub> (blue). H<sub>2</sub>/Ar (green) is excluded due to high similarity with Ar. b) pH sensing response expressed in  $\Delta I_{ds} \mu A^{-1}$  vs pH value to underline the pH sensitivity of the diverse LGFETs.

Through the capillary tubing and the peristaltic pump different pH solutions were let flow into the FET. Always fresh solvent  $0.1x$  PBS and analyte, in this case H<sup>+</sup> cations, were contemporaneously immersed in the electrochemical cell with rGO channel and the top gate rod tip. As reported above, the data were collected without waiting time and the drift was subtracted with a manually-made drift baseline.

The result is presented in **Figure 4-8a** and simplified with added sensitivities in 4-7b. Owing to the high similarity with Ar, the heat treatment under H<sub>2</sub>/Ar was excluded. Vacuum atmosphere leads to a poor pH detection, measurable in  $3.55 \pm 0.37 \mu A pH^{-1}$ , whereas Ar atmosphere profoundly improves the pH sensitivity up to a  $22.41 \pm 1.44 \mu A pH^{-1}$ . Highest performing, NH<sub>3</sub> can further enhance the sensitivity along with a minimisation of the error,  $29.59 \pm 0.34 \mu A pH^{-1}$ .

As expected by the resistance trend and the concept of reduction degree/cleaning, the pH detection capabilities grows from vacuum to Ar and again to NH<sub>3</sub>. Surprising are the actual figures of the pH sensitivity. In other words, a small variation of GO composition in O-containing functional groups (surveys and C1s detail spectra) can cause a remarkable boost in sensitivity, as we see between vacuum and Ar treatment. The further progress seen with NH<sub>3</sub> atmosphere might really be the added N-containing functionalities and the doping.<sup>102</sup> Amino groups have proven to be important pH-sensitive groups, along with hydroxy.<sup>322</sup>

However, the resulting pH detection sensibilities are competing with ones arising from multi-step reduction methods, including carcinogenic hydrazine hydrate.<sup>26,37,177</sup> Moreover,

this is done one-pot and in limited amount of time compared to the long hydrazine hydrate exposure.<sup>142</sup> Therefore, this as an important step forward in controlling GO properties in multiple fields that need cheap, semiconducting, graphene-like films.

### 4.3.2 Conclusion and outlook

Through the custom-made setup, the resistance of the GO channel decreases, while the current intensity transients are *in-situ* monitored. Consequently, it is possible to better understand the effect of the gas/vacuum atmosphere on GO and its causes. Those found stronger hypotheses amongst the thermal conductivity of the gases and their inertness/reactivity towards GO.

Different atmospheres lead to different GOs, namely to better reduced/cleaned GO films, nevertheless referred to as rGO for convenience. The hypothesis of GO cleaning from ODs is valuable enough that it cannot not be totally excluded with this set of experiments.

Better reduced/cleaned GOs means different GO properties that can be observed via all the characterisation and applications employed in the section. Certainly, the pH detection performance is remarkable considering the small effort in the reduction/cleaning.

Several are the aspects that should be involved to allow an holistic assessment of the device and its fine mechanisms. After the long discussion, what is valued the most is surely the XPS analysis that allows a detailed surface chemical characterisation, albeit not directly on the sample. The functional groups here are crucial either it be the GO, rGO, ODs or the support, and the pH sensitivities may be a difficult compromise of GO reduction/cleanliness, carried pH sensitive functional groups (either on rGO, nearby, at the gate), and also the interaction GO channel-support.

Therefore, along with the XPS analysis, current, and the resistance of the GO/rGO channel partially explains the FET behaviour. This is then further corroborated by the XRD results, by confirming how “graphitised” the layers are, and by XPS results and its C1s detail spectra outline. In this sense, Ar atmosphere, at the applied conditions, is an extremely effective reduction/cleaning method. There, a lower resistance and additional pH-sensitive functional groups completing the  $pK_a$  spectrum could further enhance the sensitivity. In fact, this seems the case of the  $NH_3$  thermal treatment that achieves  $29.59 \pm 0.34 \mu A pH^{-1}$ , with a reduction that is undeniably more practical than the ultimate hydrazine-including procedures.

Moreover, unlike other techniques XRD results can hint through the swelling the presence of intercalated water, which is everything but novel in graphite oxide and GO characterisation. This augment the questions regarding the leaving groups from thermal treated GO.

In order to further understand the behaviour of GO under thermal treatments and exclude GO reduction or cleaning, a GC-MS should be connected to the heating chamber with an Ar gas flow.

## 4.4 Linking functional groups and pH sensitivity

To detect an analyte, it is necessary to find the appropriate recognition units. In analogy, pH sensing with LGFETs must also have some, which have been identified earlier as adsorbed HO<sup>-</sup> species<sup>187,248</sup>, and later with O-containing functional groups.<sup>26,37,177,188</sup> Herein, it is presented how GO *I-V* characteristics and pH detection performance change in function of pH-sensitive functional groups and their abundance. An additional, faster, low-temperature NH<sub>3</sub> treatment was developed, which leads to further rGO modifications. This represents both an important term of comparison and surprising improvement in the pH detection performance. A comprehensive XPS investigation and the LGFET tests are used for the purpose of comparing the two NH<sub>3</sub> treatments of [subsection 2.2.2](#).

### 4.4.1 Results and discussion

*I-V* characteristics of NH<sub>3</sub>-rGO annealed in custom-made setup are reported again, and those are compared with a new developed synthesis approach in Schlenk tube, called NH<sub>3</sub> Schlenk or NH<sub>3</sub> (S) (**Figure 4-9**). From [section 4.3](#), the Dirac point position has been already discussed. Albeit, NH<sub>3</sub> (S) treatment displays a lower Dirac point current, the average current is comparable to NH<sub>3</sub> one. Nevertheless, the gap between Dirac point current and current maxima is greater. This means that NH<sub>3</sub> Schlenk creates a rGO with supplemental semiconducting properties. Moreover, NH<sub>3</sub> Dirac point potential undergoes a right shift.

Therefore, on one side, it is expectable that NH<sub>3</sub> Schlenk introduces more defects into the flakes lattice owing to the more semiconducting shape of the *I-V* plot.<sup>70,72,323</sup> On the other side, the Dirac point potential shift would suggest less N-doping and more electron-withdrawing functional groups at the rGO flakes (see [section 4.3](#)).<sup>285,302</sup>

If the pH sensitivity of GO given by the NH<sub>3</sub> treatment in the custom-made setup was already considered significant and comparable to reported papers, the pH sensitivity enabled by the NH<sub>3</sub> Schlenk is extraordinary. Practically, it doubles the figures of the other NH<sub>3</sub> treatment, going from  $29.59 \pm 0.34 \mu\text{A pH}^{-1}$  to  $59.89 \pm 1.35 \mu\text{A pH}^{-1}$ .

In light of the results of [section 4.3](#), a thorough XPS analysis was carried out to underline the differences between the two material surfaces. Once more, it is important to repeat that the XPS studies were conducted on on-purpose-prepared samples in order to enhance the amount of GO avoiding encountered LOD complications and remove the APTES variable (I remind of [subsection 4.2.3](#)).

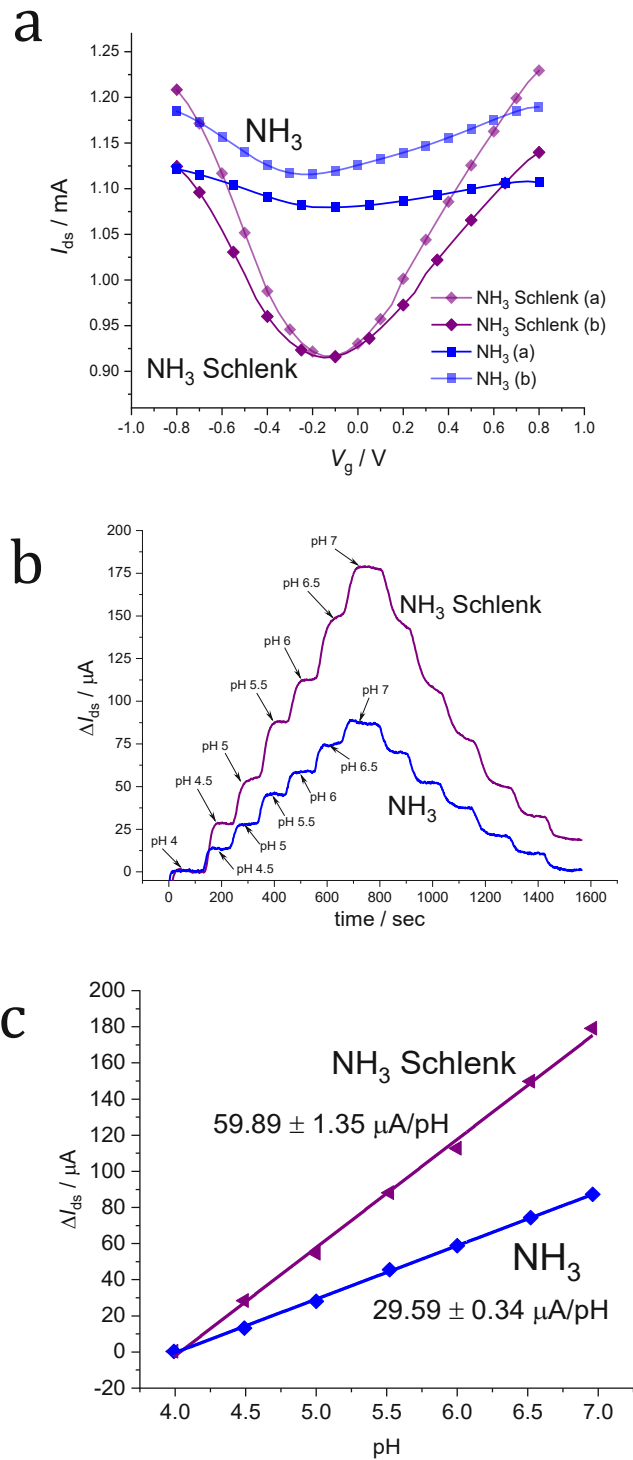


**Figure 4-9.** a)  $I$ - $V$  characteristics of LGFETs through rGOs obtained with NH<sub>3</sub> atmosphere and two diverse thermal treatments, *i.e.*, in blue NH<sub>3</sub>, in purple NH<sub>3</sub> Schlenk. The gate voltage is swept between -0.8 and 0.8 V, whereas 0.1 V is applied between source and drain. b) pH sensing response expressed in  $\Delta I_{ds}$   $\mu A^{-1}$  vs time. It is obtained with a constant applied gate voltage -0.4 V and an applied source-drain voltage of 0.1 V. The blue line represents NH<sub>3</sub> rGO, while the purple line denotes the NH<sub>3</sub> Schlenk rGO. c) pH sensing response expressed in  $\Delta I_{ds}$   $\mu A^{-1}$  vs pH value to underline the pH sensitivity of the diverse LGFETs.

In **Figure 4-10a** and **Table 4-3**, XPS surveys plots and corresponding atomic concentration percentages of  $\text{NH}_3$  and  $\text{NH}_3$  (S) are reported. For the sake of clarity, the GO composition is added once more. In the previous section, the drop of O at% and the rise of C at% from GO to  $\text{NH}_3$ -rGO have been mentioned. By contrast,  $\text{NH}_3$  Schlenk provokes a usual C at% boost and O at% diminution as all the thermal treatments, nonetheless there is in the two cases a gap of about 4%, hence C at% stops at 79.53 and O at% reaches 10.48. The relevant amount of N, which was introduced with  $\text{NH}_3$  in the setup, is now with  $\text{NH}_3$  in the Schlenk tube similarly added.

In **Figure 4-10b** and **c**, the C1s detail spectra show little amount of functional groups, either N- or O-containing ones. According to the many expected groups, it is difficult to separate all the peaks. Hence, supported by the software fittings, it is identifiable for the treated samples C-C sp<sup>2</sup> at BE 284.5 eV, C-C sp<sup>3</sup>/C=N at BE 285.2 eV, C-O/C-N at BE 286.2 eV, C=O at BE 287.5 eV, C(O)OH at BE 289.1 eV, and Pi-Pi\* at BE 291.0 eV<sup>116,117,284,324</sup>. As also observed by Stobinski et al, GO has a more compact signal<sup>311</sup>, which it is here fitted with C-C sp<sup>2</sup> at BE 284.5 eV, C-C sp<sup>3</sup> at BE 284.9 eV, C-OH at BE 286.6 eV, C-O-C at BE 287.3 eV, and C(O)OH at BE 288.3 eV.

These results do not clearly demonstrate a notable dissimilarity that would explain the two observed and discrepant pH sensitivities.

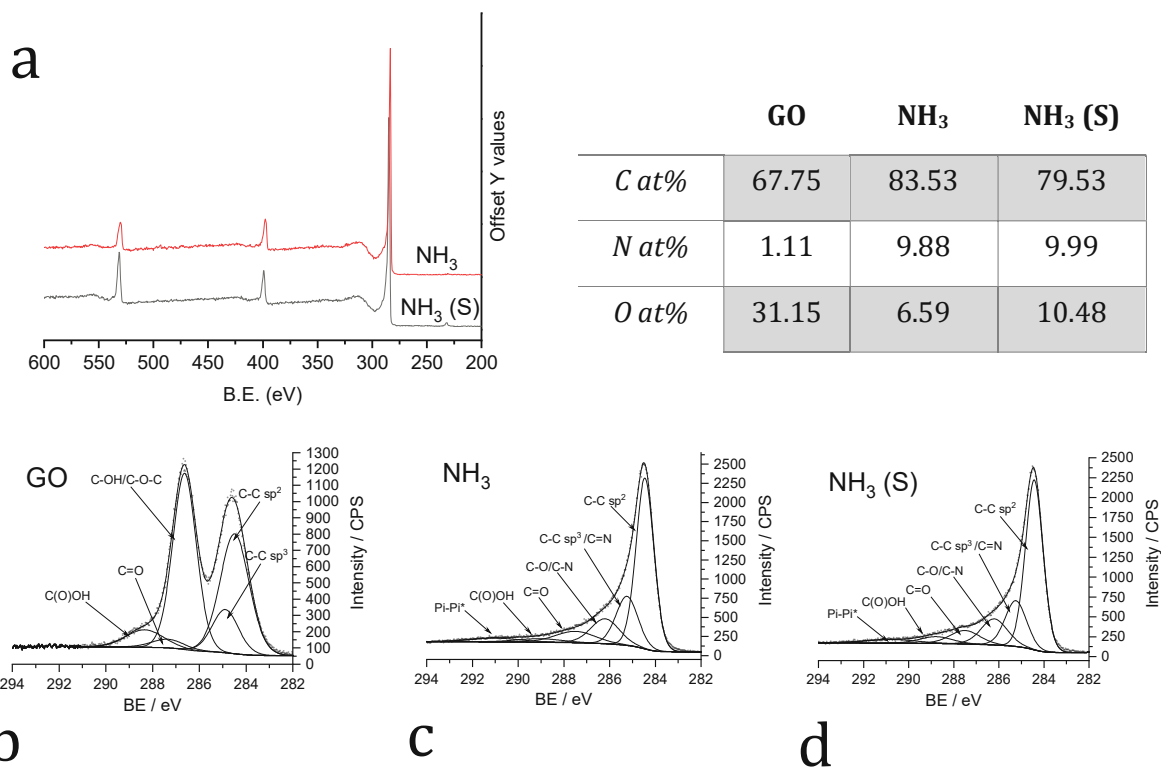


**Figure 4-10.** a) XPS survey spectra of NH<sub>3</sub>-rGOs treated in setup and in Schlenk tube. b)c)d) C1s region detail spectra of GO and NH<sub>3</sub>-rGOs.

**Table 4-3.** Atomic concentration percentages of relevant elements in NH<sub>3</sub>-rGO surveys.

The O1s detail spectra are fitted with generic peak components that stand for single, double bonds with C atom, and for a single bond in water molecules (**Figure 4-11a-c**). The O1s detail spectra for GO display two peaks, one that can be assigned to O=C at BE 530.9 eV, and the other one to O-C at BE 532.3 eV. The NH<sub>3</sub>-rGO shows three peaks at BE 530.9, BE 532.9, and at BE 535.8 eV, which correspond to O=C, O-H, and OH<sub>2</sub>. By contrast, in NH<sub>3</sub> (S) signal there is no indication of OH<sub>2</sub>, and the fitted components are identified as C=O at BE 530.9 eV and at C-O BE 532.5 eV. Here, a significant advantage is that O=C bond is always well defined at BE 530.9 eV. Thus, the other components positions, and the overall results are strengthened through this indication of reproducibility.

Additionally, it can be noticed that the intensity mismatch agrees with the samples surveys. While the signal peak maximum of NH<sub>3</sub>-rGO hovers around 500 CPS, NH<sub>3</sub>(S)-rGO peak maximum reaches 750 CPS. In light of the pH sensitivity results, of the O1s detail spectra, and of coherently reported articles, the presence of specified O-containing functional groups boosts graphene-based pH sensing, particularly OH and with minor impact of C(O)OH.

26,37,188

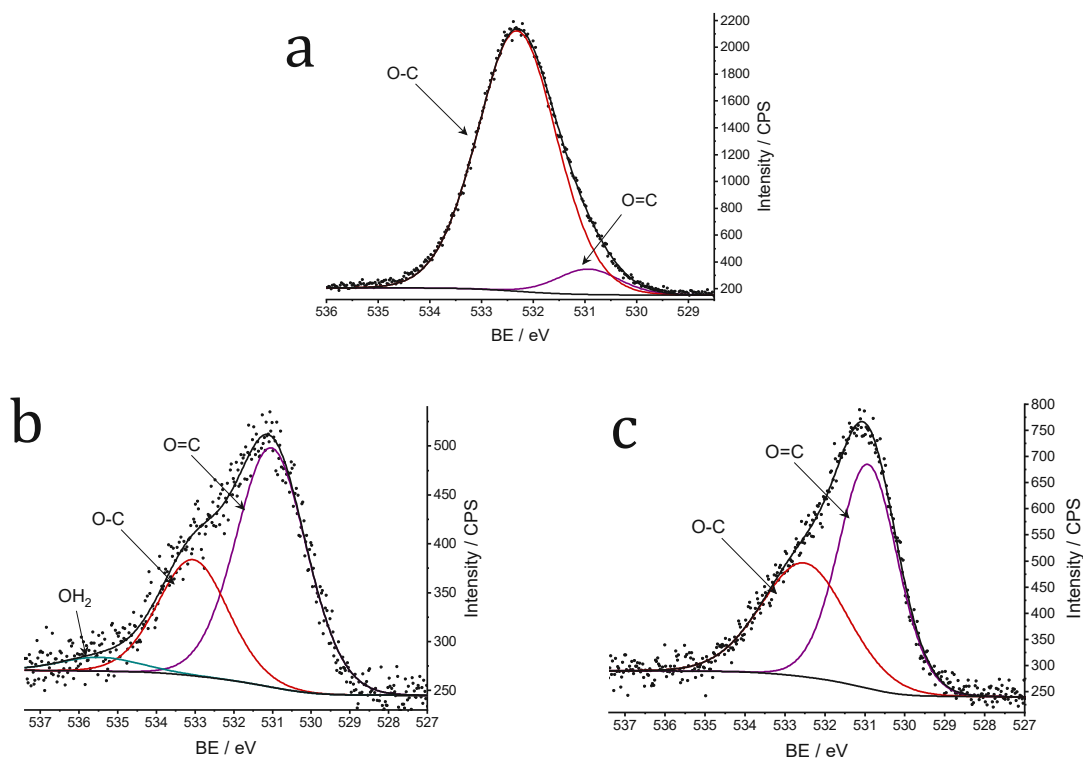


**Figure 4-11.** O1s detail spectra of a)GO, b)NH<sub>3</sub>, and c)NH<sub>3</sub> Schlenk.



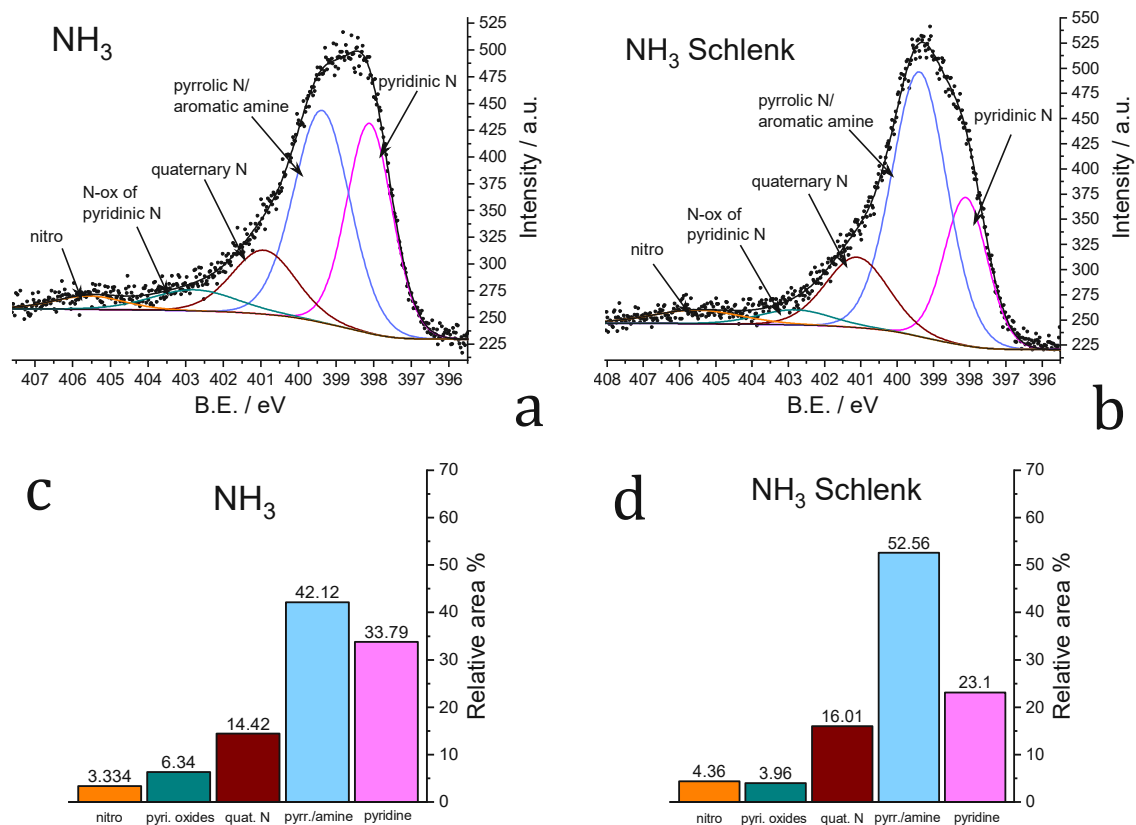


**Figure 4-12.** N1s detail spectra of a)NH<sub>3</sub> and b)NH<sub>3</sub> Schlenk with the respective components percentages in c) and d).

Therefore, by looking at the intensity of the signals, those groups should be more abundant after the NH<sub>3</sub> Schlenk treatment than NH<sub>3</sub> one. Moreover, by observing the components position, it is noticeable that O-C component can shift up to 0.6 eV from GO to NH<sub>3</sub> treatment. As it can be expected by the typical GO/rGO functional groups (see [subsection 1.2.4](#)), the component position should depend on the contribute of C-O-C and C-OH.<sup>311</sup> The O-C component of NH<sub>3</sub> (S) signal that lies at lower BEs than NH<sub>3</sub> one substantiates the hypothesis that the OH groups are contributing more to the signal than C-O-C. This is also visible by noticing the envelope of the signals, remembering that O=C remains practically constant. In other words, NH<sub>3</sub> Schlenk would not only have more O-containing functional groups, but also the most suitable for the interaction with H<sup>+</sup> ions.

Upon investigation of N1s detail spectra (**Figure 4-12a-b**), it can be identified in NH<sub>3</sub>-rGO 5 components, *i.e.*, pyridinic N at BE 398.1 eV, pyrrolic N/aromatic NH<sub>2</sub> at BE 399.4 eV, quaternary N at BE 400.9 eV, N-oxides of pyridinic N at BE 402.8 eV, and nitro group at BE 405.6 eV. In NH<sub>3</sub>(S)-rGO the BEs are essentially identical excluding two analytically negligible shifts for quaternary N to BE 401.1 eV, and for nitro group to BE 405.5. To be mentioned, the presented XPS results have been calibrated all together with C1s detail

spectra with C-C sp<sup>2</sup> at BE 284.5 eV. The components fittings agree with the previously found N-containing functional groups in graphene/rGO.<sup>306,325-327</sup>

In **Figure 4-12c** and d, the contribute of each assigned component is reported. Small variations in percentage characterise the components at higher BEs; namely, quaternary N, N-oxides of pyridinic N, and nitro group. Nonetheless, remarkable changes affect the components at lower BEs, which are also the most critical ones.

According to literature, NH<sub>2</sub> functional group is pH sensitive<sup>322</sup>, while the pyridinic N functional group belongs to the lattice and should be part of the aromaticity (as also discussed in [section 4.3](#)).<sup>328</sup> If we calculate the ratio between pyrrolic N/aromatic NH<sub>2</sub> component and pyridinic N component, it yields that NH<sub>3</sub>(S)-rGO has 2.27 and NH<sub>3</sub>-rGO has 1.25. This is a significant difference that might better explain the impressive gap between the pH sensitivities that the two ammonia treatments offer. Furthermore, this finding might lead to control specifically the N-containing functionalities in order to enhance the rGO or graphene pH sensing performance. However, it is still highly unsure which contribution is predominant, either N- or O-containing functional groups, specifically NH<sub>2</sub> or OH, or if there are other groups that have not been considered. Good SEM images after the Schlenk fast reduction should also be taken in order to exclude rGO damages. A sensible hypothesis is that rGO damages uncover NH<sub>2</sub> moieties of the APTES linker and that those become active pH-sensitive units. Nevertheless, GO cannot be compared due to the great amount of intercalated water and the possible ODs that prohibit reliable analyses.

#### 4.4.2 Conclusion and outlook

Two NH<sub>3</sub> thermal treatments bring to two differently modified GOs. The treatments have similar conditions, *e.g.*, ambient pressure, 100% NH<sub>3</sub> atmosphere, apart from the heating/cooling ramp. One heating ramp heats and cools at 10°C min, and holds the maximum T for 30 min. The other heating ramp heats at around 50°C min, holds the T for 1h at about 220°C, before cooling down at room temperature at fastest rate.

The FETs produced with the two type of rGOs show *I-V* characteristics with comparable maximum currents, however NH<sub>3</sub>(S)-rGO curve displays a Dirac point potential right shift and a deeper Dirac point current. The shift might arise from added electron-drawing functional groups, particularly O-containing. By contrast, the shape should be due to defects formation, *i.e.*, doping, functionalisation, vacancies, and wrinkles, and it would suggest a stronger semiconducting behaviour. Consequently, more responsiveness to electric field changes is expected. In fact, the pH sensitivity of NH<sub>3</sub>(S)-rGO is practically twice as much as NH<sub>3</sub>-rGO, reaching a record value of  $59.89 \pm 1.35 \mu\text{A pH}^{-1}$ .

The deep XPS investigation indicates analytically significant differences between two NH<sub>3</sub> thermal treatments. On the one hand, the formed defects in NH<sub>3</sub>(S)-rGO could be explained by the augmented O at%. More O-functionalities also translates into a higher probability of having pH-sensitive functional groups. Also, in light of the O1s detail spectra, NH<sub>3</sub>(S)-rGO presumably bears in proportion more OH than NH<sub>3</sub>-rGO, which are crucial pH sensitive groups.<sup>37,188,322</sup> On the other hand, the extremely high pH sensitivity of NH<sub>3</sub>(S)-rGO could be supported other pH sensitive groups, which are usually left aside. Thanks to N1s detail spectra, a different component is observed and is used as template, namely the ratio amongst pyrrolic N/aromatic NH<sub>2</sub> component and pyridinic N. component For NH<sub>3</sub>(S)-rGO the components ratio is 2.27 and for NH<sub>3</sub>-rGO it stops at 1.25. While amino group interacts well with protons<sup>322</sup>, pyridinic N enter the lattice and should be part of the aromaticity of the crystal.<sup>304,325,328</sup>

However, it is uncertain if it is the O-containing or N-containing functional groups contribute to play a major role in the observed pH sensing improvement. According to Cui et al investigation, it should be a combined effect, due to the different pK<sub>a</sub> values.<sup>322</sup> Factually, the most interesting finding for the community may lie in the N-containing functionalities and the novel concept of the components ratio. The rediscovery of the high heating rate for a better performing GO has been already reported albeit not that loudly that could be heard from the LGFETs community.<sup>127,329,330</sup> Still, this attempt of a more detailed investigation and bridging with FET technology should aid not only in the cheap graphene-based pH detection, but also generic cheap graphene-based biosensing. An optimised NH<sub>3</sub> Schlenk

approach could serve other fields too, such as novel conducting light coverings, papers, and more in general nano-electronics.

Then, targeted experiments with controlled defects introduction/formation and pH sensing should better explain what is the contribute of the N functional groups ratio and what is the contribute of O-functional groups. At which pH value N-containing functionalities starts and stops sensing  $H^+$  and the same for O-containing functionalities.

## 4.5 Effect of heating ramp

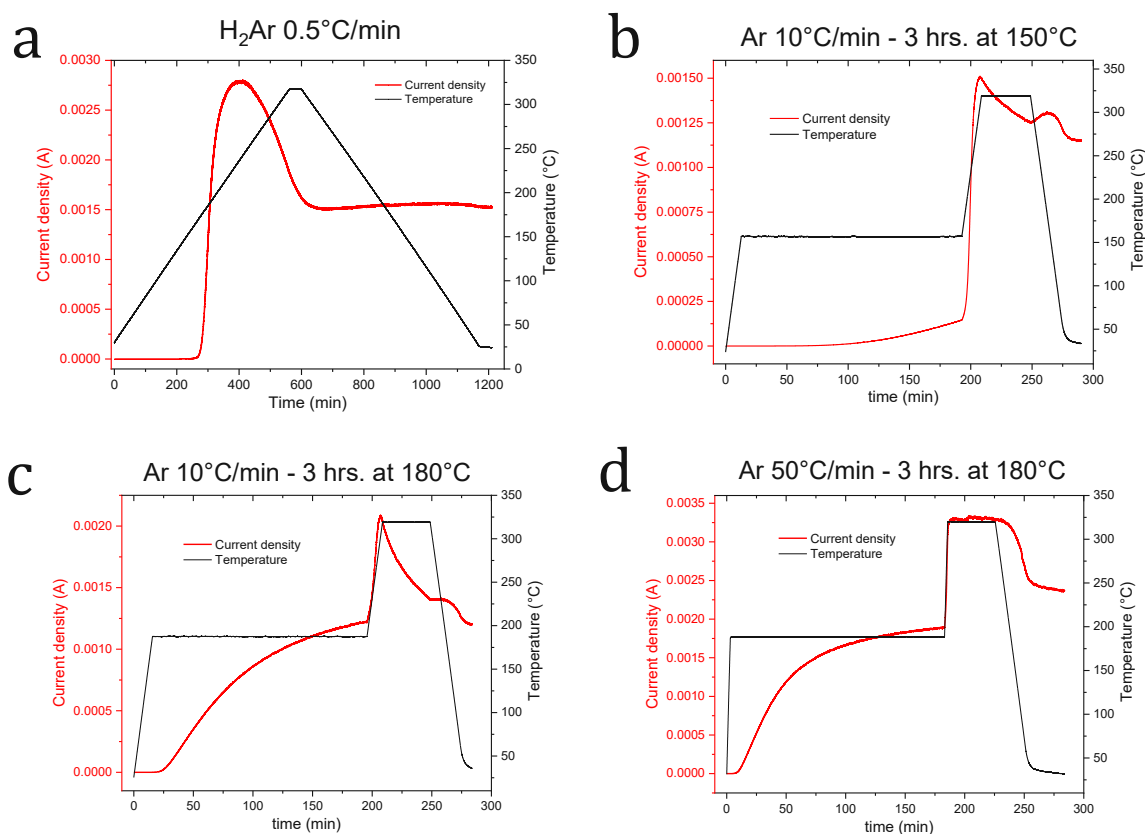


**Figure 4-13.** a) Current monitoring measurement in presence of H<sub>2</sub>/Ar with extremely low heating/cooling rate 0.5°C min<sup>-1</sup> and holding T at 310°C for 40 min. Current monitoring measurements with additional step b) at 150°C with heating/cooling 10°C min<sup>-1</sup>, c) at 180°C with heating/cooling 10°C min<sup>-1</sup>, and d) at 180°C with heating at 50°C min<sup>-1</sup>.

In order to observe the effect of the heating ramp on GO, the custom-made setup with current monitoring was further utilised. The maximum temperature was kept at 310°C for 40 min. Because it was an early experiment, in **Figure 4-13a**, the used gas was the H<sub>2</sub>/Ar mixture (as in [subsection 4.2.1](#) and [4.3.1.1](#)).

Upon a very low heating rate of 0.5°C min<sup>-1</sup>, the current does not follow the four phases that have been previously discussed, namely, heating, holding, cooling, and adjustment to room temperature. Though, it reaches a remarkable maximum of around 0.028 A before the temperature holds at 310°C. The current drops until the low rate cooling begins, and it remains at around 0.015 A.

As negligible variations were observed between the effect of H<sub>2</sub>/Ar and Ar gases (see section 4.3), only Ar was employed as inert gas during the thermal treatments. The idea of a temperature step, which is long and steady wanted to remove the whole intercalated water prior to a possible removal of functional groups. In **Figure 4-13b** and c, albeit the 30°C temperature difference of step, the current curve and the final current do not show

significant changes. In the case of a higher T step, the current rises earlier and gets to a notable greater current. Nevertheless, after the maximum, the current of the 180°C step treatment decreases faster and undergoes a little bump as in the 150°C step treatment. The heating ramp including 50°C min<sup>-1</sup> heating rate and 180°C temperature step displays immediately a superior current hovering around 0.018 A. The second heating ramp pushes the current to a record value of 0.032 A. The temperature is then held at 310°C for 40 min. Interestingly, this is the first time that the maximum temperature allows a practically constant current. Next, the fast cooling provokes a drop of almost 0.001 A, nonetheless the final current flattens at approximately the double of the previous Ar thermal treatments.

The difficulty of separating the listed possible effects, such as release of intercalated water, ODs, and O-containing functional groups has led to the absence of clarifying literature. The presented results cannot help in this sense. However, the current monitoring of GO reduction/cleaning reveals that if the release happens, it is maximised with fast heating ramps. This is testified by the current increase and behaviour with a 50°C min<sup>-1</sup> heating ramp. By contrast, the slow heating rate totally alters the current transients and suggests that at low T increases better conductive GO cannot be obtained at T >250°C.

Repeated thermal treatments should be explored to verify their utility.



## Chapter Five

# Li, Sb co-doping to enhance OER in hematite photoanodes

Se la nostra nera e nervosa civiltà basata sul carbone sarà seguita da una civiltà più tranquilla basata sull'utilizzo dell'energia solare, ciò non sarà dannoso per il progresso e per l'umana felicità.

If our black and nervous civilisation, based on coal, shall be followed by a quieter civilisation based on the utilisation of solar energy, that will not be harmful to progress and to human happiness.

Giacomo Ciamician

La chimica è una cosa che serve a tutto. Serve a coltivarci, serve a crescere, serve a inserirsi in qualche modo nelle cose concrete.

Chemistry is something extremely useful. It helps in cultivating, it helps in growing, it helps in introducing yourself into concrete things.

Primo Levi





# 5 Li, Sb co-doping to enhance OER in hematite photoanodes

Chapter number five presents few results of the many accomplished experiments on hematite-based photoanodes for photoelectrocatalytic water oxidation. Experiments, which are mainly practical and with the fast output of the checked photoelectrochemical behaviour. Herein, Sb and Li are inserted as co-dopants in hematite thin films. The feasibility of the doping method is of interest, as well as the additionality of the improvement effects on the photocurrent brought by  $\text{Sb}^{5+}$  and  $\text{Li}^+$ . Again, further experiments have been conducted to expand the knowledge on the behaviour of the template in presence of dopants used for mono-doping or co-doping.

## 5.1 Introduction

In photocatalysis and photoelectrocatalysis with metal oxide semiconductors, co-doping accounts for one of the successful approaches to further improve and understand the material properties.<sup>237,331-334</sup> Hematite fulfils several criteria to be a successful semiconductor oxide in photoelectrochemical cells, namely band gap, stability, non-toxicity, Earth abundancy.<sup>335,336</sup> However, it still suffers from poor conductivity and diffusion length of both electrons and holes, but particularly holes (2-4 nm).<sup>220,337</sup> Furthermore, to obstacle hematite theoretical efficiency, there are also sluggish OER kinetics, too short lifetimes of photo-generated carriers ( $10^{-12}$  s), and the inadequate bands position. Many transition metals entered hematite crystal lattice as electron (Sn, Si, Nb, Sb, Zr, Ta, Rh, Ge, Ru, and Pt) and hole (Mg, Cu, Mn, Ru, and Ni) donors.<sup>202,225,226,228,229,232,247,335,336,338-341</sup> As other semiconductor oxides, hematite can be doped extrinsically with additional external elements, but also intrinsically with oxygen vacancies<sup>208,236,342</sup>. Moreover, co-doping also happens due to the Sn diffusion from the substrate and occurring surface oxygen vacancies, this is a typical effect of high temperature annealing along with FTO degradation.<sup>225,343-345</sup>

Theoretical calculations have demonstrated that each  $\text{Sb}^{5+}$  cation can induce an overall charge distribution in 4 surrounding Fe atoms, which is close to  $2e^-$ . By contrast,  $\text{Sn}^{4+}$  induces only  $0.3e^-$  on one Fe atom.<sup>232, 23,24</sup> This so called double donor doping and it practically creates around itself two  $\text{Fe}^{2+}$  cations, which should be responsible for the hopping mechanism of charges in hematite bulk.<sup>346,347</sup> Instead,  $\text{Li}^+$ -doping of iron oxide has been attained<sup>348</sup>, yet no photo- electrocatalytic experiments were done, until recently.<sup>349</sup> Li

cations and hematite used to come in contact only in Li-ion batteries.<sup>350,351</sup> In photoanodic water oxidation, bismuth vanadate has profited of the result of Li introduction, *i.e.*, boost of the majority carrier concentration.<sup>352</sup>

By considering the charge transfer band (CTB) and upper Hubbard band (UHB), the most promising approach appears a bulk n-type doping and a surface p-type doping.<sup>207</sup> However, not only the photo-generated charge carriers do not live long in hematite, but there are further issues, *i.e.*, a poor photogeneration yield and a weak charge separation yield.<sup>247,353</sup> About the first, not much can be done if not updating the theoretical maximum efficiency. About the second, a strategic co-doping with n-p-type doping centres could enhance the charge separation yield, especially as soon as the electron-hole pairs are formed.<sup>247</sup>

In this chapter, we explored the role of  $\text{Sb}^{5+}$  and  $\text{Li}^+$  as co-dopants in hematite photoanode to create eventual fast-charge-separating p-n type centres. We successfully achieved *in-situ* hematite doping using precursor solutions with Sb(V), albeit the extremely rapid hydrolysis, whereas Li(I) was added to the water-based spin-coating solutions without difficulties. The counterion is chloride for all the precursors, as it is for the hematite formation. The samples are characterised with photoelectrochemical measurements in a typical three-electrode-configuration cell, and it is seen that  $\text{Sb}^{5+}$  and  $\text{Li}^+$  cations can one by one enhance the output photocurrent. Moreover, an articulated XPS analysis, in addition to grazing incidence X-ray diffraction, Raman spectroscopy and SEM in order to confirm the co-doping and analysis structural effects are performed.

## 5.2 Results and discussion

### 5.2.1 UV-Vis

In **Figure 5-1**, 4 visible absorption spectra of hematite thin films can be found. The signal originates from a series of typical peaks.<sup>268,354–356</sup> The most intense and left-shifted peak of the spectrum encroaches into the UV region, and it is a sum of two bands. The one at higher energy is expected at 375 nm and the one at lower can be identified at around 420 nm, where the curve flattening begins its descent to lower absorption intensities. The peak at 420 nm as well as an additional peak at about 490 nm, both arise from spin-flip transitions,  $2t_{2g}$ , and  $3e_g$ . Here, magnetic coupling offers higher intensities of the peaks. Instead, due to spin-forbidden ligand field transitions two peaks can be observed. A distinctive peak at around 535 nm and a smaller one is expected at 600 nm, the latter appears as a shoulder.

The layer thickness of the 4 analysed photoanodes should be identical, as the spin-coating method was carefully repeated, and it usually enables high reproducibility.<sup>269</sup> In light of this, it is noticeable that all the doped samples, mono- or co-doped, are capable of enhancing the light absorption to some extent. The degree of the increases is not large, though it should be in line with small doping amounts (1 at%) in nm-thick films. Certainly, an advantage is the diverse behaviour and the presence of the additional mono-doping photoanodes. In detail, on the one hand, the doping with Sb seems to allow a general growth of absorption intensity compared with the Std. On the other hand, Li doping boosts the absorption intensity especially at wavelengths < 550 nm, involving  $2t_{2g}$ ,  $3e_g$ , and the spin-forbidden ligand field transition at higher energy.

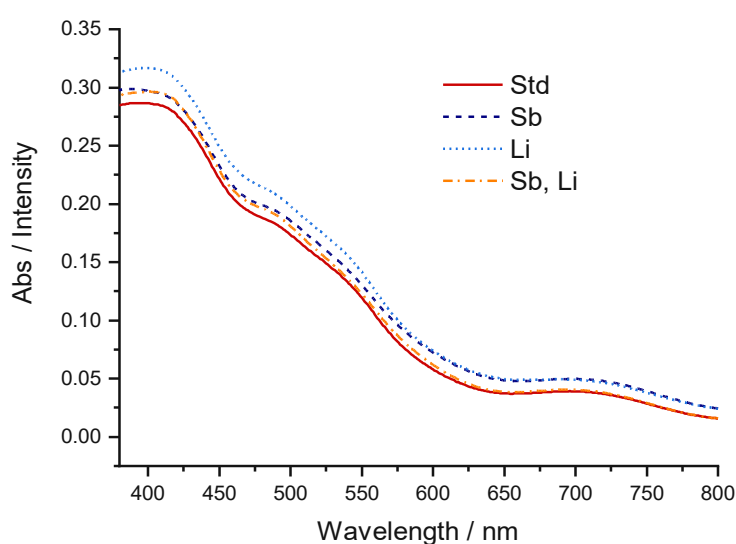


**Figure 5-1.** UV-Vis light absorption spectra of the hematite photoanodes vs clean FTO glass slide.

A same Li-doping effect is observed in  $\text{BiVO}_4$ , either in transmittance mode<sup>254</sup> or in absorbance mode<sup>357</sup>. This is likely caused by the creation of shallow and deep acceptor levels.<sup>358,359</sup> Instead, Sb doping might enhance the absorption intensity because of band gap narrowing, as it happens in comparable semiconductors.<sup>360,361</sup> Nevertheless, clear shifts cannot be observed, but an evenly augmented absorption intensity more attributable to other reasons, *e.g.*, a more defective bulk with smaller crystals size and more grain boundaries.

### 5.2.2 Raman spectroscopy

Hematite belongs to the  $D_{3d}^6$  crystal space group, thus we expect 7 modes, 2 modes with  $A_{1g}$  symmetry and 5 modes with  $E_g$  symmetry. The former ones represent the movement of the Fe atoms on the defined unit cell c-axis, while the latter ones are visualised with the O atoms breathing modes in the perpendicular to the c-axis. The micro-Raman spectra display the  $A_{1g}$  bands at 217 and 490  $\text{cm}^{-1}$ , and the  $E_g$  bands at 238, 284, 400, 603  $\text{cm}^{-1}$ . One mode is indiscernible from the mode at a slightly higher wavelength due to the high intensity of the second one and the small energy gap (only 5  $\text{cm}^{-1}$  usually separate the two peaks). Additional peaks hovering around 650 and 1301  $\text{cm}^{-1}$  are the *ungerade* symmetry modes ( $E_u$  and  $2E_u$ ), which usually should not be allowed. Owing to disorder, magnetite and/or presence of nanocrystals, such modes can be permitted.<sup>362-365</sup>

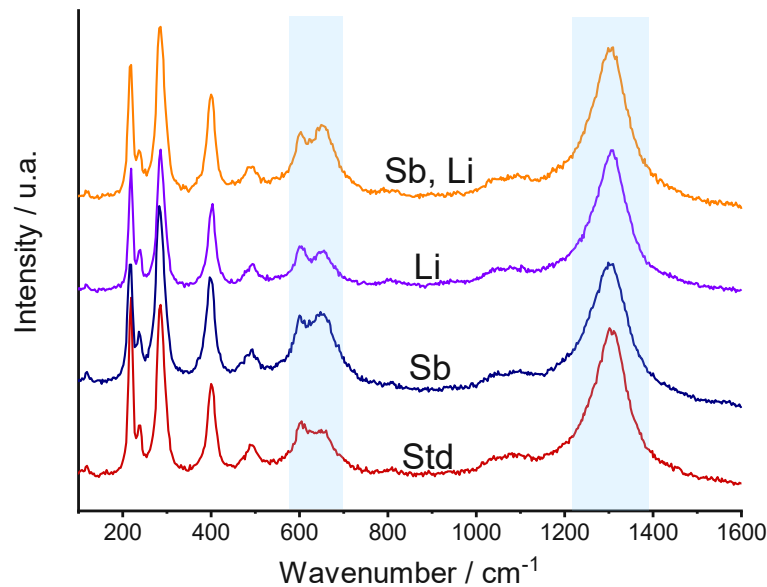


Figure 5-2. a) Micro-Raman spectra of standard, Sb mono-doped, Li mono-doped, and Sb, Li co-doped samples.

This is already true for the un-doped sample, which displays the  $E_u$  mode with a shoulder beside the  $E_g$  band at  $603\text{ cm}^{-1}$ . Nonetheless, through the mode we can recognise Sb-doped samples, as they exhibit a peak with identical shape, *i.e.*, this peak is sharp and overtakes in intensity the near band at lower wavenumbers. Li-doped sample does not clearly display a variation from the standard. Such observation is in contrast with Sb doping effect, and it may suggest interstitial doping.

### 5.2.3 XPS analysis

The XPS survey spectrum shows the typical peaks of hematite films (**Figure 5-3a**). The average penetration depth of the X-ray photoelectrons cannot reach the substrate, as it is only about 5 nm, thus, we do not identify any Sn and F in the investigated samples. In fact, we see the peaks arising from Fe and O belonging to the surface of the hematite thin layer. Furthermore, C occurs in relevant amount, about 29 at% as adventitious carbon at the surface.

By scanning a BE range of 700-740 eV at lower intensity (**Figure 5-3b**), we intercept the signal associated with electrons occupying Fe 2p orbitals. This detail spectrum displays the most intense peaks at about BE 711 and 724 eV,  $\text{Fe}2p_{3/2}$  and  $\text{Fe}2p_{1/2}$ , respectively. Those peaks also have defined satellites at 8-9 eV higher than their BE. Components plus satellites BEs are a good indication of  $\text{Fe}^{3+}$  cations, and thus it occurs in both samples. Upon simplification, we can take the peak at BE 719 eV only and if this shifts at higher BEs, around 715-716 eV, it proves the presence of  $\text{Fe}^{2+}$  cations. In these samples, also owing to the used annealing temperature, low percentages of  $\text{Fe}^{2+}$  cations are contemplated, nonetheless the high complexity of the signal does not allow for more information.

However, regarding the doping confirmation of hematite, more interesting results are offered by directly searching in the  $\text{O}1s/\text{Sb}3d$  region (**Figure 5-3c-e**). The investigated range goes from BE 527 to 542 eV. Herein, either one or two defined signals can be identified – one at lower BE and one at higher BE. The former is a mixture of  $\text{O}1s$  components, and of  $\text{Sb}3d_{5/2}$  in case Sb is added, while the latter is a single peak arising from the other spin-orbit component of Sb, *i.e.*,  $\text{Sb}3d_{3/2}$ . Upon deconvolution of the former one, the most intense peak of the signal can be assigned to  $\text{O}^{2-}$  anions at BE 529.90 eV. Furthermore, the  $\text{O}^{2-}$  component in the Sb-containing samples at  $\text{BE } 529.90 \pm 0.02\text{ eV}$  is found.

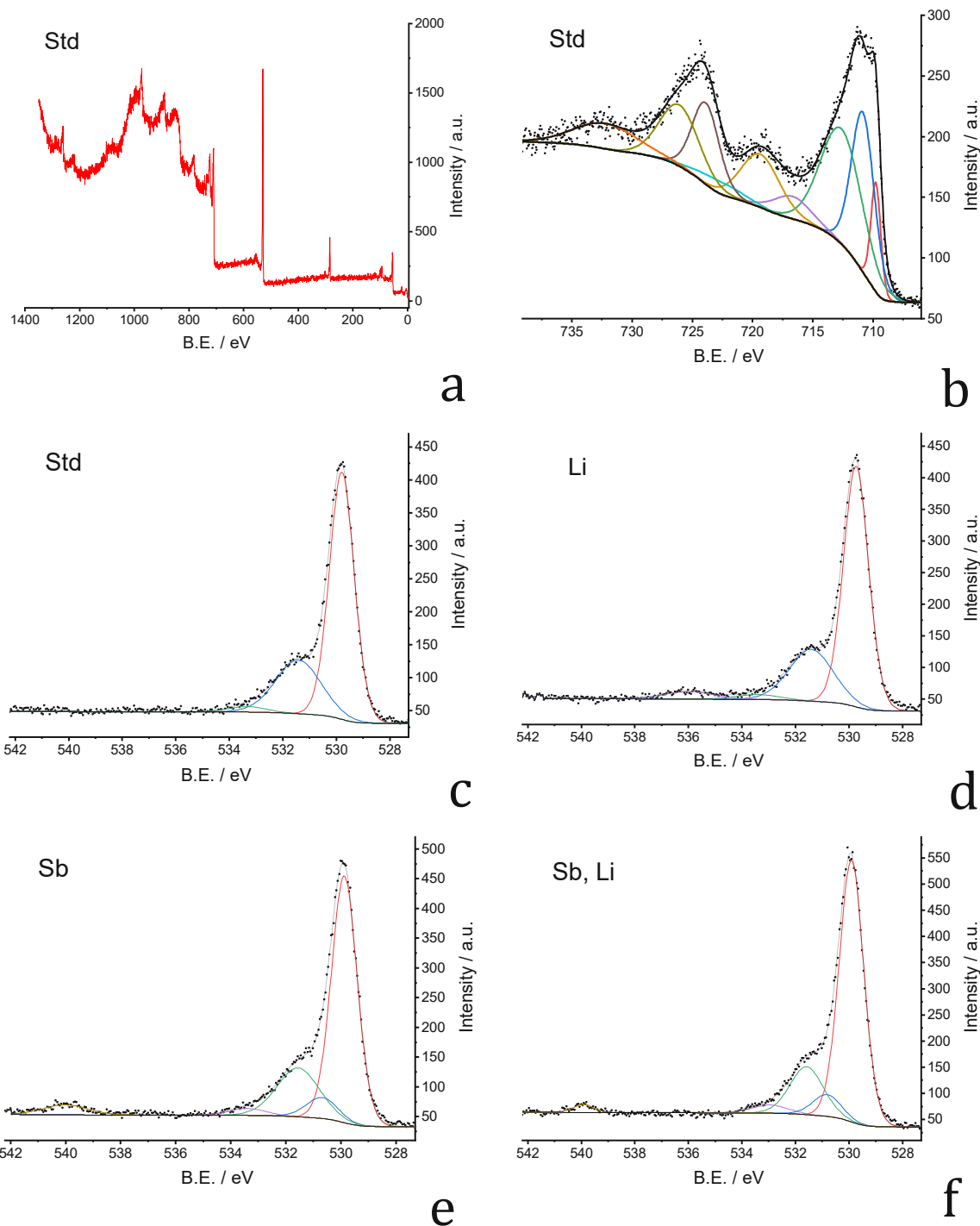


**Figure 5-3.** a) XPS survey spectrum of the standard hematite sample. b) Fe element XPS detail spectrum of the standard sample. c) O, Sb elements XPS detail spectrum of the standard sample. d) O, Sb elements XPS detail spectrum of the Li mono-doped sample. e) O, Sb elements XPS detail spectrum of the Sb mono-doped sample f) O, Sb elements XPS detail spectrum of the Sb, Li co-doped sample.

At higher BE of the same signal, a peak appears amongst BE 531.4-531.6 eV, which can be assigned to Fe-O bonding, *e.g.*, hydroxy groups (-OH). Thus, this also plays a crucial role in determining samples, which are poor or rich in oxygen vacancies.<sup>235,236,366</sup> At around 533-533.5 eV, we find another minor peak that can be designated as hydrocarbons, and surface

contaminations.<sup>367,368</sup> The latter one, which is  $Sb3d_{3/2}$  component lies around  $BE\ 539.96 \pm 0.04\ eV$  and does not carry the complication of a fitting. This further substantiate that the precursor and the annealing lead to  $Sb^{5+}$ -doping of hematite.<sup>232,369</sup> Unfortunately,  $Li^{+}$ -doping cannot be identified directly, since two more intense  $Fe3p$  components overlap with it.  $Li1s$  peak is expected at  $BE\ 55-56\ eV$ , while the  $Fe3p$  components range from  $BE\ 54\ to\ 58\ eV$ .<sup>348</sup>

## 5.2.4 XRD analysis

The diffractograms prevalently show the underneath FTO substrate (# symbols in **Figure 5-4a**), albeit the adopted lowest  $2^\circ$  grazing incidence diffraction angle. In **Figure 5-4a** and **b**, significant differences of the substrate after the doping and co-doping are not noticed. The most intense peak of crystalline hematite (110) appears, and it is distinctive. Nonetheless, it cannot be said the same for the other less intense expected peaks ( (012) (104) (024) (116) (300) ).

With a closer look at the (110) diffraction peaks of the batch samples, relevant dissimilarities are detected (zoom-in **Figure 5-4b**). Un-doped and  $Sb$  mono-doped sample (110) peak reach their maximum at  $2\theta$  about  $37.97^\circ$ . On the contrary, both XRD patterns of the  $Li$ -doped samples, mono-doped and co-doped, exhibit a gentle shift towards lower  $2\theta$  values at  $37.95^\circ$ . Albeit the observed gap is small, it is occurring only after the introduction of  $Li$  cations. This observation can be a strong proof that  $Li$  cations added with 1% at% can access the hematite lattice exclusively as interstitial dopants.<sup>370,371</sup> Larger doping percentage ratios could even enhance the expansion of the lattice parameters and push the peaks further to lower  $2\theta$  values.<sup>372</sup> As a consequence of this result, the introduction of  $Sb$  into the hematite lattice must occur substitutionally.<sup>232,369</sup> And again, as other variations cannot be noticed, we validate XPS findings, *i.e.*, oxygen vacancies do not affect singularly the samples and hence counterfeiting the photo- and electrochemical performances.<sup>373</sup>

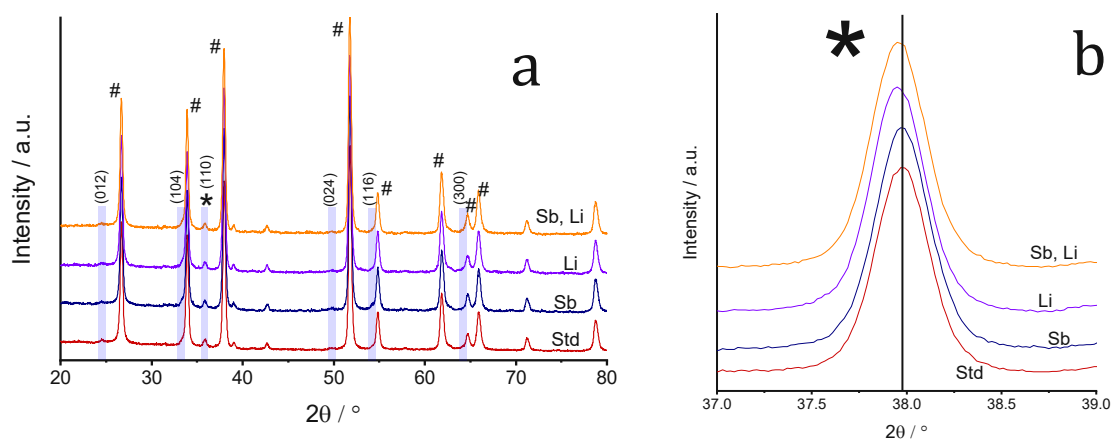


**Figure 5-4.** a) XRD patterns of standard sample,  $Sb$  and  $Li$  mono-doped samples, and  $Sb, Li$  co-doped sample. b) Zoom-in on the (110) diffraction peak of plot figure 4a, range  $2\theta\ 37.0-39.0^\circ$ .



## 5.2.5 Photoelectrochemical performance

As discussed in subsection 1.4.3 and 3.1.3, the utilisation of photoelectrochemical characterisation grants fast and simple analysis of the produced photoanodes. In photoanodic water oxidation, what best expresses the performance of the samples is the photocurrent. Albeit not being an absolute value, the photocurrent can be approximated as extremely reproducible if concentration, temperature, and pH of the electrolyte are constant. Other additional variables can be the electrodes, *i.e.*, counter, and reference ones, however by not changing any components of the electrochemical cell and by checking their state of wear, variations can be neglected. A way to maximise the exactness of a measurement, and thus of an investigation, is to produce every time a batch with a new standard sample. And that is what was done here for every batch, at least.

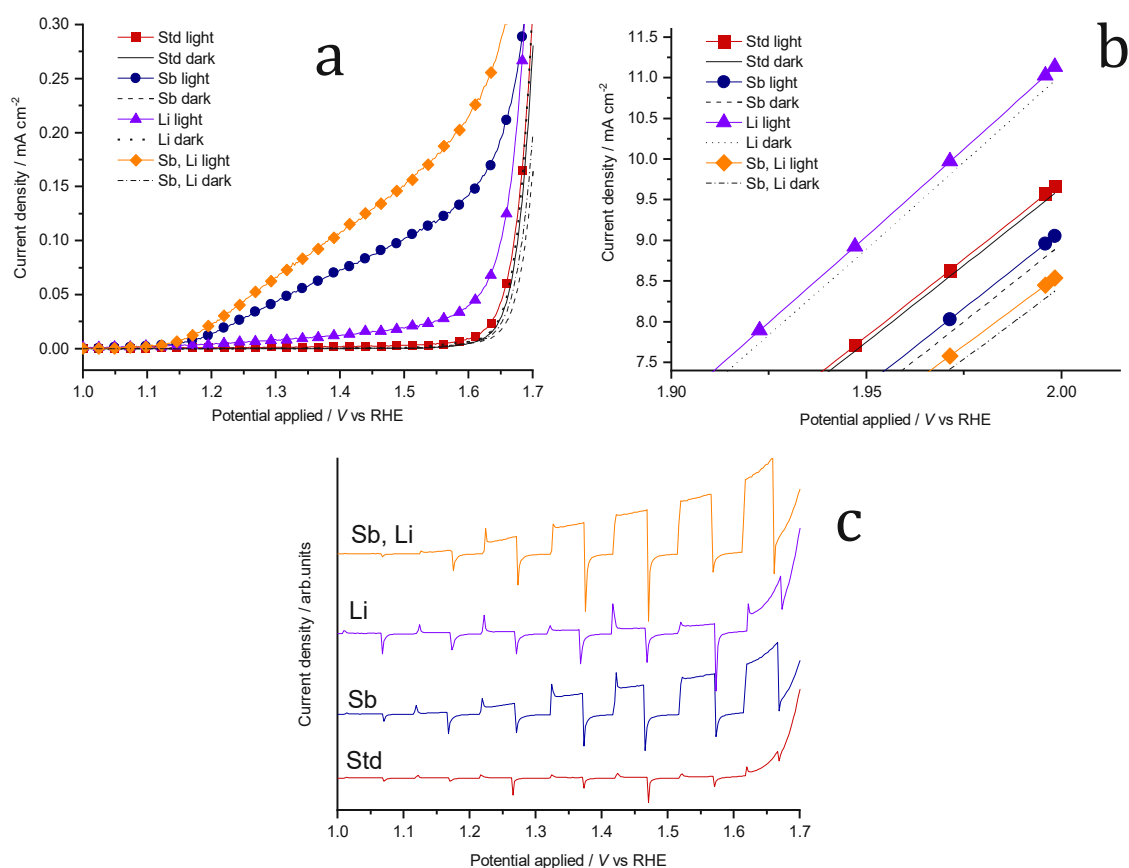


**Figure 5-5.** a) *J-V* curves light and dark recorded in 0.1 M NaOH with calomel electrode and Pt cathode. Light curves were carried out under a simulated solar light illumination of 100 mW cm<sup>-2</sup>. b) Details of current densities at high applied voltages (Faradaic regime). c) Light *J-V* curves recorded by chopping the light illumination.

To avoid any diffusion of Sn atoms from the FTO layer into the bulk, the samples were treated in muffle oven at set temperature 550°C, as described in the experimental section. All photoanodes were annealed together in the oven in order to maximise the reproducibility. Through LSV,  $J$ - $V$  curves were obtained, which resemble hematite films photocurrent deposited or annealed at 550°C.<sup>220,225,269,374</sup>

In **Figure 5-5a**, it is confirmed that doping with Li<sup>+</sup> and Sb<sup>5+</sup> is beneficial to the standard hematite sample. At 1.4 V vs RHE, while Li<sup>+</sup> cations introduction offers a moderate increase in photocurrent, 8-fold more than the standard one, Sb<sup>5+</sup>-doping, for his reported catalytic properties, pushes the photocurrent 45 times higher than the standard. As an interesting result, in the co-doped sample the combination of the two cations synergically enhances the photoelectrochemical performance to a 67-fold improvement compared to the un-doped hematite thin film photoanode. When the Faradaic current gets larger, at 1.6 V vs RHE, the increases seen before slightly shrink to around 4-, 15-, and 23-fold gains in respect to the bare hematite. However, it must be noted that the on-set potential light  $J$ - $V$  curves does not look affected by the mono- e co-dopings

At around 2 V vs RHE, the regime of the current density is almost completely Faradaic (**Figure 5-5b**). There, it is noticeable a small gap between light and dark  $J$ - $V$  curves, which makes the light curves practically negligible for a material evaluation. As second, it can be recognised that the trend observed previously in the photoelectrochemical characterisation does not repeat. The first point can be seen as an advantage because in this analysis the light absorption is removed and so the charge separation questions. Diversely, the second point is a question mark. Excluding Li<sup>+</sup> mono-doping, the observation is that the higher the photoactivity, the lower the current density at high applied voltages. At 2 V vs RHE, the current densities of dark  $J$ - $V$  curves of un-doped, Sb-doped, and Sb, Li-co doped samples reach 9.58, 8.89, and 8.38 mA cm<sup>-2</sup>, respectively. Exceptionally, Li<sup>+</sup>-doping shows a remarkable current density that stops slightly below 11 mA cm<sup>-2</sup> (black line). To date, this current density is the highest within the simple, solution-based methods. Other important results were obtained with more complicated techniques.<sup>226</sup>

In **Figure 5-5 c**, it is presented the chopped light  $J$ - $V$  curves, which display the typical current transients. The positive current transients, peaks, testify that not all the holes that reach the interface contribute to the OER, while, the negative current transients, falls, mean that there is recombination between conduction band electrons and photo-oxidised surface species (surface trapped holes too likely).<sup>375,376</sup> In order to have a better and faster understanding of the numerical result of chopped light  $J$ - $V$  curves, we find it convenient to calculate the ratio spike and fall currents over the average photocurrent in the range 1.3-1.4 V vs RHE. Albeit there are diverse potentials at which to calculate the ratios, the potential

was set far away from the Faradaic regime and where usually the photoactivity is the greatest. It is common to find similar values for the two ratios  $s/c$  and  $f/c$  (respectively spike/current, and fall/current).<sup>375,377</sup> Nonetheless, in our un-doped sample, we have a 5.0  $s/c$  ratio and 16.8  $f/c$  ratio.  $\text{Li}^+$ -doping can halve the current transient ratios by taking the values to 2.3 and 8.6. Meanwhile,  $\text{Sb}^{5+}$ -doping can almost fully heal the photoanode leading to 1.6  $s/c$  and 1.7  $f/c$  ratio. With the co-doping, and hence the addition of  $\text{Li}^+$ , the  $s/c$  ratio shrinks further to 1.1 and the  $f/c$  ratio grows to 2.0. In fact, in these hematite samples, we coherently observe that  $\text{Li}^+$ -doping keeps high values of  $f/c$  ratio compared to  $\text{Sb}^{5+}$ -doping. Therefore, including the chopped illumination measurements, the whole photoelectrochemical investigation corroborates the XRD results, namely that  $\text{Sb}^{5+}$  and  $\text{Li}^+$  must have diverging doping roles, though we do not rule out possible mutual tasks as photoanode and anode. Hence,  $\text{Sb}^{5+}$  must enter the crystal lattice or lattices as substitutional dopant. Because of the absence of an earlier potential on-sets with  $\text{Sb}^{5+}$  mono-doped sample, we tend to exclude here a role in catalysis.<sup>378</sup> However, it is expected the  $\text{Sb}^{5+}$ -doping to increase the carrier concentration and decrease the interfacial charge transfer resistance.<sup>232</sup> Both improvements can be motivated by the reduction of both current transients. The positive one more linked to the interfacial charge transfer resistance and the negative more related to the bulk-surface electron-holes recombination. By contrast, as seen in XRD, we expect  $\text{Li}^+$  to enter the hematite film only interstitially and thus it mainly leads to an expanded majority carrier concentration.<sup>254</sup> Those theories are also consistent with the high current density of  $\text{Li}^+$ -doped sample (**Figure 5-5b**) and the high  $f/c$  ratio (**Figure 5-5c**).

## 5.2.6 SEM analysis

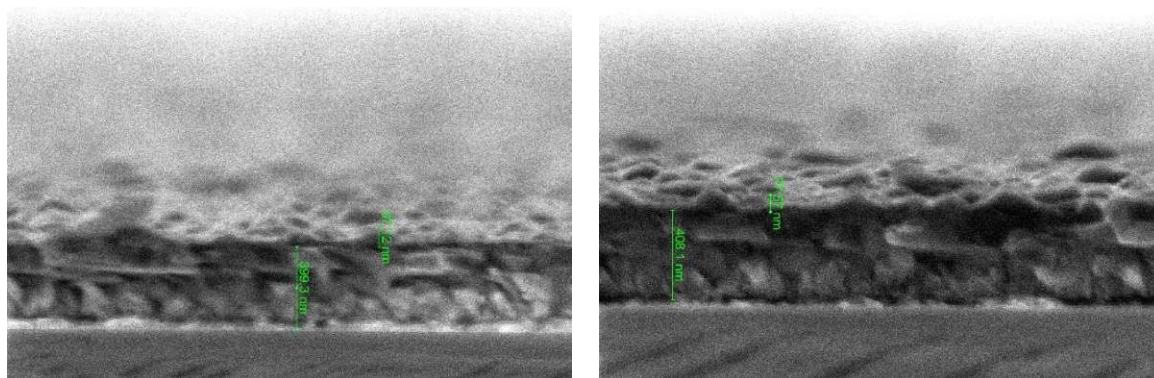


**Figure 5-6.** SEM micrographs side view of broken photoanodes for thickness confirmation.

In **Figure 5-6a** and **b**, it is shown SEM micrographs of a photoanode side view, which was prepared by cutting one photoanode in two halves. Actually, the conditions do not allow better focus; however, the FTO layer of around  $400\ \mu\text{m}$  is clearly discernible. Moreover, on top of the FTO layer, a thinner layer can be detected, which is easily ascribed to the expected hematite thin film.

The limitations of this technique for the prepared photoanode may lie in the denial of high annealing temperature, such as  $800^\circ\text{C}$ . Improvements were not observed with the deposition of thin metallic layers. Lower annealing temperature, namely  $550^\circ\text{C}$ , on the one hand, does not allow Sn diffusion into the hematite film. On the other hand, it does not enable healing of crystal lattice defects, eliminating grain boundaries. The typical  $550^\circ$  annealing temperature is the one that guarantees the conversion into hematite and only the introduction of the desired dopants.

## 5.3 Conclusion and outlook

In short, the Sb, Li co-doping of hematite thin films is beneficial and leads to a 67-fold improvement on the photoelectrochemical performance at  $1.4\ \text{V}$  vs RHE. Interestingly, the increment on the photocurrent by  $\text{Sb}^{5+}$  and  $\text{Li}^+$ -doping looks additional. According to the photoelectrochemical analysis, none of the dopants catalyses the water oxidation, however both augment the carrier concentration and particularly Sb diminishes the charge transfer resistance at the interface. Considering light chopped and dark  $J$ - $V$  measurements,  $\text{Li}^+$ -doping's aid mainly arises from the boosted majority carrier concentration. Still, as predictable, it does not seem to mild bulk-surface recombination. This effect is particularly clear when comparing  $\text{Sb}^{5+}$  mono-doped and Sb, Li coped samples in chopped light LSV. However, the obstacle of depositing from a water-based solution an extremely hydrolysable

precursor, such as  $\text{SbCl}_5$ , has been successfully overcome with HCl control. The utilisation of a direct  $\text{Sb}^{5+}$  cations source has the advantage to assure a unique  $\text{Sb}^{5+}$ -doping in the hematite lattice even at lower annealing temperatures.

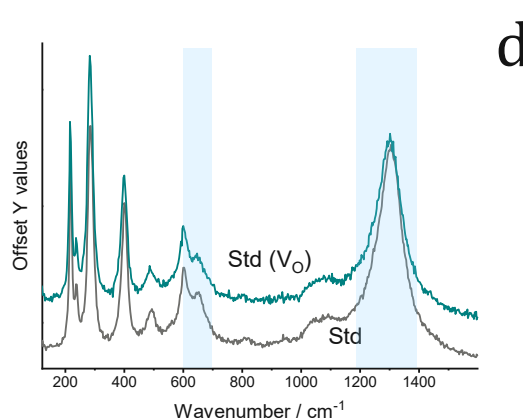
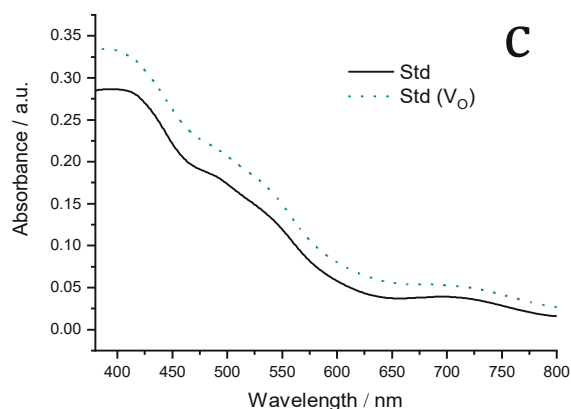
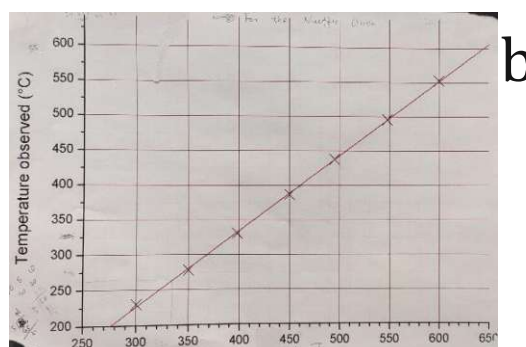
Further characterisation is needed to shine light on the kinetics of photo-generated charge carriers and to verify whether Sb, Li co-doping also enables an increased charge separation yield and prolong carriers lifetimes. However, this paper already lies the foundation for further utilisation of co-doping in other metal oxide semiconductors for photocatalysis and photoelectrocatalysis. I envision the final goal of having effective bulks by minimising the amount of doping. As it is demonstrated here, a way to do that can be the introduction of cations with different mechanisms for the performance improvement.

## 5.4 Additional investigations

### 5.4.1 Effect of oxygen vacancies

As underlined in [subsection 1.4.5](#), the presence of oxygen vacancies are intrinsic dopants for hematite. Hence, the photoactivity of hematite-based photoanodes can greatly benefit from their presence.<sup>379,380</sup> After introduction of  $V_O$ , hematite takes another formula, namely  $\alpha\text{-Fe}_2\text{O}_{3-x}$ . In light of the reported literature, the reasons for the photoactivity growth by means of  $V_O$  in hematite photoanodes are various and there is no much agreement.<sup>208,236,342,344,366,381,382</sup> Contemporaneously,  $V_O$  can also be detrimental for the photoanode performance.<sup>236,383,384</sup> Therefore, a  $V_O$  control or engineering is often the suggested option.<sup>342,385</sup>

In this sense, the supplementary project that accounts for **Figure 5-7a-j** is not well related to the control of  $V_O$ . In this subsection, the obtained results are a consequence of the utilisation of two different muffle ovens, albeit the same adopted parameters and identical samples. One small muffle oven is rather worn-out (**Figure 5-7a-b**) and is used to anneal what is referred to as Std sample, while the large muffle oven, better sealed and vigorous, is used for the sample referred to as Std ( $V_O$ ).



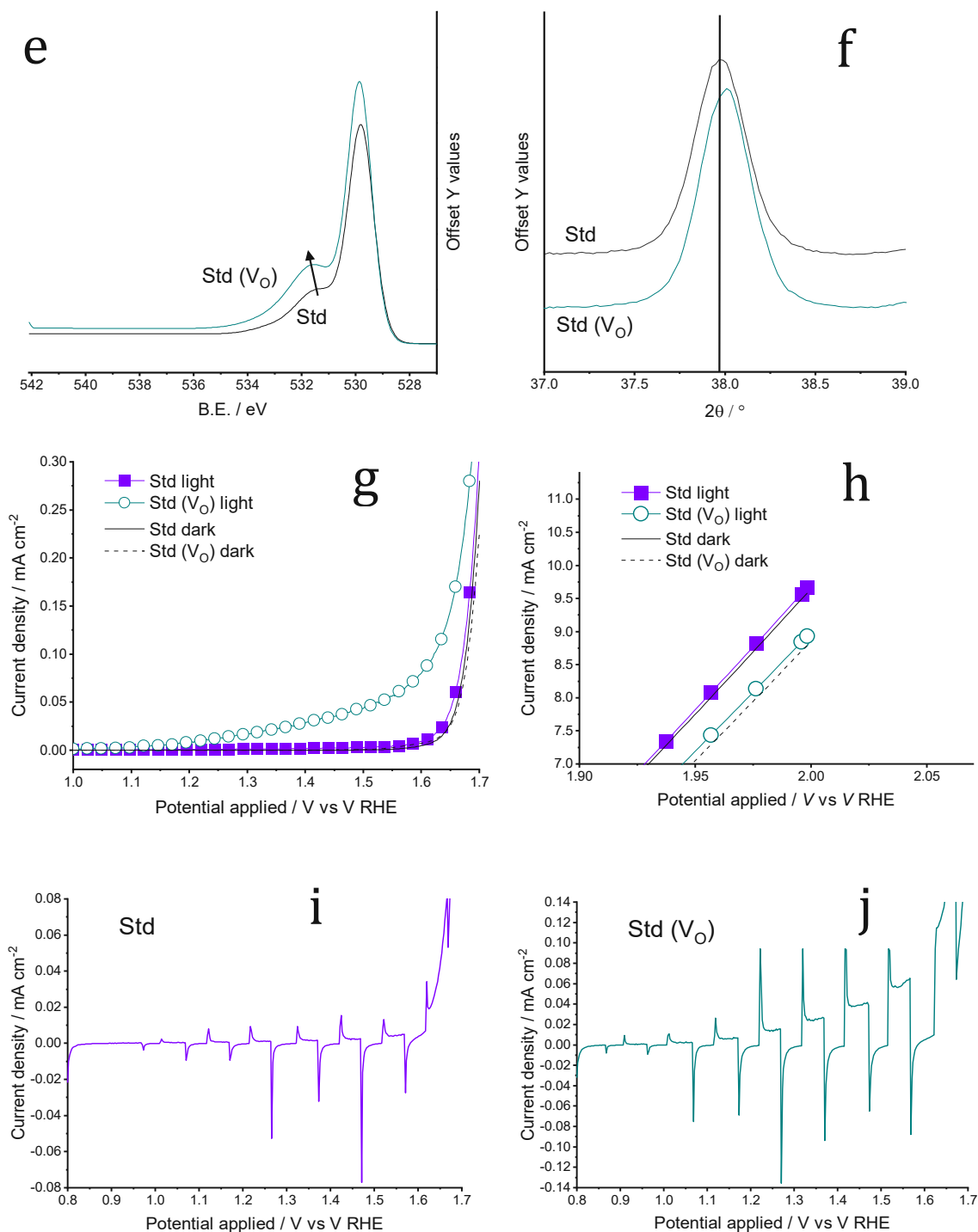


**Figure 5-7.** a) Detail of small oven fracture and glowing at extremely high T. b) Reported real temperature in the stove at a given set temperature. c) UV-Vis light absorption spectra of the hematite photoanodes standard sample, Std (solid line), and standard sample with higher amount of oxygen vacancies, Std (V<sub>o</sub>) (dotted line). d) Raman spectra of Std (violet) and Std (V<sub>o</sub>) (dark cyan) samples. e) XPS detail envelope spectra of O1s signal of Std and Std (V<sub>o</sub>). f) XRD patterns with focus on (110) peak of Std and Std (V<sub>o</sub>). g) *J-V* curves of Std and Std (V<sub>o</sub>) light and dark recorded in 0.1 M NaOH with calomel electrode and Pt cathode. Light curves were carried out under a simulated solar light illumination of 100 mW cm<sup>-2</sup>. h) Details of Std and Std (V<sub>o</sub>) light and dark current densities at high applied voltages (Faradaic regime). i) Light *J-V* curve of Std sample recorded by chopping the light illumination. j) Light *J-V* curve of Std (V<sub>o</sub>) sample recorded by chopping the light illumination.



By taking a closer look at **Figure 5-7c-j**, the sample is named exactly Std ( $V_0$ ), because it is anticipated a higher amount of oxygen vacancies ( $V_0$ ). First, the Std ( $V_0$ ) sample displays a grown UV-Vis absorption intensity than Std and it is published that  $V_0$  lead to a greater absorbance (**Figure 5-7c**).<sup>236</sup> In **Figure 5-7d**, both Raman spectra show a shoulder peak at 650  $\text{cm}^{-1}$ . As mentioned in [subsection 5.2.2](#), that is a forbidden  $E_u$  mode, which is allowed due to defects, such as grain boundaries in nanocrystals, defects, or a different phase such as magnetite. However, in this circumstance, it is not possible to analytically differentiate amongst the two materials. In fact, literature dealing with  $V_0$  in hematite rarely presents Raman spectra.<sup>208,222,342,379</sup> Here, it is likely that the amount of introduced oxygen vacancies is small and  $V_0$  signal hides behind the anyway abundant nanocrystals grain boundaries, which may give the main contribute to the  $E_u$  mode. Particularly owing to the little attention, another observation worth to be made concerns the two-phonon scattering peak at  $\sim 1300$   $\text{cm}^{-1}$ . The sample Std ( $V_0$ ) reaches its maximum at 1301.5  $\text{cm}^{-1}$ , while the Std one at 1304.1  $\text{cm}^{-1}$ . This could be due to a smaller size of the nanocrystals after  $V_0$  introduction.<sup>386</sup> It is also reported here the reduction of the intensity of the same peak for sample Std ( $V_0$ ) along with the left shift. Using the same correlation of [section 5.3](#), it is possible to immediately comment on Raman results. Albeit a surface analysis, XPS is a powerful technique to identify  $V_0$  in semiconductors such as hematite.<sup>235,236,342</sup> By presenting the spectrum envelope of the two samples (**Figure 5-7e**), it can be noticed that the peak assigned to Fe-O bonding expands and shifts left in Std ( $V_0$ ) compared to Std sample. This component of O1s signal is the one frequently ascribed to  $V_0$  alterations.<sup>236,366</sup> The degree of intensity variation and shift of the Fe-O peak is consistent with the Raman assumption, *i.e.*, that the introduction of  $V_0$  is of moderate proportions. Moreover, in Std ( $V_0$ ) sample XRD pattern, it can be observed a contraction of the crystal lattices, as the (110) peak moves to higher  $2\theta$  values (**Figure 5-7f**). Enhanced amount of  $V_0$  in semiconductors are coherent with such crystal parameters shrinkage. All of that reflects into the photoelectrochemical performance gauged with light  $J$ - $V$  curves, as seen in **Figure 5-7g**. The introduction of  $V_0$  improves the photoelectrochemistry of the hematite photoanode, at least at these described conditions. By contrast, in Faradaic regime, *i.e.*, when majority charge carriers prevail, the oxygen vacancies might work as obstacle or defect for the majority charge carrier conduction. This is a conjecture, which is complicated to compare with reported data as the main focus of hematite involves photoactivity at lowest applied  $V$ . Note, that the gap between light and dark  $J$ - $V$  at high applied  $V$  is still higher for Std ( $V_0$ ) than Std sample, a behaviour that once more highlights the ability of Std ( $V_0$ ) sample to translate absorbed photons into current. To get a first hint of how  $V_0$  influence the charge recombination, I measure light chopped  $J$ - $V$  curves and observe the produced current transients (see **Figure 5-7i-j**). As in [subsection](#)

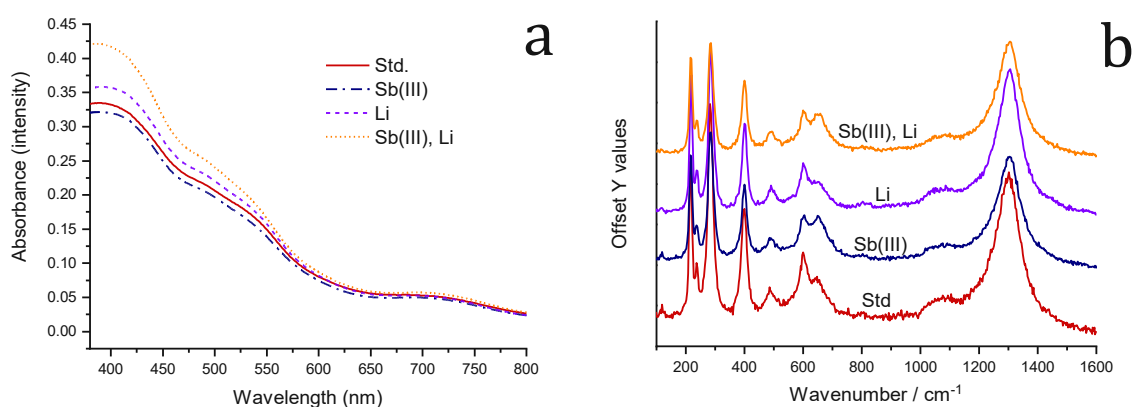


[5.2.5](#), the ratio spike/current density and fall/current density are the taken figures for comparison, called  $s/c$  and  $f/c$  for brevity. The Std sample displays 4.95 and 16.8 for the two ratios respectively, while Std ( $V_0$ ) sample presents 3.92 for both the ratios. Hence, charge recombination lowers with greater number of  $V_0$ . Furthermore, as positive current transient, ratio  $s/c$ , is more related to the interfacial charge transfer resistance, it means that  $V_0$  do not improve that dynamics substantially. On the other hand, as the negative current transient is usually assigned to the recombination between conduction band electrons and oxidised surface species (surface trapped holes too likely), <sup>222</sup> it implies the  $V_0$  minimise this recombination to give out higher photoactivity. Why this is so, it is another question that must be answered with further analyses, particularly with photoluminescence spectroscopy and *operando* techniques.<sup>206,222,345</sup>

## 5.4.2 Sb<sup>3+</sup> precursor and V<sub>0</sub>

In the previous subsection, I present a Std (V<sub>0</sub>) sample, which is annealed in a better sealed and more vigorous oven. All of this is part of my extensive investigation on *in-situ* Sb, Li co-doping in hematite photoanodes. Now, the prepared samples batch is synthesised with a less hydrolysable Sb precursor, SbCl<sub>3</sub>, which has been used elsewhere as *ex-situ* hematite dopant.<sup>232</sup>

As earlier said in subsection 5.3.1, the addition of dopants can grow the hematite films absorption intensity. In fact, in 5.5.1 subsection, the presence of a higher amount of VO is reason for a significant absorption intensity gain. Likely, the boost that the Std receives thanks to the VO is more prominent than the boost of a combination of Sb and VO (figure 5-8a). However, the Li-doped photoanodes, mono- and co-doped, display the typical behaviour observed before, i.e., the absorption intensity increments at wavelengths shorter than ~550 nm. Li cations may enable the formation of shallow and deep acceptor levels. In figure 5-8b, the situation is similar to the former one, subsection 5.3.2. Sb can be easily identified with the E<sub>u</sub> mode at ~650 cm<sup>-1</sup> and the attenuation of 2-phonon scattering also occurs. In Li mono-doped and the Std photoanode, there are no analytically relevant variations. With the usual focus on (110) peak, XRD analysis confirms the contraction/expansion assumption, namely Li cations are able to modify the lattice parameters appearing as an expansion (figure 5-8c). This is presumably owing to the interstitial nature of Li doping as Sb doping does not affect the crystal lattice parameters.



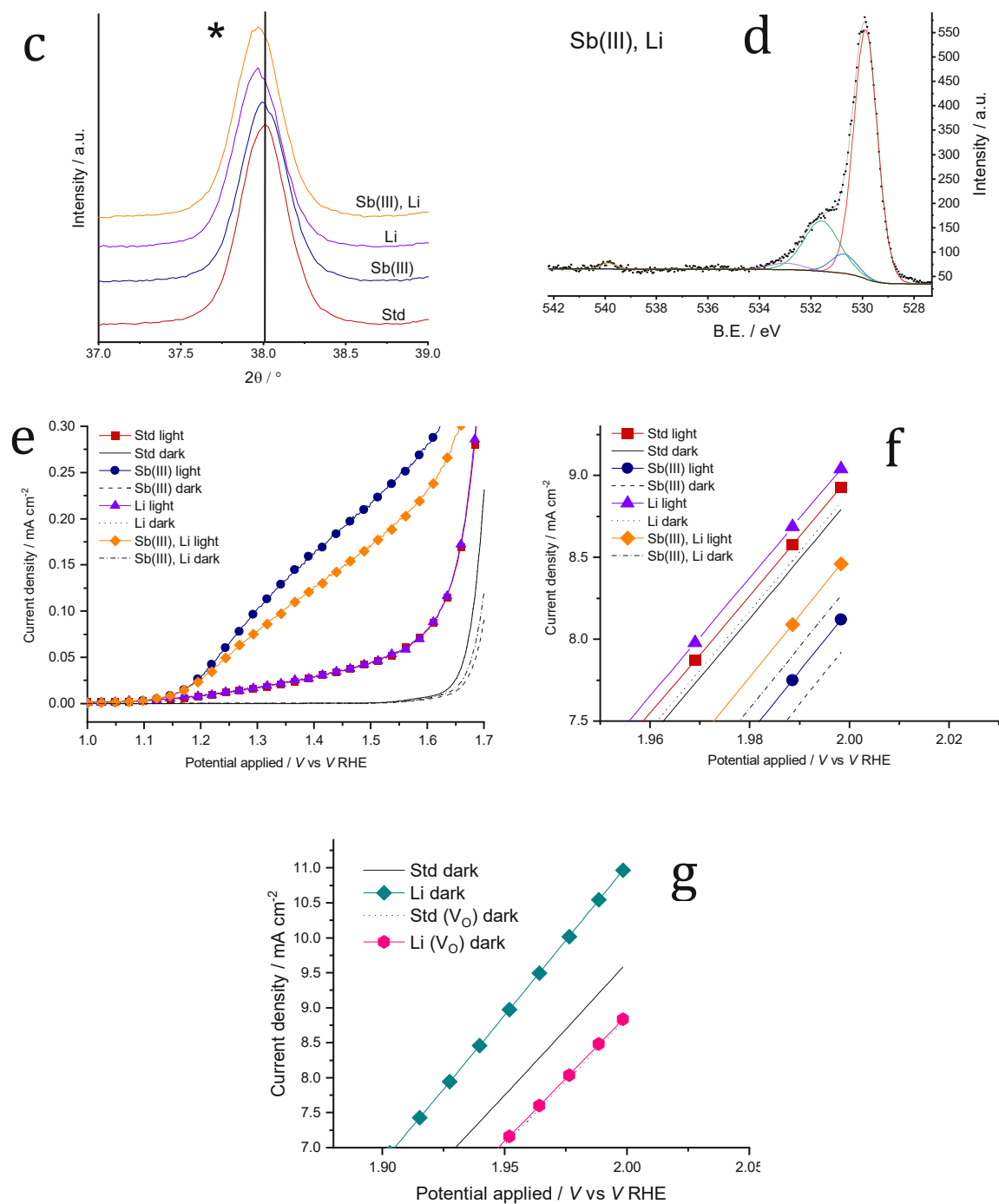


**Figure 5-8.** a) UV-Vis light absorption spectra of the hematite photoanodes, that is, Std (red solid line), Sb<sup>3+</sup> (blue dash dot), Li<sup>+</sup> (violet short dash), and Sb, Li (orange short dot). and standard sample with higher amount of oxygen vacancies, Std (V<sub>O</sub>) (dotted line). b) Micro-Raman spectra of compared photoanodes, Std (red), Sb<sup>3+</sup> (blue), Li<sup>+</sup> (violet), and Sb, Li (orange). c) Zoom-in of the XRD patterns of Sb(III)-batch samples on the (110) diffraction peak, range  $2\theta$  37.0-39.0°. d) O, Sb elements XPS detail spectrum of the Sb<sup>3+</sup>, Li<sup>+</sup> co-doped sample. e)  $J$ - $V$  curves light and dark recorded in 0.1 M NaOH with calomel electrode and Pt cathode. Light curves were carried out under a simulated solar light illumination of 100 mW cm<sup>-2</sup>. The sample performance under illumination are coloured, *i.e.*, Std (red), Sb<sup>3+</sup> (blue), Li<sup>+</sup> (violet), and Sb, Li (orange), while in the dark samples have thin black lines. f) Details of current densities at high applied voltages (Faradaic regime) in light and dark. g) Details of dark current densities of Std and Li<sup>+</sup> samples at high applied voltages (Faradaic regime) with high and low amount V<sub>O</sub>.

In **Figure 5-8d**, the peaks at BE  $\sim 540$  eV is already a strong hint of the Sb occurrence and its only oxidation state 5+. This result is supported by literature, as highlighted in the former XPS subsections. In this subsection, the Std is practically the Std ( $V_0$ ) sample presented earlier, and indeed its light  $J$ - $V$  curve shows a relevant photoactivity (**Figure 5-8e**). On the contrary, the  $\text{Li}^+$  mono-doping looks in these terms negligible, moreover, in the co-doped photoanode, its addition is detrimental. Interestingly, also in  $J$ - $V$  curves at high  $V$  (Faradaic regime),  $\text{Li}^+$  doping does not increase the Std performance significantly and it moderately enhances Sb doping. To give a clearer picture of the  $\text{Li}^+$  effect on the Std in presence of  $V_0$ , it is plotted figure **Figure 5-8e** too. There, with dark Faradaic  $J$ - $V$  curves of the samples, the intention is to illustrate the gap dissimilarities within the batches, one carrying many  $V_0$  and the other carrying it few. It is published that  $\text{Li}^+$  should principally increase the majority charge carriers and that  $V_0$  is ascribed by literature for many good actions in hematite photoanodes. This can be an issue because  $V_0$  do not take a precise role. So far, the hypotheses that can be formulated are mainly two, *i.e.*, that  $V_0$  and  $\text{Li}^+$  ions are both competing to increase the charge carrier conductivity with even an overlapping role, or the more bizarre conjecture, that  $V_0$  can partially trap the small and interstitial  $\text{Li}^+$  cations. Finally, experiments with  $V_0$  control would be necessary to complete the study. With such a mastery and a bulk spectroscopic method, any divergent effects because of Sb(III) and Sb(V) precursors should come out.

### 5.4.3 Li<sup>+</sup> leaching experiments

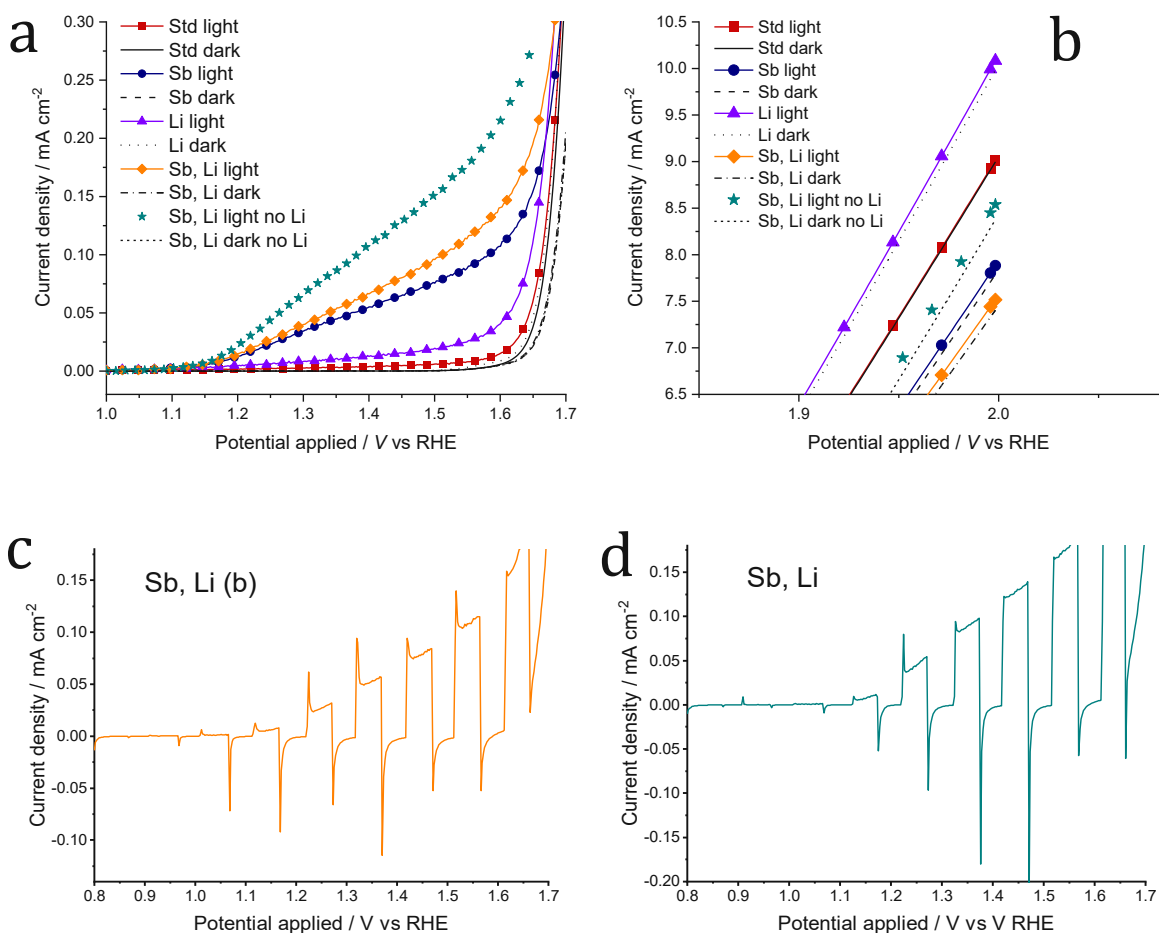


**Figure 5-9.** a)  $J$ - $V$  curves light and dark recorded in 0.1 M NaOH and 0.01 M LiCl with calomel electrode and Pt cathode. Light curves were carried out under a simulated solar light illumination of 100 mW cm<sup>-2</sup>. The sample performance under illumination and Li-buffered are coloured, *i.e.*, Std (red), Sb<sup>3+</sup> (blue), Li<sup>+</sup> (violet), and Sb, Li (orange), while in the dark samples have thin black lines. Sb, Li sample measured in electrolyte 0.1 M NaOH for comparison has dark green line. b) Details of current densities at high applied voltages (Faradaic regime) in light and dark in Li-buffered electrolyte and non-buffered. c) Light  $J$ - $V$  curve of Sb, Li sample in Li-buffered electrolyte recorded by chopping the light illumination. d) Light  $J$ - $V$  curve of Sb, Li sample in non-buffered electrolyte recorded by chopping the light illumination.

Leaching experiments are carried out to exclude the hypothesis that Li<sup>+</sup> small and interstitial dopant could leach out of the photoanode, in particular during the operation.

After adding LiCl to a final 0.01 M concentration into the usual NaOH 0.1 M electrolyte, it is measured one more time the samples of [Chapter 5](#). As a result, the trend is maintained while the photoactivity is generally lower (**figure 5-10a**). The gauged photocurrent at 1.4 V vs RHE goes from 0.11 to 0.07 mA cm<sup>-2</sup>, which translates into a 1.6-fold or a 36% relative reduction. In Faradaic regime, it is still noticeable a general decrease, which is represented

by the gap amongst stars and tilted squares (**figure 5-11a**). Also, the gap between Li<sup>+</sup> monodoped and Std decreases, not reaching anymore  $\sim 1.5 \text{ mA cm}^{-2}$ , but stopping at  $\sim 1.0 \text{ mA cm}^{-2}$ . By comparing the chopped J-V light curves in **Figure 5-12c** and d, s/c and f/c ratios both augment with Li<sup>+</sup> buffering. The most prominent growth is the s/c ratio 1.10 to 1.81, whereas the f/c ratio raises 2.00 to 2.21. The former one indicates a clear increase in recombination between CB electrons with surface holes (trapped or in form of oxidised species). The latter one suggests a moderately lower charge transfer efficiency at the interface. Furthermore, it must be said that the photoanodes might experience an aging, which is up to now uncertain, as aging experiments are yet to be planned.

## Bibliography

- (1) Roser, M.; Ortiz-Ospina, E. Global Education. *Our World Data* **2016**.
- (2) Roser, M.; Ortiz-Ospina, E.; Ritchie, H. Life Expectancy. *Our World Data* **2013**.
- (3) Roser, M.; Ritchie, H.; Dadonaite, B. Child and Infant Mortality. *Our World Data* **2013**.
- (4) *Energy Production and Consumption*. Our World in Data.  
<https://ourworldindata.org/energy-production-consumption> (accessed 2021-01-12).
- (5) Ritchie, H.; Roser, M. Access to Energy. *Our World Data* **2019**.
- (6) *World Population Prospects - Population Division - United Nations*.  
<https://population.un.org/wpp/> (accessed 2021-01-13).
- (7) WHO | *Fuel for life: household energy and health*. WHO.  
<http://www.who.int/indoorair/publications/fuelforlife/en/> (accessed 2021-02-08).
- (8) *A European Green Deal*. European Commission - European Commission.  
[https://ec.europa.eu/info/strategy/priorities-2019-2024/european-green-deal\\_en](https://ec.europa.eu/info/strategy/priorities-2019-2024/european-green-deal_en) (accessed 2021-02-08).
- (9) *Air pollution* — European Environment Agency. <https://www.eea.europa.eu/themes/air> (accessed 2021-01-14).
- (10) *Update of WHO Global Air Quality Guidelines*. <https://www.euro.who.int/en/health-topics/environment-and-health/air-quality/activities/update-of-who-global-air-quality-guidelines> (accessed 2021-02-08).
- (11) *Exceedance of air quality standards in Europe* — European Environment Agency.  
<https://www.eea.europa.eu/data-and-maps/indicators/exceedance-of-air-quality-limit-2/assessment> (accessed 2021-02-08).
- (12) *Sources of air pollution in Europe* — European Environment Agency.  
<https://www.eea.europa.eu/signals/signals-2013/infographics/sources-of-air-pollution-in-europe/view> (accessed 2021-02-08).
- (13) US EPA, O. *Criteria Air Pollutants*. US EPA. <https://www.epa.gov/criteria-air-pollutants> (accessed 2021-02-08).
- (14) *Air pollution*. <https://www.who.int/westernpacific/health-topics/air-pollution> (accessed 2021-02-08).
- (15) US EPA, O. *Research on Health Effects from Air Pollution*. US EPA.  
<https://www.epa.gov/air-research/research-health-effects-air-pollution> (accessed 2021-01-14).
- (16) *Air pollution: how it affects our health* — European Environment Agency.  
<https://www.eea.europa.eu/themes/air/health-impacts-of-air-pollution> (accessed 2021-02-08).
- (17) *The Paris Agreement* | UNFCCC. <https://unfccc.int/process-and-meetings/the-paris-agreement/the-paris-agreement> (accessed 2021-02-08).
- (18) Together We Can Move Forwards: Building a Sustainable Planet after the Corona Shock — European Environment Agency.
- (19) Organization, W. H. Laboratory Testing Strategy Recommendations for COVID-19: Interim Guidance, 21 March 2020. **2020**.
- (20) Mak, G. C.; Cheng, P. K.; Lau, S. S.; Wong, K. K.; Lau, C.; Lam, E. T.; Chan, R. C.; Tsang, D. N. Evaluation of Rapid Antigen Test for Detection of SARS-CoV-2 Virus. *J. Clin. Virol.* **2020**, *129*, 104500. <https://doi.org/10.1016/j.jcv.2020.104500>.
- (21) Moncrieff, R. W. *The Chemical Senses*; The chemical senses; Wiley: Oxford, England, 1946.
- (22) Kim, T. H.; Lee, S. H.; Lee, J.; Song, H. S.; Oh, E. H.; Park, T. H.; Hong, S. Single-Carbon-Atomic-Resolution Detection of Odorant Molecules Using a Human Olfactory Receptor-

Based Bioelectronic Nose. *Adv. Mater.* **2009**, *21* (1), 91–94.

<https://doi.org/10.1002/adma.200801435>.

(23) Park, S. J.; Kwon, O. S.; Lee, S. H.; Song, H. S.; Park, T. H.; Jang, J. Ultrasensitive Flexible Graphene Based Field-Effect Transistor (FET)-Type Bioelectronic Nose. *Nano Lett.* **2012**, *12* (10), 5082–5090. <https://doi.org/10.1021/nl301714x>.

(24) Lee, S. H.; Oh, E. H.; Park, T. H. Cell-Based Microfluidic Platform for Mimicking Human Olfactory System. *Biosens. Bioelectron.* **2015**, *74*, 554–561. <https://doi.org/10.1016/j.bios.2015.06.072>.

(25) Larisika, M.; Kotlowski, C.; Steininger, C.; Mastrogiacomo, R.; Pelosi, P.; Schütz, S.; Peteu, S. F.; Kleber, C.; Reiner-Rozman, C.; Nowak, C.; Knoll, W. Electronic Olfactory Sensor Based on A. Mellifera Odorant-Binding Protein 14 on a Reduced Graphene Oxide Field-Effect Transistor. *Angew. Chem.* **2015**, *127* (45), 13443–13446. <https://doi.org/10.1002/ange.201505712>.

(26) Reiner-Rozman, C.; Larisika, M.; Nowak, C.; Knoll, W. Graphene-Based Liquid-Gated Field Effect Transistor for Biosensing: Theory and Experiments. *Biosens. Bioelectron.* **2015**, *70* (Supplement C), 21–27. <https://doi.org/10.1016/j.bios.2015.03.013>.

(27) Baller, M. K.; Lang, H. P.; Fritz, J.; Gerber, C.; Gimzewski, J. K.; Drechsler, U.; Rothuizen, H.; Despont, M.; Vettiger, P.; Battiston, F. M.; Ramseyer, J. P.; Fornaro, P.; Meyer, E.; Güntherodt, H.-J. A Cantilever Array-Based Artificial Nose. *Ultramicroscopy* **2000**, *82* (1), 1–9. [https://doi.org/10.1016/S0304-3991\(99\)00123-0](https://doi.org/10.1016/S0304-3991(99)00123-0).

(28) Lang, H. P.; Baller, M. K.; Berger, R.; Gerber, C.; Gimzewski, J. K.; Battiston, F. M.; Fornaro, P.; Ramseyer, J. P.; Meyer, E.; Güntherodt, H. J. An Artificial Nose Based on a Micromechanical Cantilever Array. *Anal. Chim. Acta* **1999**, *393* (1), 59–65. [https://doi.org/10.1016/S0003-2670\(99\)00283-4](https://doi.org/10.1016/S0003-2670(99)00283-4).

(29) Fitzgerald, J. E.; Bui, E. T. H.; Simon, N. M.; Fenniri, H. Artificial Nose Technology: Status and Prospects in Diagnostics. *Trends Biotechnol.* **2017**, *35* (1), 33–42. <https://doi.org/10.1016/j.tibtech.2016.08.005>.

(30) Wasilewski, T.; Gębicki, J.; Kamysz, W. Bioelectronic Nose: Current Status and Perspectives. *Biosens. Bioelectron.* **2017**, *87*, 480–494. <https://doi.org/10.1016/j.bios.2016.08.080>.

(31) Liu, Q.; Cai, H.; Xu, Y.; Li, Y.; Li, R.; Wang, P. Olfactory Cell-Based Biosensor: A First Step towards a Neurochip of Bioelectronic Nose. *Biosens. Bioelectron.* **2006**, *22* (2), 318–322. <https://doi.org/10.1016/j.bios.2006.01.016>.

(32) Son, M.; Lee, J. Y.; Ko, H. J.; Park, T. H. Bioelectronic Nose: An Emerging Tool for Odor Standardization. *Trends Biotechnol.* **2017**, *35* (4), 301–307. <https://doi.org/10.1016/j.tibtech.2016.12.007>.

(33) *Smell Sensing 2.0 - Towards an Electronic Nose (Fast Forward Science 2017)*; 2017.

(34) *A Biomimetic Smell Sensor | Johannes Binting | TEDxKlagenfurt*; 2018.

(35) Pumera, M. Graphene in Biosensing. *Mater. Today* **2011**, *14* (7), 308–315. [https://doi.org/10.1016/S1369-7021\(11\)70160-2](https://doi.org/10.1016/S1369-7021(11)70160-2).

(36) R. Dreyer, D.; Park, S.; W. Bielawski, C.; S. Ruoff, R. The Chemistry of Graphene Oxide. *Chem. Soc. Rev.* **2010**, *39* (1), 228–240. <https://doi.org/10.1039/B917103G>.

(37) Sohn, I.-Y.; Kim, D.-J.; Jung, J.-H.; Yoon, O. J.; Nguyen Thanh, T.; Tran Quang, T.; Lee, N.-E. PH Sensing Characteristics and Biosensing Application of Solution-Gated Reduced Graphene Oxide Field-Effect Transistors. *Biosens. Bioelectron.* **2013**, *45*, 70–76. <https://doi.org/10.1016/j.bios.2013.01.051>.

(38) Bai, S.; Chen, S.; Shen, X.; Zhu, G.; Wang, G. Nanocomposites of Hematite ( $\alpha$ -Fe<sub>2</sub>O<sub>3</sub>) Nanospindles with Crumpled Reduced Graphene Oxide Nanosheets as High-Performance Anode



- Material for Lithium-Ion Batteries. *RSC Adv.* **2012**, *2* (29), 10977–10984.  
<https://doi.org/10.1039/C2RA21411C>.
- (39) Flouda, P.; Feng, X.; Boyd, J. G.; Thomas, E. L.; Lagoudas, D. C.; Lutkenhaus, J. L. Interfacial Engineering of Reduced Graphene Oxide for Aramid Nanofiber-Enabled Structural Supercapacitors. *Batter. Supercaps* **2019**, *2* (5), 464–472. <https://doi.org/10.1002/batt.201800137>.
- (40) Lee, B.; Koo, M. Y.; Jin, S. H.; Kim, K. T.; Hong, S. H. Simultaneous Strengthening and Toughening of Reduced Graphene Oxide/Alumina Composites Fabricated by Molecular-Level Mixing Process. *Carbon* **2014**, *78*, 212–219. <https://doi.org/10.1016/j.carbon.2014.06.074>.
- (41) Tarcan, R.; Todor-Boer, O.; Petrovai, I.; Leordean, C.; Astilean, S.; Botiz, I. Reduced Graphene Oxide Today. *J. Mater. Chem. C* **2020**, *8* (4), 1198–1224.  
<https://doi.org/10.1039/C9TC04916A>.
- (42) Brodie, B. C. XIII. On the Atomic Weight of Graphite. *Philos. Trans. R. Soc. Lond.* **1859**, *149*, 249–259. <https://doi.org/10.1098/rstl.1859.0013>.
- (43) Staudenmaier, L. Verfahren Zur Darstellung Der Graphitsäure. *Berichte Dtsch. Chem. Ges.* **1898**, *31* (2), 1481–1487. <https://doi.org/10.1002/cber.18980310237>.
- (44) Hummers, W. S.; Offeman, R. E. Preparation of Graphitic Oxide. *J. Am. Chem. Soc.* **1958**, *80* (6), 1339–1339. <https://doi.org/10.1021/ja01539a017>.
- (45) Novoselov, K. S.; Geim, A. K.; Morozov, S. V.; Jiang, D.; Zhang, Y.; Dubonos, S. V.; Grigorieva, I. V.; Firsov, A. A. Electric Field Effect in Atomically Thin Carbon Films. *Science* **2004**, *306* (5696), 666–669. <https://doi.org/10.1126/science.1102896>.
- (46) Geim, A. K.; Novoselov, K. S. The Rise of Graphene. *Nat. Mater.* **2007**, *6* (3), 183–191.  
<https://doi.org/10.1038/nmat1849>.
- (47) Gerstner, E. Nobel Prize 2010: Andre Geim & Konstantin Novoselov. *Nat. Phys.* **2010**, *6* (11), 836–836. <https://doi.org/10.1038/nphys1836>.
- (48) Mermin, N. D. Crystalline Order in Two Dimensions. *Phys. Rev.* **1968**, *176* (1), 250–254.  
<https://doi.org/10.1103/PhysRev.176.250>.
- (49) Venables, J. A.; Spiller, G. D. T. Nucleation and Growth of Thin Films. In *Surface Mobilities on Solid Materials: Fundamental Concepts and Applications*; Binh, V. T., Ed.; NATO Advanced Science Institutes Series; Springer US: Boston, MA, 1983; pp 341–404.  
[https://doi.org/10.1007/978-1-4684-4343-1\\_16](https://doi.org/10.1007/978-1-4684-4343-1_16).
- (50) Ataca, C.; Şahin, H.; Ciraci, S. Stable, Single-Layer MX<sub>2</sub> Transition-Metal Oxides and Dichalcogenides in a Honeycomb-Like Structure. *J. Phys. Chem. C* **2012**, *116* (16), 8983–8999.  
<https://doi.org/10.1021/jp212558p>.
- (51) Zhou, W.; Zou, X.; Najmaei, S.; Liu, Z.; Shi, Y.; Kong, J.; Lou, J.; Ajayan, P. M.; Yakobson, B. I.; Idrobo, J.-C. Intrinsic Structural Defects in Monolayer Molybdenum Disulfide. *Nano Lett.* **2013**, *13* (6), 2615–2622. <https://doi.org/10.1021/nl4007479>.
- (52) Huang, J.-K.; Pu, J.; Hsu, C.-L.; Chiu, M.-H.; Juang, Z.-Y.; Chang, Y.-H.; Chang, W.-H.; Iwasa, Y.; Takenobu, T.; Li, L.-J. Large-Area Synthesis of Highly Crystalline WSe<sub>2</sub> Monolayers and Device Applications. *ACS Nano* **2014**, *8* (1), 923–930. <https://doi.org/10.1021/nn405719x>.
- (53) Liu, H.; Neal, A. T.; Zhu, Z.; Luo, Z.; Xu, X.; Tománek, D.; Ye, P. D. Phosphorene: An Unexplored 2D Semiconductor with a High Hole Mobility. *ACS Nano* **2014**, *8* (4), 4033–4041.  
<https://doi.org/10.1021/nn501226z>.
- (54) Li, X.; Cai, W.; An, J.; Kim, S.; Nah, J.; Yang, D.; Piner, R.; Velamakanni, A.; Jung, I.; Tutuc, E.; Banerjee, S. K.; Colombo, L.; Ruoff, R. S. Large-Area Synthesis of High-Quality and Uniform Graphene Films on Copper Foils. *Science* **2009**, *324* (5932), 1312–1314.  
<https://doi.org/10.1126/science.1171245>.

- (55) Ambrosi, A.; Pumera, M. The CVD Graphene Transfer Procedure Introduces Metallic Impurities Which Alter the Graphene Electrochemical Properties. *Nanoscale* **2014**, *6* (1), 472–476. <https://doi.org/10.1039/C3NR05230C>.
- (56) Yang, X.; Yan, M. Removing Contaminants from Transferred CVD Graphene. *Nano Res.* **2020**, *13* (3), 599–610. <https://doi.org/10.1007/s12274-020-2671-6>.
- (57) Lotya, M.; King, P. J.; Khan, U.; De, S.; Coleman, J. N. High-Concentration, Surfactant-Stabilized Graphene Dispersions. *ACS Nano* **2010**, *4* (6), 3155–3162. <https://doi.org/10.1021/nn1005304>.
- (58) Park, S.; An, J.; Piner, R. D.; Jung, I.; Yang, D.; Velamakanni, A.; Nguyen, S. T.; Ruoff, R. S. Aqueous Suspension and Characterization of Chemically Modified Graphene Sheets. *Chem. Mater.* **2008**, *20* (21), 6592–6594. <https://doi.org/10.1021/cm801932u>.
- (59) Stankovich, S.; D. Piner, R.; Chen, X.; Wu, N.; T. Nguyen, S.; S. Ruoff, R. Stable Aqueous Dispersions of Graphitic Nanoplatelets via the Reduction of Exfoliated Graphite Oxide in the Presence of Poly(Sodium 4-Styrenesulfonate). *J. Mater. Chem.* **2006**, *16* (2), 155–158. <https://doi.org/10.1039/B512799H>.
- (60) Eda, G.; Fanchini, G.; Chhowalla, M. Large-Area Ultrathin Films of Reduced Graphene Oxide as a Transparent and Flexible Electronic Material. *Nat. Nanotechnol.* **2008**, *3* (5), 270–274. <https://doi.org/10.1038/nnano.2008.83>.
- (61) Wan, Y.-J.; Tang, L.-C.; Gong, L.-X.; Yan, D.; Li, Y.-B.; Wu, L.-B.; Jiang, J.-X.; Lai, G.-Q. Grafting of Epoxy Chains onto Graphene Oxide for Epoxy Composites with Improved Mechanical and Thermal Properties. *Carbon* **2014**, *69*, 467–480. <https://doi.org/10.1016/j.carbon.2013.12.050>.
- (62) Yang, H.; Li, F.; Shan, C.; Han, D.; Zhang, Q.; Niu, L.; Ivaska, A. Covalent Functionalization of Chemically Converted Graphene Sheets via Silane and Its Reinforcement. *J. Mater. Chem.* **2009**, *19* (26), 4632–4638. <https://doi.org/10.1039/B901421G>.
- (63) Xu, L. Q.; Yang, W. J.; Neoh, K.-G.; Kang, E.-T.; Fu, G. D. Dopamine-Induced Reduction and Functionalization of Graphene Oxide Nanosheets. *Macromolecules* **2010**, *43* (20), 8336–8339. <https://doi.org/10.1021/ma101526k>.
- (64) Feicht, P.; Eigler, S. Defects in Graphene Oxide as Structural Motifs. *ChemNanoMat* **2018**, *4* (3), 244–252. <https://doi.org/10.1002/cnma.201700357>.
- (65) J. Cote, L.; Kim, J.; Zhang, Z.; Sun, C.; Huang, J. Tunable Assembly of Graphene Oxide Surfactant Sheets: Wrinkles, Overlaps and Impacts on Thin Film Properties. *Soft Matter* **2010**, *6* (24), 6096–6101. <https://doi.org/10.1039/C0SM00667J>.
- (66) Zhang, C.; Dabbs, D. M.; Liu, L.-M.; Aksay, I. A.; Car, R.; Selloni, A. Combined Effects of Functional Groups, Lattice Defects, and Edges in the Infrared Spectra of Graphene Oxide. *J. Phys. Chem. C* **2015**, *119* (32), 18167–18176. <https://doi.org/10.1021/acs.jpcc.5b02727>.
- (67) Park, S.; Ruoff, R. S. Chemical Methods for the Production of Graphenes. *Nat. Nanotechnol.* **2009**, *4* (4), 217–224. <https://doi.org/10.1038/nnano.2009.58>.
- (68) Gómez-Navarro, C.; Meyer, J. C.; Sundaram, R. S.; Chuvilin, A.; Kurasch, S.; Burghard, M.; Kern, K.; Kaiser, U. Atomic Structure of Reduced Graphene Oxide. *Nano Lett.* **2010**, *10* (4), 1144–1148. <https://doi.org/10.1021/nl9031617>.
- (69) Rozada, R.; I. Paredes, J.; J. López, M.; Villar-Rodil, S.; Cabria, I.; A. Alonso, J.; Martínez-Alonso, A.; D. Tascón, J. M. From Graphene Oxide to Pristine Graphene: Revealing the Inner Workings of the Full Structural Restoration. *Nanoscale* **2015**, *7* (6), 2374–2390. <https://doi.org/10.1039/C4NR05816J>.
- (70) Banhart, F.; Kotakoski, J.; Krasheninnikov, A. V. Structural Defects in Graphene. *ACS Nano* **2011**, *5* (1), 26–41. <https://doi.org/10.1021/nn102598m>.

- (71) Boukhvalov, D. W.; Katsnelson, M. I. Chemical Functionalization of Graphene with Defects. *Nano Lett.* **2008**, *8* (12), 4373–4379. <https://doi.org/10.1021/nl802234n>.
- (72) Kumar, B.; Min, K.; Bashirzadeh, M.; Farimani, A. B.; Bae, M.-H.; Estrada, D.; Kim, Y. D.; Yasaei, P.; Park, Y. D.; Pop, E.; Aluru, N. R.; Salehi-Khojin, A. The Role of External Defects in Chemical Sensing of Graphene Field-Effect Transistors. *Nano Lett.* **2013**, *13* (5), 1962–1968. <https://doi.org/10.1021/nl304734g>.
- (73) Chen, J.; Zhang, Y.; Zhang, M.; Yao, B.; Li, Y.; Huang, L.; Li, C.; Shi, G. Water-Enhanced Oxidation of Graphite to Graphene Oxide with Controlled Species of Oxygenated Groups. *Chem. Sci.* **2016**, *7* (3), 1874–1881. <https://doi.org/10.1039/C5SC03828F>.
- (74) Chang, H.; Sun, Z.; Saito, M.; Yuan, Q.; Zhang, H.; Li, J.; Wang, Z.; Fujita, T.; Ding, F.; Zheng, Z.; Yan, F.; Wu, H.; Chen, M.; Ikuhara, Y. Regulating Infrared Photoresponses in Reduced Graphene Oxide Phototransistors by Defect and Atomic Structure Control. *ACS Nano* **2013**, *7* (7), 6310–6320. <https://doi.org/10.1021/nn4023679>.
- (75) Chen, D.; Feng, H.; Li, J. Graphene Oxide: Preparation, Functionalization, and Electrochemical Applications. *Chem. Rev.* **2012**, *112* (11), 6027–6053. <https://doi.org/10.1021/cr300115g>.
- (76) Hofmann, U.; König, E. Untersuchungen über Graphitoxyd. *Z. Für Anorg. Allg. Chem.* **1937**, *234* (4), 311–336. <https://doi.org/10.1002/zaac.19372340405>.
- (77) Boehm, H. P.; Clauss, A.; Fischer, G. O.; Hofmann, U. Dünne Kohlenstoff-Folien. *Z. Für Naturforschung B* **1962**, *17* (3), 150–153. <https://doi.org/10.1515/znb-1962-0302>.
- (78) Sun, Z.; Hu, Y. H. Ultrafast, Low-Cost, and Mass Production of High-Quality Graphene. *Angew. Chem. Int. Ed.* **2020**, *59* (24), 9232–9234. <https://doi.org/10.1002/anie.202002256>.
- (79) Zhu, Y.; Ji, H.; Cheng, H.-M.; Ruoff, R. S. Mass Production and Industrial Applications of Graphene Materials. *Natl. Sci. Rev.* **2018**, *5* (1), 90–101. <https://doi.org/10.1093/nsr/nwx055>.
- (80) *Simultaneous Electrochemical Reduction and Delamination of Graphene Oxide Films* | *ACS Nano*. <https://pubs.acs.org/doi/abs/10.1021/acsnano.5b03814> (accessed 2022-04-19).
- (81) Hirata, M.; Gotou, T.; Horiuchi, S.; Fujiwara, M.; Ohba, M. Thin-Film Particles of Graphite Oxide 1:: High-Yield Synthesis and Flexibility of the Particles. *Carbon* **2004**, *42* (14), 2929–2937. <https://doi.org/10.1016/j.carbon.2004.07.003>.
- (82) Chua, C. K.; Sofer, Z.; Pumera, M. Graphite Oxides: Effects of Permanganate and Chlorate Oxidants on the Oxygen Composition. *Chem. – Eur. J.* **2012**, *18* (42), 13453–13459. <https://doi.org/10.1002/chem.201202320>.
- (83) Dreyer, D. R.; Todd, A. D.; Bielawski, C. W. Harnessing the Chemistry of Graphene Oxide. *Chem. Soc. Rev.* **2014**, *43* (15), 5288–5301. <https://doi.org/10.1039/C4CS00060A>.
- (84) Wissler, M. Graphite and Carbon Powders for Electrochemical Applications. *J. Power Sources* **2006**, *156* (2), 142–150. <https://doi.org/10.1016/j.jpowsour.2006.02.064>.
- (85) Ding, S. F.; Niu, Y. P. Research on Purification Technics of Some Flake Graphite. *Adv. Mater. Res.* **2013**, *753–755*, 119–123. <https://doi.org/10.4028/www.scientific.net/AMR.753-755.119>.
- (86) Jara, A. D.; Kim, J. Y. Chemical Purification Processes of the Natural Crystalline Flake Graphite for Li-Ion Battery Anodes. *Mater. Today Commun.* **2020**, *25*, 101437. <https://doi.org/10.1016/j.mtcomm.2020.101437>.
- (87) Szabó, T.; Szeri, A.; Dékány, I. Composite Graphitic Nanolayers Prepared by Self-Assembly between Finely Dispersed Graphite Oxide and a Cationic Polymer. *Carbon* **2005**, *43* (1), 87–94. <https://doi.org/10.1016/j.carbon.2004.08.025>.

- (88) Paredes, J. I.; Villar-Rodil, S.; Martínez-Alonso, A.; Tascón, J. M. D. Graphene Oxide Dispersions in Organic Solvents. *Langmuir* **2008**, *24* (19), 10560–10564. <https://doi.org/10.1021/la801744a>.
- (89) You, S.; Luzan, S. M.; Szabó, T.; Talyzin, A. V. Effect of Synthesis Method on Solvation and Exfoliation of Graphite Oxide. *Carbon* **2013**, *52*, 171–180. <https://doi.org/10.1016/j.carbon.2012.09.018>.
- (90) Szabó, T.; Berkesi, O.; Forgó, P.; Josepovits, K.; Sanakis, Y.; Petridis, D.; Dékány, I. Evolution of Surface Functional Groups in a Series of Progressively Oxidized Graphite Oxides. *Chem. Mater.* **2006**, *18* (11), 2740–2749. <https://doi.org/10.1021/cm060258+>.
- (91) Yu, H.; Zhang, B.; Bulin, C.; Li, R.; Xing, R. High-Efficient Synthesis of Graphene Oxide Based on Improved Hummers Method. *Sci. Rep.* **2016**, *6* (1), 36143. <https://doi.org/10.1038/srep36143>.
- (92) Lu, W.; Birmingham, B.; Voronine, D. V.; Stolpman, D.; Ambardar, S.; Altunoz Erdogan, D.; Ozensoy, E.; Zhang, Z.; Solouki, T. From Aluminum Foil to Two-Dimensional Nanocrystals Using Ultrasonic Exfoliation. *J. Phys. Chem. C* **2021**, *125* (14), 7746–7755. <https://doi.org/10.1021/acs.jpcc.0c10935>.
- (93) Munonde, T. S.; Zheng, H.; Nomngongo, P. N. Ultrasonic Exfoliation of NiFe LDH/CB Nanosheets for Enhanced Oxygen Evolution Catalysis. *Ultrason. Sonochem.* **2019**, *59*, 104716. <https://doi.org/10.1016/j.ultsonch.2019.104716>.
- (94) Štengl, V.; Henych, J.; Slušná, M.; Ecorchard, P. Ultrasound Exfoliation of Inorganic Analogues of Graphene. *Nanoscale Res. Lett.* **2014**, *9* (1), 167. <https://doi.org/10.1186/1556-276X-9-167>.
- (95) Mellado, C.; Figueroa, T.; Baez, R.; Meléndrez, M.; Fernández, K. Effects of Probe and Bath Ultrasonic Treatments on Graphene Oxide Structure. *Mater. Today Chem.* **2019**, *13*, 1–7. <https://doi.org/10.1016/j.mtchem.2019.04.006>.
- (96) Le, G. T. T.; Chanlek, N.; Manyam, J.; Opaprakasit, P.; Grisdanurak, N.; Sreearunothai, P. Insight into the Ultrasonication of Graphene Oxide with Strong Changes in Its Properties and Performance for Adsorption Applications. *Chem. Eng. J.* **2019**, *373*, 1212–1222. <https://doi.org/10.1016/j.cej.2019.05.108>.
- (97) Matsuura, K.; Umahara, Y.; Gotoh, K.; Hoshijima, Y.; Ishida, H. Surface Modification Effects on the Tensile Properties of Functionalised Graphene Oxide Epoxy Films. *RSC Adv.* **2018**, *8* (18), 9677–9684. <https://doi.org/10.1039/C8RA00252E>.
- (98) Marcano, D. C.; Kosynkin, D. V.; Berlin, J. M.; Sinitskii, A.; Sun, Z.; Slesarev, A.; Alemany, L. B.; Lu, W.; Tour, J. M. Improved Synthesis of Graphene Oxide. *ACS Nano* **2010**, *4* (8), 4806–4814. <https://doi.org/10.1021/nn1006368>.
- (99) Huh, S. H. *Thermal Reduction of Graphene Oxide*. <https://cdn.intechopen.com/pdfs-wm/15270.pdf> (accessed 2017-09-15).
- (100) Cui, P.; Lee, J.; Hwang, E.; Lee, H. One-Pot Reduction of Graphene Oxide at Subzero Temperatures. *Chem. Commun.* **2011**, *47* (45), 12370–12372. <https://doi.org/10.1039/C1CC15569E>.
- (101) Stankovich, S.; Dikin, D. A.; Piner, R. D.; Kohlhaas, K. A.; Kleinhammes, A.; Jia, Y.; Wu, Y.; Nguyen, S. T.; Ruoff, R. S. Synthesis of Graphene-Based Nanosheets via Chemical Reduction of Exfoliated Graphite Oxide. *Carbon* **2007**, *45* (7), 1558–1565. <https://doi.org/10.1016/j.carbon.2007.02.034>.
- (102) Li, X.; Wang, H.; Robinson, J. T.; Sanchez, H.; Diankov, G.; Dai, H. Simultaneous Nitrogen Doping and Reduction of Graphene Oxide. *J. Am. Chem. Soc.* **2009**, *131* (43), 15939–15944. <https://doi.org/10.1021/ja907098f>.



- (103) Zhang, J.; Yang, H.; Shen, G.; Cheng, P.; Zhang, J.; Guo, S. Reduction of Graphene Oxide via l - Ascorbic Acid. *Chem. Commun.* **2010**, *46* (7), 1112–1114. <https://doi.org/10.1039/B917705A>.
- (104) Voiry, D.; Yang, J.; Kupferberg, J.; Fullon, R.; Lee, C.; Jeong, H. Y.; Shin, H. S.; Chhowalla, M. High-Quality Graphene via Microwave Reduction of Solution-Exfoliated Graphene Oxide. *Science* **2016**, *353* (6306), 1413–1416. <https://doi.org/10.1126/science.aah3398>.
- (105) Pei, S.; Cheng, H.-M. The Reduction of Graphene Oxide. *Carbon* **2012**, *50* (9), 3210–3228. <https://doi.org/10.1016/j.carbon.2011.11.010>.
- (106) Gao, W.; Alemany, L. B.; Ci, L.; Ajayan, P. M. New Insights into the Structure and Reduction of Graphite Oxide. *Nat. Chem.* **2009**, *1* (5), 403–408. <https://doi.org/10.1038/nchem.281>.
- (107) Wei, Z.; Wang, D.; Kim, S.; Kim, S.-Y.; Hu, Y.; Yakes, M. K.; Laracuenta, A. R.; Dai, Z.; Marder, S. R.; Berger, C.; King, W. P.; de Heer, W. A.; Sheehan, P. E.; Riedo, E. Nanoscale Tunable Reduction of Graphene Oxide for Graphene Electronics. *Science* **2010**, *328* (5984), 1373–1376. <https://doi.org/10.1126/science.1188119>.
- (108) Cheng, M.; Yang, R.; Zhang, L.; Shi, Z.; Yang, W.; Wang, D.; Xie, G.; Shi, D.; Zhang, G. Restoration of Graphene from Graphene Oxide by Defect Repair. *Carbon* **2012**, *50* (7), 2581–2587. <https://doi.org/10.1016/j.carbon.2012.02.016>.
- (109) De Silva, K. K. H.; Huang, H.-H.; Joshi, R.; Yoshimura, M. Restoration of the Graphitic Structure by Defect Repair during the Thermal Reduction of Graphene Oxide. *Carbon* **2020**, *166*, 74–90. <https://doi.org/10.1016/j.carbon.2020.05.015>.
- (110) Su, C.-Y.; Xu, Y.; Zhang, W.; Zhao, J.; Liu, A.; Tang, X.; Tsai, C.-H.; Huang, Y.; Li, L.-J. Highly Efficient Restoration of Graphitic Structure in Graphene Oxide Using Alcohol Vapors. *ACS Nano* **2010**, *4* (9), 5285–5292. <https://doi.org/10.1021/nn101691m>.
- (111) Peng, X.-Y.; Liu, X.-X.; Diamond, D.; Lau, K. T. Synthesis of Electrochemically-Reduced Graphene Oxide Film with Controllable Size and Thickness and Its Use in Supercapacitor. *Carbon* **2011**, *49* (11), 3488–3496. <https://doi.org/10.1016/j.carbon.2011.04.047>.
- (112) Li, W.; Geng, X.; Guo, Y.; Rong, J.; Gong, Y.; Wu, L.; Zhang, X.; Li, P.; Xu, J.; Cheng, G.; Sun, M.; Liu, L. Reduced Graphene Oxide Electrically Contacted Graphene Sensor for Highly Sensitive Nitric Oxide Detection. *ACS Nano* **2011**, *5* (9), 6955–6961. <https://doi.org/10.1021/nn201433r>.
- (113) Robinson, J. T.; Perkins, F. K.; Snow, E. S.; Wei, Z.; Sheehan, P. E. Reduced Graphene Oxide Molecular Sensors. *Nano Lett.* **2008**, *8* (10), 3137–3140. <https://doi.org/10.1021/nl8013007>.
- (114) Liu, L.; Qing, M.; Wang, Y.; Chen, S. Defects in Graphene: Generation, Healing, and Their Effects on the Properties of Graphene: A Review. *J. Mater. Sci. Technol.* **2015**, *31* (6), 599–606. <https://doi.org/10.1016/j.jmst.2014.11.019>.
- (115) Bai, Z.; Zhang, L.; Liu, L. Bombarding Graphene with Oxygen Ions: Combining Effects of Incident Angle and Ion Energy To Control Defect Generation. *J. Phys. Chem. C* **2015**, *119* (47), 26793–26802. <https://doi.org/10.1021/acs.jpcc.5b09620>.
- (116) Larciprete, R.; Fabris, S.; Sun, T.; Lacovig, P.; Baraldi, A.; Lizzit, S. Dual Path Mechanism in the Thermal Reduction of Graphene Oxide. *J. Am. Chem. Soc.* **2011**, *133* (43), 17315–17321. <https://doi.org/10.1021/ja205168x>.
- (117) Park, S.; An, J.; Potts, J. R.; Velamakanni, A.; Murali, S.; Ruoff, R. S. Hydrazine-Reduction of Graphite- and Graphene Oxide. *Carbon* **2011**, *49* (9), 3019–3023. <https://doi.org/10.1016/j.carbon.2011.02.071>.

- (118) Akhavan, O.; Ghaderi, E. Toxicity of Graphene and Graphene Oxide Nanowalls Against Bacteria. *ACS Nano* **2010**, *4* (10), 5731–5736. <https://doi.org/10.1021/nn101390x>.
- (119) Shin, H.-J.; Kim, K. K.; Benayad, A.; Yoon, S.-M.; Park, H. K.; Jung, I.-S.; Jin, M. H.; Jeong, H.-K.; Kim, J. M.; Choi, J.-Y.; Lee, Y. H. Efficient Reduction of Graphite Oxide by Sodium Borohydride and Its Effect on Electrical Conductance. *Adv. Funct. Mater.* **2009**, *19* (12), 1987–1992. <https://doi.org/10.1002/adfm.200900167>.
- (120) Fernández-Merino, M. J.; Guardia, L.; Paredes, J. I.; Villar-Rodil, S.; Solís-Fernández, P.; Martínez-Alonso, A.; Tascón, J. M. D. Vitamin C Is an Ideal Substitute for Hydrazine in the Reduction of Graphene Oxide Suspensions. *J. Phys. Chem. C* **2010**, *114* (14), 6426–6432. <https://doi.org/10.1021/jp100603h>.
- (121) Pei, S.; Zhao, J.; Du, J.; Ren, W.; Cheng, H.-M. Direct Reduction of Graphene Oxide Films into Highly Conductive and Flexible Graphene Films by Hydrohalic Acids. *Carbon* **2010**, *48* (15), 4466–4474. <https://doi.org/10.1016/j.carbon.2010.08.006>.
- (122) Moon, I. K.; Lee, J.; Ruoff, R. S.; Lee, H. Reduced Graphene Oxide by Chemical Graphitization. *Nat. Commun.* **2010**, *1* (1), 73. <https://doi.org/10.1038/ncomms1067>.
- (123) Williams, G.; Seger, B.; Kamat, P. V. TiO<sub>2</sub>-Graphene Nanocomposites. UV-Assisted Photocatalytic Reduction of Graphene Oxide. *ACS Nano* **2008**, *2* (7), 1487–1491. <https://doi.org/10.1021/nn800251f>.
- (124) Zhou, M.; Wang, Y.; Zhai, Y.; Zhai, J.; Ren, W.; Wang, F.; Dong, S. Controlled Synthesis of Large-Area and Patterned Electrochemically Reduced Graphene Oxide Films. *Chem. – Eur. J.* **2009**, *15* (25), 6116–6120. <https://doi.org/10.1002/chem.200900596>.
- (125) Zhou, Y.; Bao, Q.; Tang, L. A. L.; Zhong, Y.; Loh, K. P. Hydrothermal Dehydration for the “Green” Reduction of Exfoliated Graphene Oxide to Graphene and Demonstration of Tunable Optical Limiting Properties. *Chem. Mater.* **2009**, *21* (13), 2950–2956. <https://doi.org/10.1021/cm9006603>.
- (126) Department of Energy. <https://www.energy.gov/> (accessed 2022-04-21).
- (127) Dolbin, A. V.; Khlistyuck, M. V.; Esel’son, V. B.; Gavrilko, V. G.; Vinnikov, N. A.; Basnukaeva, R. M.; Maluenda, I.; Maser, W. K.; Benito, A. M. The Effect of the Thermal Reduction Temperature on the Structure and Sorption Capacity of Reduced Graphene Oxide Materials. *Appl. Surf. Sci.* **2016**, *361*, 213–220. <https://doi.org/10.1016/j.apsusc.2015.11.167>.
- (128) Jeong, H.-K.; Lee, Y. P.; Jin, M. H.; Kim, E. S.; Bae, J. J.; Lee, Y. H. Thermal Stability of Graphite Oxide. *Chem. Phys. Lett.* **2009**, *470* (4), 255–258. <https://doi.org/10.1016/j.cplett.2009.01.050>.
- (129) Lu, G.; Ocola, L. E.; Chen, J. Reduced Graphene Oxide for Room-Temperature Gas Sensors. *Nanotechnology* **2009**, *20* (44), 445502. <https://doi.org/10.1088/0957-4484/20/44/445502>.
- (130) Zou, T.; Zhao, B.; Xin, W.; Wang, Y.; Wang, B.; Zheng, X.; Xie, H.; Zhang, Z.; Yang, J.; Guo, C. High-Speed Femtosecond Laser Plasmonic Lithography and Reduction of Graphene Oxide for Anisotropic Photoresponse. *Light Sci. Appl.* **2020**, *9* (1), 69. <https://doi.org/10.1038/s41377-020-0311-2>.
- (131) Zhang, Y.; Guo, L.; Wei, S.; He, Y.; Xia, H.; Chen, Q.; Sun, H.-B.; Xiao, F.-S. Direct Imprinting of Microcircuits on Graphene Oxides Film by Femtosecond Laser Reduction. *Nano Today* **2010**, *5* (1), 15–20. <https://doi.org/10.1016/j.nantod.2009.12.009>.
- (132) Kumar, R.; Avasthi, D. K.; Kaur, A. Fabrication of Chemiresistive Gas Sensors Based on Multistep Reduced Graphene Oxide for Low Parts per Million Monitoring of Sulfur Dioxide at Room Temperature. *Sens. Actuators B Chem.* **2017**, *242*, 461–468. <https://doi.org/10.1016/j.snb.2016.11.018>.

- (133) Álvarez, P.; Blanco, C.; Santamaría, R.; Blanco, P.; González, Z.; Fernández-García, L.; Sierra, U.; Granda, M.; Páez, A.; Menéndez, R. Tuning Graphene Properties by a Multi-Step Thermal Reduction Process. *Carbon* **2015**, *90*, 160–163. <https://doi.org/10.1016/j.carbon.2015.04.022>.
- (134) Pisani, L.; Montanari, B.; Harrison, N. M. A Defective Graphene Phase Predicted to Be a Room Temperature Ferromagnetic Semiconductor. *New J. Phys.* **2008**, *10* (3), 033002. <https://doi.org/10.1088/1367-2630/10/3/033002>.
- (135) Lu, G.; Yu, K.; Wen, Z.; Chen, J. Semiconducting Graphene : Converting Graphene from Semimetal to Semiconductor. *Nanoscale* **2013**, *5* (4), 1353–1368. <https://doi.org/10.1039/C2NR32453A>.
- (136) Virtual Issue: Graphene and Functionalized Graphene. *J. Phys. Chem. C* **2011**, *115* (8), 3195–3197. <https://doi.org/10.1021/jp200538f>.
- (137) Pan, Q.; Chung, C.-C.; He, N.; Jones, J. L.; Gao, W. Accelerated Thermal Decomposition of Graphene Oxide Films in Air via in Situ X-Ray Diffraction Analysis. *J. Phys. Chem. C* **2016**, *120* (27), 14984–14990. <https://doi.org/10.1021/acs.jpcc.6b05031>.
- (138) Eda, G.; Chhowalla, M. Chemically Derived Graphene Oxide: Towards Large-Area Thin-Film Electronics and Optoelectronics. *Adv. Mater.* **2010**, *22* (22), 2392–2415. <https://doi.org/10.1002/adma.200903689>.
- (139) Wang, Z.; Dong, Y.; Li, H.; Zhao, Z.; Bin Wu, H.; Hao, C.; Liu, S.; Qiu, J.; Lou, X. W. (David). Enhancing Lithium–Sulphur Battery Performance by Strongly Binding the Discharge Products on Amino-Functionalized Reduced Graphene Oxide. *Nat. Commun.* **2014**, *5* (1), 5002. <https://doi.org/10.1038/ncomms6002>.
- (140) Zhu, X.; Zhu, Y.; Murali, S.; Stoller, M. D.; Ruoff, R. S. Nanostructured Reduced Graphene Oxide/Fe<sub>2</sub>O<sub>3</sub> Composite As a High-Performance Anode Material for Lithium Ion Batteries. *ACS Nano* **2011**, *5* (4), 3333–3338. <https://doi.org/10.1021/nn200493r>.
- (141) Meng, F.; Li, J.; Cushing, S. K.; Bright, J.; Zhi, M.; Rowley, J. D.; Hong, Z.; Manivannan, A.; Bristow, A. D.; Wu, N. Photocatalytic Water Oxidation by Hematite/Reduced Graphene Oxide Composites. *ACS Catal.* **2013**, *3* (4), 746–751. <https://doi.org/10.1021/cs300740e>.
- (142) Kim, D.-J.; Sohn, I. Y.; Jung, J.-H.; Yoon, O. J.; Lee, N.-E.; Park, J.-S. Reduced Graphene Oxide Field-Effect Transistor for Label-Free Femtomolar Protein Detection. *Biosens. Bioelectron.* **2013**, *41*, 621–626. <https://doi.org/10.1016/j.bios.2012.09.040>.
- (143) Cai, B.; Wang, S.; Huang, L.; Ning, Y.; Zhang, Z.; Zhang, G.-J. Ultrasensitive Label-Free Detection of PNA–DNA Hybridization by Reduced Graphene Oxide Field-Effect Transistor Biosensor. *ACS Nano* **2014**, *8* (3), 2632–2638. <https://doi.org/10.1021/nn4063424>.
- (144) *Strong reduced graphene oxide – polymer composites: hydrogels and wires - RSC Advances (RSC Publishing) DOI:10.1039/C2RA20644G*. <https://pubs.rsc.org/en/content/articlehtml/2012/ra/c2ra20644g> (accessed 2022-04-21).
- (145) Yan, D.-X.; Pang, H.; Li, B.; Vajtai, R.; Xu, L.; Ren, P.-G.; Wang, J.-H.; Li, Z.-M. Structured Reduced Graphene Oxide/Polymer Composites for Ultra-Efficient Electromagnetic Interference Shielding. *Adv. Funct. Mater.* **2015**, *25* (4), 559–566. <https://doi.org/10.1002/adfm.201403809>.
- (146) Li, N.; Zheng, M.; Lu, H.; Hu, Z.; Shen, C.; Chang, X.; Ji, G.; Cao, J.; Shi, Y. High-Rate Lithium–Sulfur Batteries Promoted by Reduced Graphene Oxide Coating. *Chem. Commun.* **2012**, *48* (34), 4106–4108. <https://doi.org/10.1039/C2CC17912A>.
- (147) Zheng, Q.; Li, Z.; Yang, J.; Kim, J.-K. Graphene Oxide-Based Transparent Conductive Films. *Prog. Mater. Sci.* **2014**, *64*, 200–247. <https://doi.org/10.1016/j.pmatsci.2014.03.004>.

- (148) Dikin, D. A.; Stankovich, S.; Zimney, E. J.; Piner, R. D.; Dommett, G. H. B.; Evmenenko, G.; Nguyen, S. T.; Ruoff, R. S. Preparation and Characterization of Graphene Oxide Paper. *Nature* **2007**, *448* (7152), 457–460. <https://doi.org/10.1038/nature06016>.
- (149) David, L.; Singh, G. Reduced Graphene Oxide Paper Electrode: Opposing Effect of Thermal Annealing on Li and Na Cyclability. *J. Phys. Chem. C* **2014**, *118* (49), 28401–28408. <https://doi.org/10.1021/jp5080847>.
- (150) Park, S.; Suk, J. W.; An, J.; Oh, J.; Lee, S.; Lee, W.; Potts, J. R.; Byun, J.-H.; Ruoff, R. S. The Effect of Concentration of Graphene Nanoplatelets on Mechanical and Electrical Properties of Reduced Graphene Oxide Papers. *Carbon* **2012**, *50* (12), 4573–4578. <https://doi.org/10.1016/j.carbon.2012.05.042>.
- (151) Gao, Z.; Xia, H.; Zauberman, J.; Tomaiuolo, M.; Ping, J.; Zhang, Q.; Ducos, P.; Ye, H.; Wang, S.; Yang, X.; Lubna, F.; Luo, Z.; Ren, L.; Johnson, A. T. C. Detection of Sub-FM DNA with Target Recycling and Self-Assembly Amplification on Graphene Field-Effect Biosensors. *Nano Lett.* **2018**, *18* (6), 3509–3515. <https://doi.org/10.1021/acs.nanolett.8b00572>.
- (152) Ganguli, A.; Faramarzi, V.; Mostafa, A.; Hwang, M. T.; You, S.; Bashir, R. High Sensitivity Graphene Field Effect Transistor-Based Detection of DNA Amplification. *Adv. Funct. Mater.* **2020**, *30* (28), 2001031. <https://doi.org/10.1002/adfm.202001031>.
- (153) Campos, R.; Borme, J.; Guerreiro, J. R.; Machado, G.; Cerqueira, M. F.; Petrovykh, D. Y.; Alpuim, P. Attomolar Label-Free Detection of DNA Hybridization with Electrolyte-Gated Graphene Field-Effect Transistors. *ACS Sens.* **2019**, *4* (2), 286–293. <https://doi.org/10.1021/acssensors.8b00344>.
- (154) Ahn, S. R.; An, J. H.; Lee, S. H.; Song, H. S.; Jang, J.; Park, T. H. Peptide Hormone Sensors Using Human Hormone Receptor-Carrying Nanovesicles and Graphene FETs. *Sci. Rep.* **2020**, *10* (1), 388. <https://doi.org/10.1038/s41598-019-57339-1>.
- (155) Zhan, B.; Li, C.; Yang, J.; Jenkins, G.; Huang, W.; Dong, X. Graphene Field-Effect Transistor and Its Application for Electronic Sensing. *Small* **2014**, *10* (20), 4042–4065. <https://doi.org/10.1002/sml.201400463>.
- (156) Danielson, E.; Dindo, M.; Porkovich, A. J.; Kumar, P.; Wang, Z.; Jain, P.; Mete, T.; Ziadi, Z.; Kikkeri, R.; Laurino, P.; Sowwan, M. Non-Enzymatic and Highly Sensitive Lactose Detection Utilizing Graphene Field-Effect Transistors. *Biosens. Bioelectron.* **2020**, *165*, 112419. <https://doi.org/10.1016/j.bios.2020.112419>.
- (157) I. Khan, N.; Mousazadehkasin, M.; Ghosh, S.; G. Tsavalas, J.; Song, E. An Integrated Microfluidic Platform for Selective and Real-Time Detection of Thrombin Biomarkers Using a Graphene FET. *Analyst* **2020**, *145* (13), 4494–4503. <https://doi.org/10.1039/D0AN00251H>.
- (158) Singh, E.; Meyyappan, M.; Nalwa, H. S. Flexible Graphene-Based Wearable Gas and Chemical Sensors. *ACS Appl. Mater. Interfaces* **2017**, *9* (40), 34544–34586. <https://doi.org/10.1021/acsami.7b07063>.
- (159) Islam, S.; Shukla, S.; Bajpai, V. K.; Han, Y.-K.; Huh, Y. S.; Ghosh, A.; Gandhi, S. Microfluidic-Based Graphene Field Effect Transistor for Femtomolar Detection of Chlorpyrifos. *Sci. Rep.* **2019**, *9* (1), 276. <https://doi.org/10.1038/s41598-018-36746-w>.
- (160) Kotlowski, C.; Larisika, M.; Guerin, P. M.; Kleber, C.; Kröber, T.; Mastrogiacomo, R.; Nowak, C.; Pelosi, P.; Schütz, S.; Schwaighofer, A.; Knoll, W. Fine Discrimination of Volatile Compounds by Graphene-Immobilized Odorant-Binding Proteins. *Sens. Actuators B Chem.* **2018**, *256*, 564–572. <https://doi.org/10.1016/j.snb.2017.10.093>.
- (161) Park, S. J.; Kwon, O. S.; Lee, S. H.; Song, H. S.; Park, T. H.; Jang, J. Ultrasensitive Flexible Graphene Based Field-Effect Transistor (FET)-Type Bioelectronic Nose. *Nano Lett.* **2012**, *12* (10), 5082–5090. <https://doi.org/10.1021/nl301714x>.



- (162) Lee, J. A.; Hwang, S.; Kwak, J.; Park, S. I.; Lee, S. S.; Lee, K.-C. An Electrochemical Impedance Biosensor with Aptamer-Modified Pyrolyzed Carbon Electrode for Label-Free Protein Detection. *Sens. Actuators B Chem.* **2008**, *129* (1), 372–379. <https://doi.org/10.1016/j.snb.2007.08.034>.
- (163) Zhang, H.; Zhang, H.; Aldalbahi, A.; Zuo, X.; Fan, C.; Mi, X. Fluorescent Biosensors Enabled by Graphene and Graphene Oxide. *Biosens. Bioelectron.* **2017**, *89*, 96–106. <https://doi.org/10.1016/j.bios.2016.07.030>.
- (164) Fang, Y.; Wang, E. Electrochemical Biosensors on Platforms of Graphene. *Chem. Commun.* **2013**, *49* (83), 9526–9539. <https://doi.org/10.1039/C3CC44735A>.
- (165) Zhao, Q.; Zhou, Y.; Li, Y.; Gu, W.; Zhang, Q.; Liu, J. Luminescent Iridium(III) Complex Labeled DNA for Graphene Oxide-Based Biosensors. *Anal. Chem.* **2016**, *88* (3), 1892–1899. <https://doi.org/10.1021/acs.analchem.5b04324>.
- (166) Fu, H.; Zhang, S.; Chen, H.; Weng, J. Graphene Enhances the Sensitivity of Fiber-Optic Surface Plasmon Resonance Biosensor. *IEEE Sens. J.* **2015**, *15* (10), 5478–5482. <https://doi.org/10.1109/JSEN.2015.2442276>.
- (167) Kim, J.; Park, S.-J.; Min, D.-H. Emerging Approaches for Graphene Oxide Biosensor. *Anal. Chem.* **2017**, *89* (1), 232–248. <https://doi.org/10.1021/acs.analchem.6b04248>.
- (168) Waldrop, M. M. The Chips Are down for Moore’s Law. *Nat. News* **2016**, *530* (7589), 144. <https://doi.org/10.1038/530144a>.
- (169) Ghasemi, S.; Moth-Poulsen, K. Single Molecule Electronic Devices with Carbon-Based Materials: Status and Opportunity. *Nanoscale* **2021**, *13* (2), 659–671. <https://doi.org/10.1039/D0NR07844A>.
- (170) Schwierz, F. Graphene Transistors. *Nat. Nanotechnol.* **2010**, *5* (7), 487–496. <https://doi.org/10.1038/nnano.2010.89>.
- (171) Bergveld, P. Development, Operation, and Application of the Ion-Sensitive Field-Effect Transistor as a Tool for Electrophysiology. *IEEE Trans. Biomed. Eng.* **1972**, *BME-19* (5), 342–351. <https://doi.org/10.1109/TBME.1972.324137>.
- (172) Kawarada, H.; Araki, Y.; Sakai, T.; Ogawa, T.; Umezawa, H. Electrolyte-Solution-Gate FETs Using Diamond Surface for Biocompatible Ion Sensors. *Phys. Status Solidi A* **2001**, *185* (1), 79–83. [https://doi.org/10.1002/1521-396X\(200105\)185:1<79::AID-PSSA79>3.0.CO;2-8](https://doi.org/10.1002/1521-396X(200105)185:1<79::AID-PSSA79>3.0.CO;2-8).
- (173) Martín, C.; Kostarelos, K.; Prato, M.; Bianco, A. Biocompatibility and Biodegradability of 2D Materials: Graphene and Beyond. *Chem. Commun.* **2019**, *55* (39), 5540–5546. <https://doi.org/10.1039/C9CC01205B>.
- (174) Wang, Z.; Hao, Z.; Yu, S.; De Moraes, C. G.; Suh, L. H.; Zhao, X.; Lin, Q. An Ultraflexible and Stretchable Aptameric Graphene Nanosensor for Biomarker Detection and Monitoring. *Adv. Funct. Mater.* **2019**, *29* (44), 1905202. <https://doi.org/10.1002/adfm.201905202>.
- (175) Kumar, S.; Bukkitgar, S. D.; Singh, S.; Pratibha; Singh, V.; Reddy, K. R.; Shetti, N. P.; Venkata Reddy, Ch.; Sadhu, V.; Naveen, S. Electrochemical Sensors and Biosensors Based on Graphene Functionalized with Metal Oxide Nanostructures for Healthcare Applications. *ChemistrySelect* **2019**, *4* (18), 5322–5337. <https://doi.org/10.1002/slct.201803871>.
- (176) Nandanapalli, K. R.; Mudusu, D.; Lee, S. Functionalization of Graphene Layers and Advancements in Device Applications. *Carbon* **2019**, *152*, 954–985. <https://doi.org/10.1016/j.carbon.2019.06.081>.
- (177) Piccinini, E.; Bliem, C.; Reiner-Rozman, C.; Battaglini, F.; Azzaroni, O.; Knoll, W. Enzyme-Polyelectrolyte Multilayer Assemblies on Reduced Graphene Oxide Field-Effect Transistors for Biosensing Applications. *Biosens. Bioelectron.* **2017**, *92*, 661–667. <https://doi.org/10.1016/j.bios.2016.10.035>.

- (178) Kim, B.; Lee, J.; Namgung, S.; Kim, J.; Park, J. Y.; Lee, M.-S.; Hong, S. DNA Sensors Based on CNT-FET with Floating Electrodes. *Sens. Actuators B Chem.* **2012**, *169*, 182–187. <https://doi.org/10.1016/j.snb.2012.04.063>.
- (179) Ithantola, H. K. J.; Moll, J. L. Design Theory of a Surface Field-Effect Transistor. *Solid-State Electron.* **1964**, *7* (6), 423–430. [https://doi.org/10.1016/0038-1101\(64\)90039-5](https://doi.org/10.1016/0038-1101(64)90039-5).
- (180) Bergveld, P. Development of an Ion-Sensitive Solid-State Device for Neurophysiological Measurements. *IEEE Trans. Biomed. Eng.* **1970**, *BME-17* (1), 70–71. <https://doi.org/10.1109/TBME.1970.4502688>.
- (181) Abe, H.; Esashi, M.; Matsuo, T. ISFET's Using Inorganic Gate Thin Films. *IEEE Trans. Electron Devices* **1979**, *26* (12), 1939–1944. <https://doi.org/10.1109/T-ED.1979.19799>.
- (182) Akiyama, T.; Ujihira, Y.; Okabe, Y.; Sugano, T.; Niki, E. Ion-Sensitive Field-Effect Transistors with Inorganic Gate Oxide for PH Sensing. *IEEE Trans. Electron Devices* **1982**, *29* (12), 1936–1941. <https://doi.org/10.1109/T-ED.1982.21054>.
- (183) Knopfmacher, O.; Tarasov, A.; Fu, W.; Wipf, M.; Niesen, B.; Calame, M.; Schönenberger, C. Nernst Limit in Dual-Gated Si-Nanowire FET Sensors. *Nano Lett.* **2010**, *10* (6), 2268–2274. <https://doi.org/10.1021/nl100892y>.
- (184) Jakob, M. H.; Dong, B.; Gutsch, S.; Chatelle, C.; Krishnaraja, A.; Weber, W.; Zacharias, M. Label-Free SnO<sub>2</sub> Nanowire FET Biosensor for Protein Detection. *Nanotechnology* **2017**, *28* (24), 245503. <https://doi.org/10.1088/1361-6528/aa7015>.
- (185) Takeda, S.; Nakamura, M.; Ishii, A.; Subagyo, A.; Hosoi, H.; Sueoka, K.; Mukasa, K. A PH Sensor Based on Electric Properties of Nanotubes on a Glass Substrate. *Nanoscale Res. Lett.* **2007**, *2* (4), 207–212. <https://doi.org/10.1007/s11671-007-9053-9>.
- (186) Khan, M. I.; Mukherjee, K.; Shoukat, R.; Dong, H. A Review on PH Sensitive Materials for Sensors and Detection Methods. *Microsyst. Technol.* **2017**, *23* (10), 4391–4404. <https://doi.org/10.1007/s00542-017-3495-5>.
- (187) Ang, P. K.; Chen, W.; Wee, A. T. S.; Loh, K. P. Solution-Gated Epitaxial Graphene as PH Sensor. *J. Am. Chem. Soc.* **2008**, *130* (44), 14392–14393. <https://doi.org/10.1021/ja805090z>.
- (188) Fu, W.; Nef, C.; Knopfmacher, O.; Tarasov, A.; Weiss, M.; Calame, M.; Schönenberger, C. Graphene Transistors Are Insensitive to PH Changes in Solution. *Nano Lett.* **2011**, *11* (9), 3597–3600. <https://doi.org/10.1021/nl201332c>.
- (189) Kwon, J.-H.; Lee, K.-S.; Lee, Y.-H.; Ju, B.-K. Single-Wall Carbon Nanotube-Based PH Sensor Fabricated by the Spray Method. *Electrochem. Solid State Lett.* **2006**, *9* (9), H85. <https://doi.org/10.1149/1.2217131>.
- (190) Dukovic, G.; White, B. E.; Zhou, Z.; Wang, F.; Jockusch, S.; Steigerwald, M. L.; Heinz, T. F.; Friesner, R. A.; Turro, N. J.; Brus, L. E. Reversible Surface Oxidation and Efficient Luminescence Quenching in Semiconductor Single-Wall Carbon Nanotubes. *J. Am. Chem. Soc.* **2004**, *126* (46), 15269–15276. <https://doi.org/10.1021/ja046526r>.
- (191) Kasting, J. F.; Siefert, J. L. Life and the Evolution of Earth's Atmosphere. *Science* **2002**, *296* (5570), 1066–1068. <https://doi.org/10.1126/science.1071184>.
- (192) *Earth's Energy Budget Poster : Home*. [https://web.archive.org/web/20140421050855/http://science-edu.larc.nasa.gov/energy\\_budget/](https://web.archive.org/web/20140421050855/http://science-edu.larc.nasa.gov/energy_budget/) (accessed 2021-06-15).
- (193) *Solar radiation modeling*. <https://solargis.com/docs/methodology/solar-radiation-modeling> (accessed 2022-10-20).
- (194) *Global Solar Atlas*. <https://globalsolaratlas.info/support/faq> (accessed 2021-06-16).
- (195) Sunlight. *Wikipedia*; 2021.

- (196) Maeda, K.; Domen, K. New Non-Oxide Photocatalysts Designed for Overall Water Splitting under Visible Light. *J. Phys. Chem. C* **2007**, *111* (22), 7851–7861. <https://doi.org/10.1021/jp070911w>.
- (197) Fujishima, A.; Honda, K. Electrochemical Photolysis of Water at a Semiconductor Electrode. *Nature* **1972**, *238* (5358), 37–38. <https://doi.org/10.1038/238037a0>.
- (198) Gerischer, H. Electrochemical Behavior of Semiconductors under Illumination. *J. Electrochem. Soc.* **1966**, *113* (11), 1174–1182. <https://doi.org/10.1149/1.2423779>.
- (199) Grätzel, M. Photoelectrochemical Cells. *Nature* **2001**, *414* (6861), 338–344. <https://doi.org/10.1038/35104607>.
- (200) Maeda, K.; Domen, K. Photocatalytic Water Splitting: Recent Progress and Future Challenges. *J. Phys. Chem. Lett.* **2010**, *1* (18), 2655–2661. <https://doi.org/10.1021/jz1007966>.
- (201) Tan, M. X.; Laibinis, P. E.; Nguyen, S. T.; Kesselman, J. M.; Stanton, C. E.; Lewis, N. S. Principles and Applications of Semiconductor Photoelectrochemistry. In *Progress in Inorganic Chemistry*; Karlin, K. D., Ed.; John Wiley & Sons, Inc.: Hoboken, NJ, USA, 2007; pp 21–144. <https://doi.org/10.1002/9780470166420.ch2>.
- (202) Kim, J. Y.; Magesh, G.; Youn, D. H.; Jang, J.-W.; Kubota, J.; Domen, K.; Lee, J. S. Single-Crystalline, Wormlike Hematite Photoanodes for Efficient Solar Water Splitting. *Sci. Rep.* **2013**, *3* (1), 1–8. <https://doi.org/10.1038/srep02681>.
- (203) Abdi, Z.; Vandichel, M.; Sologubenko, A. S.; Willinger, M.-G.; Shen, J.-R.; Allakhverdiev, S. I.; Najafpour, M. M. The Importance of Identifying the True Catalyst When Using Randles-Sevcik Equation to Calculate Turnover Frequency. *Int. J. Hydrog. Energy* **2021**, *46* (76), 37774–37781. <https://doi.org/10.1016/j.ijhydene.2021.09.039>.
- (204) Cox, C. R.; Lee, J. Z.; Nocera, D. G.; Buonassisi, T. Ten-Percent Solar-to-Fuel Conversion with Nonprecious Materials. *Proc. Natl. Acad. Sci.* **2014**, *111* (39), 14057–14061. <https://doi.org/10.1073/pnas.1414290111>.
- (205) Corby, S.; Rao, R. R.; Steier, L.; Durrant, J. R. The Kinetics of Metal Oxide Photoanodes from Charge Generation to Catalysis. *Nat. Rev. Mater.* **2021**, *6* (12), 1136–1155. <https://doi.org/10.1038/s41578-021-00343-7>.
- (206) Mesa, C. A.; Francàs, L.; Yang, K. R.; Garrido-Barros, P.; Pastor, E.; Ma, Y.; Kafizas, A.; Rosser, T. E.; Mayer, M. T.; Reisner, E.; Grätzel, M.; Batista, V. S.; Durrant, J. R. Multihole Water Oxidation Catalysis on Hematite Photoanodes Revealed by Operando Spectroelectrochemistry and DFT. *Nat. Chem.* **2020**, *12* (1), 82–89. <https://doi.org/10.1038/s41557-019-0347-1>.
- (207) Zhang, J.; Eslava, S. Understanding Charge Transfer, Defects and Surface States at Hematite Photoanodes. *Sustain. Energy Fuels* **2019**, *3* (6), 1351–1364. <https://doi.org/10.1039/C9SE00145J>.
- (208) Forster, M.; Potter, R. J.; Ling, Y.; Yang, Y.; Klug, D. R.; Li, Y.; Cowan, A. J. Oxygen Deficient  $\alpha$ -Fe<sub>2</sub>O<sub>3</sub> Photoelectrodes: A Balance between Enhanced Electrical Properties and Trap-Mediated Losses. *Chem. Sci.* **2015**, *6* (7), 4009–4016. <https://doi.org/10.1039/C5SC00423C>.
- (209) Hirakawa, H.; Hashimoto, M.; Shiraiishi, Y.; Hirai, T. Photocatalytic Conversion of Nitrogen to Ammonia with Water on Surface Oxygen Vacancies of Titanium Dioxide. *J. Am. Chem. Soc.* **2017**, *139* (31), 10929–10936. <https://doi.org/10.1021/jacs.7b06634>.
- (210) Lettieri, S.; Gargiulo, V.; Alfè, M.; Amati, M.; Zeller, P.; Maraloiu, V.-A.; Borbone, F.; Pavone, M.; Muñoz-García, A. B.; Maddalena, P. Simple Ethanol Refluxing Method for Production of Blue-Colored Titanium Dioxide with Oxygen Vacancies and Visible Light-Driven Photocatalytic Properties. *J. Phys. Chem. C* **2020**, *124* (6), 3564–3576. <https://doi.org/10.1021/acs.jpcc.9b08993>.

- (211) Su, J.; Zou, X.; Chen, J.-S. Self-Modification of Titanium Dioxide Materials by Ti<sup>3+</sup> and/or Oxygen Vacancies: New Insights into Defect Chemistry of Metal Oxides. *RSC Adv.* **2014**, *4* (27), 13979–13988. <https://doi.org/10.1039/C3RA47757F>.
- (212) Sivula, K.; van de Krol, R. Semiconducting Materials for Photoelectrochemical Energy Conversion. *Nat. Rev. Mater.* **2016**, *1* (2), 15010. <https://doi.org/10.1038/natrevmats.2015.10>.
- (213) Liu, S.; Luo, Z.; Li, L.; Li, H.; Chen, M.; Wang, T.; Gong, J. Multifunctional TiO<sub>2</sub> Overlayer for P-Si/n-CdS Heterojunction Photocathode with Improved Efficiency and Stability. *Nano Energy* **2018**, *53*, 125–129. <https://doi.org/10.1016/j.nanoen.2018.08.024>.
- (214) Zhang, J.; Sun, Y.; Ye, S.; Song, J.; Qu, J. Heterostructures in Two-Dimensional CdSe Nanoplatelets: Synthesis, Optical Properties, and Applications. *Chem. Mater.* **2020**, *32* (22), 9490–9507. <https://doi.org/10.1021/acs.chemmater.0c02593>.
- (215) Chen, Z.; Jaramillo, T. F.; Deutsch, T. G.; Kleiman-Shwarsstein, A.; Forman, A. J.; Gaillard, N.; Garland, R.; Takanabe, K.; Heske, C.; Sunkara, M.; McFarland, E. W.; Domen, K.; Miller, E. L.; Turner, J. A.; Dinh, H. N. Accelerating Materials Development for Photoelectrochemical Hydrogen Production: Standards for Methods, Definitions, and Reporting Protocols. *J. Mater. Res.* **2010**, *25* (1), 3–16. <https://doi.org/10.1557/JMR.2010.0020>.
- (216) Wang, C.; Long, X.; Wei, S.; Wang, T.; Li, F.; Gao, L.; Hu, Y.; Li, S.; Jin, J. Conformally Coupling CoAl-Layered Double Hydroxides on Fluorine-Doped Hematite: Surface and Bulk Co-Modification for Enhanced Photoelectrochemical Water Oxidation. *ACS Appl. Mater. Interfaces* **2019**, *11* (33), 29799–29806. <https://doi.org/10.1021/acsami.9b07417>.
- (217) Li, H.-M.; Wang, Z.-Y.; Jing, H.-J.; Yi, S.-S.; Zhang, S.-X.; Yue, X.-Z.; Zhang, Z.-T.; Lu, H.-X.; Chen, D.-L. Synergetic Integration of Passivation Layer and Oxygen Vacancy on Hematite Nanoarrays for Boosted Photoelectrochemical Water Oxidation. *Appl. Catal. B Environ.* **2021**, *284*, 119760. <https://doi.org/10.1016/j.apcatb.2020.119760>.
- (218) Zhang, Y.; Jiang, S.; Song, W.; Zhou, P.; Ji, H.; Ma, W.; Hao, W.; Chen, C.; Zhao, J. Nonmetal P-Doped Hematite Photoanode with Enhanced Electron Mobility and High Water Oxidation Activity. *Energy Environ. Sci.* **2015**, *8* (4), 1231–1236. <https://doi.org/10.1039/C4EE03803G>.
- (219) Ahn, H.-J.; Kwak, M.-J.; Lee, J.-S.; Yoon, K.-Y.; Jang, J.-H. Nanoporous Hematite Structures to Overcome Short Diffusion Lengths in Water Splitting. *J. Mater. Chem. A* **2014**, *2* (47), 19999–20003. <https://doi.org/10.1039/C4TA04890C>.
- (220) Kennedy, J. H.; Frese, K. W. Photooxidation of Water at  $\alpha$ -Fe<sub>2</sub>O<sub>3</sub> Electrodes. *J. Electrochem. Soc.* **1978**, *125* (5), 709–714. <https://doi.org/10.1149/1.2131532>.
- (221) Klahr, B.; Gimenez, S.; Fabregat-Santiago, F.; Hamann, T.; Bisquert, J. Water Oxidation at Hematite Photoelectrodes: The Role of Surface States. *J. Am. Chem. Soc.* **2012**, *134* (9), 4294–4302. <https://doi.org/10.1021/ja210755h>.
- (222) Barroso, M.; Pendlebury, S. R.; Cowan, A. J.; Durrant, J. R. Charge Carrier Trapping, Recombination and Transfer in Hematite ( $\alpha$ -Fe<sub>2</sub>O<sub>3</sub>) Water Splitting Photoanodes. *Chem. Sci.* **2013**, *4* (7), 2724–2734. <https://doi.org/10.1039/C3SC50496D>.
- (223) Le Formal, F.; Pastor, E.; Tilley, S. D.; Mesa, C. A.; Pendlebury, S. R.; Grätzel, M.; Durrant, J. R. Rate Law Analysis of Water Oxidation on a Hematite Surface. *J. Am. Chem. Soc.* **2015**, *137* (20), 6629–6637. <https://doi.org/10.1021/jacs.5b02576>.
- (224) Annamalai, A.; Subramanian, A.; Kang, U.; Park, H.; Choi, S. H.; Jang, J. S. Activation of Hematite Photoanodes for Solar Water Splitting: Effect of FTO Deformation. *J. Phys. Chem. C* **2015**, *119* (7), 3810–3817. <https://doi.org/10.1021/jp512189c>.



- (225) Ling, Y.; Wang, G.; Wheeler, D. A.; Zhang, J. Z.; Li, Y. Sn-Doped Hematite Nanostructures for Photoelectrochemical Water Splitting. *Nano Lett.* **2011**, *11* (5), 2119–2125. <https://doi.org/10.1021/nl200708y>.
- (226) Orlandi, M.; Mazzi, A.; Arban, G.; Bazzanella, N.; Rudatis, P.; Caramori, S.; Patel, N.; Fernandes, R.; Bignozzi, C. A.; Miotello, A. On the Effect of Sn-Doping in Hematite Anodes for Oxygen Evolution. *Electrochimica Acta* **2016**, *214*, 345–353. <https://doi.org/10.1016/j.electacta.2016.08.046>.
- (227) Lee, M. H.; Park, J. H.; Han, H. S.; Song, H. J.; Cho, I. S.; Noh, J. H.; Hong, K. S. Nanostructured Ti-Doped Hematite ( $\alpha$ -Fe<sub>2</sub>O<sub>3</sub>) Photoanodes for Efficient Photoelectrochemical Water Oxidation. *Int. J. Hydrog. Energy* **2014**, *39* (30), 17501–17507. <https://doi.org/10.1016/j.ijhydene.2013.10.031>.
- (228) Dias, P.; Lopes, T.; Andrade, L.; Mendes, A. Temperature Effect on Water Splitting Using a Si-Doped Hematite Photoanode. *J. Power Sources* **2014**, *272*, 567–580. <https://doi.org/10.1016/j.jpowsour.2014.08.108>.
- (229) Fu, Y.; Dong, C.-L.; Lee, W.-Y.; Chen, J.; Guo, P.; Zhao, L.; Shen, S. Nb-Doped Hematite Nanorods for Efficient Solar Water Splitting: Electronic Structure Evolution versus Morphology Alteration. *ChemNanoMat* **2016**, *2* (7), 704–711. <https://doi.org/10.1002/cnma.201600024>.
- (230) Gurudayal; Chiam, S. Y.; Kumar, M. H.; Bassi, P. S.; Seng, H. L.; Barber, J.; Wong, L. H. Improving the Efficiency of Hematite Nanorods for Photoelectrochemical Water Splitting by Doping with Manganese. *ACS Appl. Mater. Interfaces* **2014**, *6* (8), 5852–5859. <https://doi.org/10.1021/am500643y>.
- (231) Zhao, L.; Xiao, J.; Huang, H.; Huang, Q.; Zhao, Y.; Li, Y. Enhanced Efficiency of Hematite Photoanode for Water Splitting with the Doping of Ge. *Int. J. Hydrog. Energy* **2018**, *43* (28), 12646–12652. <https://doi.org/10.1016/j.ijhydene.2018.04.115>.
- (232) Annamalai, A.; Sandström, R.; Gracia-Espino, E.; Boulanger, N.; Boily, J.-F.; Mühlbacher, I.; Shchukarev, A.; Wågberg, T. Influence of Sb<sup>5+</sup> as a Double Donor on Hematite (Fe<sup>3+</sup>) Photoanodes for Surface-Enhanced Photoelectrochemical Water Oxidation. *ACS Appl. Mater. Interfaces* **2018**, *10* (19), 16467–16473. <https://doi.org/10.1021/acsami.8b02147>.
- (233) Mohapatra, M.; Padhi, T.; Anand, S.; Mishra, B. K. CTAB Mediated Mg-Doped Nano Fe<sub>2</sub>O<sub>3</sub>: Synthesis, Characterization, and Fluoride Adsorption Behavior. *Desalination Water Treat.* **2012**.
- (234) Tsege, E. L.; Atabaev, T. Sh.; Hossain, Md. A.; Lee, D.; Kim, H.-K.; Hwang, Y.-H. Cu-Doped Flower-like Hematite Nanostructures for Efficient Water Splitting Applications. *J. Phys. Chem. Solids* **2016**, *98*, 283–289. <https://doi.org/10.1016/j.jpcs.2016.07.014>.
- (235) Xiao, C.; Zhou, Z.; Li, L.; Wu, S.; Li, X. Tin and Oxygen-Vacancy Co-Doping into Hematite Photoanode for Improved Photoelectrochemical Performances. *Nanoscale Res. Lett.* **2020**, *15* (1), 54. <https://doi.org/10.1186/s11671-020-3287-1>.
- (236) Wang, Z.; Mao, X.; Chen, P.; Xiao, M.; Monny, S. A.; Wang, S.; Konarova, M.; Du, A.; Wang, L. Understanding the Roles of Oxygen Vacancies in Hematite-Based Photoelectrochemical Processes. *Angew. Chem.* **2019**, *131* (4), 1042–1046. <https://doi.org/10.1002/ange.201810583>.
- (237) Luo, H.; Takata, T.; Lee, Y.; Zhao, J.; Domen, K.; Yan. Photocatalytic Activity Enhancing for Titanium Dioxide by Co-Doping with Bromine and Chlorine. *Chem. Mater.* **2004**, *16* (5), 846–849. <https://doi.org/10.1021/cm035090w>.
- (238) Burkhardt, W.; Christmann, T.; Franke, S.; Krieger, W.; Meister, D.; Meyer, B. K.; Niessner, W.; Schalch, D.; Scharmann, A. Tungsten and Fluorine Co-Doping of VO<sub>2</sub> Films. *Thin Solid Films* **2002**, *402* (1), 226–231. [https://doi.org/10.1016/S0040-6090\(01\)01603-0](https://doi.org/10.1016/S0040-6090(01)01603-0).

- (239) Shen, C. H.; Liu, R. S.; Gundakaram, R.; Chen, J. M.; Huang, S. M.; Chen, J. S.; Wang, C. M. Effect of Co Doping in LiMn<sub>2</sub>O<sub>4</sub>. *J. Power Sources* **2001**, *102* (1), 21–28. [https://doi.org/10.1016/S0378-7753\(01\)00765-0](https://doi.org/10.1016/S0378-7753(01)00765-0).
- (240) Dong, Z.; Ding, D.; Li, T.; Ning, C. Facile Preparation of Ti<sub>3</sub>+Ni Co-Doped TiO<sub>2</sub> Nanotubes Photoanode for Efficient Photoelectrochemical Water Splitting. *Appl. Surf. Sci.* **2019**, *480*, 219–228. <https://doi.org/10.1016/j.apsusc.2019.02.237>.
- (241) Saxena, S.; Verma, A.; Biswas, N. K.; Khan, S. A.; Satsangi, V. R.; Shrivastav, R.; Dass, S. Zr–W Co-Doping in BiVO<sub>4</sub> – Synergistic Effect in Photoelectrochemical Water Splitting. *Mater. Chem. Phys.* **2021**, *267*, 124675. <https://doi.org/10.1016/j.matchemphys.2021.124675>.
- (242) Zhang, L.; Yang, Y.; Fan, R.; Yu, J.; Li, L. Improving the Efficiency of ZnO-Based Dye-Sensitized Solar Cells by Pr and N Co-Doping. *J. Mater. Chem. A* **2013**, *1* (39), 12066–12073. <https://doi.org/10.1039/C3TA11570D>.
- (243) Zhang, M.; Luo, W.; Li, Z.; Yu, T.; Zou, Z. Improved Photoelectrochemical Responses of Si and Ti Codoped  $\alpha$ -Fe<sub>2</sub>O<sub>3</sub> Photoanode Films. *Appl. Phys. Lett.* **2010**, *97* (4), 042105. <https://doi.org/10.1063/1.3470109>.
- (244) Tang, H.; Yin, W.-J.; Matin, M. A.; Wang, H.; Deutsch, T.; Al-Jassim, M. M.; Turner, J. A.; Yan, Y. Titanium and Magnesium Co-Alloyed Hematite Thin Films for Photoelectrochemical Water Splitting. *J. Appl. Phys.* **2012**, *111* (7), 073502. <https://doi.org/10.1063/1.3699016>.
- (245) Tamirat, A. G.; Su, W.-N.; Dubale, A. A.; Chen, H.-M.; Hwang, B.-J. Photoelectrochemical Water Splitting at Low Applied Potential Using a NiOOH Coated Codoped (Sn, Zr)  $\alpha$ -Fe<sub>2</sub>O<sub>3</sub> Photoanode. *J. Mater. Chem. A* **2015**, *3* (11), 5949–5961. <https://doi.org/10.1039/C4TA06915C>.
- (246) Annamalai, A.; Lee, H. H.; Choi, S. H.; Lee, S. Y.; Gracia-Espino, E.; Subramanian, A.; Park, J.; Kong, K.; Jang, J. S. Sn/Be Sequentially Co-Doped Hematite Photoanodes for Enhanced Photoelectrochemical Water Oxidation: Effect of Be<sup>2+</sup> as Co-Dopant. *Sci. Rep.* **2016**, *6*, 23183. <https://doi.org/10.1038/srep23183>.
- (247) Guo, X.; Wang, L.; Tan, Y. Hematite Nanorods Co-Doped with Ru Cations with Different Valence States as High Performance Photoanodes for Water Splitting. *Nano Energy* **2015**, *16*, 320–328. <https://doi.org/10.1016/j.nanoen.2015.07.005>.
- (248) Ohno, Y.; Maehashi, K.; Yamashiro, Y.; Matsumoto, K. Electrolyte-Gated Graphene Field-Effect Transistors for Detecting PH and Protein Adsorption. *Nano Lett.* **2009**, *9* (9), 3318–3322. <https://doi.org/10.1021/nl901596m>.
- (249) Wang, X.; Li, X.; Zhang, L.; Yoon, Y.; Weber, P. K.; Wang, H.; Guo, J.; Dai, H. N-Doping of Graphene Through Electrothermal Reactions with Ammonia. *Science* **2009**, *324* (5928), 768–771. <https://doi.org/10.1126/science.1170335>.
- (250) Scholz, W.; Boehm, H.-P. Die thermische Zersetzung von Graphitoxyd. *Naturwissenschaften* **1964**, *51* (7), 160–160. <https://doi.org/10.1007/BF00622288>.
- (251) Boehm, H.-P. Graphen – Wie Eine Laborkuriosität Plötzlich Äußerst Interessant Wurde. *Angew. Chem.* **2010**, *122* (49), 9520–9523. <https://doi.org/10.1002/ange.201004096>.
- (252) Fan, L.-Z.; Liu, J.-L.; Ud-Din, R.; Yan, X.; Qu, X. The Effect of Reduction Time on the Surface Functional Groups and Supercapacitive Performance of Graphene Nanosheets. *Carbon* **2012**, *50* (10), 3724–3730. <https://doi.org/10.1016/j.carbon.2012.03.046>.
- (253) Ling, Y.; Li, Y. Review of Sn-Doped Hematite Nanostructures for Photoelectrochemical Water Splitting. *Part. Part. Syst. Charact.* **2014**, *31* (11), 1113–1121. <https://doi.org/10.1002/ppsc.201400051>.
- (254) Zhou, C.; Sanders-Bellis, Z.; Smart, T. J.; Zhang, W.; Zhang, L.; Ping, Y.; Liu, M. Interstitial Lithium Doping in BiVO<sub>4</sub> Thin Film Photoanode for Enhanced Solar Water Splitting

- Activity. *Chem. Mater.* **2020**, *32* (15), 6401–6409.  
<https://doi.org/10.1021/acs.chemmater.0c01481>.
- (255) Feicht, P.; Siegel, R.; Thurn, H.; Neubauer, J. W.; Seuss, M.; Szabó, T.; Talyzin, A. V.; Halbig, C. E.; Eigler, S.; Kunz, D. A.; Fery, A.; Papastavrou, G.; Senker, J.; Brey, J. Systematic Evaluation of Different Types of Graphene Oxide in Respect to Variations in Their In-Plane Modulus. *Carbon* **2017**, *114*, 700–705. <https://doi.org/10.1016/j.carbon.2016.12.065>.
- (256) *Interdigitated Electrodes (IDE)*. <https://www.micruxfluidic.com/en/electrochemical-solutions/thin-film-electrochemical-sensors/interdigitated-electrodes-ide/> (accessed 2018-03-23).
- (257) Yang, J.; Kim, J.-W.; Shin, H. S. Facile Method for RGO Field Effect Transistor: Selective Adsorption of RGO on SAM-Treated Gold Electrode by Electrostatic Attraction. *Adv. Mater.* **2012**, *24* (17), 2299–2303. <https://doi.org/10.1002/adma.201104094>.
- (258) Malviya, K. D.; Dotan, H.; Yoon, K. R.; Kim, I.-D.; Rothschild, A. Rigorous Substrate Cleaning Process for Reproducible Thin Film Hematite ( $\alpha$ -Fe<sub>2</sub>O<sub>3</sub>) Photoanodes. *J. Mater. Res.* **2016**, *31* (11), 1565–1573. <https://doi.org/10.1557/jmr.2015.300>.
- (259) Hickling, A. Studies in Electrode Polarisation. Part IV.—The Automatic Control of the Potential of a Working Electrode. *Trans. Faraday Soc.* **1942**, *38* (0), 27–33.  
<https://doi.org/10.1039/TF9423800027>.
- (260) Randles, J. E. B. A Cathode Ray Polarograph. Part II.—The Current-Voltage Curves. *Trans. Faraday Soc.* **1948**, *44* (0), 327–338. <https://doi.org/10.1039/TF9484400327>.
- (261) Laser, D.; Gottesfeld, S. Photocurrents Induced by Subbandgap Illumination in a Ti-Oxide Film Electrode. *J. Electrochem. Soc.* **1979**, *126* (3), 475.  
<https://doi.org/10.1149/1.2129065>.
- (262) Abrantes, L. M.; Peter, L. M. Transient Photocurrents at Passive Iron Electrodes. *J. Electroanal. Chem. Interfacial Electrochem.* **1983**, *150* (1), 593–601.  
[https://doi.org/10.1016/S0022-0728\(83\)80238-1](https://doi.org/10.1016/S0022-0728(83)80238-1).
- (263) *ITS-90 Thermocouple Database, Download Files*.  
<https://srdata.nist.gov/its90/download/download.html> (accessed 2018-08-04).
- (264) S. Cherevan, A.; Gebhardt, P.; J. Shearer, C.; Matsukawa, M.; Domen, K.; Eder, D. Interface Engineering in Nanocarbon–Ta<sub>2</sub>O<sub>5</sub> Hybrid Photocatalysts. *Energy Environ. Sci.* **2014**, *7* (2), 791–796. <https://doi.org/10.1039/C3EE42558D>.
- (265) Moya, A.; Cherevan, A.; Marchesan, S.; Gebhardt, P.; Prato, M.; Eder, D.; Vilatela, J. J. Oxygen Vacancies and Interfaces Enhancing Photocatalytic Hydrogen Production in Mesoporous CNT/TiO<sub>2</sub> Hybrids. *Appl. Catal. B Environ.* **2015**, *179*, 574–582.  
<https://doi.org/10.1016/j.apcatb.2015.05.052>.
- (266) Häusler, T.; Gebhardt, P.; Iglesias, D.; Rameshan, C.; Marchesan, S.; Eder, D.; Grothe, H. Ice Nucleation Activity of Graphene and Graphene Oxides. *J. Phys. Chem. C* **2018**, *122* (15), 8182–8190. <https://doi.org/10.1021/acs.jpcc.7b10675>.
- (267) King, A. A. K.; Davies, B. R.; Noorbehesht, N.; Newman, P.; Church, T. L.; Harris, A. T.; Razal, J. M.; Minett, A. I. A New Raman Metric for the Characterisation of Graphene Oxide and Its Derivatives. *Sci. Rep.* **2016**, *6*. <https://doi.org/10.1038/srep19491>.
- (268) Itoh, K.; Bockris, J. O. Thin Film Photoelectrochemistry: Iron Oxide. *J. Electrochem. Soc.* **1984**, *131* (6), 1266. <https://doi.org/10.1149/1.2115798>.
- (269) Carbonare, N. D.; Carli, S.; Argazzi, R.; Orlandi, M.; Bazzanella, N.; Miotello, A.; Caramori, S.; A. Bignozzi, C. Improvement of the Electron Collection Efficiency in Porous Hematite Using a Thin Iron Oxide Underlayer: Towards Efficient All-Iron Based Photoelectrodes. *Phys. Chem. Chem. Phys.* **2015**, *17* (44), 29661–29670. <https://doi.org/10.1039/C5CP04152J>.

- (270) Strohmeier, B. R. An ESCA Method for Determining the Oxide Thickness on Aluminum Alloys. *Surf. Interface Anal.* **1990**, *15* (1), 51–56. <https://doi.org/10.1002/sia.740150109>.
- (271) Barr, T. L.; Seal, S. Nature of the Use of Adventitious Carbon as a Binding Energy Standard. *J. Vac. Sci. Technol. A* **1995**, *13* (3), 1239–1246. <https://doi.org/10.1116/1.579868>.
- (272) Haselmann, G. M. TiO<sub>2</sub>-Based Photocatalysis : Role of Defects during Photocatalytic Hydrogen Evolution and Oxidation of Methanol. Thesis, Wien, 2018.
- (273) Matsuo, T.; Esashi, M. Methods of Isfet Fabrication. *Sens. Actuators* **1981**, *1*, 77–96. [https://doi.org/10.1016/0250-6874\(81\)80006-6](https://doi.org/10.1016/0250-6874(81)80006-6).
- (274) Sakurai, Toshinari.; Husimi, Yuzuru. Real-Time Monitoring of DNA Polymerase Reactions by a Micro ISFET PH Sensor. *Anal. Chem.* **1992**, *64* (17), 1996–1997. <https://doi.org/10.1021/ac00041a040>.
- (275) Moore, C. E.; Jaselskis, B. THE PH METER, A PRODUCT OF TECHNOLOGICAL CROSSOVERS. *Bull Hist Chem* **1998**, *6*.
- (276) Lee, S. H.; Kim, H. W.; Hwang, J. O.; Lee, W. J.; Kwon, J.; Bielawski, C. W.; Ruoff, R. S.; Kim, S. O. Three-Dimensional Self-Assembly of Graphene Oxide Platelets into Mechanically Flexible Macroporous Carbon Films. *Angew. Chem.* **2010**, *122* (52), 10282–10286. <https://doi.org/10.1002/ange.201006240>.
- (277) An, S. J.; Zhu, Y.; Lee, S. H.; Stoller, M. D.; Emilsson, T.; Park, S.; Velamakanni, A.; An, J.; Ruoff, R. S. Thin Film Fabrication and Simultaneous Anodic Reduction of Deposited Graphene Oxide Platelets by Electrophoretic Deposition. *J. Phys. Chem. Lett.* **2010**, *1* (8), 1259–1263. <https://doi.org/10.1021/jz100080c>.
- (278) Mathkar, A.; Tozier, D.; Cox, P.; Ong, P.; Galande, C.; Balakrishnan, K.; Leela Mohana Reddy, A.; Ajayan, P. M. Controlled, Stepwise Reduction and Band Gap Manipulation of Graphene Oxide. *J. Phys. Chem. Lett.* **2012**, *3* (8), 986–991. <https://doi.org/10.1021/jz300096t>.
- (279) Kwon, S. S.; Yi, J.; Lee, W. W.; Shin, J. H.; Kim, S. H.; Cho, S. H.; Nam, S.; Park, W. I. Reversible and Irreversible Responses of Defect-Engineered Graphene-Based Electrolyte-Gated PH Sensors. *ACS Appl. Mater. Interfaces* **2016**, *8* (1), 834–839. <https://doi.org/10.1021/acsami.5b10183>.
- (280) Jung, I.; Dikin, D. A.; Piner, R. D.; Ruoff, R. S. Tunable Electrical Conductivity of Individual Graphene Oxide Sheets Reduced at “Low” Temperatures. *Nano Lett.* **2008**, *8* (12), 4283–4287. <https://doi.org/10.1021/nl8019938>.
- (281) Joung, D.; Chunder, A.; Zhai, L.; Khondaker, S. I. High Yield Fabrication of Chemically Reduced Graphene Oxide Field Effect Transistors by Dielectrophoresis. *Nanotechnology* **2010**, *21* (16), 165202. <https://doi.org/10.1088/0957-4484/21/16/165202>.
- (282) Reiner-Rozman, C.; Kotlowski, C.; Knoll, W. Electronic Biosensing with Functionalized RGO FETs. *Biosensors* **2016**, *6* (2), 17. <https://doi.org/10.3390/bios6020017>.
- (283) Sahoo, M.; Antony, R. P.; Mathews, T.; Dash, S.; Tyagi, A. K. Raman Studies of Chemically and Thermally Reduced Graphene Oxide. *AIP Conf. Proc.* **2013**, *1512* (1), 1262–1263. <https://doi.org/10.1063/1.4791511>.
- (284) Ganguly, A.; Sharma, S.; Papakonstantinou, P.; Hamilton, J. Probing the Thermal Deoxygenation of Graphene Oxide Using High-Resolution In Situ X-Ray-Based Spectroscopies. *J. Phys. Chem. C* **2011**, *115* (34), 17009–17019. <https://doi.org/10.1021/jp203741y>.
- (285) Guo, B.; Liu, Q.; Chen, E.; Zhu, H.; Fang, L.; Gong, J. R. Controllable N-Doping of Graphene. *Nano Lett.* **2010**, *10* (12), 4975–4980. <https://doi.org/10.1021/nl103079j>.
- (286) Thomas, H. R.; Day, S. P.; Woodruff, W. E.; Vallés, C.; Young, R. J.; Kinloch, I. A.; Morley, G. W.; Hanna, J. V.; Wilson, N. R.; Rourke, J. P. Deoxygenation of Graphene Oxide:



- Reduction or Cleaning? *Chem. Mater.* **2013**, *25* (18), 3580–3588.  
<https://doi.org/10.1021/cm401922e>.
- (287) Becerril, H. A.; Mao, J.; Liu, Z.; Stoltenberg, R. M.; Bao, Z.; Chen, Y. Evaluation of Solution-Processed Reduced Graphene Oxide Films as Transparent Conductors. *ACS Nano* **2008**, *2* (3), 463–470. <https://doi.org/10.1021/nn700375n>.
- (288) Liu, F.; Kim, Y. H.; Cheon, D. S.; Seo, T. S. Micropatterned Reduced Graphene Oxide Based Field-Effect Transistor for Real-Time Virus Detection. *Sens. Actuators B Chem.* **2013**, *186*, 252–257. <https://doi.org/10.1016/j.snb.2013.05.097>.
- (289) Claramunt, S.; Varea, A.; López-Díaz, D.; Velázquez, M. M.; Cornet, A.; Cirera, A. The Importance of Interbands on the Interpretation of the Raman Spectrum of Graphene Oxide. *J. Phys. Chem. C* **2015**, *119* (18), 10123–10129. <https://doi.org/10.1021/acs.jpcc.5b01590>.
- (290) Huh, S. H. Thermal Reduction of Graphene Oxide. 20.
- (291) Pei, S.; Cheng, H.-M. The Reduction of Graphene Oxide. *Carbon* **2012**, *50* (9), 3210–3228. <https://doi.org/10.1016/j.carbon.2011.11.010>.
- (292) Hung Pham, V.; Hyun Hur, S.; Jung Kim, E.; Sung Kim, B.; Suk Chung, J. Highly Efficient Reduction of Graphene Oxide Using Ammonia Borane. *Chem. Commun.* **2013**, *49* (59), 6665–6667. <https://doi.org/10.1039/C3CC43503B>.
- (293) Feng, H.; Cheng, R.; Zhao, X.; Duan, X.; Li, J. A Low-Temperature Method to Produce Highly Reduced Graphene Oxide. *Nat. Commun.* **2013**, *4* (1), 1539. <https://doi.org/10.1038/ncomms2555>.
- (294) Kim, M. J.; Jeong, Y.; Sohn, S.; Lee, S. Y.; Kim, Y. J.; Lee, K.; Kahng, Y. H.; Jang, J.-H. Fast and Low-Temperature Reduction of Graphene Oxide Films Using Ammonia Plasma. *AIP Adv.* **2013**, *3* (1), 012117. <https://doi.org/10.1063/1.4789545>.
- (295) Singh, G.; Sutar, D. S.; Botcha, V. D.; Narayanam, P. K.; Talwar, S. S.; Srinivasa, R. S.; Major, S. S. Study of Simultaneous Reduction and Nitrogen Doping of Graphene Oxide Langmuir–Blodgett Monolayer Sheets by Ammonia Plasma Treatment. *Nanotechnology* **2013**, *24* (35), 355704. <https://doi.org/10.1088/0957-4484/24/35/355704>.
- (296) Muhammad Hafiz, S.; Ritikos, R.; Whitcher, T. J.; Md. Razib, N.; Bien, D. C. S.; Chanlek, N.; Nakajima, H.; Saisopa, T.; Songsirithigul, P.; Huang, N. M.; Rahman, S. A. A Practical Carbon Dioxide Gas Sensor Using Room-Temperature Hydrogen Plasma Reduced Graphene Oxide. *Sens. Actuators B Chem.* **2014**, *193*, 692–700. <https://doi.org/10.1016/j.snb.2013.12.017>.
- (297) Li, J.; Chen, C.; Wei, J.; Li, J.; Wang, X. Enhanced Electrochemical Performance of Reduced Graphene Oxides by H<sub>2</sub>/Ar Plasma Treatment. *J. Phys. Chem. C* **2014**, *118* (49), 28440–28447. <https://doi.org/10.1021/jp509182g>.
- (298) Zhang, L.-S.; Wang, W.; Liang, X.-Q.; Chu, W.-S.; Song, W.-G.; Wang, W.; Wu, Z.-Y. Characterization of Partially Reduced Graphene Oxide as Room Temperature Sensor for H<sub>2</sub>. *Nanoscale* **2011**, *3* (6), 2458–2460. <https://doi.org/10.1039/C1NR10187K>.
- (299) Tu, Y.; Nakamoto, H.; Ichii, T.; Utsunomiya, T.; Khatri, O. P.; Sugimura, H. Fabrication of Reduced Graphene Oxide Micro Patterns by Vacuum-Ultraviolet Irradiation: From Chemical and Structural Evolution to Improving Patterning Precision by Light Collimation. *Carbon* **2017**, *119*, 82–90. <https://doi.org/10.1016/j.carbon.2017.04.008>.
- (300) Sandoval, S.; Kumar, N.; Oro-Solé, J.; Sundaresan, A.; Rao, C. N. R.; Fuertes, A.; Tobias, G. Tuning the Nature of Nitrogen Atoms in N-Containing Reduced Graphene Oxide. *Carbon* **2016**, *96*, 594–602. <https://doi.org/10.1016/j.carbon.2015.09.085>.

- (301) Kiang Chua, C.; Pumera, M. The Reduction of Graphene Oxide with Hydrazine: Elucidating Its Reductive Capability Based on a Reaction-Model Approach. *Chem. Commun.* **2016**, 52 (1), 72–75. <https://doi.org/10.1039/C5CC08170J>.
- (302) Lee, J.; Hwang, E.; Lee, E.; Seo, S.; Lee, H. Tuning of N- and p-Type Reduced Graphene Oxide Transistors with the Same Molecular Backbone. *Chem. – Eur. J.* **2012**, 18 (17), 5155–5159. <https://doi.org/10.1002/chem.201103554>.
- (303) Rourke, J. P.; Pandey, P. A.; Moore, J. J.; Bates, M.; Kinloch, I. A.; Young, R. J.; Wilson, N. R. The Real Graphene Oxide Revealed: Stripping the Oxidative Debris from the Graphene-like Sheets. *Angew. Chem. Int. Ed.* **2011**, 50 (14), 3173–3177. <https://doi.org/10.1002/anie.201007520>.
- (304) Li, D.; Yu, C.; Wang, M.; Zhang, Y.; Pan, C. Synthesis of Nitrogen Doped Graphene from Graphene Oxide within an Ammonia Flame for High Performance Supercapacitors. *RSC Adv.* **2014**, 4 (98), 55394–55399. <https://doi.org/10.1039/C4RA10761F>.
- (305) Nolan, H.; Mendoza-Sanchez, B.; Kumar, N. A.; McEvoy, N.; O’Brien, S.; Nicolosi, V.; S. Duesberg, G. Nitrogen-Doped Reduced Graphene Oxide Electrodes for Electrochemical Supercapacitors. *Phys. Chem. Chem. Phys.* **2014**, 16 (6), 2280–2284. <https://doi.org/10.1039/C3CP54877E>.
- (306) Zhang, Y.; Sun, Z.; Wang, H.; Wang, Y.; Liang, M.; Xue, S. Nitrogen-Doped Graphene as a Cathode Material for Dye-Sensitized Solar Cells: Effects of Hydrothermal Reaction and Annealing on Electrocatalytic Performance. *RSC Adv.* **2015**, 5 (14), 10430–10439. <https://doi.org/10.1039/C4RA13224F>.
- (307) X-Ray Photoelectron Spectroscopy (XPS) Reference Pages.
- (308) *XPS Interpretation of Carbon*. <https://www.jp.xpssimplified.com/elements/carbon.php> (accessed 2022-05-10).
- (309) de Lima, B. S.; Bernardi, M. I. B.; Mastelaro, V. R. Wavelength Effect of Ns-Pulsed Radiation on the Reduction of Graphene Oxide. *Appl. Surf. Sci.* **2020**, 506, 144808. <https://doi.org/10.1016/j.apsusc.2019.144808>.
- (310) Kiang Chua, C.; Pumera, M. Renewal of Sp<sup>2</sup> Bonds in Graphene Oxides via Dehydrobromination. *J. Mater. Chem.* **2012**, 22 (43), 23227–23231. <https://doi.org/10.1039/C2JM34358D>.
- (311) Stobinski, L.; Lesiak, B.; Malolepszy, A.; Mazurkiewicz, M.; Mierzwa, B.; Zemek, J.; Jiricek, P.; Bieloshapka, I. Graphene Oxide and Reduced Graphene Oxide Studied by the XRD, TEM and Electron Spectroscopy Methods. *J. Electron Spectrosc. Relat. Phenom.* **2014**, 195, 145–154. <https://doi.org/10.1016/j.elspec.2014.07.003>.
- (312) Chen, Y.; Xie, B.; Ren, Y.; Yu, M.; Qu, Y.; Xie, T.; Zhang, Y.; Wu, Y. Designed Nitrogen Doping of Few-Layer Graphene Functionalized by Selective Oxygenic Groups. *Nanoscale Res. Lett.* **2014**, 9, 646. <https://doi.org/10.1186/1556-276X-9-646>.
- (313) Bag, S.; Mondal, B.; Das, A. K.; Raj, C. R. Nitrogen and Sulfur Dual-Doped Reduced Graphene Oxide: Synergistic Effect of Dopants Towards Oxygen Reduction Reaction. *Electrochimica Acta* **2015**, 163, 16–23. <https://doi.org/10.1016/j.electacta.2015.02.130>.
- (314) Lin, Y.-C.; Teng, P.-Y.; Yeh, C.-H.; Koshino, M.; Chiu, P.-W.; Suenaga, K. Structural and Chemical Dynamics of Pyridinic-Nitrogen Defects in Graphene. *Nano Lett.* **2015**, 15 (11), 7408–7413. <https://doi.org/10.1021/acs.nanolett.5b02831>.
- (315) Lee, D. W.; De Los Santos V., L.; Seo, J. W.; Felix, L. L.; Bustamante D., A.; Cole, J. M.; Barnes, C. H. W. The Structure of Graphite Oxide: Investigation of Its Surface Chemical Groups. *J. Phys. Chem. B* **2010**, 114 (17), 5723–5728. <https://doi.org/10.1021/jp1002275>.

- (316) Karteri, İ.; Karataş, Ş.; Yakuphanoglu, F. Electrical Characterization of Graphene Oxide and Organic Dielectric Layers Based on Thin Film Transistor. *Appl. Surf. Sci.* **2014**, *318*, 74–78. <https://doi.org/10.1016/j.apsusc.2014.01.013>.
- (317) *Solubility of Ammonia* | *Flinn Scientific*. <https://www.flinnsci.com/solubility-of-ammonia/dc10832/> (accessed 2022-05-12).
- (318) *Argon (Ar) and water*. <https://www.lenntech.com/periodic/water/argon/argon-and-water.htm> (accessed 2022-05-12).
- (319) Acik, M.; Mattevi, C.; Gong, C.; Lee, G.; Cho, K.; Chhowalla, M.; Chabal, Y. J. The Role of Intercalated Water in Multilayered Graphene Oxide. *ACS Nano* **2010**, *4* (10), 5861–5868. <https://doi.org/10.1021/nn101844t>.
- (320) Kim, D.; Kim, D. W.; Lim, H.-K.; Jeon, J.; Kim, H.; Jung, H.-T.; Lee, H. Intercalation of Gas Molecules in Graphene Oxide Interlayer: The Role of Water. *J. Phys. Chem. C* **2014**, *118* (20), 11142–11148. <https://doi.org/10.1021/jp5026762>.
- (321) Buchsteiner, A.; Lurf, A.; Pieper, J. Water Dynamics in Graphite Oxide Investigated with Neutron Scattering. *J. Phys. Chem. B* **2006**, *110* (45), 22328–22338. <https://doi.org/10.1021/jp0641132>.
- (322) Cui, Y.; Wei, Q.; Park, H.; Lieber, C. M. Nanowire Nanosensors for Highly Sensitive and Selective Detection of Biological and Chemical Species. *Science* **2001**, *293* (5533), 1289–1292. <https://doi.org/10.1126/science.1062711>.
- (323) Salvo, P.; Melai, B.; Calisi, N.; Paoletti, C.; Bellagambi, F.; Kirchhain, A.; Trivella, M. G.; Fuoco, R.; Di Francesco, F. Graphene-Based Devices for Measuring PH. *Sens. Actuators B Chem.* **2018**, *256*, 976–991. <https://doi.org/10.1016/j.snb.2017.10.037>.
- (324) Dubin, S.; Gilje, S.; Wang, K.; Tung, V. C.; Cha, K.; Hall, A. S.; Farrar, J.; Varshneya, R.; Yang, Y.; Kaner, R. B. A One-Step, Solvothermal Reduction Method for Producing Reduced Graphene Oxide Dispersions in Organic Solvents. *ACS Nano* **2010**, *4* (7), 3845–3852. <https://doi.org/10.1021/nn100511a>.
- (325) Wang, Y.; Shao, Y.; Matson, D. W.; Li, J.; Lin, Y. Nitrogen-Doped Graphene and Its Application in Electrochemical Biosensing. *ACS Nano* **2010**, *4* (4), 1790–1798. <https://doi.org/10.1021/nn100315s>.
- (326) Das, T. K.; Banerjee, S.; Kumar, A.; Debnath, A. K.; Sudarsan, V. Electrochemical Performance of Hydrothermally Synthesized N-Doped Reduced Graphene Oxide Electrodes for Supercapacitor Application. *Solid State Sci.* **2019**, *96*, 105952. <https://doi.org/10.1016/j.solidstatesciences.2019.105952>.
- (327) Luo, Z.; Lim, S.; Tian, Z.; Shang, J.; Lai, L.; MacDonald, B.; Fu, C.; Shen, Z.; Yu, T.; Lin, J. Pyridinic N Doped Graphene: Synthesis, Electronic Structure, and Electrocatalytic Property. *J. Mater. Chem.* **2011**, *21* (22), 8038–8044. <https://doi.org/10.1039/C1JM10845J>.
- (328) Senthilnathan, J.; Sanjeeva Rao, K.; Yoshimura, M. Submerged Liquid Plasma – Low Energy Synthesis of Nitrogen-Doped Graphene for Electrochemical Applications. *J. Mater. Chem. A* **2014**, *2* (10), 3332–3337. <https://doi.org/10.1039/C3TA14946C>.
- (329) Oliveira, A. E. F.; Braga, G. B.; Tarley, C. R. T.; Pereira, A. C. Thermally Reduced Graphene Oxide: Synthesis, Studies and Characterization. *J. Mater. Sci.* **2018**, *53* (17), 12005–12015. <https://doi.org/10.1007/s10853-018-2473-3>.
- (330) Chen, X.; Meng, D.; Wang, B.; Li, B.-W.; Li, W.; Bielawski, C. W.; Ruoff, R. S. Rapid Thermal Decomposition of Confined Graphene Oxide Films in Air. *Carbon* **2016**, *101*, 71–76. <https://doi.org/10.1016/j.carbon.2016.01.075>.

- (331) Sun, Z.; Fang, G.; Li, J.; Mo, J.; He, X.; Wang, X.; Yu, Z. Preparation of (Ti, Zr) Co-Doped Hematite Photoanode for Enhanced Photoelectrochemical Water Splitting. *Chem. Phys. Lett.* **2020**, *754*, 137736. <https://doi.org/10.1016/j.cplett.2020.137736>.
- (332) Wang, J.; Du, C.; Peng, Q.; Yang, J.; Wen, Y.; Shan, B.; Chen, R. Enhanced Photoelectrochemical Water Splitting Performance of Hematite Nanorods by Co and Sn Co-Doping. *Int. J. Hydrog. Energy* **2017**, *42* (49), 29140–29149. <https://doi.org/10.1016/j.ijhydene.2017.10.080>.
- (333) Prasad, U.; L. Young, J.; C. Johnson, J.; L. McGott, D.; Gu, H.; Garfunkel, E.; M. Kannan, A. Enhancing Interfacial Charge Transfer in a WO<sub>3</sub>/BiVO<sub>4</sub> Photoanode Heterojunction through Gallium and Tungsten Co-Doping and a Sulfur Modified Bi<sub>2</sub>O<sub>3</sub> Interfacial Layer. *J. Mater. Chem. A* **2021**, *9* (29), 16137–16149. <https://doi.org/10.1039/D1TA03786B>.
- (334) Venkata Reddy, C.; Reddy, I. N.; Akkinapally, B.; Reddy, K. R.; Shim, J. Synthesis and Photoelectrochemical Water Oxidation of (Y, Cu) Codoped  $\alpha$ -Fe<sub>2</sub>O<sub>3</sub> Nanostructure Photoanode. *J. Alloys Compd.* **2020**, *814*, 152349. <https://doi.org/10.1016/j.jallcom.2019.152349>.
- (335) Yoon, K.-Y.; Park, J.; Jung, M.; Ji, S.-G.; Lee, H.; Seo, J. H.; Kwak, M.-J.; Il Seok, S.; Lee, J. H.; Jang, J.-H. NiFeOx Decorated Ge-Hematite/Perovskite for an Efficient Water Splitting System. *Nat. Commun.* **2021**, *12* (1), 4309. <https://doi.org/10.1038/s41467-021-24428-7>.
- (336) Zhang, H.; Li, D.; Byun, W. J.; Wang, X.; Shin, T. J.; Jeong, H. Y.; Han, H.; Li, C.; Lee, J. S. Gradient Tantalum-Doped Hematite Homo Junction Photoanode Improves Both Photocurrents and Turn-on Voltage for Solar Water Splitting. *Nat. Commun.* **2020**, *11* (1), 4622. <https://doi.org/10.1038/s41467-020-18484-8>.
- (337) Sivula, K.; Formal, F. L.; Grätzel, M. WO<sub>3</sub>-Fe<sub>2</sub>O<sub>3</sub> Photoanodes for Water Splitting: A Host Scaffold, Guest Absorber Approach. *Chem. Mater.* **2009**, *21* (13), 2862–2867. <https://doi.org/10.1021/cm900565a>.
- (338) Jeong, I. K.; Mahadik, M. A.; Hwang, J. B.; Chae, W.-S.; Choi, S. H.; Jang, J. S. Lowering the Onset Potential of Zr-Doped Hematite Nanocoral Photoanodes by Al Co-Doping and Surface Modification with Electrodeposited Co-Pi. *J. Colloid Interface Sci.* **2021**, *581*, 751–763. <https://doi.org/10.1016/j.jcis.2020.08.003>.
- (339) Lin, Y.; Xu, Y.; Mayer, M. T.; Simpson, Z. I.; McMahon, G.; Zhou, S.; Wang, D. Growth of P-Type Hematite by Atomic Layer Deposition and Its Utilization for Improved Solar Water Splitting. *J. Am. Chem. Soc.* **2012**, *134* (12), 5508–5511. <https://doi.org/10.1021/ja300319g>.
- (340) Liao, P.; Carter, E. A. Hole Transport in Pure and Doped Hematite. *J. Appl. Phys.* **2012**, *112* (1), 013701. <https://doi.org/10.1063/1.4730634>.
- (341) Rauf, A.; Adil, M.; Mian, S. A.; Rahman, G.; Ahmed, E.; Mohy Ud Din, Z.; Qun, W. Tuning the Optoelectronic Properties of Hematite with Rhodium Doping for Photoelectrochemical Water Splitting Using Density Functional Theory Approach. *Sci. Rep.* **2021**, *11* (1), 41. <https://doi.org/10.1038/s41598-020-78824-y>.
- (342) Yang, T.-Y.; Kang, H.-Y.; Sim, U.; Lee, Y.-J.; Lee, J.-H.; Koo, B.; Tae Nam, K.; Joo, Y.-C. A New Hematite Photoanode Doping Strategy for Solar Water Splitting: Oxygen Vacancy Generation. *Phys. Chem. Chem. Phys.* **2013**, *15* (6), 2117–2124. <https://doi.org/10.1039/C2CP44352J>.
- (343) Sivula, K.; Zboril, R.; Le Formal, F.; Robert, R.; Weidenkaff, A.; Tucek, J.; Frydrych, J.; Grätzel, M. Photoelectrochemical Water Splitting with Mesoporous Hematite Prepared by a Solution-Based Colloidal Approach. *J. Am. Chem. Soc.* **2010**, *132* (21), 7436–7444. <https://doi.org/10.1021/ja101564f>.



- (344) Zhou, Y.; Yan, M.; Hou, J.; Niu, Y.; Ni, D.; Shen, H.; Niu, P.; Ma, Y. Introduction of Oxygen Vacancies into Hematite in Local Reducing Atmosphere for Solar Water Oxidation. *Sol. Energy* **2019**, *179*, 99–105. <https://doi.org/10.1016/j.solener.2018.12.059>.
- (345) Pyeon, M.; Ruoko, T.-P.; Leduc, J.; Gönüllü, Y.; Deo, M.; Tkachenko, N. V.; Mathur, S. Critical Role and Modification of Surface States in Hematite Films for Enhancing Oxygen Evolution Activity. *J. Mater. Res.* **2018**, *33* (4), 455–466. <https://doi.org/10.1557/jmr.2017.465>.
- (346) Papaioannou, J. C.; Patermarakis, G. S.; Karayianni, H. S. Electron Hopping Mechanism in Hematite ( $\alpha$ -Fe<sub>2</sub>O<sub>3</sub>). *J. Phys. Chem. Solids* **2005**, *66* (5), 839–844. <https://doi.org/10.1016/j.jpcs.2004.11.002>.
- (347) Ling, Y.; Wang, G.; Reddy, J.; Wang, C.; Zhang, J. Z.; Li, Y. The Influence of Oxygen Content on the Thermal Activation of Hematite Nanowires. *Angew. Chem.* **2012**, *124* (17), 4150–4155. <https://doi.org/10.1002/ange.201107467>.
- (348) Barik, R.; Pandey, B.; Anand, S.; Mohapatra, M. A Facile, Single-Step Synthesis of Flowery Shaped, Pure/Lithium-Doped 3D Iron Oxides. *J. Mater. Chem. A* **2014**, *2* (31), 12380–12389. <https://doi.org/10.1039/C4TA00270A>.
- (349) Cai, J.; Xu, L.; Tang, X.; Kong, L.; Wang, J.; Wang, R.; Li, X.; Xie, Q.; Mao, K.; Pan, H. Role of Lithium Doping on  $\alpha$ -Fe<sub>2</sub>O<sub>3</sub> Photoanode for Enhanced Photoelectrochemical Water Oxidation. *J. Alloys Compd.* **2022**, *915*, 165349. <https://doi.org/10.1016/j.jallcom.2022.165349>.
- (350) Lu, J.; Peng, Q.; Wang, Z.; Nan, C.; Li, L.; Li, Y. Hematite Nanodiscs Exposing (001) Facets: Synthesis, Formation Mechanism and Application for Li-Ion Batteries. *J. Mater. Chem. A* **2013**, *1* (17), 5232–5237. <https://doi.org/10.1039/C3TA01539D>.
- (351) Kim, H.-J.; Choi, K.-I.; Pan, A.; Kim, I.-D.; Kim, H.-R.; Kim, K.-M.; Woong Na, C.; Cao, G.; Lee, J.-H. Template-Free Solvothermal Synthesis of Hollow Hematite Spheres and Their Applications in Gas Sensors and Li-Ion Batteries. *J. Mater. Chem.* **2011**, *21* (18), 6549–6555. <https://doi.org/10.1039/C0JM03516E>.
- (352) Abdi, F. F.; Han, L.; Smets, A. H. M.; Zeman, M.; Dam, B.; van de Krol, R. Efficient Solar Water Splitting by Enhanced Charge Separation in a Bismuth Vanadate-Silicon Tandem Photoelectrode. *Nat. Commun.* **2013**, *4*, 2195. <https://doi.org/10.1038/ncomms3195>.
- (353) Piekner, Y.; S. Ellis, D.; A. Grave, D.; Tsyganok, A.; Rothschild, A. Wasted Photons: Photogeneration Yield and Charge Carrier Collection Efficiency of Hematite Photoanodes for Photoelectrochemical Water Splitting. *Energy Environ. Sci.* **2021**, *14* (8), 4584–4598. <https://doi.org/10.1039/D1EE01772A>.
- (354) Marusak, L. A.; Messier, R.; White, W. B. Optical Absorption Spectrum of Hematite, AFe<sub>2</sub>O<sub>3</sub> near IR to UV. *J. Phys. Chem. Solids* **1980**, *41* (9), 981–984. [https://doi.org/10.1016/0022-3697\(80\)90105-5](https://doi.org/10.1016/0022-3697(80)90105-5).
- (355) Bjoerksten, U.; Moser, J.; Graetzel, M. Photoelectrochemical Studies on Nanocrystalline Hematite Films. *Chem. Mater.* **1994**, *6* (6), 858–863. <https://doi.org/10.1021/cm00042a026>.
- (356) Beermann, N.; Vayssieres, L.; Lindquist, S.-E.; Hagfeldt, A. Photoelectrochemical Studies of Oriented Nanorod Thin Films of Hematite. *J. Electrochem. Soc.* **2000**, *147* (7), 2456–2461. <https://doi.org/10.1149/1.1393553>.
- (357) Prakash, J.; Prasad, U.; Shi, X.; Peng, X.; Azeredo, B.; Kannan, A. M. Photoelectrochemical Water Splitting Using Lithium Doped Bismuth Vanadate Photoanode with Near-Complete Bulk Charge Separation. *J. Power Sources* **2020**, *448*, 227418. <https://doi.org/10.1016/j.jpowsour.2019.227418>.
- (358) Meyer, B. K.; Sann, J.; Zeuner, A. Lithium and Sodium Acceptors in ZnO. *Superlattices Microstruct.* **2005**, *38* (4), 344–348. <https://doi.org/10.1016/j.spmi.2005.08.006>.

- (359) Rauch, C.; Gehlhoff, W.; Wagner, M. R.; Malguth, E.; Callsen, G.; Kirste, R.; Salameh, B.; Hoffmann, A.; Polarz, S.; Aksu, Y.; Driess, M. Lithium Related Deep and Shallow Acceptors in Li-Doped ZnO Nanocrystals. *J. Appl. Phys.* **2010**, *107* (2), 024311. <https://doi.org/10.1063/1.3275889>.
- (360) Çelik, Ö.; Baturay, Ş.; Ocak, Y. S. Sb Doping Influence on Structural Properties of ZnO Thin Films. *Mater. Res. Express* **2020**, *7* (2), 026403. <https://doi.org/10.1088/2053-1591/ab6c8a>.
- (361) Mendoza-Galván, A.; Trejo-Cruz, C.; Lee, J.; Bhattacharyya, D.; Metson, J.; Evans, P. J.; Pal, U. Effect of Metal-Ion Doping on the Optical Properties of Nanocrystalline ZnO Thin Films. *J. Appl. Phys.* **2006**, *99* (1), 014306. <https://doi.org/10.1063/1.2158503>.
- (362) Glasscock, J. A.; Barnes, P. R. F.; Plumb, I. C.; Savvides, N. Enhancement of Photoelectrochemical Hydrogen Production from Hematite Thin Films by the Introduction of Ti and Si. *J. Phys. Chem. C* **2007**, *111* (44), 16477–16488. <https://doi.org/10.1021/jp0745561>.
- (363) Bersani, D.; Lottici, P. P.; Montenero, A. Micro-Raman Investigation of Iron Oxide Films and Powders Produced by Sol–Gel Syntheses. *J. Raman Spectrosc.* **1999**, *30* (5), 355–360. [https://doi.org/10.1002/\(SICI\)1097-4555\(199905\)30:5<355::AID-JRS398>3.0.CO;2-C](https://doi.org/10.1002/(SICI)1097-4555(199905)30:5<355::AID-JRS398>3.0.CO;2-C).
- (364) Fu, Y. Y.; Wang, R. M.; Xu, J.; Chen, J.; Yan, Y.; Narlikar, A. V.; Zhang, H. Synthesis of Large Arrays of Aligned  $\alpha$ -Fe<sub>2</sub>O<sub>3</sub> Nanowires. *Chem. Phys. Lett.* **2003**, *379* (3), 373–379. <https://doi.org/10.1016/j.cplett.2003.08.061>.
- (365) Jubb, A. M.; Allen, H. C. Vibrational Spectroscopic Characterization of Hematite, Maghemite, and Magnetite Thin Films Produced by Vapor Deposition. *ACS Appl. Mater. Interfaces* **2010**, *2* (10), 2804–2812. <https://doi.org/10.1021/am1004943>.
- (366) Zhu, C.; Li, C.; Zheng, M.; Delaunay, J.-J. Plasma-Induced Oxygen Vacancies in Ultrathin Hematite Nanoflakes Promoting Photoelectrochemical Water Oxidation. *ACS Appl. Mater. Interfaces* **2015**, *7* (40), 22355–22363. <https://doi.org/10.1021/acsami.5b06131>.
- (367) Sima, M.; Matei, E.; Vasile, E.; Sima, A.; Preda, N.; Logofatu, C. Water Oxidation at Photoanodes Based on Hematite Films and Nanowire Arrays. *Thin Solid Films* **2021**, *724*, 138626. <https://doi.org/10.1016/j.tsf.2021.138626>.
- (368) Wang, R. X.; Beling, C. D.; Fung, S.; Djurišić, A. B.; Ling, C. C.; Kwong, C.; Li, S. Influence of Annealing Temperature and Environment on the Properties of Indium Tin Oxide Thin Films. *J. Phys. D: Appl. Phys.* **2005**, *38* (12), 2000–2005. <https://doi.org/10.1088/0022-3727/38/12/022>.
- (369) Esteves Nogueira, A.; Soares, M. R. S.; Junior, J. B. S.; Ramirez, C. A. O.; Leandro Souza, F.; Roberto Leite, E. Discovering a Selective Semimetal Element to Increase Hematite Photoanode Charge Separation Efficiency. *J. Mater. Chem. A* **2019**, *7* (28), 16992–16998. <https://doi.org/10.1039/C9TA05452A>.
- (370) Yi, J. B.; Lim, C. C.; Xing, G. Z.; Fan, H. M.; Van, L. H.; Huang, S. L.; Yang, K. S.; Huang, X. L.; Qin, X. B.; Wang, B. Y.; Wu, T.; Wang, L.; Zhang, H. T.; Gao, X. Y.; Liu, T.; Wee, A. T. S.; Feng, Y. P.; Ding, J. Ferromagnetism in Dilute Magnetic Semiconductors through Defect Engineering: Li-Doped ZnO. *Phys. Rev. Lett.* **2010**, *104* (13), 137201. <https://doi.org/10.1103/PhysRevLett.104.137201>.
- (371) Ullah Awan, S.; Hasanain, S. K.; Bertino, M. F.; Hassnain Jaffari, G. Ferromagnetism in Li Doped ZnO Nanoparticles: The Role of Interstitial Li. *J. Appl. Phys.* **2012**, *112* (10), 103924. <https://doi.org/10.1063/1.4767364>.
- (372) Shigesato, Y.; Hayashi, Y.; Haranoh, T. Doping Mechanisms of Tin-doped Indium Oxide Films. *Appl. Phys. Lett.* **1992**, *61* (1), 73–75. <https://doi.org/10.1063/1.107673>.

- (373) Li, X.; Wang, Y.; Liu, W.; Jiang, G.; Zhu, C. Study of Oxygen Vacancies' Influence on the Lattice Parameter in ZnO Thin Film. *Mater. Lett.* **2012**, *85*, 25–28. <https://doi.org/10.1016/j.matlet.2012.06.107>.
- (374) Hardee, K. L.; Bard, A. J. Semiconductor Electrodes V. The Application of Chemically Vapor Deposited Iron Oxide Films to Photosensitized Electrolysis. *J. Electrochem. Soc.* **1976**, *123* (7), 1024–1026. <https://doi.org/10.1149/1.2132984>.
- (375) Dotan, H.; Sivula, K.; Grätzel, M.; Rothschild, A.; C. Warren, S. Probing the Photoelectrochemical Properties of Hematite ( $\alpha\text{-Fe}_2\text{O}_3$ ) Electrodes Using Hydrogen Peroxide as a Hole Scavenger. *Energy Environ. Sci.* **2011**, *4* (3), 958–964. <https://doi.org/10.1039/C0EE00570C>.
- (376) Iwanski, P.; Curran, J. S.; Gissler, W.; Memming, R. The Photoelectrochemical Behavior of Ferric Oxide in the Presence of Redox Reagents. *J. Electrochem. Soc.* **1981**, *128* (10), 2128. <https://doi.org/10.1149/1.2127202>.
- (377) K. Dunn, H.; M. Feckl, J.; Müller, A.; Fattakhova-Rohlfing, D.; G. Morehead, S.; Roos, J.; M. Peter, L.; Scheu, C.; Bein, T. Tin Doping Speeds up Hole Transfer during Light-Driven Water Oxidation at Hematite Photoanodes. *Phys. Chem. Chem. Phys.* **2014**, *16* (44), 24610–24620. <https://doi.org/10.1039/C4CP03946G>.
- (378) Tilley, S. D.; Cornuz, M.; Sivula, K.; Grätzel, M. Light-Induced Water Splitting with Hematite: Improved Nanostructure and Iridium Oxide Catalysis. *Angew. Chem. Int. Ed.* **2010**, *49* (36), 6405–6408. <https://doi.org/10.1002/anie.201003110>.
- (379) Pu, A.; Deng, J.; Li, M.; Gao, J.; Zhang, H.; Hao, Y.; Zhong, J.; Sun, X. Coupling Ti-Doping and Oxygen Vacancies in Hematite Nanostructures for Solar Water Oxidation with High Efficiency. *J. Mater. Chem. A* **2014**, *2* (8), 2491–2497. <https://doi.org/10.1039/C3TA14575A>.
- (380) Rajendran, R.; Yaakob, Z.; Pudukudy, M.; Rahaman, M. S. A.; Sopian, K. Photoelectrochemical Water Splitting Performance of Vertically Aligned Hematite Nanoflakes Deposited on FTO by a Hydrothermal Method. *J. Alloys Compd.* **2014**, *608*, 207–212. <https://doi.org/10.1016/j.jallcom.2014.04.105>.
- (381) Ling, Y.; Wang, G.; Wang, H.; Yang, Y.; Li, Y. Low-Temperature Activation of Hematite Nanowires for Photoelectrochemical Water Oxidation. *ChemSusChem* **2014**, *7* (3), 848–853. <https://doi.org/10.1002/cssc.201301013>.
- (382) Biswas, P.; Ainabayev, A.; Zhussupbekova, A.; Jose, F.; O'Connor, R.; Kaisha, A.; Walls, B.; Shvets, I. V. Tuning of Oxygen Vacancy-Induced Electrical Conductivity in Ti-Doped Hematite Films and Its Impact on Photoelectrochemical Water Splitting. *Sci. Rep.* **2020**, *10* (1), 7463. <https://doi.org/10.1038/s41598-020-64231-w>.
- (383) Fernández-Climent, R.; Giménez, S.; García-Tecedor, M. The Role of Oxygen Vacancies in Water Splitting Photoanodes. *Sustain. Energy Fuels* **2020**, *4* (12), 5916–5926. <https://doi.org/10.1039/D0SE01305F>.
- (384) Rioult, M.; Stanescu, D.; Fonda, E.; Barbier, A.; Magnan, H. Oxygen Vacancies Engineering of Iron Oxides Films for Solar Water Splitting. *J. Phys. Chem. C* **2016**, *120* (14), 7482–7490. <https://doi.org/10.1021/acs.jpcc.6b00552>.
- (385) Zhang, X.; Klaver, P.; van Santen, R.; van de Sanden, M. C. M.; Bieberle-Hütter, A. Oxygen Evolution at Hematite Surfaces: The Impact of Structure and Oxygen Vacancies on Lowering the Overpotential. *J. Phys. Chem. C* **2016**, *120* (32), 18201–18208. <https://doi.org/10.1021/acs.jpcc.6b07228>.
- (386) Owens, F. J.; Orosz, J. Effect of Nanosizing on Lattice and Magnon Modes of Hematite. *Solid State Commun.* **2006**, *138* (2), 95–98. <https://doi.org/10.1016/j.ssc.2006.01.049>.







## Curriculum Vitae

Name	Paolo Rudatis
Date of birth	5 <sup>th</sup> September 1991
Place of birth	Bondeno, Ferrara, Italy
Nationality	Italian
<b>School education</b>	
2005 – 2010	Perito chimico industriale – Industrial chemical technician at I.T.I. Copernico-Carpeggiani, Ferrara
07/2010	Diploma
<b>Higher education</b>	
09/2010 – 10/2013	Diploma thesis in chemistry at University of Ferrara Title: Passivation techniques of DSSC photoanode: a comparison
09/2013 – 03/2016	Diploma thesis in chemical sciences at University of Ferrara Title: Interfacial modifications of iron oxide surfaces for electrochemical and photoelectrochemical processes
<b>PhD studies</b>	
12/2016	Beginning of PhD studies at the institute of material chemistry under the supervision of Prof. Dr. D. Eder.
06/2018	PhD studies continue with University assistant role
<b>Skills</b>	
09/2016	C1 English proficiency IELTS academic certificate
03/2018	B2/1 German proficiency Vienna University Language Centre certificate

## List of publications

1. M. V. Kharlamova, C. Kramberger, P. Rudatis, T. Pichler, and D. Eder “Revealing the doping effect of encapsulated lead halogenides on single-walled carbon nanotube” *Appl. Phys. A*, **2019**, *125*, 320; DOI: 10.1007/s00339-019-2626-5
2. M. V. Kharlamova, C. Kramberger, P. Rudatis, K. Yanagi, and D. Eder “Characterization of the Electronic Properties of Single-Walled Carbon Nanotubes Filled with an Electron Donor – Rubidium Iodide: Multifrequency Raman and X-ray Photoelectron Spectroscopy Studies” *Phys. Status Solidi B*, **2019**, *256*, 1900209; DOI: 10.1002/pssb.20190020
3. M. Orlandi, A. Mazzi, G. Arban, N. Bazzanella, P. Rudatis, S. Caramori, N. Patel, R. Fernandes, C. A. Bignozzi, and A. Miotello “On the effect of Sn-doping in hematite anodes for oxygen evolution” *Electrochim. Acta.*, **2016**, *214*, 345-353; DOI: 10.1016/j.electacta.2016.08.046
4. P. Rudatis, J. Hrubesch, S. Kremshuber, D. H. Apaydin, and D. Eder “Enhanced OER Activity in Hematite Photoanodes: Effect of Sb-Li Co-doping”, *accepted for publication in ACS Omega* on 1<sup>st</sup> December 2022.

Further manuscripts are in the process of being published or in the draft phase.

- P. Rudatis, P. Aspermaier, J. Binting, D. H. Apaydin, W. Knoll, and D. Eder, “Comparing NH<sub>3</sub> and hydrazine treatments on graphene oxide for FET live pH sensing” ..., *drafting*

## List of conferences

- nanoGe Fall Meeting. Symposium “Solar Fuel Synthesis: From Bio-inspired Catalysis to Devices”. 04.11 – 08.11.2019, Berlin, Germany.  
Poster contribution: P. Rudatis, S. Kremshuber, and D. Eder “Alternative Approaches for Hematite-Based Photoanodes in Water Oxidation”

- 34. Workshop on Novel Materials and Superconductors, 10.02 – 15.02.2019, Schladming, Austria.  
Oral contribution: P. Rudatis, G. Haselmann, A. Cherevan, J. Bintinger, W. Knoll and D. Eder “From Graphene Biosensing to Hematite (Photo)sensing”
- Doctoral College TU-D meeting, 24.09 – 26.09.2018, Langenlois, Austria.  
Oral contribution: P. Rudatis, J. Bintinger, W. Knoll and D. Eder “Unravelling the Effect of Reduction and N-Doping of Graphene Oxide on its Performance as Transducer and pH Sensor in Liquid-Gated GFETs”
- Nanomat International Conference on Nanomaterials and Nanodevices, 03.09. – 05.09.2018, Vienna, Austria.  
Oral contribution: P. Rudatis, J. Bintinger, W. Knoll, and D. Eder “Unravelling the Effect of Reduction and N-Doping of Graphene Oxide on its Performance as Transducer and pH Sensor in Liquid-Gated GFETs”
- 32. Workshop on Novel Materials and Superconductors, 11.02. – 17.02.2018, Obertraun, Austria.  
Poster contribution: P. Rudatis, J. Bintinger, A. Cherevan, H. Mikula, W. Knoll and D. Eder “Unravelling the Effect of Reduction and Amino-Functionalisation of Graphene Oxide on its Performance as Transducer and pH Sensor”
- Doctoral College TU-D meeting, 26.09 – 28.09.2017, Langenlois, Austria.  
Oral contribution: P. Rudatis, J. Bintinger, W. Knoll and D. Eder “Reducing Graphene Oxide towards liquid-gated GFET”

## Acknowledgements

First of all, I would like to acknowledge my supervisor, who allowed me to perform research with a huge deal of independency. Dominik hired me and offered me not only a salary and his outstanding experience, but a chance to express my potential in academia. Additionally, it was valuable that he could well understand and hence support me during particularly hard times. Along with him, a big thank goes to the TU-D Doctoral College for funding, organisation of the lectures and activities, and the cordial environment they could create.

Since I am talking about work, I would like to recognise all the people I have met there with a sort of chronological order.

Johannes Bintinger for the introduction to AIT, to the sensing project, and to the first lab teachings; Wolfgang Knoll for the warm and kind welcome in the AIT biosensing research group, the fruitful discussions, and the feeling to be valued; and Patrik Aspermaier for his kindness, friendliness, collaboration, and co-work.

Next, I come to the doctoral college TU-D and its members, a maniple of clever and dreamy minds amongst professors and PhD students, who I must deeply thank for the knowledge exchange, and the good time together. Of course, Dominik and I were not there by chance. And I am a bit sorry I could not find shared projects or not be a better team player.

Dogukan, my Sun and Moon, and polar star, in times of darkness and extremely low self-assurance. He had even doubted not to appear in the acknowledgements, "Mate, I should make you a monument, how could you doubt it?" However, this was the chance to sing even louder his praises and to tell another funny story.

Now, I would like to thank heartily my all research group members, for their friendship, patience, help, measurements, chats, relaxing moments. Always proceeding chronologically, I am very grateful to Oliver, Alexey, Jia, Paul, Greta, Leonie, Sreejith, Ariane, Tushar, Ralf, Stefan K., Jakob H., Luca, Jakob B., Jakob R., Bernhard B-S., Dogukan, Stephen, Samar, Bernhard F., Markus. Particularly, I have to thank those who could help me out in learning new techniques, gave me access to analysis, measured my samples, correct this monography and other manuscripts. In this context, there are other people, whom I have to acknowledge, that is, Werner, Annette, Markus S for the expertise and allowance to conduct analyses in their centres. I must also recognise other research groups and their members, Prof Fleig's group and especially Maximilian and Matthias for the uncomplicated and helpful hand, for collaborating and introducing me to their facilities. A big thank goes to Miriam's, Peter's, Kirchner's, members too. Specifically, to the people who aided my personal research and during students laboratories. Then, I can hardly mention the many students; master's and bachelor's ones, who helped the whole group to keep delivering good work and bring in

some new energy and good vibes. Furthermore, I must also thank the organisational stuff, with which I mean Stephan R-P, Martina, Tammy, Julia, Angelika who could make the work much smoother and easy, and also bringing along their positive attitude with jokes and managing the stress of the research-related personnel.

Last but not least, all the people who sustained my motivation and curiosity out the working environment. That means all the friends, acquaintances, and love partners, I have met in my Viennese life path. With them, I could free my mind from work-related labyrinths, feeling at the same time appreciated and understood. Conversely, some friends have always been there, from the rural little village, throughout academic studies to PhD beginning and end of it (quite a while indeed). Amongst these many, some have become essential friends because of strong similarities either that means personality, reasoning, or that means interests, hobbies. I want to name the ones who have stood out of the crowd, for many rational and irrational reasons – Manuel, Giuseppe, Marco, and Niccolò. I should add a little and specific mention for my dear Austrian tandem partners in Vienna, namely, Lea Alice and Susanne, who had facilitated my integration process in Austria and helped me out to feel less stupid (fundamental during PhD time). Again, I would like to express my deep gratitude to my family – I would have never arrived at this point without them. Thank you immensely for the love, dignity, moral values, and the critical trust/doubts.

At the end, I offer some uncommon thanks to German language, cycling/running, and climbing; that is, activities that allowed me to further socialise, relax, change perspectives, and challenge physically. Body training is not part of a PhD programme; however, it is well supported by many professors and PIs, who I thank a second time. And regarding Goethe's language, I recall myself saying a year after some hard moments: "German has saved my life, and so my PhD". It could guarantee tangible rewards after made efforts, something that PhD has been hardly able to offer, according to my view.

All in all, I can admit it was a good experience, the PhD. Unfortunately, you say it afterwards only because in the meanwhile you try to forget you are in there, similarly to any other real deep relationships you live one-to-one and in a cosmic intrinsic solitude.

A córar e cagàr a sa sa smèrda i garìt.

By running and emptying the bowels at the same time,  
you make your heels dirty.

---

Emilian popular wisdom

Quant'è bella giovinezza  
che si fugge tuttavia!  
Chi vuole esser lieto, sia,  
di doman non c'è certezza.

How is beautiful youth  
that it flees yet!  
Who wants to be glad, let her be,  
about tomorrow there is no  
certainty.

---

Lorenzo De' Medici

Ho dentro la tempesta che desidera tempesta.

I have got inside the storm that desires a storm.

---

Myself

The question is: have I learned anything about life. Only that human beings are divided into mind and body. The mind embraces all the nobler aspirations, like poetry and philosophy, but the body has all the fun. The important thing, I think, is not to be bitter. You know, if it turns about that there is a god, I don't think that he is evil, I think that the worst thing you could say about him is that he is, basically, an underachiever. After all, there are worse things in life than death. If you've ever spent an evening with an insurance salesman, you know exactly what I mean.

---

Woody Allen

